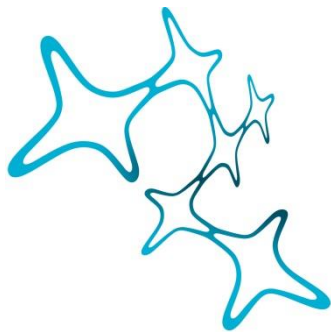


DISCOVERING NOVEL MECHANISMS OF HUMAN
CORTICAL DEVELOPMENT & DISEASE
USING *IN VIVO* MOUSE MODEL AND *IN VITRO*
HUMAN-DERIVED CEREBRAL ORGANOIDS

Isabel Yasmin Buchsbaum



Graduate School of
Systemic Neurosciences

LMU Munich



Dissertation at the
Graduate School of Systemic Neurosciences
Ludwig-Maximilians-Universität München

April 2019

Supervisor and first Reviewer:
Dr. Silvia Cappello
Developmental Neurobiology
Max Planck Institute of Psychiatry

Second Reviewer: Prof. Dr. Elisabeth Binder
External Reviewer: Dr. Felipe Ortega de la O

Date of Submission: 10th April 2019
Date of Defense: 22nd July 2019

ABSTRACT

This thesis combines three research studies with the common interest of identifying novel mechanisms underlying human cortical development. This aim is pursued from different angles, always basing the investigations on human induced pluripotent stem cell-derived 2D and 3D *in vitro* model systems that are partly combined with *in vivo* studies in the developing mouse cortex. Namely, in the pieces of work combined here, we 1) bring to light a neurodevelopmental role of a gene already implicated in adult nervous system function, 2) discover a novel mechanism that fine-tunes human neurogenesis, and 3) identify a novel gene whose mutations lead to a malformation of cortical development. The entirety of this work thus adds several aspects to the existing knowledge.

In the first study, we identified a neurodevelopmental function of a gene mutated in patients with the progressive gait disorder hereditary spastic paraplegia (HSP). In this group of inherited neurodegenerative diseases, mutations in lipid, mitochondrial, cytoskeletal or transport proteins lead to degeneration of primary motor neurons, which, due to the length of their axons, are particularly sensitive to disruption of these processes. Here, we generated cerebral organoids (COs) derived from HSP patients with mutations in *SPG11* coding for spatacsin. Previous work had shown impaired proliferation of *SPG11* patient-derived neural progenitor cells (NPCs). We found a proliferation defect also in CO NPCs, leading to a thinner progenitor zone and premature neurogenesis due to increased asymmetric progenitor divisions, along with smaller size of patient-derived COs. Molecularly, we found a decrease in deactivated GSK3 β and increase in P- β catenin at the basis of the observed proliferation/neurogenesis imbalance. We thus confirmed the neurodevelopmental role of *SPG11* that had previously been suggested from 2D human *in vitro* findings. Both the observed reduction in proliferating progenitors and in organoid size were rescued through inhibition of GSK3 β , with the Food and Drug Administration (FDA) approved compound tideglusib only affecting patient COs. These rescue experiments thus stressed the opportunity that COs represent for drug testing and translation of findings to precision medicine.

In the second study, we investigated the role of a novel posttranslational modification (PTM) termed AMPylation in neurogenesis. Using a novel probe for the detection of AMPylated proteins and a combination of mass spectrometry-based proteomics, immunohistochemistry, and acute interference with the expression of the AMPylating enzyme, we made several interesting findings: AMPylation takes place on a cell type-specific set of proteins, is responsive to the predominant environmental condition, and both AMPylator and targets localize to cell type-specific intracellular localizations. During the process of neuronal differentiation, the set of AMPylated proteins is completely remodeled, with a very high number of unique targets in neurons. These include metabolic enzymes as in all analyzed cell types and, additionally and specifically, cytoskeletal and motor proteins. Cytoskeletal and motor proteins in neural progenitors and neurons are known to be differentially modified by several PTMs whose correct establishment is highly important during neurodevelopment; AMPylation may thus be an additional one. To assess the role of AMPylation in neurodevelopment, we manipulated the expression of the AMPylating enzyme FICD in COs. Downregulation kept cells in a proliferating progenitor state, whereas overexpression increased neurogenesis. We thus suggest AMPylation as a novel PTM fine-tuning neurogenesis.

The third study focused on the identification of new mechanisms underlying cortical malformations, aiming at a better understanding of how the human brain develops. In patients with periventricular heterotopia (PH), a neuronal migration disorder in which a subset of neurons fail to migrate to the developing cortical plate and instead form nodules of grey matter lining the lateral ventricles as their site of production, biallelic mutations in *endothelin converting enzyme 2 (ECE2)* were identified as candidate causative. Combining *in vitro* and *in vivo* models, we found a role for *ECE2* in neuronal migration and cortical development. In the absence of *ECE2*, several processes of general importance to proper neuronal migration were disrupted. Namely, changes in progenitor cell polarity and morphology and in apical adherens junctions led to their delamination, restricting their use as a scaffold for neuronal migration. This resulted in ectopic neurons reminiscent of nodules in PH. Besides a deregulation of cytoskeletal, polarity, and apical adhesion proteins, extracellular matrix (ECM) proteins were reduced in absence of *ECE2*, suggesting its role in ECM production and underlining the necessity of ECM components for proper neuronal migration during cortical development. Moreover, we detected differential phosphorylation of several cytoskeletal, motor and adhesion proteins in the absence of *ECE2*, which is functionally in line with the former findings and suggests an additional involvement of *ECE2* in the regulation of PTMs.

Altogether, the studies presented here underline the heterogeneity and complexity of pathways and mechanisms that contribute to human cortical development and its disorders, converging on the regulation of cytoskeleton and transport within the involved cells and of the ECM on their outside.

ACKNOWLEDGEMENTS

Before starting this PhD, I never considered alternative routes and not do a PhD. Not for the sake of the title: I took it for the natural way to go if you want to do science, which is what I have wanted since my childhood. But then, facing the reality of failures and ups and downs of the PhD life, I more than once thought about quitting it. It was thanks to many people that I overcame these hurdles and now hopefully finish this big chapter of my life with success. I would like to express my heartfelt gratitude...

to Silvia, for being the most enthusiastic and positive supervisor I could have imagined, for supporting my New Zealand experience and attendance of numerous conferences, for enabling me to work on several different projects and sharing my fascination of diversity, for your scientific advice and encouragement, and for believing in me and my work. Thank you for your always open door and ear and for readily sharing your own experiences – also outside the sciences.

to Stephen and Adam, for guiding me into the PhD and enriching me with an invaluable experience on the other side of the world.

to my TAC members Elisabeth, Magdalena and Jürgen, for supporting and steering my work with fruitful discussions and to Felipe for reviewing this thesis – thanks for your time and support.

to the GSN and the GSN team, for selecting me for the Fast-track PhD program, for their friendly support both with advice and financially, which enabled me to make my New Zealand experience and to visit international conferences, and for this scientific and cultural inspiration and supportive network that the GSN represents.

to my collaborators in all projects, especially to Pavel and Stephan, for the great teamwork and constructive discussions and for broadening my angle of view.

to Magdalena and her group at the Helmholtz, for housing us while our lab at the MPI was being renovated.

to Ane, for many hours and meters of height with precious talking, a huge backpack and a camera in our Alps and the Taiwanese mountains, and for proofreading my discussion. ¡Muchas gracias mi amiga!

to Johannes, for being great company in the beginning of my PhD, for teaching me the *in vitro* methods and for proofreading my discussion – danke; to Grazia, for your support in the hardest phase of the ECE2 project – mille grazie; to Christina, for sharing your *in vivo* expertise and always knowing advice – ευχαριστώ; to Timo and Barbara for your technical support. And thanks to all yet unmentioned members of the C-lab, the A-, Z- and Binder-labs, and Marisa and her group for sharing and enriching this section of my life.

to Antonietta – without your coffee and smile, life at the MPI would not have been the same!

to Sara, for introducing me to Lindy Hop, which became a great source of positive energy for me; to my roomies Ines, Patrick, and Grandma Hilde, and to my Munich

ACKNOWLEDGEMENTS

family of friends, for believing in me and being there for me with uplifting chats, good coffees and food, handicraft sessions, game nights, and innumerable hugs.

to Babaganouch, for teaching me not to let the failures close to me and that “time will graduate everyone”.

to my parents and my sisters, for your steadfast support and love over this far too far distance, for enduring my fluctuations and complaints, and for believing in me and my dreams not only during these last years but throughout my whole life.

an Andrej, mein Lieblingsmensch. Danke, dass Du an meiner Seite bist, mich durch die stressigen letzten Monate begleitet, getragen, aufgemuntert und ausgehalten hast, und mich in jeder Hinsicht unterstützt. Я люблю тебя и с нетерпением жду нашего будущего!

TABLE OF CONTENTS

Abstract	i
Acknowledgements	iii
Table of Contents	v
1. INTRODUCTION	1
1.1. Cortical Development and Evolution	1
1.1.1. Neurogenesis	1
1.1.2. Neuronal Migration	2
1.1.3. Cytoskeleton and Associated Proteins in Neurodevelopment	5
1.1.4. Posttranslational Modifications regulate Cytoskeletal Dynamics	10
1.1.5. Evolution: Differences between the Mouse and Human Neocortex	15
1.2. Neuronal Migration Disorders – a Heterogeneous Group of Cortical Malformations	18
1.2.1. Traditional Classification of MCDs and NMDs	18
1.2.2. Genetic, Cellular & Physiological Heterogeneity of NMDs	20
1.3. Animal Models of Cortical Development: Their Relevance, Advantages and Limitations	24
1.3.1. Mouse Models of NMDs	24
1.3.2. Non-Rodent Models of Cortical Development	25
1.4. <i>In Vitro</i> Models of Cortical Development	26
1.4.1. 2D <i>In Vitro</i> Models	26
1.4.2. 3D <i>In Vitro</i> Models of Increasing Complexity	27
1.4.3. From the Dish back to the Mouse: Transplantation	28
1.5. Modelling Human-Specific Features of Neurodevelopment and its Disorders <i>In Vitro</i>	29
1.6. About this Thesis	33
2. Human <i>SPG11</i> Cerebral Organoids Reveal Cortical Neurogenesis Impairment	35
2.1. Citation	36
2.2. Author Contributions	36
3. FICD Activity and AMPylation Remodelling Modulate Human Neurogenesis.	61
3.1. Citation	62
3.2. Author Contributions	62
4. <i>ECE2</i> Regulates Neurogenesis and Neuronal Migration during Human Cortical Development	127
4.1. Citation	128

TABLE OF CONTENTS

4.2. Author Contributions	128
5. DISCUSSION	165
5.1. SPG11 - A Developmental Role for a Known Neurological Disease Gene	165
5.2. AMPylation - A Novel Parameter to Fine-Tune Neurogenesis	171
5.3. ECE2 - A Novel PH Candidate with Old and Novel Disease-Causing Mechanisms	181
5.4. Summary of the Knowledge gained in this Thesis	192
REFERENCES	195
APPENDIX	223
I. List of Figures	223
II. List of Tables	224
III. List of Abbreviations	225
IV. List of Publications	227

1. INTRODUCTION

The central nervous system was portrayed as an intricate network with a highly complex organization already more than 100 years ago by Ramon Y Cajal. The human cerebral cortex represents the largest region of the cerebrum – the most highly developed part of the human brain. It plays vital roles in processing and integrating information from all bodily senses to result in social and motor behaviors, in planning and organization, and in determining intelligence and personality (Kandel, 2000). The series of events involved in its development are thus highly coordinated and regulated. Their disruption can lead to malformations of cortical development (MCDs), affecting the structure and functioning of the cerebral cortex, and can cause a wide range of physiological and functional consequences. Indeed in humans, MCDs are a recognized cause of developmental delay, intellectual disability and epilepsy, and are also associated with dysmorphic features (Guerrini and Dobyns, 2014; Jamuar and Walsh, 2015; Romero et al., 2018).

This introduction shall set the basis for understanding the research results presented and discussed in this thesis. To this end, it will commence with an introduction into cortical development and evolution with spotlights on mechanisms that are subject to the presented investigations, namely cytoskeletal components and their regulation by post-translational modifications (PTMs). With this background knowledge at hand, additional attention will be directed to introducing MCDs with a focus on neuronal migration disorders (NMDs) and *in vivo* and *in vitro* model systems applied for their investigation. Parts of the introduction have been adapted from my recent review (Buchsbaum and Cappello, 2019) with permission from *Development* and were expanded to cover all basics of the different presented research studies.

1.1. CORTICAL DEVELOPMENT AND EVOLUTION

The cerebral cortex forms through a series of tightly regulated processes starting with the generation of neurons through neurogenesis (Götz and Huttner, 2005; Noctor et al., 2004; Sun and Hevner, 2014), followed by neuronal migration, neuronal differentiation, and their spatial organisation into networks (Kriegstein and Noctor, 2004). Neurogenesis and neuronal migration will be shortly introduced here, followed by some regulatory mechanisms.

1.1.1. NEUROGENESIS

Neurogenesis is the process in which neurons are generated from stem and progenitor cells. The first structure that forms in early brain development is the neural tube, consisting of a single pseudostratified layer of neuroepithelial cells (NECs), which are the primary neural stem cells (NSCs) that will give rise to all brain structures in the anterior end of the neural tube. The pseudostratified appearance originates from a process called interkinetic nuclear migration (IKNM): in synchronization with the cell cycle, nuclei move basally (G1 to S-phase) within the cell to acquire most basal positions for their S-phase and move back to the apical surface during the G2-phase, to then undergo mitosis at the apical surface. This makes room for more cells per area, increasing the density of the neuroepithelium (Ohnuma and Harris, 2003). Polarized NECs are connected to both inner

(apical = future ventricular) and outer (basal = future pial) surfaces at which they will generate the ventricular zone (VZ) and cortical plate (CP) (Stiles and Jernigan, 2010). After a phase of symmetric, self-renewing proliferations (around embryonic day 9 (E9) in mouse cortical development) enlarging the forebrain progenitor population, NECs acquire more fate-restricted identity and convert to apical radial glia cells (aRG; around E11). These aRG also undergo IKNM and keep their apico-basal polarity (see **1.1.3.**) and connections to both ventricular and pial surface. As neural progenitor cells (NPCs), they continue to increase the founder stem cell pool in the VZ by symmetric divisions until E13, and then switch to more asymmetric divisions to produce neurons directly (direct neurogenesis) or via basal intermediate neural progenitors (bIPs; indirect neurogenesis). Multipolar bIPs delaminate from the apical and basal surface and form an additional neurogenic zone, the subventricular zone (SVZ) (Götz and Huttner, 2005; Lui et al., 2011; Taverna et al., 2014).

Neural progenitors in the VZ and SVZ, located adjacent to the lateral ventricles of the mammalian brain, generate excitatory projection neurons and inhibitory interneurons in distinct regions (**Fig. 1A**). In mouse, excitatory neurons are generated from aRG and bIPs in the dorsal VZ and SVZ (**Fig. 1B**). In humans, aRG generate more heterogeneous populations of basal proliferative progenitors (BPs): in addition to bIPs, they give rise to a second population of RG that lose their apical anchoring. While keeping their basal process, these basal radial glia (bRG) move their cell body into the outer SVZ (oSVZ), forming an additional germinal zone (**Fig. 2**). BRG were recently identified as human-enriched progenitor population that is essential for the expansion of the cerebral cortex and the formation of folds, a process called gyrification (Fietz and Huttner, 2010; Hansen et al., 2010; Reillo et al., 2011) (see **1.1.5.**).

While excitatory neurons are generated in the dorsal germinal zones, inhibitory GABAergic interneurons are specified in the distant medial and caudal ganglionic eminences (GEs), which are part of the ventral telencephalon (Anderson et al., 2001) (**Fig. 1A**). Within the mouse GEs, a RG-containing VZ develops, as well as a SVZ that contains bIPs and numerous subapical progenitors (SAPs) (Pilz et al., 2013). BIPs and SAPs undergo 60-70% of all mitoses found in the GEs, thus expanding the neural progenitors and with that the resulting interneuron population prior to its migration.

Neurogenesis is followed by astrogliogenesis by the same NPCs and towards the end of cortical development, the majority of neural progenitors symmetrically divide and give rise to two cells that will differentiate, thereby eventually depleting the NPC pool (Caviness and Takahashi, 1995).

1.1.2. NEURONAL MIGRATION

As postmitotic neurons arise from NSCs and NPCs localized in the dorsal and ventral VZs and SVZs, they are required to migrate towards their future location on the outer surface of the cortex (**Fig. 1A, B**). Neuronal migration is thus an essential process for the development of the mammalian nervous system (Kriegstein and Noctor, 2004). In humans and rodents, a highly coordinated and regulated series of neuronal migration events is required to establish the different laminae of the cortex.

Excitatory neurons of the dorsal cortex have their origin in the dorsal VZ and are thus required to migrate in basal direction through different modes of radial migration, which is perpendicular to the apical surface (**Fig. 1A**). At early stages of neurogenesis in mice, new-born deep-layer excitatory neurons move basally towards the marginal zone (MZ) by

somal translocation. In this RG-independent neuronal migration mode, neurons residing in the VZ extend a long radially directed leading process towards the pial surface; the leading process is attached to the pial surface and progressively shortens to pull the soma up to the developing CP (Nadarajah et al., 2001; Nadarajah et al., 2003). Once the cortex becomes thicker, new-born neurons shift to multipolar migration, a slow and undirected migration mode which functions through extension and retraction of multiple processes, until they reach the intermediate zone (IZ) (Tabata and Nakajima, 2003). In the upper SVZ, they undergo a morphological transition from multipolar to bipolar shape and get oriented for radial migration. Neurons then begin directed radial migration to the CP, using both glia-independent somal translocation and RG-dependent locomotion (**Fig. 1B**). Locomoting neurons use RG fibers as a migratory scaffold (Nadarajah et al., 2001; Rakic, 1972), attaching to their basal process, and move through the thickness of the developing CP. Migration along RG represents the most prominent mode of migration to the CP (Rakic, 2009). Bipolar locomoting neurons bear a leading process, preceded by a growth cone that explores the microenvironment, and a thin trailing process, which will become their axon (Noctor et al., 2004). In a cyclic, saltatory movement pattern, the leading process extends and swells before the nucleus is pulled up into the leading neurite and, finally, the trailing process is retracted before a new cycle begins. The nuclear movement, called nucleokinesis, is coupled with movement of centrosomes within the neurons (Marín, 2013), which position ahead of the nucleus to pull it upward (see also **1.1.3**) (Ayala et al., 2007).

On their way towards the pia, attracted by Cajal Retzius cells in the MZ, waves of locomoting neurons pass earlier-born ones, thus forming the six layers of the cortex in a birth-date-dependent and inside-out manner (Sun and Hevner, 2014). During this lamination, migrating neurons sense local environmental cues to establish their layer fate (Kriegstein and Noctor, 2004), such as the extracellular matrix (ECM; secreted macromolecules serving cell-cell communication, cell adhesion, proliferation and differentiation (Long and Huttner, 2019)) glycoprotein reelin, produced by Cajal Retzius neurons, that is crucial for neuronal correct positioning (D'Arcangelo et al., 1995). Beneath the MZ, excitatory neurons switch to RG-independent terminal translocation, resembling early somal translocation, to reach their final position within the CP where they terminate their migration (Sekine et al., 2011).

Inhibitory GABAergic interneurons initially migrate tangentially, that means in parallel to the ventricular surface, in several streams over long distances from their origin in the ventral telencephalon into the cerebral cortex (**Fig. 1A**). At early and mid-embryonic stages, MGE-derived streams of interneurons enter the dorsal CP through the MZ and subplate and through the SVZ and lower IZ, respectively. At late embryonic stages, a MGE-derived stream enters the dorsal cortex through the MZ, while a LGE-derived one crosses through the SVZ (Marín, 2013). In the cerebral cortex, interneurons switch to radial migration to disperse and integrate into the various cortical layers (**Fig. 1B**) (Anderson et al., 1997; Peyre et al., 2015; Silbereis et al., 2016; Wonders and Anderson, 2006). Remarkably, although the distance that they need to overcome is quite different, excitatory projection neurons and inhibitory interneurons generated at the same time will ultimately reach the same layer in the CP. This was suggested to originate from their ability to sense the same layer-fate determining microenvironmental cues (Marín and Rubenstein, 2003).

An additional route of tangential migration goes from the LGE to the olfactory bulb and persists into adulthood in mouse, where it is called rostral migratory stream (Kriegstein and Noctor, 2004).

Ultimately, once neurons have reached their final position within the CP, they differentiate and establish dendritic and axonal connections characteristic of mature cortical neurons (Ohnuma and Harris, 2003).

The correct establishment of the cortical layers by neuronal migration is tightly controlled by a variety of extracellular and intracellular signals that regulate the actin and microtubule cytoskeleton, as well as their dynamics and interplay (Stouffer et al., 2015). The following paragraphs are thus dedicated to the cytoskeleton and associated proteins, as well as their regulation by posttranslational modifications (PTMs).

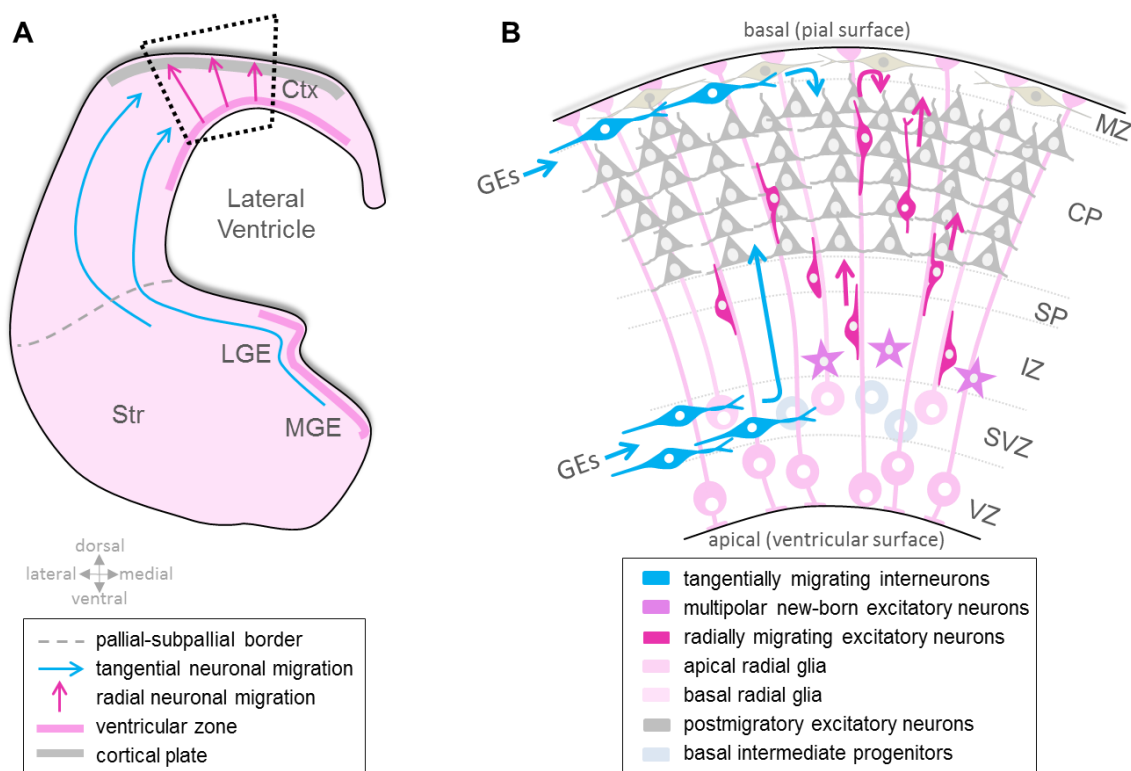


Figure 1: Mammalian cortical development exemplified in the mouse. **A**, Schematic of a coronal section of the early developing anterior telencephalon of the mouse at E14 as example mammal, showing neurogenic ventricular zones and routes of neuronal migration. The black dotted box is enlarged in panel **B**. **B**, Schematic of the cell composition of the developing mouse cerebral cortex showing radially migrating excitatory neurons and interneurons that enter the cortex tangentially and then switch to radial migration within the dorsal cortex (Abbreviations: Ctx, cerebral cortex; CP, cortical plate; GEs, ganglionic eminences; E, embryonic day; IZ, intermediate zone; LGE, lateral ganglionic eminence; MGE, medial ganglionic eminence; MZ, marginal zone; SP, subplate; Str, Striatum; SVZ, subventricular zone, VZ, ventricular zone). *Adapted from* (Buchsbbaum and Cappello, 2019) *with permission from Development*.

1.1.3. CYTOSKELETON AND ASSOCIATED PROTEINS IN NEURODEVELOPMENT

We have seen that neurodevelopment requires precise control of behaviors of different cell types. Control of adhesion, morphology, proliferation, motility, intracellular transport, and many other processes is exerted via pathways ultimately converging on cytoskeletal regulation. Here, the neurodevelopmental functions of the RG and neuronal cytoskeletal components actin and microtubules (MTs), as well as their associated proteins, shall be introduced. Many aspects described here will set the basis for the studies presented in **Chapter 3** and, especially, in **Chapter 4**. Some processes of neurogenesis and neuronal migration touched upon above will be explained in more detail in the following, but only few examples of molecules were chosen for each described function as an extensive review would overshoot the mark of this introduction.

Actin, microtubules, and associated proteins. The actin cytoskeleton is engaged in the movement of cellular components such as vesicles and organelles, in cell signaling, and in the establishment and maintenance of cell junctions and cell shape. Actin-associated proteins regulate the formation of actin filaments (F-actin: filamentous actin) from monomeric globular actin (G-actin), such as small GTPases like Rho GTPases (e.g. RhoA, Cdc42, and Rac1), which function as master regulators of the cytoskeleton (Cappello, 2013; Gonzalez-Billault et al., 2012). They modulate and support the actin cytoskeleton in its diverse functions in cell polarity, adhesion, division, and migration (Lian and Sheen, 2015). While for example RhoA and Cdc42 are essential for the assembly and stability of localized actin cables, F-actin binding and crosslinking filamins are responsible for anchoring membrane proteins to the actin cytoskeleton (Gorlin et al., 1990). The scaffolding protein filamin-1 (FLNA), in turn, has a huge number of known interaction partners including cell adhesion proteins (integrins) and cell cycle regulators (Lian and Sheen, 2015). Actin fibers additionally serve cargo transport, which is mediated by myosins (Semenova et al., 2008).

The MT cytoskeleton is built by internally polarized tubes assembled from α - and β -tubulin heterodimers and acts as physical support to shape the different cell types of the developing and adult brain. MTs originate from MT organizing centers like the centrosome and from there reach into the fine cell structures such as neuronal processes. They function not only as structural scaffold, though – they serve as tracks for directed transport and as transducers of force generated by MT-based motors, which in turn play important roles in diverse processes such as nucleokinesis and protrusion and retraction of processes (Sakakibara et al., 2013). Cargo transport along MTs functions through ATP-hydrolyzing minus-end directed dynein motors and (mostly) plus-end directed kinesins, all of which influence MT dynamics and are pivotal in neuronal morphogenesis and migration. Mutations in tubulin genes and such affecting genes encoding MT-related proteins lead to a spectrum of brain defects and disorders summarized with the term “tubulinopathies” (see also 1.2.2). The stability and dynamics of the MT cytoskeleton is regulated by “classical”, e.g. MAP1A, MAP1B, MAP2 and Tau (*MAPT*), and “non-classical” microtubule-associated proteins (MAPs), e.g. Lis1, Dcx, Ndel1, dynein complex components, and dynactin (Dehmelt and Halpain, 2004; Moores et al., 2004; Morris et al., 1998).

The coordination between actin and MT cytoskeleton is further regulated by crosslinking proteins. Neuron-specific MAPs like MAP1B and MAP2, for instance, can bind both microtubules and F-actin (Dehmelt and Halpain, 2004).

Role in polarity and adherens junctions. As already mentioned, NECs and derived aRG are bipolar cells. Their polarity and morphology is generated by differential distribution of cytoskeletal components and of cell fate determining proteins such as strictly apically localized Notch (Del Bene et al., 2008). F-actin fibers are selectively concentrated at the apical side along the ventricles where, together with adhesion molecules, they form a tight but dynamic belt. These apical cell-cell connections, consisting of membrane-spanning cadherins (such as N-cadherin), cytosolic catenins (e.g. β -catenin and α -E-catenin) and actin microfilaments (Mège et al., 2006), are called tight junctions in the case of NECs and – with different molecular constitution – adherens junctions (AJ) in aRG. For the function of aRG, AJs and the apico-basal polarity they uphold play a crucial role (Florio and Huttner, 2014). This becomes obvious from interfering with AJ components, which results in drastic changes in cerebral development due to disruption of the RG scaffold integrity (Kadowaki et al., 2007; Schmid et al., 2014; Yamamoto et al., 2015) (see **1.2.2**). Actin filaments and associated proteins regulate these cell-cell adhesions and serve as binding partners for polarity proteins. The following examples shall illustrate this. Numb, for instance, interacts with E-cadherin to regulate its localization to cell-cell junctions and engages the polarity complex Par3-aPKC-Par6 by binding to Par3 (Wang et al., 2009b). Actin associated Rho GTPases are involved in remodeling of the actin cytoskeleton (Etienne-Manneville, 2004; Gonzalez-Billault et al., 2012), together with their effectors, such as non-muscle myosin II, which is indispensable both in cell polarity and adhesion (Ma and Adelstein, 2014). Lgl1, an interactor of both non-muscle myosin II and Par6 in lateral junctions, is needed for AJ integrity, cell polarity and with that also for RG proliferation, morphology, and function as locomotion scaffold (Assémat et al., 2008; Zhang et al., 2019). Afadin (encoded by *Mlt4*) is another AJ-to-actin scaffolding protein important for the maintenance of AJs, RG apical endfeet and the RG scaffold (Yamamoto et al., 2015). The MT cytoskeleton is also associated with apical AJ: MT-based transport of (N)-cadherin-containing vesicles by kinesin supplies and supports AJs (Mary et al., 2002).

In addition to cell-cell anchoring and polarity maintenance, AJ proteins can be directly involved in signal transduction: AJ-localized β -catenin, which links cadherins to actin filaments, is at the same time an essential intracellular component of the Wnt signaling cascade in RG that regulates cell fate determination of progenitor self-renewal *versus* neuronal differentiation in the developing forebrain (Hirabayashi et al., 2004). In the study presented in **Chapter 2**, this pathway was identified as misregulated, leading to reduced NPC self-renewal.

Primary cilia. Another structure involved in apico-basal polarity of aRG that shall be briefly introduced here are primary cilia. These microtubule-based protrusions are maintained apically in aRG, where they can sense signals from the cerebrospinal fluid in the ventricles (Johansson et al., 2013). Primary cilia function as key integrators of such extracellular ligand-based signals, e.g. the neurodevelopmental sonic hedgehog and Wnt pathways. Arl13b, a small GTPase enriched in primary cilia, plays a critical role in the establishment of RG polarity (Higginbotham et al., 2013). Through these functions, primary cilia are involved in the regulation of neuronal cell fate, migration and differentiation (Guemez-Gamboa et al., 2014; Han et al., 2008). In addition to aRG in the developing cortex, motile and immotile (primary) cilia are present on cells of nearly every major body organ. To this end, disruptions of genes engaged in the cilia structure, their anchoring in basal bodies, centrosomes, or involved in their sensing and signaling ability lead to disorders affecting diverse organ systems, summarized with the term

“ciliopathies”. This emphasizes the importance of the cilium in development and homeostasis (Goetz and Anderson, 2010).

Role in proliferation and cell fate. As indicated earlier, cytoskeletal proteins also regulate cell proliferation and cell fate specification (Taverna et al., 2014), e.g. by symmetric *versus* asymmetric inheritance of cell fate determining proteins like Notch. Distribution of intracellular signals works via actin polarization and actin-dependent trafficking, as well as degradation of cell fate determinants like integrins and cadherins (Cappello et al., 2006). For example, conditional deletion of *RhoA* and *Lgl1* causes accelerated NPC proliferation and reduced cell-cycle exit (Katayama et al., 2011; Zhang et al., 2019) and so does acute downregulation of the cadherins *Fat4* and *Dchs1* (Cappello et al., 2013). Conditional deletion of *Cdc42* results in increased basal mitoses, which induces aRG-to-BP fate change (Cappello et al., 2006).

MTs function during cell division in the segregation of the chromosomes (Wloga et al., 2017). MT-based motors additionally participate in the up-and-down movement of the nucleus during IKNM of aRG with basally and apically directed movements involving kinesins and dyneins, respectively (Taverna and Huttner, 2010).

While symmetric proliferative division of NSCs and NPCs results in two equal daughter cells through symmetric inheritance of polarity factors, asymmetric division gives rise to IPs or neurons directly. The first step following asymmetric neural progenitor division is the loss of the apical connection, a process called delamination. Delamination was shown to involve AJ disassembly and abscission mediated, among others, by acto-myosin (Kasioulis et al., 2017). The centrosome translocates and both actin and MT cytoskeletal components and their cross-linker drebrin orchestrate delamination through actin fiber constriction and MT condensation (Kasioulis et al., 2017). Recently, it was shown that the centrosomal protein AKNA is also required during the delamination process of aRG: As an organizer of centrosomal microtubule nucleation and growth, high levels of AKNA promote the detachment from neighboring cells to trigger their differentiation to SVZ BPs and it further regulates the exit from the SVZ (Camargo Ortega et al., 2019).

Role in neuronal migration. The polarisation and locomotion of new-born neurons necessitates a complete remodeling of the cell morphology. For polarization, for instance, N-cadherin, reelin, and Rap1 are needed to orient multipolar neurons (Jossin and Cooper, 2011), Cdk5 and FlnA are required for neuronal multipolar-to-bipolar transition (Nagano et al., 2004), and Cdc42 forms a complex with the polarizing factors Par3 and Par6 and recruits these to the leading edge to guide the reorientation of the MTs and centrosome (Lian and Sheen, 2015).

Neuronal migration represents a highly dynamic process involving adhesion, extension, protrusion of filopodia and lamellipodia at the leading edge, and formation of a contractile structure for retraction of the rear edge. All these processes again require remodeling of the cytoskeleton and actin and MTs function in close association (Rottner and Stradal, 2011). In the tip of growth cones, actin cytoskeletal remodeling results from sensing of extracellular signals to determine the direction of migration. Microtubules also extend into the periphery, where they interact with Rho GTPases, which then produce changes in actin dynamics (Dehmelt and Halpain, 2004). Actin, in turn, mediates the alignment of MTs from the growth cone down to the neurite shaft with the help of MAPs that also bind actin (Dehmelt and Halpain, 2004; Schaefer et al., 2002). Moreover, MT-based transport serves the shuffling of membrane to the leading edge for its extension (Ayala et al., 2007).

For the upward movement of the nucleus, a process called nucleokinesis, MTs and MT-based motors are highly important. Originating at the centrosome that gets positioned in front of the nucleus, MTs extend to and engulf the nucleus in a MT cage by attaching to the nuclear envelope, which is facilitated by Ndel1 (Guo et al., 2006), and on the other side extend into the leading process (Tsai and Gleeson, 2005; Xie et al., 2003). The centrosome moves up into the neurite and, engaging dynein, polarized MTs in the leading edge produce a pulling force onto the nucleus (Sakakibara et al., 2013; Tanaka et al., 2004). The centrosome- and MT-associated proteins Lis1, Ndel1 and dynein promote the integrity of MT cytoskeleton during nucleokinesis (Sapir et al., 1997). At the same time, below the nucleus, RhoA promotes the retraction of the rear end of the neuron and advances the translocation of the nucleus and, via contraction of acto-myosin, generates a pushing force (Ayala et al., 2007; Lian and Sheen, 2015; Schaar and McConnell, 2005).

For the formation of short-lived focal adhesion contacts of the neuronal leading edge membrane on the RG scaffold membrane (or in translocating neurons for adhesion to ECM components), actin and associated components are also needed (Lian and Sheen, 2015). Local disruption of actin fibers along the leading process therefore disrupts somal translocation and neuronal migration (He et al., 2010). In mice lacking Flna, for example, migration into the CP is slower and their adhesion to the ECM is impaired (Zhang et al., 2013). MAPs also act synergistically to support neuronal migration - and in mouse deletion mutants, both neuronal migration and neuronal morphology are disrupted (Dehmelt and Halpain, 2004).

Role in intracellular trafficking. Cytoskeleton-based intracellular transport processes are required throughout all the described processes of RG polarity and AJs, polarization of neurons for locomotion, and RG-guided or -independent neuronal migration (Rodriguez-Boulan et al., 2005). Dynamic and directional vesicle trafficking is involved in the transmission of extracellular signals into the cytoplasm and nucleus, for degradation of cell cycle associated proteins, for exocytosis. And cytoskeleton-associated proteins again mediate this trafficking. Rho GTPases, for example, act in endocytosis - the internalization of plasma membrane and extracellular molecules (Ridley et al., 2003). They bind FlnA and direct various aspects of intracellular actin dynamics, which are required for endosomal vesicle transport (Cappello et al., 2006; Katayama et al., 2011). Vesicle transport from the Golgi complex to the plasma membrane for exocytosis requires filamins, myosins and Cdc42 for myosin-driven movement along actin filament tracks. The interplay of FlnA with the guanine exchange factor Big2 orchestrates this process (Zhang et al., 2012a). The rate of intracellular trafficking thus influences the turnover of proteins and membrane towards the leading edge and with that the migration speed of neurons.

Role of SPG11. The tight regulation of the cytoskeleton and its associated proteins becomes especially obvious when they are dysregulated as occurs in neurodevelopmental disorders such as NMDs (see **Chapter 1.2; Chapter 4**) and mental disorders or in neurodegenerative diseases. A spectrum disorder classified as neurodegenerative is Hereditary Spastic Paraplegia (HSP). HSPs are clinically and genetically heterogeneous progressive gait disorders with mutations identified in more than 60 genes that have been linked to HSPs with both dominant and recessive inheritance modes, and overlapping phenotypes between HSPs and other neurodegenerative disorders (Boutry et al., 2019; Elert-Dobkowska et al., 2019). Pathophysiological mechanisms include abnormal intracellular transport, changes in

endoplasmic reticulum (ER) shape, defects in lipid metabolism, and abnormal lysosome physiology, autophagy, myelination, or mitochondrial function. All of these ultimately lead to the loss of primary motor neurons and other neurological conditions (Boutry et al., 2019; Crosby and Proukakis, 2002). Due to the length of their axons, which require constant maintenance, corticospinal motor neurons are particularly sensitive to disruptions in energy metabolism, cytoskeletal or vesicle trafficking processes. In the study presented in **Chapter 2**, we focused on HSP caused by mutations in *Spastic Paraplegia Gene 11 (SPG11)*, coding for spatacsin. Mutations in *SPG11* account for about 25% of autosomal recessive HSP cases and progressive spastic paraparesis co-occurs with thin corpus callosum, cortical atrophy and mental retardation, and may also cause rare forms of Charcot-Marie-Tooth disease and progressive juvenile-onset amyotrophic lateral sclerosis (Faber et al., 2018; Mishra et al., 2016). Even cases of association with juvenile-onset parkinsonism were reported (Anheim et al., 2009). The affected protein, spatacsin, contains a transmembrane domain and colocalizes with synaptic vesicles, MTs and actin in both neuronal axons and dendrites, even in the most distal tips of filopodias and membrane protrusions (Pérez-Brangulí et al., 2014). Functionally, spatacsin was implicated in anterograde axonal vesicle transport processes (towards the plus end of MTs) by influencing kinesin expression and MT turnover (Pérez-Brangulí et al., 2014). In absence or upon disruption of spatacsin, membranous deposits accumulate within axonal processes (Pérez-Brangulí et al., 2014) and the clearance of lipids from lysosomes is disturbed (Branchu et al., 2017). In addition to engagement in the endolysosomal pathway, a critical role for spatacsin in autophagy was identified (Vantaggiato et al., 2019).

Most research has been conducted on the role of *SPG11* in the dying back of axons that can start as early as in childhood. In our study, we added findings about the role of *SPG11* in neurodevelopment, which was suggested from patients' thin cortical callosum and cortical atrophy. Preceding work identified transcriptional dysregulation of genes associated with cortical development, including callosal developmental pathways and maintenance of neuronal homeostasis, in patient-derived cells, which led to compromised NPC proliferation and neurogenesis (Mishra et al., 2016).

This excursion towards the published study presented in **Chapter 2** highlights again the role of cytoskeleton-based vesicle trafficking in cortical development and maintenance (Pérez-Brangulí et al., 2018).

Role in terminating migration. Once migrating neurons reach their destined position, they are required to stop migration and establish neuronal networks. Examples of extracellular stop signals are laminin and reelin: reelin acts through receptor-mediated activation of intracellular pathways which ultimately stabilize the actin cytoskeleton (Frotscher, 2010) and facilitate the detachment of migrating neurons from the RG scaffold (Ayala et al., 2007). The importance of basement membrane components and receptors for their sensing becomes apparent in disorders in which neurons fail to stop their migration and hence overmigrate (see **1.2.2**).

Regulation of the cytoskeleton. The tight regulation of the cytoskeleton was already pointed out in the context of the numerous intracellular actin- and MT-associated proteins, examples of which were brought in this section. Extrinsic mechanisms influencing the organization and dynamics of actin and MT cytoskeleton are, for example, locally secreted ECM components such as reelin and laminin (see above). Laminin and its integrin receptors play a role in the formation of the basal membrane and the anchorage of RG endfeet (Marín and Rubenstein, 2003). Additionally, long distance

guidance molecules such as Netrins, Semaphorins and Slits influence neuronal motility by eliciting intracellular responses that ultimately influence the actin and MT cytoskeleton. Slit2 and its receptor Robo, for example, guide both tangential and radial migration of neurons via modification of an intracellular pathway that converges on actin regulation (Ayala et al., 2007). Furthermore, neurotransmitters like GABA and neurotrophins represent such extracellular regulators (Behar et al., 2001; Gallo and Letourneau, 2000). Intracellularly, especially MTs and associated proteins are heavily regulated by PTMs.

1.1.4. POSTTRANSLATIONAL MODIFICATIONS REGULATE CYTOSKELETAL DYNAMICS

Many different tubulin genes with tissue- and cell state specific expression lead to diversity in MTs: There are 7 α - and 8 β -tubulin genes known in mice. Alternatively to hollow tube-like MTs, tubulins can build other architectures such as cilium scaffold, basal body or centrioles. To acquire different organizations and dynamics, tubulins have to differ in their properties extending the gene level (Wloga et al., 2017). In addition to the regulation of MT growth, dynamics and stability by MAPs, as was mentioned above (see 1.1.3), PTMs of tubulins and MAPs further contribute to this heterogeneity, increasing the number of “proteoforms” on top of gene expression regulation (Aebersold et al., 2018; Song and Brady, 2015). The numerous PTMs can co-occur and a huge effort has been invested to understand the “tubulin code” of site-specific MT PTMs in defined intracellular locations (Yu et al., 2015). Locally and temporally defined PTMs act as molecular landmarks for proteins that can alter their structure and function, thus increasing the functional diversity of target proteins. These include reversible and irreversible “simple” site-specific PTMs like acetylation and phosphorylation and “complex” branched ones like polyglutamylation and ubiquitination (Aebersold et al., 2018). Most tubulin PTMs target the most variable C-terminal region which lies on the outer surface of MTs and acts in binding MT-interacting proteins. This already indicates a regulation of MT interaction with its binding partners by PTMs (Ayala et al., 2007). Molecular motor proteins also serve many different functions in cargo transport, regulation of MT dynamics, and as mitotic motors. In addition to a plethora of different genes encoding the components of these giant molecular complexes, their mechano-chemical behavior is also modified by PTMs (Muretta et al., 2018). The same accounts for actin: additionally to above mentioned non-covalent regulation of the actin cytoskeleton by associated proteins, widely employed covalent actin PTMs have been identified that regulate the monomer-polymer equilibrium and organization of actin and have been linked to different normal and disease processes (Terman and Kashina, 2013). In the following, some cytoskeletal PTMs shall be introduced together with examples of their function.

Tubulin tyrosination and detyrosination. Most α -tubulins contain a terminal tyrosin. It is needed to form heterodimers with β -tubulins to be assembled into MTs and tyrosinated tubulin (tyr-tub) is thus enriched in newly formed, labile MTs: Highly dynamic MTs in growth cones are rich in tyr-tub. For MT stabilization, the terminal tyrosin is then reversibly removed to give rise to detyrosinated tubulin (detyr-tub), which is abundant in proximal axon shaft segments and in differentiated neurons that contain stable, long-lived MTs (Song and Brady, 2015). Functionally, the tyrosination state of MTs influences their interaction with motor proteins. Detyrosination of α -tubulin is for example specifically required for robust kinesin-2 motility (Sirajuddin et al., 2014).

In a next step, the new terminal glutamate can also be irreversibly removed to result in $\Delta 2$ -tubulin (missing the last 2 amino-acids). $\Delta 2$ -tubulin is enriched in long-lived MTs in neurons, centrioles and primary cilia and may represent > 35% of all tubulin in the brain (Paturle-Lafanechère et al., 1994).

Actin, tubulin and motor acetylation. Acetylation of tubulin occurs on the canonical site Lys40 in α -tubulin, which localizes to the luminal side of MTs, and is distributed along MTs. Like de-tyr-tub, acetylated tubulin (ac-tub) accumulates in postmitotic cells and is associated with long-lived, stable MTs (Song and Brady, 2015). In differentiating neurons, both ac-tub and tyr-tub are thus not uniformly distributed: the ratio of ac-tub over tyr-tub is highest in the shaft of the future axon, suggesting a role for these PTMs in neuronal polarization (Witte and Bradke, 2008). Furthermore, ac-tub is absent from highly dynamic MTs in growth cones during development, but is increasingly found in the distal axon and presynaptic regions with neuronal maturation (Song and Brady, 2015).

The binding of kinesin-1 occurs preferentially on de-tyr- and ac-tub, providing a potential basis for spatial targeting of kinesin-1-based cargo transport (Dunn et al., 2008). The MT-severing protein katanin preferentially binds to and further severs acetylated MT domains (Song and Brady, 2015). Motor proteins can also be acetylated themselves, which may fine-tune their motor behavior to fit specific physiological need. For example, acetylation of kinesin-5 family member Eg5 in mitosis renders it more resistant to dissociation from MTs and increases its motor performance under load, while increasing its propensity to stall – properties required for slow spindle pole separation during mitosis (Muretta et al., 2018).

Acetylation of actin has been identified at many sites throughout the protein, but only N-terminal acetylation has so far been functionally implicated: The maturation and maintenance of actin's structural and functional properties may require N-terminal acetylation and the role of actin in cell movement and intracellular trafficking was suggested to be modulated by acetylation (Terman and Kashina, 2013).

Tubulin polyglutamylation, polyglycylation and polyamination. C-terminal domains of α - and β -tubulins can be modified by additions of one or more glutamate or glycine residues to amino acid side chains. While glycylation is restricted to tubulin in primary cilia, where it was suggested to play a role in cilia assembly and maintenance, polyglutamylation is abundant in neurons in general, where it increases over development and is specifically enriched in cilia and centrioles (Okada et al., 2004; Song and Brady, 2015). Polyglutamylation adds negative charge to the modified tubulin C-terminals and differentially alters the binding efficiency of different MAPs, such as Tau, MAP2, MAP1A and MAP1B. Their binding depends for example on the length of the polyglutamyl chain and thus, polyglutamylation functions in selective MAP recruitment (Bonnet et al., 2001). The MT severing protein spastin specifically binds polyglutamylated domains of MTs in the absence of tyr-tub (Song and Brady, 2015).

Synaptic vesicle transport by motor proteins is also regulated by polyglutamylation and local changes in this PTM may serve to target selected cargoes (Bonnet et al., 2001; Ikegami et al., 2007; Maas et al., 2009). For example, kinesin-1 motility on neuronal $\beta 3$ -tubulin is increased by polyglutamylation (Sirajuddin et al., 2014).

Polyamination, in contrast, adds positive charge to MTs and was identified as yet another PTM that protects axonal MTs from depolymerization (Song and Brady, 2015).

Phosphorylation of cytoskeleton(-associated) proteins. Phosphorylation is one of the most common PTMs and is more long-lived than other cytoskeletal PTMs (Yu et al.,

2015). The phosphorylation of tubulins occurs both in soluble and polymerized states and has been implicated in polymerization efficacy and in MT interaction with membranes (Song and Brady, 2015). Actin phosphorylation can both induce and inhibit its polymerization and was linked to F-actin redistribution (Terman and Kashina, 2013).

Moreover, molecular motors get functionally regulated by phosphorylation: phosphorylation of dynein heavy chains influences motor properties, while phosphorylation of intermediate chains may modulate dynein interaction with its vesicle cargoes (King, 2000) or with Ndel1, with phosphorylation inhibiting Ndel1 interaction and contribution to dynein force generation (Gao et al., 2015). Dynein ATPase activity is again regulated by phosphorylation, for example by dynactin-dependent phosphorylation of dynein light chain (Kumar et al., 2000).

Especially phosphorylation of MAPs has received substantial attention, though: the function of MAPs in stabilization of MTs is dependent on their phosphorylation status. The number of identified kinases and their overlapping targets is constantly growing, which makes a holistic overview impossible in the context of this thesis. To this end, only a few examples of this complex functional fine-tuning shall be brought up here.

MAP1B, which is highly expressed during neuronal development, associates mostly with dynamic MTs such as in distal parts and growth cones of growing axons. This interaction is regulated by phosphorylation (Tortosa et al., 2013): Different kinases, such as Cdk5, GSK3 and CK2 phosphorylate MAP1B in response to extracellular cues like Netrin. This results in an increasing gradient of phosphorylated MAP1B towards the growth cones, with phosphorylated MAP1B showing increased interaction with MTs (Ayala et al., 2007; Riederer, 2007). The interaction of MAP1B with MT plus-end binding proteins EB1/3 is in turn inhibited by MAP1B phosphorylation, which releases EB1/3 to interact with and stabilize MTs in growth cones (Tortosa et al., 2013).

MAP4, which is present in proliferating cells, binds to and stabilizes MTs. This interaction again depends on phosphorylation of MAP4: Only phosphorylated MAP4 can support increased MT turnover/dynamics at the mitotic stage through its MT polymerization function and phosphorylation site mutants show impaired MT binding and altered progression into and through cell division (Chang et al., 2001).

The kinase Cdk5 phosphorylates numerous key cytoskeletal proteins apart from MAP1B, for example Tau, Ndel1, DCX, several actin regulatory proteins, other kinases like the focal adhesion kinase FAK, and β -catenin. Thereby, Cdk5 regulates many different aspects of cellular functions (Ayala et al., 2007). Phosphorylation of DCX by GSK3 β or Cdk5 decreases its association with MTs (Ayala et al., 2007; Hur and Zhou, 2010). So does the phosphorylation of Tau: in the presence of GSK3 β , Tau's MT binding and stabilization properties are reduced (Lovestone et al., 1996).

The cell adhesion protein β -catenin can also be phosphorylated by GSK3 β , which triggers its proteasome-dependent ubiquitination and degradation. Another component of the β -catenin destruction complex is Axin, whose intracellular localization is in turn regulated by Cdk5-mediated phosphorylation (Ye et al., 2015). Interestingly, the activity of Cdk5 is spatially restricted to the radial migration zone, where it phosphorylates also RapGEF2, which is essential for the formation of a radially oriented leading process and regulation of N-cadherin-mediated adhesion of the migrating neuron to the RG scaffold during multipolar-to-bipolar transition (Ye et al., 2014).

With these examples of protein function regulation by phosphorylation, we are equipped with the basic knowledge for the research studies presented in **Chapter 2** and **Chapter 4**, in which changes in phosphorylation of different cytoskeleton-associated and signalling

proteins were detected and suggested to mechanistically contribute to neurodevelopmental disorders.

Protein ubiquitination, sumoylation and neddylation. Ubiquitination (also termed ubiquitylation) and the closely related sumoylation and neddylation are complex PTMs that have been implicated, among others, in CNS function. Ubiquitin and SUMO are evolutionary conserved polypeptides whose polymers can be reversibly conjugated to mark target proteins for proteasomal degradation. Addition of monomers, though, may affect enzymatic activity, protein interactions and protein transport or localization. Sumoylation of tubulins, for example, modifies MT functions such as intracellular trafficking (Song and Brady, 2015). Sumoylated actin is retained in the nucleus, while mono-ubiquitination of actin increases its stability and regulates its subcellular localization (Terman and Kashina, 2013). The ubiquitin ligase parkin binds and ubiquitylates (misfolded) tubulin dimers, which leads to increased tubulin degradation and recycling (Ren et al., 2003).

A set of histone PTMs, targeting the N-termini that protrude out of the nucleosomes, has been described and functionally categorized in a “histone code” that influences cellular outcome (Cobos et al., 2018). Among those, ubiquitination of histone H2A, which is involved in regulation of the accessibility of DNA for epigenetic modifications, for DNA damage and repair response, has been implicated in brain development. For instance, it acts in pluripotency, differentiation and cell lineage commitment (Srivastava et al., 2017). Neddylation is abundant in neurons and regulates synaptogenesis during development and in mature neurons, where it promotes spine stability. Among the abundant synaptic targets of neddylation is the postsynaptic scaffolding protein PSD95 and this PTM is required for PSD95-mediated spatial organization of postsynaptic proteins (Vogl et al., 2015).

AMPylation – a novel PTM. AMPylation, also termed adenylation, is the covalent addition of adenosine monophosphate (AMP) to hydroxyl side chains of serine, threonine, or tyrosine residues by enzymes containing a conserved Fic domain (Engel et al., 2012). The AMPylation activity of Fic domain containing proteins is regulated by a conserved mechanism of an auto-inhibitory loop that obstructs ATP-binding (Engel et al., 2012). Alternative (non-Fic) adenylyltransferases are the bacterial glutamine synthase adenylyltransferase and the recently discovered pseudokinase SelO (Kingdon et al., 1967; Sreelatha et al., 2018).

AMPylation is more and more recognized as tuner of diverse signaling pathways including regulation of bacterial pathogenesis, drug tolerance, cellular trafficking, and prokaryotic and eukaryotic stress response (Casey and Orth, 2018). In bacteria, in which more than 1000 Fic domain containing proteins were identified, AMPylation serves for example bacterial toxicity: secreted Fic proteins AMPylate mammalian host cell Rho GTPases RhoA, Rac1, and Cdc42, rendering them inactive, which leads to cytoskeletal collapse (Mattoo et al., 2011; Worby et al., 2009). Host cell endocytosis and exocytosis was also found to be altered by bacterial AMPylation of Rab1 (Mukherjee et al., 2011). For the sole eukaryotic Fic domain-bearing enzyme FICD/HYPE, which is conserved from *C. elegans* to human, only a few protein targets are known so far that function in pathways of gene expression, ATP biosynthesis, and maintenance of the cytoskeleton (Broncel et al., 2016). FICD was shown to both AMPylate and deAMPylate the ER chaperone BiP, thereby altering its ATPase activity and the downstream activation of the unfolded protein response (UPR), making AMPylation a key regulator of ER homeostasis via UPR (Preissler et al., 2017b; Sanyal et al., 2015). Cellular expression of the

transmembrane protein FICD was – in line with its function in regulating UPR – detected in the ER. ER localisation was recently confirmed via a novel labeling and cryo electron tomography method (Sengupta et al., 2019). In yeast, Ficd was found to inactivate the cytosolic heat shock protein Hsp70, suggesting a function for AMPylation in protein homeostasis outside the ER (Truttmann et al., 2017). Further studies found that the *drosophila* Fic catalytic domain can be secreted into the lumen of the secretory pathway and that Fic localizes to the surface of glia cells (Rahman et al., 2012).

Recently, α -synuclein, a pre-synaptic protein involved in Parkinson's disease, was found to be AMPylated by FICD and this modification reduced the neurotoxic aggregation of α -synuclein (Mattoo et al., 2019). Namely, steric hindrance by the covalently bound AMP was suggested to interfere both with α -synuclein mediated membrane permeabilization and invasion to the ER and with its fibril formation by aggregation. Thus, AMPylation of alpha-synuclein is neuroprotective (Mattoo et al., 2019). In *C. elegans* models of neurodegeneration, chaperone AMPylation was shown to modulate aggregation and toxicity of neurodegenerative disease associated polypeptides amyloid- β , polyglutamine-extended polypeptide, and α -synuclein (Truttmann et al., 2018). Another nervous system function of AMPylation was identified in *drosophila*: Flies lacking *Fic* were blind due to a neurotransmission defect, caused by glia-specific defect in histamine recycling (Rahman et al., 2012).

AMPylation has actually been known for half a century, but due to long-lasting lack of methods for its *in situ* monitoring, its profiling has not been a trivial task (Hedberg and Itzen, 2015). Only recent findings have started bringing some light into this black box. In the study presented in **Chapter 3**, we developed a probe to monitor AMPylation under physiological conditions and with its help identified a huge number of novel AMPylation targets in diverse human cell types including NPCs and neurons, characterized the intracellular localization of FICD and AMPylated proteins, and by manipulating levels of FICD got an insight into the role of this under-studied PTM in neurodevelopment.

PTMs in neurodevelopmental and neurodegenerative disorders. PTMs vary with time, cell type, subcellular compartment and physiological state (Song and Brady, 2015). The diverse PTMs and their functions exemplified in this chapter indicate that dysregulation of enzymes responsible for these PTMs or mutations of PTM sites in target proteins may result in a diversity of nervous system-related disorders. Again, some examples of such disorders shall be given here.

A role for irreversible oxidant-induced PTMs has been found in the etiology of epilepsy: The increase in reactive oxygen species levels during epileptogenesis may lead to carbonylation of complex I of the mitochondrial electron transport chain, which causes disruptive conformational changes of the active site of complex I and impaired mitochondrial ATP production (Ryan et al., 2012).

Aberrant function or regulation of ubiquitylating enzymes has been associated with developmental disorders, cancer, and neurodegeneration (Werner et al., 2017). For example, disruptions in the H2A ubiquitination axis were identified as cause of neurodevelopmental disorders such as autism and microcephaly (Srivastava et al., 2017). Histone PTMs may even contribute to sex-specific differences in the brain during development and to different susceptibility and outcome of autism spectrum disorder (ASD), schizophrenia and major depressive disorder (Singh et al., 2018).

A link between histone PTMs and neurodegenerative diseases such as ALS, frontotemporal dementia and ataxias has also been identified (Cobos et al., 2018). Parkin mutations found in patients with Parkinson's disease or ALS disable parkin's

ubiquitylation and degradation activity. This causes complexes of parkin and misfolded tubulin to accumulate in toxic aggregates (Ren et al., 2003).

Altogether, PTMs thus represent an additional level of regulation, fine-tuning protein function, interaction and localization – and adding to the complexity of processes involved in cortical development. This stresses the need for good model systems and analysis methods to uncover their functions. The following paragraph treats evolution-based differences in neurodevelopment between mouse and human, which will lead us to the necessity of human model systems of neurodevelopment.

1.1.5. EVOLUTION: DIFFERENCES BETWEEN THE MOUSE AND HUMAN NEOCORTEX

The widely used mouse model shows a variety of common features of neurogenesis, like the basic steps required for the generation and the migration of excitatory and inhibitory neurons described above (see **1.1.1.** and **1.1.2.**). The great macroscopic differences in brain morphologies between mouse and primates including humans, though, suggest that specific changes occurred during evolution (Betizeau et al., 2013; Borrell and Reillo, 2012; Lewitus et al., 2014; Lui et al., 2011). Many studies have highlighted fine differences distinguishing the process of neurogenesis in mouse and human, and a number of primate- and human-specific mechanisms of neocortical development and expansion have recently been identified (reviewed in (Florio et al., 2017)). Some of the findings that relate to our current understanding of neurogenesis and neuronal migration within the cortex shall be summarized here.

Key aspects in which the mouse and human neocortex development diverge (**Fig. 2**) include differences in progenitor cell numbers, types and expansion capacity, and in the composition of the ECM (Pollen et al., 2015). Strikingly, the human cerebral cortex is significantly larger than the rodent cortex based on neuronal numbers. Moreover, it is highly folded, has greater complexity, and has acquired higher cognitive functions (Lui et al., 2011; Rakic, 2009; Sousa et al., 2017). The expansion of cortical progenitor pools and increased neuronal production in humans are the main underlying cellular mechanisms of the increased neuronal numbers (Borrell and Reillo, 2012). At the onset of neurogenesis, the initial pool of stem and progenitor cells per unit of cortical volume is larger, and additionally the neurogenic period is prolonged (Charvet et al., 2011; Hansen et al., 2010; Noctor et al., 2004).

Neurogenesis in humans begins with the expansion of the neuroepithelium and aRG, just like in mouse. But there are differences both in human aRG morphology and proliferation (Kriegstein and Alvarez-Buylla, 2009; Nowakowski et al., 2016), such as more regenerative asymmetric cell divisions compared to non-human primates and mice (Fish et al., 2008; Lukaszewicz et al., 2005). After the onset of neurogenesis, human aRG divide to give rise to an initial population of bRG, which delaminate from the apical surface (keeping their basal process and attachment to the pial surface) and migrate basally to give rise to the oSVZ (**Fig. 2**) (Fietz et al., 2010; Reillo et al., 2011; Wang et al., 2011). Within the oSVZ, bRG then expand massively through several rounds of division before terminal differentiation and make the oSVZ the predominant germinal region in the human neocortex, thereby increasing neuronal output and cortical folding and complexity (Lui et al., 2011; Nonaka-Kinoshita et al., 2013; Stahl et al., 2013). BRG are pivotal in the

evolutionary increase in human cortex size and complexity (Fietz et al., 2010; Hansen et al., 2010; Lewitus et al., 2013; Lui et al., 2011). Although the focus was set here on the evolutionary and developmental differences between mouse and human brain, it remains to be clarified that bRG are not a human-specific cell type but are generally found in higher number in gyrencephalic than in lissencephalic species, which led to their association to the generation of cortical folds (de Juan Romero et al., 2015).

Migrating new-born excitatory neurons use the basal processes of bRG as additional guides for their radial migration. In addition to radial migration, excitatory neurons in the human developing cortex disperse tangentially, thereby increasing the surface area of the cerebral cortex (Reillo et al., 2011). The basal process of aRG, on the other hand, is later lost in human cortical development, resulting in truncated RG bearing only an apical process (Nowakowski et al., 2016).

The germinal zone in the human oSVZ gets further specified as neurogenic niche by human-enriched ECM proteins and growth factors that are produced by bRG (Pollen et al., 2015) (**Fig. 2**). The ECM has been implicated both in neocortical expansion and in gyrification (Fietz et al., 2012; Florio et al., 2015; Long et al., 2018). As the ECM was already touched upon several times throughout this introduction, a few more words shall be spent here on its role. It consists of a complex network of proteins surrounding single cells within a tissue. ECM components and their receptors have been implicated in many aspects of neurodevelopment: proteoglycans, laminins and integrins (laminin receptors) constitute the pial basement membrane and influence the structure and basal anchoring of aRG and, via signalling pathways, regulate their proliferation. Laminin also promotes neuronal differentiation and neurite morphology. In neuronal migration, the proteoglycan reelin, secreted by Cajal-Retzius cells, and other ECM components play a role: reelin promotes the interaction of migrating neurons with the ECM and the RG scaffold and is involved both in locomotion and in the switch from locomotion to terminal translation (Long and Huttner, 2019). Recently, the ECM components HAPLN1, lumican and collagen I were shown to directly and quickly induce folding of the CP in human fetal cortical explants via local changes in ECM stiffness (Long et al., 2018).

A second mechanism regulating gyrification, which is independent of progenitor cell expansion, has recently been uncovered (del Toro et al., 2017): Differential expression of adhesion molecules such as FLRT1 and FLRT3 between future gyri and sulci leads to changes in intercellular adhesion, thereby influencing the migration of cortical neurons.

At the basis of the above described cellular-specific differences lie discriminative gene expression and regulation. For example, local differences in gene expression in the developing neocortex of gyrified species contribute to cortical folding (de Juan Romero et al., 2015), as has been shown for adhesion molecules (del Toro et al., 2017) and for *Trnp1*: high levels of *Trnp1* in fetal sulci underlie tangential expansion of NSCs, whereas in gyri with low *Trnp1* expression, radial expansion increases the number of IPs and bRG (Stahl et al., 2013).

Additionally, gene duplications represent a major evolutionary driving force (Dennis and Eichler, 2016) and may contribute to species-specific features of neocortical development. For example, the human-specific gene *ARHGAP11B*, a truncated duplicate of the ancestral form, promotes the generation of basal progenitors upon forced expression in the developing mouse neocortex (Florio et al., 2015). Overexpression of *TBC1D3*, multiple copies of which are present in humans but not mice, promotes BP generation via aRG delamination and induces local cortical folding in mice (Ju et al., 2016). The *NOTCH2NL* genes, which arose from human-specific gene duplications of

NOTCH2, also expand cortical progenitors and increase neuronal output when overexpressed in the developing mouse cortex (Fiddes et al., 2018; Suzuki et al., 2018). The increase in dendritic spine number and complexity in human neurons is also partly caused by a human-specific duplication: The human paralog of *SRGAP2*, *SRGAP2C*, acts as an inhibitor of its ancestral gene, causing delayed but ultimately increased development of dendritic spines (Charrier et al., 2012).

Altogether, this overview on genetic and cellular heterogeneity between human and mouse neurogenesis and neuronal migration shall stress the additional complexity of processes governing human cortical development. This increased complexity underlines the necessity for tight regulation and control of human embryonic brain development and makes humans particularly vulnerable to MCDs and associated psychiatric disorders (Bae et al., 2015; Doan et al., 2017). MCDs, with a focus on NMDs, will be introduced in the subsequent chapter.

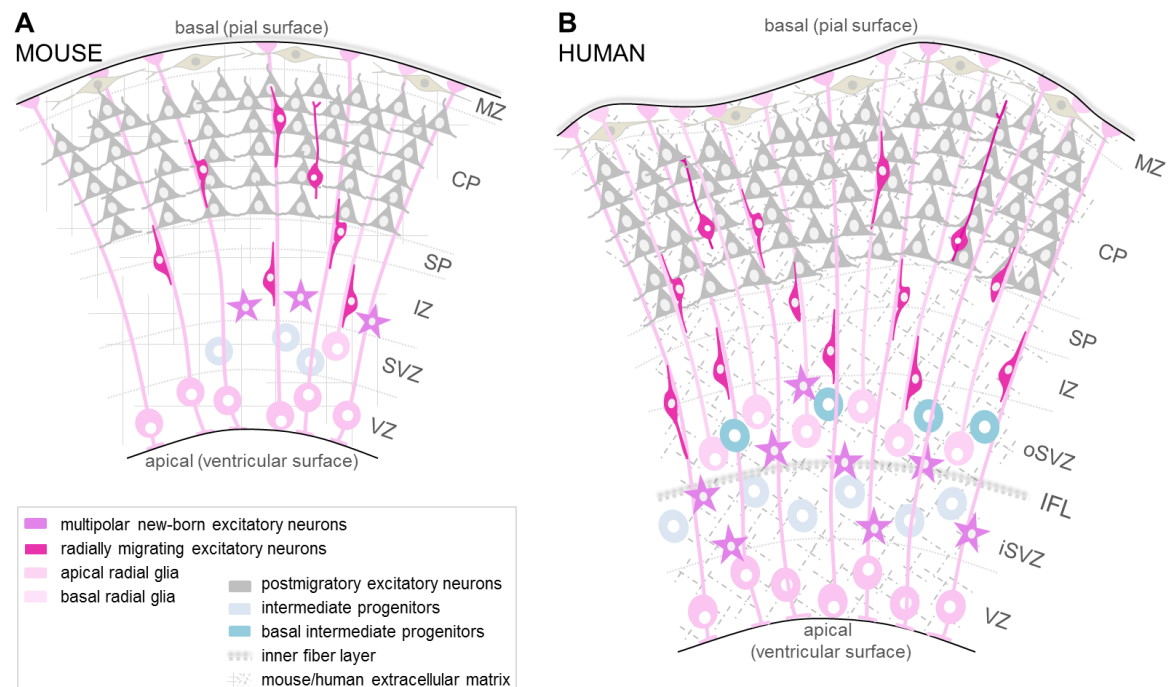


Figure 2: Differences between mouse and human dorsal cortical development. Schematics illustrating the cell composition and extracellular matrix in the developing mouse (**A**) and human (**B**) dorsal cortex. **A**, Cell composition in the developing mouse lissencephalic cerebral cortex with aRG giving rise to neurons directly or indirectly through IPs. New-born neurons undergo multipolar-to-bipolar transition and locomote or translocate to the CP. **B**, Cell composition in the developing human gyrencephalic cerebral cortex, where the SVZ is subdivided by the IFL into iSVZ – corresponding to the mouse SVZ – and oSVZ. As an additional germinal zone, the oSVZ is populated by oRG and bIPs that proliferate and generate neurons. Differences in extracellular matrix composition between mouse and human are indicated by different shading. Abbreviations: aRG, apical radial glia; bIPs, basal intermediate progenitors; bRG, basal radial glia; CP, cortical plate; IFL, inner fiber layer; IPs, intermediate progenitors; iSVZ, inner subventricular zone; IZ, intermediate zone; MZ, marginal zone; oSVZ, outer subventricular zone; SP, subplate; SVZ, subventricular zone, VZ, ventricular zone. *Adapted from* (Buchsbaum and Cappello, 2019) *with permission from Development*.

1.2. NEURONAL MIGRATION DISORDERS – A HETEROGENEOUS GROUP OF CORTICAL MALFORMATIONS

1.2.1. TRADITIONAL CLASSIFICATION OF MCDs AND NMDs

MCDs that affect the structure and functioning of the cerebral cortex and that are caused by deregulation of the molecular and cellular mechanisms of cortical development (outlined in 1.1) are a recognized cause of developmental delay, intellectual disability and epilepsy, and are also associated with dysmorphic features (Guerrini and Dobyns, 2014; Jamuar and Walsh, 2015; Romero et al., 2018). Traditionally, MCDs been classified according to the stage or process of cortical development that is affected (see **Table 1**) (Barkovich et al., 2012; Pang et al., 2008). However, the boundaries between the differentially classified MCDs are beginning to fade due to recent findings suggesting that MCDs are highly heterogeneous on the genetic, cellular and physiological level.

Table 1:

Traditional classification scheme for malformations of cortical development (MCDs)

Affected process	MCDs resulting from the disturbance	Short definition of the MCD
Neural progenitor cell proliferation and apoptosis	○ Microcephaly	Abnormally small head and brain
	○ Macrocephaly	Abnormally big head and brain
	○ Hemimegalencephaly	Overgrowth of (part of) a cerebral hemisphere
	○ Focal cortical dysplasia	Disturbed lamination, dysmorphic neurons
Neuronal migration	○ Lissencephaly type I	Absence of normal gyri
	○ Periventricular heterotopia (PH)	Subset of neurons accumulating at the ventricles underneath a normal cortex
	○ Subcortical band heterotopia / double cortex	Band of grey matter located between the lateral ventricular wall and the cortex
	○ Cobblestone lissencephaly / lissencephaly type II	Overmigration of neurons to localize on the surface of a brain with reduced gyri
Neuronal organisation	○ Polymicrogyria	Increase in (usually small) gyri
	○ Schizencephaly	Fluid-filled cleft from ventricle(s) to pia lined by heterotopic grey matter

Adapted from (Buchsbaum and Cappello, 2019) with permission from Development.

Although they often overlap with other MCDs, the focus here shall be on NMDs. The genetic, cellular and physiological heterogeneity of NMDs shall be discussed and a brief summary of the immense existing knowledge shall be given. In the past decades, this knowledge has mostly been gained by analyzing mouse models with specific mutations in genes that in human lead to NMDs. Additionally, some mouse models have been characterized which show features of human NMDs, but with a genetic basis not (yet) identified in human patients. Evolutionarily arisen developmental differences between

mouse and human (see **1.1.5**), though, have led to problems in the recapitulation of human diseases in the mouse. To this end, the use of more recently developed human *in vitro* models of cortical development (see **1.4 and 1.5**) opens the opportunity to understand human-specific neurodevelopmental mechanisms in health and disease.

A schematic summary of the brain morphological and cellular defects characterizing different NMDs is given in **Figure 3**, illustrating that 1) in lissencephaly type I, disruptions in IKNM and both radial and tangential neuronal migration result in a smooth cortex with lamination defect; 2) subcortical band heterotopia (SBH) is caused by defects in RG morphology and radial neuronal migration, resulting in a second, thin band of ectopic neurons in the white matter that runs parallel to the cortex (also called “double cortex”); 3) in periventricular heterotopia (PH), due to disturbed RG morphology and radial neuronal migration, a subset of neurons remains at the ventricular surface and forms nodules or sheets of apical grey matter; 4) in cobblestone lissencephaly/lissencephaly type II, defects in the basal lamina lead to overmigration of neurons that build so-called “cobblestones” on top of the pial cortical surface (Barkovich et al., 2012).

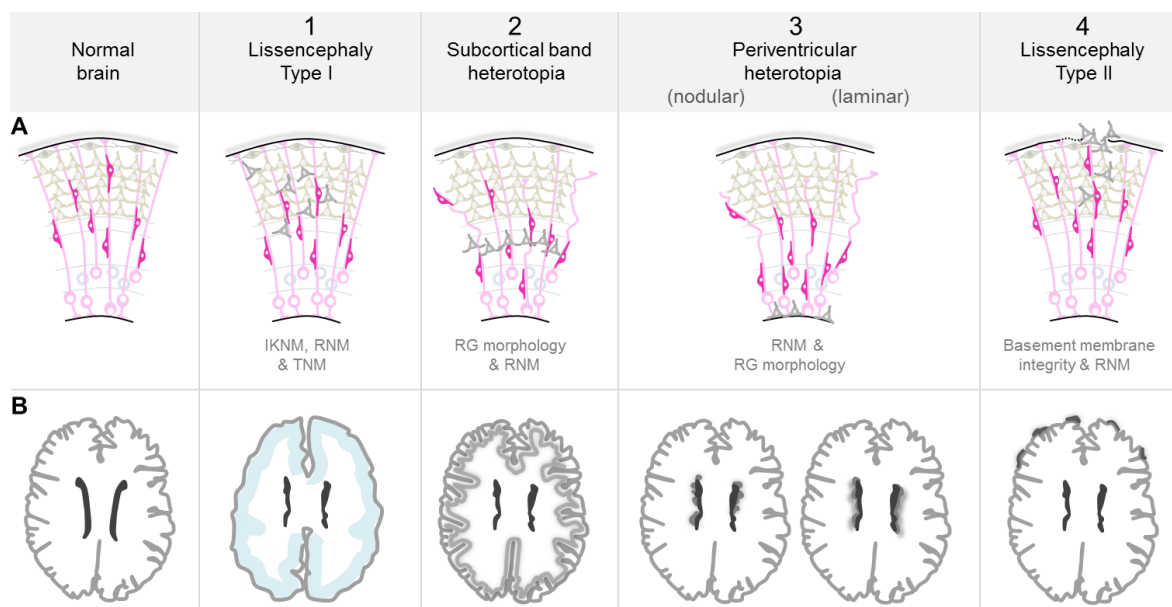


Figure 3: Cellular and morphological defects associated with neuronal migration disorders.

A, Schematics highlighting the cellular basis of neuronal migration disorders (NMDs) in the developing human cortex. RG, cortical layers and radially migrating neuron are depicted. Normal cortical anatomy is shown on the left, followed by the cellular defects associated with 1) lissencephaly type I, 2) subcortical band heterotopia, 3) periventricular heterotopia, and 4) lissencephaly type II. Ectopic neurons are shown in grey and the affected structures or processes are indicated. **B**, Schematic showing the MRI-detectable morphological defects in the adult human brain that are caused by the cellular defects of each NMD (A). Ectopically located clusters of affected neurons are shown as grey shading. 1) Lissencephaly Type I is characterized by a smooth brain surface and a simplified 4-layered cortex (indicated by blue shading). 2) In subcortical band heterotopia, the cortex contains an additional band of grey matter underneath the white matter. 3) Periventricular heterotopia is characterized by clusters (nodular) or sheets (laminar) of neurons accumulating at the ventricles. 4) In lissencephaly Type II, neurons overmigrate onto the cortical surface. Schematics are adapted from MRI images, see e.g. (Bizzotto and Francis, 2015; Francis et al., 2006; Guerrini and Parrini, 2010). Abbreviations: IKNM interkinetic nuclear migration; RG radial glia; RNM radial neuronal migration, TNM, tangential neuronal migration. *Adapted from* (Buchsbaum and Cappello, 2019) *with permission from Development*.

1.2.2. GENETIC, CELLULAR & PHYSIOLOGICAL HETEROGENEITY OF NMDs

As indicated above, recent findings suggest increased complexity in possible causes of NMDs, and of MCDs more generally, resulting in a breakdown of traditional boundaries between disorders of NSC proliferation, neuronal migration, and cortical organization (Guerrini and Dobyns, 2014). In this section, the multiple genetic, molecular, cellular, and physiological levels of heterogeneity recently identified in NMDs (see scheme in **Fig. 4**) shall be shortly summarized (Buchsbaum and Cappello, 2019), without touching on environmental insults that may additionally predispose to or cause MCDs and, ultimately, psychiatric disorders.

The majority of NMDs are now conceived to have a genetic basis (see **Table 2**). To this end, the focus here will be on genetic causes to date associated with NMDs.

Genetic variants and mutations that are associated with NMDs often affect genetically and functionally interdependent stages of cortical development. Indeed, current evidence suggests that distinct clinically defined disorders might be caused by shared risk loci (see **Table 2, Fig. 3, Fig. 4A**) (Sullivan et al., 2012; Zhu et al., 2014), with the resulting phenotype influenced by the degree of protein dysfunction or by the levels of remaining functional protein. An example of this are tubulinopathies, a wide and overlapping range of brain malformations caused by mutation of one of seven genes encoding different isoforms of tubulin. Thus, in tubulinopathies, the synthesis and function of microtubule and centrosome key components, as well as their interaction with molecular motors and other MAPs may be affected. Mutations in *TUBA1A*, for example, can cause severe lissencephaly type I, microgyria, SBH, and abnormal gyrification (Aiken et al., 2017; Cushion et al., 2013). Mutations in two genes coding for microtubule-binding proteins, namely the dynein regulator *PAFAH1B1* (*LIS1*) and the microtubule stabilizer *DCX*, can cause both lissencephaly type I and SBH, while cases of microcephaly have also been reported (Sheen et al., 2006). Further examples of different MCDs caused by disruption in the same gene are summarized in **Figure 4** as their detailed discussion goes beyond the scope of this introduction.

In the recent years, it has become more and more obvious that the genetics underlying NMDs are highly complex and heterogeneous. As a result, genomics approaches, such as next generation sequencing (NGS) and whole exome sequencing (WES), are being used increasingly to identify the genes that contribute to MCDs. Indeed, the use of NGS to investigate families with two or more affected individuals has proven to be extraordinarily effective at identifying novel, recessive mutations that contribute to neurodevelopmental and other disorders (Karaca et al., 2015; Yu et al., 2013). However, this approach is less useful in non-consanguineous families with a single, affected patient, which is the case for most patients with NMDs.

As a result, and since *de novo* variants are also strongly associated with neurodevelopmental conditions, WES combined with *in silico* prediction has been used to identify and prioritize new candidate genes for various neurodevelopmental disorders, including ASD (De Rubeis et al., 2014; Iossifov et al., 2012), schizophrenia (Fromer et al., 2014) and epileptic encephalopathy (Epi4K Consortium et al., 2013).

Table 2: Genes known to cause NMDs in humans upon disruption.

Gene	Cortical malformation	Main protein function	References
Lissencephaly type I and subcortical band heterotopia			
<i>LIS1 (PAFAH1B1)</i>	Lissencephaly type I; subcortical band heterotopia; (microcephaly)	Cytoskeleton (microtubules, dynein)	des Portes et al., 1998; Faulkner et al., 2000; Reiner et al., 1993; Sheen et al., 2006
<i>DCX</i>	Lissencephaly type I; subcortical band heterotopia; periventricular heterotopia; (microcephaly)	Cytoskeleton (microtubule stability), dynein binding, nucleokinesis	Bahi-Buisson et al., 2013; des Portes et al., 1998; Francis et al., 1999; Gleeson et al., 1998; Horesh et al., 1999; Sicca et al., 2003
<i>14-3-3e (YWHAE)</i>	Lissencephaly type I	Cytoskeleton (microtubules), intracellular signalling	Reiner et al., 1993
<i>TUBA1A</i>	Lissencephaly type I; subcortical band heterotopia; polymicrogyria (with microcephaly, corpus callosum agenesis, and cerebellar hypoplasia)	Cytoskeleton (microtubule component)	Bahi-Buisson et al., 2008; Bahi-Buisson et al., 2013; Keays et al., 2007; Poirier et al., 2007
<i>RELN</i>	Lissencephaly type I with cerebellar hypoplasia; (microcephaly)	Secreted ECM protein; Cytoskeleton (microtubules and actin), cell adhesion	Dulabon et al., 2000; Hirota and Nakajima, 2017; Hong et al., 2000
<i>ARX</i>	Lissencephaly type I with corpus callosum agenesis	Transcription factor	Colombo et al., 2007; Kato et al., 2004; Kitamura et al., 2002
<i>VLDLR</i>	Lissencephaly type I with cerebellar hypoplasia	Reelin receptor: RELN to microtubule signalling	Schlotawa et al., 2013; Trommsdorff et al., 1999
<i>NDE1</i>	Extreme microcephaly with lissencephaly type I	Cytoskeleton (microtubules/ centrosome); nuclear migration, centrosome duplication, mitotic spindle assembly	Alkuraya et al., 2011
<i>ACTG1</i>	Lissencephaly type I	Cytoskeleton (actin component)	Verloes et al., 2015
<i>ACTB</i>	Lissencephaly type I	Cytoskeleton (actin component)	Verloes et al., 2015
Periventricular heterotopia			
<i>FLNA</i>	Periventricular nodular heterotopia; polymicrogyria	Cytoskeleton (actin binding and crosslinking protein), junction formation	Fox et al., 1998; Lu et al., 2006; Parrini et al., 2006; Sheen et al., 2004b
<i>KIF2A</i>	Heterotopia; subcortical band heterotopia; agyria, pachygyria; (thin corpus callosum, congenital microcephaly)	Kinesin: microtubule-associated motor	Poirier et al., 2013
<i>TUBG1</i>	Laminar heterotopia; agyria, pachygyria; (microcephaly, dysmorphic corpus callosum)	Cytoskeleton (microtubule component)	Poirier et al., 2013
<i>ARFGEF2</i>	Periventricular nodular heterotopia with microcephaly	Golgi vesicle formation and trafficking; cell-cell adhesion; interaction with FLNA; Rac/Rho signalling	Bardón-Cancho et al., 2014; Lu and Sheen, 2005; Lu et al., 2006; Sheen, 2014; Sheen et al., 2004a; Shin et al., 2005
<i>EML1</i>	Periventricular heterotopia; ribbon-like subcortical band heterotopia; lissencephaly type I; (macrocephaly)	Cytoskeleton (microtubules), mitotic spindle orientation, cell adhesion	Bizzotto et al., 2017; Kielar et al., 2014
<i>FAT4</i>	Periventricular nodular heterotopia	Protocadherin: cell-cell and apical adhesion	Badouel et al., 2015; Cappello et al., 2013
<i>DCHS1</i>	Periventricular nodular heterotopia	Protocadherin: cell-cell and apical adhesion	Cappello et al., 2013
<i>ERMARD (C6orf70)</i>	Periventricular nodular heterotopia with polymicrogyria and corpus callosum agenesis	ER membrane-associated RNA degradation; trafficking; cell-cell adhesion	Conti et al., 2013
<i>NEDD4L</i>	Periventricular nodular heterotopia; polymicrogyria	Ubiquitin ligation and protein degradation, mTOR and (PI3K) AKT pathway	Broix et al., 2016
<i>AKT3</i>	Periventricular heterotopia with megalencephaly; polymicrogyria	(PI3K) AKT pathway	Alcantara et al., 2017
<i>MAP1B</i>	Periventricular heterotopia; (polymicrogyria)	Cytoskeleton (microtubules)	Heinzen et al., 2018
<i>MCPH1</i>	Microcephaly with periventricular nodular heterotopia and pachygyria	DNA damage response (G2/M checkpoint)	Trimborn et al., 2004
<i>INTS8</i>	Periventricular nodular heterotopia	RNA processing and transcription regulation	Oegema et al., 2017
Cobblestone lissencephaly (lissencephaly type II)			
<i>TMTC3</i>	Cobblestone lissencephaly; periventricular heterotopia; lissencephaly type I	Protein degradation in the endoplasmic reticulum; regulation of GABAergic inhibitory synapses	Farhan et al., 2017; Jerber et al., 2016
<i>POMT1</i>	Cobblestone lissencephaly; pachygyria	O-glycosylase: basement membrane integrity	Beltrán-Valero de Bernabé et al., 2002; Mercuri et al., 2009
<i>POMT2</i>	Cobblestone lissencephaly; (microcephaly)	O-glycosylase: basement membrane integrity	Mercuri et al., 2009; van Reeuwijk et al., 2005
<i>FKRP</i>	Cobblestone lissencephaly	O-glycosylase: basement membrane integrity	Mercuri et al., 2009
<i>FCMD (FKTN)</i>	Cobblestone lissencephaly	O-glycosylase: basement membrane integrity	Mercuri et al., 2009; Yamamoto et al., 2004
<i>POMGNT1</i>	Cobblestone lissencephaly; (microcephaly)	O-glycosylase: basement membrane integrity	Mercuri et al., 2009; Vuillaumier-Barrot et al., 2011
<i>LARGE (LARGE1)</i>	Cobblestone lissencephaly	O-glycosylase: basement membrane integrity	Longman et al., 2003; Vuillaumier-Barrot et al., 2011
<i>LAMB1</i>	Cobblestone lissencephaly; (macrocephaly)	ECM component: basement membrane integrity	Radmanesh et al., 2013
<i>GPR56 (ADGRG1)</i>	Bilateral fronto-parietal polymicrogyria and/or cobblestone lissencephaly; (white matter abnormalities, cerebellar dysplasia)	G-protein coupled receptor: basement membrane integrity	Bahi-Buisson et al., 2010; Li et al., 2008
<i>COL4A1</i>	Cobblestone lissencephaly	ECM component: basement membrane integrity/linkage of RG to the pial basement membrane	Labelle-Dumais et al., 2011

Accompanying MCDs are listed in brackets; owing to partial overlap in causative genes, polymicrogyria was taken into this list of NMDs.

Reprinted from (Buchsbaum and Cappello, 2019) with permission from Development.

Several recent studies (Heinzen et al., 2018; O'Neill et al., 2018a; O'Neill et al., 2018b) have identified novel candidate genes for PH by focusing on *de novo* variants and very rare inherited risk alleles. The first study (Heinzen et al., 2018) used trio-based WES of 202 patients with PH and epilepsy to identify a significant enrichment of non-synonymous *de novo* variants in intolerant genes. By combining both *de novo* and very rare inherited variants, they found that loss-of-function *MAP1B* variants are enriched in patients with this disorder, thereby identifying *MAP1B* as a new locus significantly associated with PH. Interestingly, again underlining phenotypic overlap of independently classified MCD, patients with *MAP1B* mutations and PH also had deep perisylvian or insular polymicrogyria (Heinzen et al., 2018). The same study also identified *de novo* variants in *DCX* in patients with PH. In a second trio-based WES study on patients with PH (O'Neill et al., 2018a), rare biallelic loss-of-function mutations in the Hippo pathway signaling factor *MOB2* were identified as candidate disease-causing. In a subfraction of the Heinzen *et al.* cohort, it was additionally demonstrated that a fraction of *de novo* coding variants in patients with PH localize to recently evolved genes associated with bRG generation and function, such as a human-specific isoform of *PLEKHG6*, adding a role of bRG to the mechanisms underlying PH etiology (Kyrrousi et al., Under Revision; O'Neill et al., 2018b).

Additional novel, relatively fast and cost-effective approaches to identifying MCD-associated loci were recently reported (Cellini et al., 2019; Lu et al., 2018). The first approach used a forward genetic screen in mice using transposon-mediated somatic mutagenesis in the developing mouse cortex to identify 33 candidate genes with potential roles in NPC proliferation, neuronal migration or differentiation (Lu et al., 2018). The second approach used array-CGH in patients with different MCDs and identified an enrichment of copy number variants (CNVs) or other *de novo* pathogenic chromosomal rearrangements in PH, with an overrepresentation of affected genes involved in vesicle-mediated transport regulation or encoding plasma membrane receptor complexes such as ion channels (Cellini et al., 2019). This finding was in line with an implication of the previously known PH-genes *FLNA*, *ARFGEF2*, and *MAP1B* in vesicle trafficking (Heinzen et al., 2018; Sheen, 2014), and *ERMARD* coding a putative vesicle associated protein (Conti et al., 2013) and added plasma receptor and ion channel complexes as new protein classes affected in PH.

Overall, these findings highlight that multiple genes and types of genetic variants can contribute to NMDs, and that the timing, severity and type of genetic factors involved in NMDs may influence the type and extent of the resulting malformation.

The heterogeneous genetic causes of NMDs are mirrored by the heterogeneous cellular phenotypes and functional outcomes that characterize these disorders. The genes implicated in NMDs encode proteins involved in various progenitor and neuronal properties and functions (**Table 2**). These include the maintenance and regulation of the morphology of the RG scaffold, the integrity of the neuroepithelium and the delamination of neurons from it, the polarity and motility of neurons, signaling between neurons and the RG scaffold, basal membrane integrity, and the signaling that terminates migration in the CP (Bizzotto and Francis, 2015) (**Fig. 4B**). Neuronal migration may be affected by the disruption of any of these protein functions – and many implicated proteins function in more than one step of neuronal migration and in more than one cell type. The PH-implicated actin binding protein *FLNA* (Fox et al., 1998; Lu et al., 2006; Parrini et al., 2006; Sheen et al., 2004b), for example, is involved in the polarized morphology of aRG, as well as in their proliferation (Carabalona et al., 2012), in establishing neuronal polarity,

and in neuronal migration itself. *FLNA* mutations, therefore, can result in an array of defects. Similarly, *LIS1* has been shown to be essential for both IKNM of aRG and neuronal migration (Hippenmeyer et al., 2010; Moon et al., 2014). Thus, the genetic heterogeneity that underlies NMDs translates into complexity in terms of the affected molecules and processes in neural stem and progenitor cells and neurons (**Fig. 4B**).

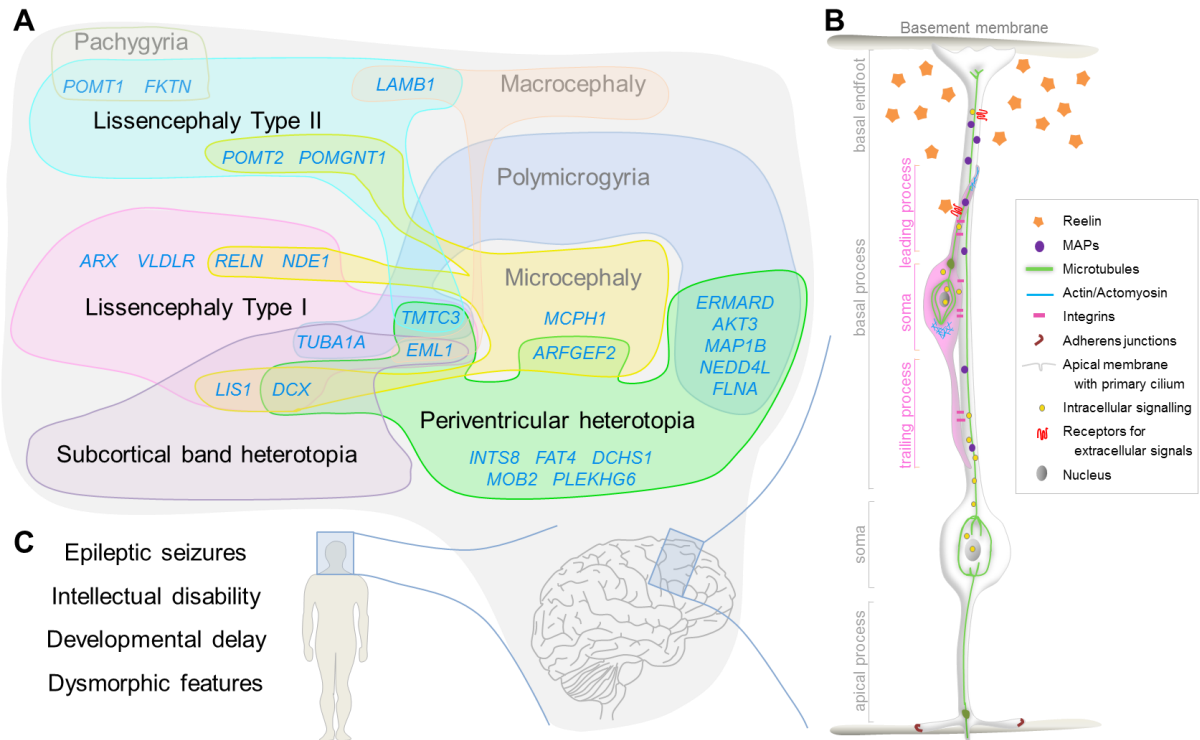


Figure 4. Heterogeneity and complexity of neuronal migration disorders at the genetic, cellular and clinical levels. **A.** Scheme depicting NMDs (black) and some overlapping identified causative genes (blue). Additional overlap with other differentially classified MCDs, which are not currently classified as NMDs (grey), is illustrated. **B.** Schematic of an aRG cell (white; cellular compartments labelled in grey), extending from the apical surface to the basement membrane, and a new-born neuron (pink; cellular compartments labelled in pink) using the RG cell as guide for its locomotion under healthy conditions. Examples of molecules and processes at the cellular level that can be compromised in NMDs in aRG and radially migrating neurons are exemplified to picture the complexity of the disorders. **C.** Common clinical features of patients suffering from NMDs. *Adapted from* (Buchsbaum and Cappello, 2019) *with permission from Development*.

Finally, the genetic and molecular heterogeneity of NMDs results in highly variable clinical features of patients with regard to the absence or presence of seizures, as well as intellectual function and congenital neurological deficits (**Fig. 4C**). PH patient outcome, for example, ranges from mild, sometimes subclinical, to very severe (Barkovich and Kuzniecky, 2000; Dubeau et al., 1995), and about 40% of NMD patients present with various types of epilepsy, while the rest are seizure free. Even PH patients that share mutations in the same gene, such as those with familial or sporadic *FLNA* mutations, show phenotypic heterogeneity (Parrini et al., 2006). Furthermore, there is no clear relationship between the severity of epilepsy in PH and the extent of neuronal heterotopia (Chang et al., 2005), and epileptic activity can originate from a general imbalance of excitation versus inhibition, or it can arise locally from heterotopic clusters of neurons that

can become intrinsically epileptogenic (Kothare et al., 1998), or from neurons surrounding heterotopic nodules.

Altogether, the heterogeneity of NMDs on genetic, cellular and functional levels (**Figure 4**) makes the study of human NMDs highly complex and suggests that NMDs should be considered as spectrum disorders. Also, this suggests that appropriate model systems are needed for the study of mechanisms contributing to NMDs. In the following, an overview of different *in vivo* and *in vitro* model systems applied for the investigation of cortical development, their advantages and shortcomings in recapitulating human features and NMDs shall be given.

1.3. ANIMAL MODELS OF CORTICAL DEVELOPMENT: THEIR RELEVANCE, ADVANTAGES AND LIMITATIONS

Ideally, research into cortical development and its disorders would be performed using human tissue. However, access to human tissue – in the form of post-mortem and pathological specimens – is quite limited, particularly in the case of rare diseases, stressing the need for suitable model systems.

1.3.1. MOUSE MODELS OF NMDs

The principal *in vivo* model system used for the study of general mechanisms of neurodevelopment is the mouse, as extensively reviewed (e.g. (Guerrini and Dobyns, 2014; Jamuar and Walsh, 2015; Romero et al., 2018)). However, when it comes to NMDs and other MCDs, the species differences between mouse and human cortical development, outlined in 1.1.5., represent a key challenge. Several mouse models recapitulate the morphological phenotypes of MCDs and have thus served as valuable tools in the identification of basic disease mechanisms for example of microcephaly, lissencephaly type I and neuronal heterotopia (Guerrini and Parrini, 2010; Stouffer et al., 2015) – even though often, no human patient with mutations in the homologous gene has been identified to date. Especially the fact that the mouse cortex is smooth complicates the study of lissencephaly type I etiology. For that reason, after two examples of efforts to mimic human lissencephaly type I in mouse, the focus here shall be on the other NMDs. Insertion of a heterozygous human *Lis1* mutation into the mouse caused ectopic hippocampal – but not cortical – pyramidal neurons and resulted in increased neuronal excitability and seizures (Fleck et al., 2000; Greenwood et al., 2009). Mice carrying different human *Arx* variants showed cortical lamination defects similar to human patients, defects in interneurons and spontaneous seizures (Kitamura et al., 2009; Marsh et al., 2009; Price et al., 2009).

Conditional knockout (cKO) of genes playing a role in apical AJs, such as *Ctnna1* (Schmid et al., 2014), *Mllt4* and *Cdh2* (Gil-Sanz et al., 2014), and *Rapgef2* and *Rapgef6* (Maeta et al., 2016) in the mouse brain resulted in neuronal migration phenotypes reminiscent of SBH and thus revealed the importance of apical adhesion regulation for proper neuronal migration. Conditional inactivation of the small GTPase *RhoA* similarly led to SBH: *RhoA* is involved in the regulation of both actin and microtubule cytoskeleton, including focal adhesion formation and microtubule stabilization. The cKO mouse revealed the importance of the integrity of both actin and microtubule cytoskeleton in RG for their function as scaffold for locomoting neurons (Cappello et al., 2012).

Examples of successful models of *FLNA*-signaling-mediated PH are the cKO of *Mekk4* (Sarkisian et al., 2006) and acute knockdown (KD) of *Rcan1* (Li et al., 2015), while PH due to vesicle trafficking defect, as is the case in patients with *ARFGEF2* mutations, was mimicked missense mutations in *Napa* (α Snap), which is involved in vesicle fusion (Chae et al., 2004).

In the context of cytoskeletal genes, it is important to mention an excellent full KO mouse model: KO of the microtubule-associated *Eml1* leads to SBH in the mouse, while human patients show ribbon-like PH (Bizzotto et al., 2017; Kielar et al., 2014), stressing interference with the cytoskeleton as common mechanism of malpositioned neurons in mouse and human. *Eml1* functions in microtubule dynamics and its disruptions affect the microtubule-based centrosome, primary cilium, and orientation of mitotic spindle and with that influence NPC proliferation (Bizzotto et al., 2017).

Acute KD of the cadherins *Fat4* and *Dchs1* (Cappello et al., 2013) showed that changes in NPC proliferation and neuronal differentiation can result in PH-like accumulation of ectopic neurons. In contrast to that, *Fat4* KO in mice does not cause cortical heterotopia found in patients with *FAT4* mutations (Badouel et al., 2015).

Mouse models of lissencephaly type II (Bizzotto and Francis, 2015) revealed the importance of the basement membrane and Cajal-Retzius cells, reelin-producing cells in the MZ/layer I, for cortical development and lamination (e.g. (Georges-Labouesse et al., 1998; Hartmann et al., 1999; Niewmierzycka et al., 2005)).

We have thus seen that mouse models are highly valuable for the identification of general mechanisms and processes underlying NMDs. Though, when manipulating the mouse homolog of a gene identified as mutated in patients with NMDs, the expected human phenotype is not always produced. In such cases, acute KD in the mouse or rat may lead to a better morphological recapitulation of cortical phenotypes, for example of aberrant electrophysiology reminiscent of epilepsy by *Dcx* KD in the rat (but no cortical lamination defect in *Dcx* KO mice) (Nosten-Bertrand et al., 2008; Ramos, 2005) and ectopic neurons upon *FlnA* KD in the rat, highlighting that the underlying genetics are different from humans. This indicates that, although highly valuable in modelling basic mechanisms of neurogenesis and neuronal migration and differentiation, rodent models remain simplified systems lacking human-specific features, including evolutionarily dynamic mechanisms.

1.3.2. NON-RODENT MODELS OF CORTICAL DEVELOPMENT

The above described challenges of modelling human MCDs in rodents may be partly overcome by the use of other *in vivo* model systems that more closely resemble some features of human brain development and morphology, such as the presence of oRG and cortical folds. Ferrets and non-human primates are increasingly used to this end (**Figure 5A**), aiming at a higher degree of fidelity to which animal models mimic human cortical development and MCDs. As in the work related to this thesis these *in vivo* models were not used, this paragraph will be kept rather short.

The ferret neocortex is folded and contains an oSVZ with abundant bRG (Fietz et al., 2010). The fact that gyrification is very similar between different animals helped to identify discrete domains of differential gene expression between future sulci and gyri (de Juan Romero et al., 2015), for example of adhesion molecules (del Toro et al., 2017). With the start of gyrification, migrating neurons in the ferret neocortex acquire migration patterns that are similar to those in developing primate brains. Namely, they disperse tangentially

by using processes of neighboring RG (Gertz and Kriegstein, 2015). Importantly, *in utero* electroporation can be performed in the developing ferret brain, enabling acute manipulation of gene expression and making the ferret a powerful model (Kawasaki et al., 2013; Smith et al., 2018).

A step further towards the human represent non-human gyrencephalic primates such as the macaque, whose brains are very similar to the human cortex in terms of their size, neuronal numbers and gyrification. In the developing macaque brain, an inner and outer SVZ can be clearly distinguished and the oSVZ contains an abundant population of bRG (Dehay et al., 2015; Smart et al., 2002). The diversity of precursor cell types is also much higher in primates than in rodent germinal zones, with heterogeneity of bRG evident in primates (Betizeau et al., 2013; Dehay and Kennedy, 2007; Dehay et al., 2015; Lukaszewicz et al., 2005). Although there are some successful examples of the generation of transgenic animals with germ line transmission (e.g. in marmosets (Sasaki et al., 2009) and macaques (Liu et al., 2016)), genetic manipulation remains difficult compared to mice. Together with their long gestational time and remaining decisive size difference in the cortex compared to humans, this stresses the need for more accessible human-like model systems. Several human *in vitro* models have therefore been developed to bridge limitations of animal models. As these represented the main model systems the studies of this thesis were based on, they will be introduced in detail in the following chapter.

1.4. IN VITRO MODELS OF CORTICAL DEVELOPMENT

The *in vitro* models that will be presented in the following are based on embryonic and, mostly, induced pluripotent stem cells (iPSCs) (Evans and Kaufman, 1981; Takahashi and Yamanaka, 2006; Thomson et al., 1998). Both 2-dimensional (2D) and 3-dimensional (3D) models make use of the ability of PSCs to spontaneously acquire neural identity and self-organize and differentiate *in vitro* (Ying et al., 2003). It has been known for many decades that very few external factors are needed for neuroectoderm induction (Holtfreter, 1944) and the default fate of NPCs is to give rise to forebrain cells (Levine and Brivanlou, 2007). Together with their great accessibility and relatively simple acute and permanent (Ran et al., 2013) genetic manipulation, as well as the possibility to transplant *in vitro* generated 2D and 3D systems into animal models, this opens numerous opportunities in the exploration of molecular, cellular, and even functional properties of human NPCs and neurons (**Figure 5B**).

1.4.1. 2D IN VITRO MODELS

In vitro protocols for the 2D generation of neural cells are based on the capacity of polarized neuroepithelial cells to self-organize into so-called neural rosettes around a pseudo-lumen (Elkabatz et al., 2008): Developing neuroepithelial cells arrange radially with neural progenitors in the center that sequentially generate layer-specific neurons in the typical temporal order and arrange in inside-out manner as happens *in vivo*. They then mature to build networks of actively firing neurons (Espuny-Camacho et al., 2013; Gaspard et al., 2008; Pankratz et al., 2007; Paşca et al., 2011; Shi et al., 2012). Also species-specific timing of development and maturation are recapitulated (Suzuki and Vanderhaeghen, 2015), rendering 2D *in vitro* models useful in the study of

neurodevelopment and its disorders (Iefremova et al., 2017; Paşca et al., 2014). The obvious limitation of 2D systems in the light of neuronal migration is the restricted spatial organization – which motivated the development of 3D models.

1.4.2. 3D *IN VITRO* MODELS OF INCREASING COMPLEXITY

To generate neural model systems that more closely resemble *in vivo* tissue, 3D suspension cultures have recently been developed. NPCs can self-organize to form 3D aggregates – termed *spheroids* or *organoids* – that produce various central nervous system lineages (Eiraku et al., 2011; Nakano et al., 2012; Reynolds and Weiss, 1992; Turner et al., 2016). In this context, “spheroid” generation aims at acquiring a specific brain region identity, which is achieved through the addition of morphogens mimicking endogenous patterning events. This patterning shall also reduce the variability between different organoids of the same and of independent batches (Bagley et al., 2017; Bershteyn et al., 2017; Chambers et al., 2009; Eiraku et al., 2008; Kadoshima et al., 2013; Krefft et al., 2018; Li et al., 2017; Mariani et al., 2012; Qian et al., 2016). Cerebral or brain “organoids”, on the other hand, are produced through less directed protocols, relying on the intrinsic capacity of cells to differentiate along a lineage and self-organize, and may thus contain germinal zones of different regional identities (Lancaster and Knoblich, 2014; Lancaster et al., 2013; Lindborg et al., 2016; Renner et al., 2017). As the detailed discrimination of existing 3D protocols goes beyond the scope of this introduction and has been extensively reviewed (e.g. (Di Lullo and Kriegstein, 2017; Paşca, 2018), Table 2 in (Buchsbaum and Cappello, 2019) may serve as a summary of those applied in the field of MCD research. Within this work, only an overview shall be given to stress the applicability of COs in the presented research studies.

All approaches exhibit features of 3D organization that are reminiscent of the developing cortex and reach higher degree of maturation than 2D cultures. Namely, VZs containing aRG are generated that are organized around a ventricle-like lumen. Basally to this lumen lie SVZ- and oSVZ-like zones that contain IPs and bRG, a CP-like zone with neurons of different layer identities (not clearly separated according to layer identity), and a marginal-like zone with Cajal-Retzius neurons. Mostly, 3D models are reminiscent of the first trimester of fetal brain development, with reports of spheroids recapitulating mid-fetal (Paşca et al., 2015) or even postnatal stages with primary-like mature astrocytes (Sloan et al., 2017).

Cerebral organoids (COs) may contain germinal zones with cells of all brain region identities, including dorsal and ventral forebrain and forebrain organizing centers, midbrain, hindbrain, midbrain-hindbrain boundary, choroid plexus, and photo-responsive retinal cells (Lancaster and Knoblich, 2014; Quadrato et al., 2017). Single-cell RNA-sequencing (scRNA-seq) was used to compare COs to human fetal brain in an unbiased way, which demonstrated that cell types are generated via the same transcriptional programs and developmental trajectories (Camp et al., 2015; Quadrato et al., 2017). Nevertheless, organoids are not without limitations, and they clearly represent a simplification of *in vivo* neural tissue, being relatively immature, small and heterogeneous (Camp et al., 2015; Jabaudon and Lancaster, 2018; Paşca, 2018; Quadrato et al., 2017). The proportion of astrocytes in COs is lower than in primary tissue and endothelial cells are missing, as well as white matter regions and meninges. Due to the absence of vascularization, organoid size remains limited. Alternative culturing methods are continuously being developed, such as so-called “organoids on a chip” that enable long-

term *in situ* live imaging of organoids over weeks (Karzbrun et al., 2018). In addition to the use of instructive factors that mimic morphogen gradients, approaches aiming at improving CO and spheroid protocols include the addition of microfilaments and scaffolding components. This was shown to ameliorate neural induction efficiency, the production of regions with dorsal cortical identity, and the generation of a basement membrane needed for the establishment of functional radial units (Kadoshima et al., 2013; Krefft et al., 2018; Lancaster et al., 2017; Zhu et al., 2017). It was recently demonstrated that mesoderm-derived progenitors in COs can generate mature microglia (Ormel et al., 2018).

Although showing variability in the efficiency of neural induction and in the generated brain regions between organoids of the same batch, as well as between batches (Camp et al., 2015; Jabaudon and Lancaster, 2018; Quadrato et al., 2017), a key advantage of undirected protocols is the high complexity of the interacting areas - reminiscent of different brain regions - that they generate. They thus enable a more comprehensive study of brain development and disease, enabling the identification of exact cell types affected by (candidate) disease genes. To this end, an undirected protocol was used (Lancaster and Knoblich, 2014) in the investigations that are part of this thesis, with analysis of a higher number of analyzed germinal zones, isogenic controls, and COs from several batches counterbalancing their variability.

Recently, several groups have fused formerly patterned spheroids of determined regional identity to result in “fused-organoids” or “assembloids”: This approach results in increased and highly defined complexity. For instance, spheroids of dorsal and ventral telencephalic identity have been fused to create mature glutamatergic projection neurons of all layer identities, as well as several different GABAergic interneuron types. Interneurons subsequently migrated towards a dorsal cortex-like region, integrated into dorsal laminae and established electrophysiologically active microcircuits (Bagley et al., 2017; Birey et al., 2017; Xiang et al., 2017). In the light of NMDs, these models will be highly valuable for future research, e.g. by combining control- and patient-derived spheroids.

Finally, the presented 2D and 3D *in vitro* human models can be combined with *in vivo* models again by transplantation, increasing the level of complexity, to study their functional characteristics *in vivo* (**Figure 5**).

1.4.3. FROM THE DISH BACK TO THE MOUSE: TRANSPLANTATION

Examples of transplantation of *in vitro* generated human NPCs and neurons into the mouse or rat brain have shown that they migrated into the host tissue, underwent morphological and functional maturation at species-specific rate, and functionally integrated into neural circuits (Espuny-Camacho et al., 2013; Kriks et al., 2011; Reddington et al., 2014; Suzuki and Vanderhaeghen, 2015; Zhu et al., 2016). Disease mechanisms may thus be elucidated by studying the development, migration, integration and physiological function of neurons *in vivo* (Espuny-Camacho et al., 2017). This has also been demonstrated for iPSC-derived glial progenitors from controls and schizophrenia patients, which revealed a role for oligodendrocytes and astrocytes in the disease etiology, even changing behavioral outcomes (Windrem et al., 2017). A method for implanting human COs into the adult mouse brain has also been described (Mansour et al., 2018): The transplanted organoids integrated into the host brain and became vascularized, with grafted neurons establishing functional synaptic connections with host neurons and responding to physiological stimuli.

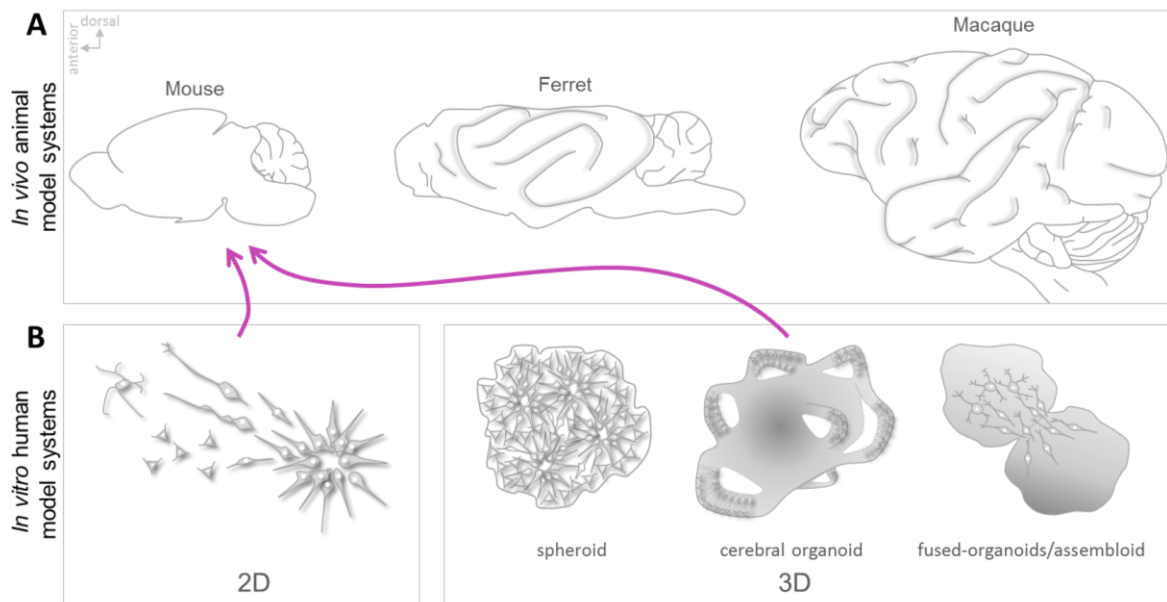


Figure 5: *In vivo* and *in vitro* model systems of neurodevelopment and its disorders. Schematic depicting animal model systems (A) and pluripotent stem cell-based human model systems (B) of increasing complexity and similarity to the developing human brain. **A**, Schematics of mouse, ferret and non-human primate brains as *in vivo* model systems (Axes are indicated for orientation). **B**, Human *in vitro* 2D models include NPCs and neurons and 3D models include rosette-based spheroids, brain region spheroids or whole-brain organoids, and fused-organoids/assembleoids with different brain regions fused together, which are particularly promising for the study of both radial and tangential neuronal migration. Pink arrows indicate the possibility to transplant *in vitro*-derived cells/aggregates into the mouse brain, where neurons can integrate, mature, become vascularized and generate functional circuits with the host cells, enabling the study of physiological functions. Adapted from (Buchsbbaum and Cappello, 2019) with permission from *Development*.

Altogether, human-derived *in vitro* and animal *in vivo* models may optimally be combined to succeed in improved modelling of human cortical development and MCDs. To stress the power of 2D and especially 3D human *in vitro* systems further, successful examples shall be introduced in the following.

1.5. MODELLING HUMAN-SPECIFIC FEATURES OF NEURODEVELOPMENT AND ITS DISORDERS *IN VITRO*

2D human model systems have been used to model a diversity of general neural cell processes (Flaherty and Brennand, 2017; Wen et al., 2016) and of human neurological disorders, such as schizophrenia (Brennand et al., 2011), bipolar disorder (Madison et al., 2015; Mertens et al., 2015), and Rett syndrome (Marchetto et al., 2010). Also, species-specific differences between mouse, macaque, chimpanzee, and human have been investigated with the help of both 2D and 3D systems (Mora-Bermúdez et al., 2016; Otani et al., 2016; Pollen et al., 2019). These studies revealed a species-specific cell-autonomously regulated neuronal maturation timing, a protracted period of progenitor proliferation in primates and especially in human NPCs in parallel to neurogenesis, as well as cell cycle differences between the primates, which may contribute to a greater neocortical expansion in humans. ScRNA-seq of COs of the analyzed species showed

highly preserved cell types, developmental trajectories, and gene co-expression relationships between different primates. Genes more highly (co-)expressed in human apical progenitors (Mora-Bermúdez et al., 2016) and bRG (Pollen et al., 2019) pointed to increased proliferative capacity, supporting evolutionary expansion of the human neocortex.

To elaborate further on evolutionary aspects, effects of genomic variants between humans and their hominid ancestors may be elucidated using 3D *in vitro* models (Cohen, 2018; Hajdinjak et al., 2018). The regulation of cortical folding have also be addressed (Karzbrun et al., 2018; Li et al., 2017).

Several human neuropsychiatric disorders and MCDs, such microcephaly (Cugola et al., 2016; Gabriel et al., 2016; Gabriel et al., 2017; Lancaster et al., 2013; Li et al., 2017; Ming et al., 2016) have been modelled in 3D human *in vitro* models. Furthermore, cerebral spheroids, organoids and assembloids have been applied by several groups to investigate the pathophysiology of ASD (recently reviewed in (Ilieva et al., 2018)), for example in patient-derived forebrain spheroids with increased FOXP1 expression (Mariani et al., 2015), and in Timothy patient-derived forebrain assembloids (Birey et al., 2017), which both suggest that neuronal migration and perhaps the (consequent) imbalance of excitatory/inhibitory neurons is at the basis of ASD. Importantly, many of these studies have provided novel insights into how aberrant neuronal migration can contribute to human disease, indicating that human 3D *in vitro* models may be used to model NMDs, thereby circumventing problems of mouse models carrying human disease variants to mimic the human neocortical phenotype (see 1.3.1.).

The following studies successfully modelled aspects of NMDs in COs.

As the mouse brain cannot serve as a model system for lissencephaly type I due to its intrinsic physiological lack of folds, many approaches have focused on modeling lissencephaly type I *in vitro*. Of note, three recent studies, using different, complementary 3D cell culture technologies, have identified several novel factors that contribute to this disease: In the first study (Bershteyn et al., 2017), COs were generated from lissencephaly patient-derived iPSCs, with the patient carrying a heterozygous 17p13.3 deletion which results in Miller-Dieker syndrome (MDS), the most severe form of lissencephaly that features epilepsy and intellectual disability. The patient-derived organoids recapitulated specific cellular phenotypes previously identified in mouse models of this syndrome, e.g. mitotic spindle and neuronal migration defects. However, they also revealed additional human-specific features, including severe apoptosis and increased horizontal division of aRG, resulting in more neurogenic aRG divisions, overproduction of deep-layer neurons, and smaller organoid size. The nuclei of aRG were less elongated, consistent with a reduced tension during nucleokinesis, and bRG showed a cell-type-specific mitotic defect, causing delayed cell division. In a second study, forebrain-specific spheroids were used to elucidate mechanisms contributing to MDS (Ilfremova et al., 2017). In line with the first study, they identified an increase in asymmetric aRG divisions, resulting in reduced NPC expansion and premature neurogenesis. In addition, the MT cytoskeleton network of aRG in patient organoids was altered and truncated in appearance, with reduced extension towards the basal membrane. Altered expression of cell adhesion molecules added to the disruption of cortical niche architecture, leading to a non-cell-autonomous disturbance of the N-cadherin/ β -catenin signaling axis. A third study used the “organoids on a chip” approach with CRISPR/Cas9-engineered *LIS1*(+/-) mutant iPSCs (Karzbrun et al., 2018) and found that *LIS1*(+/-) mutant organoids generated fewer convolutions as determined from a

decreased gyrification index that is consistent with the lissencephaly patient phenotype. Using atomic force microscopy, mutant cells were found to be softer and to swell less than control S-phase cells, indicating defective IKNM.

It is of particular interest in this thesis to model PH (**Chapter 4**), which is only partially recapitulated in mouse models with human mutations, in COs. Recently, our group published for the first time that COs derived from patients with PH and known causative mutations in the cadherin receptor-ligand pair *FAT4* and *DCSH1* or from isogenic KO iPSCs reproduce the NMD (Klaus et al., 2019): COs show neuronal heterotopia, disrupted NPC morphology and a defective neuronal migration and navigation system in a subset of cells, as well as dysregulated genes involved in axon guidance, neuronal migration and patterning in a subpopulation of mutant neurons as identified by scRNA-seq. This makes sense considering that in patients with PH, only a subset of neurons fails to undergo radial migration to the CP and suggests that the described abnormal subpopulation may be the neurons that acquire ectopic apical location. Thus, the use of COs enabled the identification of human-specific facets of this form of PH (Klaus et al., 2019).

Moreover, COs can also be used to identify a cellular role for novel candidate causative genes identified in patients with MCDs. In a recent study, COs were used to confirm the phenotype seen in a mouse acute KD model of *Mob2*, biallelic mutations of which were associated with PH in a WES study (O'Neill et al., 2018a). As in the KD mouse model, defects in primary cilia numbers were observed in COs, stressing the importance of proper MOB2 levels for cilia maintenance and neuronal positioning in human neurons. In a further study, an enrichment of *de novo* coding variants associated with bRG was identified in patients with PH. One of the variants localized to a human-specific isoform of *PLEKHG6*. Acute manipulations of its expression both *in vivo* and *in vitro* revealed its role in bRG production and with that a role for bRG in the etiology of PH (O'Neill et al., 2018b).

These examples are highly important in the context of the project presented in **Chapter 4**, in which COs were used to model the role of a novel candidate PH gene in neurodevelopment and in the etiology of the disorder.

Taken together, these studies exemplify how COs can serve both to reveal human-specific roles of known disease-associated genes, adding human-specific aspects to knowledge gained in *in vivo* models, and to decipher new candidate causative genes and their human-specific mechanisms of action. A combination of the described novel *in vitro* models with recently advanced methods, such as genome editing (Ben Jehuda et al., 2018), scRNA-seq (Camp et al., 2015; Klaus et al., 2019; Pollen et al., 2019; Quadrato et al., 2017), mass spectrometry (MS)-based proteomics (McClure-Begley et al., 2018), single-cell life imaging, and fluorescence-activated cell sorting (FACS) (Klaus et al., 2019) enables their unbiased analysis. A complementary approach, combining *in vivo* and *in vitro* models, will serve to broaden the knowledge of the molecular and cellular mechanisms underlying defective neuronal positioning in the human cerebral cortex.

Specifically, for all the studies presented in this thesis, 2D and 3D *in vitro* systems were applied both for the study of a novel mechanism contributing to neurodevelopment (**Chapter 3**), as well as to decipher neurodevelopmental disease mechanisms (**Chapter 2 and 4**), and were partly paralleled by mouse *in vivo* studies (**Chapter 4**).

1.6. ABOUT THIS THESIS

This thesis was composed in a cumulative style, embedding three research studies into a frame of a common introduction and discussion.

In the preceding introduction, I aimed at giving a summary of the background knowledge required for understanding the research studies presented in **Chapters 2-4**.

In the first study (**Chapter 2**; (Pérez-Brangulí et al., 2018)), we investigated a neurodevelopmental role of the HSP gene *SPG11*. HSP is a progressive juvenile onset gait disorder caused by disruption of long corticospinal motoneurons. The role of the encoded protein spatacsin in endo- and lysosomal trafficking, together with reduced grey matter thickness and corpus callosum agensis in *SPG11* patient brains hinted at a developmental function of spatacsin. Indeed, a preceding study identified dysregulated genes with known neurodevelopmental functions in patient-derived NPCs and suggested a mechanism via GSK3 β (Mishra et al., 2016). Based on these findings, we generated and analyzed neurospheres and cerebral organoids from *SPG11* patient and control iPSCs. We find an early neurodevelopmental defect upon *SPG11* mutations that can be rescued by interfering with the altered GSK3 β pathway, suggesting a possible therapeutical strategy.

The topic of the second study (**Chapter 3**; (Kielkowski et al., Under Revision)) is the PTM AMPylation. With the help of a novel probe and proteomics, multiple AMPylated proteins were identified under physiological conditions in different human cell lines and in 2D and 3D *in vitro* models of human neurodevelopment. The sets of AMPylated protein were cell-type specific and so was the intracellular distribution of both AMPylating enzyme FICD and AMPylated protein targets, with enrichment in AMPylated cytoskeletal and motor proteins in neurons. Functionally, we found that 1) AMPylation of amino acid residues close to the enzymatic active site can inhibit enzymatic function, which may represent a general mechanism of action and 2) that manipulation of the levels of the AMPylating enzyme FICD in COs leads to a redistribution of AMPylated proteins and a slight but significant change in progenitor cell proliferation vs. neuronal differentiation. In the light of the multiple regulatory functions that have been described for PTMs targeting cytoskeletal and associated proteins in the developing nervous system, we suggest that AMPylation may be an additional such mechanism that fine-tunes neurogenesis.

The third study (**Chapter 4**; (Buchsbaum et al., Under Revision)) aims at the identification and characterization of a novel candidate gene for the NMD PH specifically and, more generally, at increasing our knowledge on mechanisms and pathways that are important during cortical development and that lead to MCDs upon disruption. The project started out as collaboration with Stephen Robertson's lab in New Zealand, where I learned how to analyze WES data from parent-patient trios. One of the genes I found mutated in a patient with PH and mega cisterna magna was *LGALS3BP*, which has been studied by a postdoc in our lab in Munich over the last few years (Kyrousi et al.; Under Revision). In parallel, Adam O'Neill and the Epi4K study in the recently published work (Heinzen et al., 2018) identified – for the first time in their cohort of PH patients – two unrelated patients with biallelic variants in the same gene: *ECE2*. Both the fact that two patients were found with predicted to be damaging SNVs in the same gene and that most recessive diseases are caused by loss-of-function mutations in enzymes (Jimenez-Sanchez et al., 2001) drove us to choose *ECE2* as a probable candidate for PH. In this study, we combined *in vivo* mouse and *in vitro* human model systems to study the role of *ECE2* in

neurodevelopment. Indeed, we found that ECE2 plays a role in neuronal migration and positioning, being involved in apico-basal polarity and cytoskeletal integrity, as well as in the production and secretion of ECM factors and in the regulation of protein phosphorylation.

In the discussion, I start by debating the three presented studies separately, followed by setting all findings into a common context.

2. HUMAN *SPG11* CEREBRAL ORGANIDS REVEAL CORTICAL NEUROGENESIS IMPAIRMENT

2.1. CITATION

Human Molecular Genetics, 2018, Vol. 00, No. 00 1–11

Human SPG11 cerebral organoids reveal cortical neurogenesis impairment

Francesc Perez-Branguli^{1,‡,*}, Isabel Y Buchsbaum^{2,3,‡}, Tatyana Pozner^{1,‡}, Martin Regensburger^{1,4}, Wenqiang Fan⁶, Annika Schray¹, Tom Borstler¹, Himanshu Mishra¹, Daniela Graf¹, Zacharias Kohl^{5,8}, Jurgen Winkler^{5,8}, Benedikt Berninger^{6,7}, Silvia Cappello^{2,*} and Beate Winner^{1,8,*},‡

¹Department of Stem Cell Biology (former IZKF Junior Research Group III), Friedrich–Alexander-Universität Erlangen–Nürnberg (FAU), Erlangen, Germany,

²Max-Planck Institute of Psychiatry, Munich, Germany,

³Graduate School of Systemic Neurosciences (GSN), Ludwig-Maximilians University (LMU), Planegg/Martinsried, Germany,

⁴Department of Neurology, Friedrich–Alexander-Universität Erlangen–Nürnberg (FAU), Erlangen, Germany,

⁵Department of Molecular Neurology, Friedrich–Alexander-Universität Erlangen–Nürnberg (FAU), Erlangen, Germany,

⁶Adult Neurogenesis and Cellular Reprogramming, Institute of Physiological Chemistry and Focus Program Translational Neuroscience, University Medical Center, Johannes Gutenberg University Mainz, Mainz, Germany

⁷Institute of Psychiatry, Psychology & Neuroscience, Centre for Developmental Neurobiology and MRC Centre for Neurodevelopmental Disorders, King's College London, London, UK

⁸Zentrum für Seltene Erkrankungen Erlangen (ZSEER), Friedrich–Alexander-Universität Erlangen–Nürnberg (FAU), Erlangen, Germany

*To whom correspondence should be addressed.

Beate Winner, Tel: +49-9131-85-39301; Fax: +49-9131-85-39311, Email: beate.winner@fau.de; Francesc Pérez-Brangulí, Email: fpbranguli@gmail.com and Silvia Cappello, Tel: +49-89-30622253; Fax: +49-89-30646639 Email: silvia.cappello@psych.mpg.de

‡Beate Winner, <http://orcid.org/0000-0002-6909-0564>

‡These authors contributed equally to this work.

Reprinted with the permission from *Oxford Journals*.

2.2. AUTHOR CONTRIBUTIONS

Conceptualization: F.P.B., I.Y.B., S.C., and B.W.

Methodology: F.P.B., I.Y.B., T.P., W.F., A.S., H.M., S.C., and B.W.

Investigation: F.P.B., I.Y.B., T.P., W.F., A.S., and D.G.

Manuscript writing and editing of manuscript and figures: F.P.B., I.Y.B., M.R., T.P., J.W., S.C., and B.W.

I.Y.B. conceptualized the cerebral organoids-based parts of this study together with S.C. and performed all experiments and analyzes presented in Figures 1 (except for panels I–J) and Figure 5 (except for panels E–F) and generated the organoids for experiments presented in Figure 1I–J, Figure 3E–G, Figure 5E–F. I.Y.B. contributed to manuscript writing and editing and to editing of the figures.

GENERAL ARTICLE

Human SPG11 cerebral organoids reveal cortical neurogenesis impairment

Francesc Pérez-Brangulí^{1,‡,*}, Isabel Y Buchsbaum^{2,3,‡}, Tatyana Pozner^{1,‡}, Martin Regensburger^{1,4}, Wenqiang Fan⁶, Annika Schray¹, Tom Börstler¹, Himanshu Mishra¹, Daniela Gräf¹, Zacharias Kohl^{5,8}, Jürgen Winkler^{5,8}, Benedikt Berninger^{6,7}, Silvia Cappello^{2,*} and Beate Winner^{1,8,*}†

¹Department of Stem Cell Biology (former IZKF junior research group III), Friedrich–Alexander-Universität Erlangen–Nürnberg (FAU), Erlangen, Germany, ²Max-Planck Institute of Psychiatry, Munich, Germany, ³Graduate School of Systemic Neurosciences (GSN), Ludwig-Maximilians University (LMU), Planegg/Martinsried, Germany, ⁴Department of Neurology, Friedrich–Alexander-Universität Erlangen–Nürnberg (FAU), Erlangen, Germany, ⁵Department of Molecular Neurology, Friedrich–Alexander-Universität Erlangen–Nürnberg (FAU), Erlangen, Germany, ⁶Adult Neurogenesis and Cellular Reprogramming, Institute of Physiological Chemistry and Focus Program Translational Neuroscience, University Medical Center, Johannes Gutenberg University Mainz, Mainz, Germany ⁷Institute of Psychiatry, Psychology & Neuroscience, Centre for Developmental Neurobiology and MRC Centre for Neurodevelopmental Disorders, King's College London, London, UK, and ⁸Zentrum für Seltene Erkrankungen Erlangen (ZSEER), Friedrich–Alexander-Universität Erlangen–Nürnberg (FAU), Erlangen, Germany

*To whom correspondence should be addressed. Beate Winner, Tel: +49-9131-85-39301; Fax: +49-9131-85-39311; Email: beate.winner@fau.de; Francesc Pérez-Brangulí, Email: fpbranguli@gmail.com and Silvia Cappello, Tel: +49-89-30622253; Fax: +49-89-30646639; Email: silvia_cappello@psych.mpg.de

Abstract

Spastic paraplegia gene 11 (SPG11)-linked hereditary spastic paraplegia is a complex monogenic neurodegenerative disease that in addition to spastic paraplegia is characterized by childhood onset cognitive impairment, thin corpus callosum and enlarged ventricles. We have previously shown impaired proliferation of SPG11 neural progenitor cells (NPCs). For the delineation of potential defect in SPG11 brain development we employ 2D culture systems and 3D human brain organoids derived from SPG11 patients' iPSC and controls. We reveal that an increased rate of asymmetric divisions of NPCs leads to proliferation defect, causing premature neurogenesis. Correspondingly, SPG11 organoids appeared smaller than controls and had larger ventricles as well as thinner germinal wall. Premature neurogenesis and organoid size were rescued by GSK3 inhibitors including the Food and Drug Administration-approved tideglusib. These findings shed light on the neurodevelopmental mechanisms underlying disease pathology.

†Beate Winner, <http://orcid.org/0000-0002-6909-0564>

‡These authors contributed equally to this work.

Received: July 6, 2018. Revised: October 23, 2018. Accepted: November 10, 2018

© The Author(s) 2018. Published by Oxford University Press.

This is an Open Access article distributed under the terms of the Creative Commons Attribution Non-Commercial License (<http://creativecommons.org/licenses/by-nc/4.0/>), which permits non-commercial re-use, distribution, and reproduction in any medium, provided the original work is properly cited. For commercial re-use, please contact journals.permissions@oup.com

Introduction

Mutations in *ALS5/SPG11/KIAA1840*-encoding SPATACSIN cause a spectrum of neurodevelopmental and neurodegenerative diseases including the most frequent form of autosomal recessive hereditary spastic paraplegia (HSP) (36), termed spastic paraplegia gene 11 (SPG11), young onset amyotrophic lateral sclerosis (ALS5) (28) and Charcot–Marie–Tooth disease (CMT1a) (26). Spatacsinopathies converge a clinical spectrum ranging from cognitive impairment and thin corpus callosum (TCC) to spastic paraplegia and peripheral motor neuropathy. This multisystemic involvement points towards distinct temporal and spatial, yet incompletely understood functions of SPATACSIN. The prominent nervous system involvement in *SPG11*-linked HSP is connected to SPATACSIN's active temporal and spatial expression throughout the nervous system. The neurodegenerative phenotype was linked to autophagy: together with another HSP-related protein (ZFYVE26), the *SPG11* protein SPATACSIN is instrumental for the reformation of lysosomes from autophagolysosomes, i.e. a recycling pathway that generates new lysosomes (7,39).

Among others, SPG11-HSP belongs to a subset of complex forms of HSPs characterized by TCC and is often associated with cognitive impairment (15), indicative of a neurodevelopmental defect. In conjunction, a majority of SPG11 patients show mild to severe enlargement of the lateral ventricles and of the cerebral sulci, in addition to a TCC and diffuse white matter hyperintensity (31).

The functional role of *SPG11* in neurodevelopmental alterations remains largely unexplored. Induced pluripotent stem cell (iPSC)-derived neuronal models have been decisive for characterizing the cellular phenotypes of neurodevelopmental deficits in autism, Rett syndrome and Williams syndrome (6,22,23). We have previously described a proliferation deficit in neural progenitor cells (NPCs) derived from SPG11 patients' iPSC (25). More recently, 3D iPSC-derived organoid systems opened the opportunity to model brain diseases in a system with remarkable similarities to human organogenesis (18,24,34).

Here, we took advantage of the cerebral organoid system and of live-cell imaging to recapitulate the temporal and spatial pattern of NPC division and differentiation in SPG11HSP patients. Using 2D and 3D culture conditions, namely differentiating NPCs, neurospheres and cerebral organoids, we identified an increased asymmetric division in SPG11-NPCs at the germinal zone of cortical ventricles at the expense of symmetric division. This impairment in self-renewal contributes to the premature generation of cortical neuroblasts and neurons and is dependent on GSK3 signalling. Inhibition of GSK3 activity using the Food and Drug Administration (FDA) approved compound tideglusib is sufficient to rescue premature neurogenesis and more importantly increases organoid size in SPG11. Our data provide insights into how *SPG11* alters neurodevelopment and further links this disease to the group of neurodevelopmental disorders. Moreover, we provide a proof of concept that 3D brain organoids are valuable tools for precision medicine.

Results

SPG11 patients and controls included in the study

The SPG11-HSP patients reported in this study are characterized by an early onset of cognitive impairment in the first and second

decade (15). In total, we derived iPSC from three patients (two lines each), referred to as SPG11-1, SPG11-2 and SPG11-3. SPG11-1 and SPG11-2 are sisters with compound heterozygous mutations c.3036C>A/ p.Tyr1012X in exon 16 and c.5798 delC/ p.Ala1933ValfsX18 in exon 30. SPG11-3 has compound heterozygous mutations at c.267G>A/ p.Trp89X in exon 2 and at 1457-2A>G in intron 6 (splice site mutation corresponding to the previously reported mutation c.1757-2A>G) (15). The detailed clinical, genetic and imaging characteristics of the patients were previously published (15). The controls are two age-matched healthy Caucasian individuals with no history of movement disorder or neurologic disease.

SPG11-NPCs display an altered self-renewal pattern in cerebral organoids

To experimentally mimic the temporal and spatial division of neural cells in SPG11 patients and controls, we generated and analyzed cerebral organoids derived from iPSC. The size of organoids derived from SPG11-iPSC (SPG11 organoids) was significantly smaller compared to controls during early development of the organoids (6 days) and was not compensated over time (6 weeks, Fig. 1A and B). Organoids developed a structural organization into germinal zones and cortical regions (Fig. 1C; Supplementary Material, Fig. S1A). Germinal zones of SPG11 organoids cultured for both 6 and 9 weeks contained significantly less proliferating phospho-histone H3 positive (PH3+) cells when compared to controls (Fig. 1D, E and G). The thickness of the progenitor zone was significantly reduced in SPG11 organoids after 9 weeks, but not at 6 weeks (Fig. 1F and H), indicating that fewer dividing cells impact the thickness of the germinal wall already at 6 weeks (young organoid stage). In addition, the lumen of the ventricles appeared larger in SPG11 organoids compared to controls (Fig. 1D). It is important to note that cell death levels did not differ between controls and SPG11 organoids (Supplementary Material, Fig. S5), possibly due to a constant rate of ongoing cell death occurring in cerebral organoids model (21).

While vertically dividing NPCs in the apical ventricular zone result in two daughter cells (symmetric division), horizontal (asymmetric) divisions give rise to one stem cell and one neuroblast (13,27). Spindle orientations were evaluated by analyzing division angles of nuclear mitotic apparatus-positive cells in the progenitor zone of organoids. We found a significantly increased amount of horizontally dividing cells at the expense of vertically dividing cells in SPG11 organoids, indicating a shift towards asymmetric division in SPG11 (Fig. 1I and J). We also noticed structural changes in the ventricular zone; while the apico-basal polarity was correctly established as shown by β -catenin (β Cat) staining next to the ventricle-like lumen, the progenitor zone and the cortical plate were less clearly separated as visible by more neuroblasts within the progenitor zone in SPG11 organoids (Fig. 1D; Supplementary Material, Fig. S1B and C).

Longer cell cycle duration in SPG11-NPCs

To explore the duration and the frequency of cell division, we carried out single-cell tracking time-lapse microscopy in SPG11 and control-NPCs (Supplementary Material, Fig. S1D). SPG11NPCs underwent lesser divisions than controls after 6 days in culture (Supplementary Material, Fig. S1E). To follow the fate of individual cells and their progeny, single-cell tracking of GFP-labeled NPCs was performed acquiring phase contrast

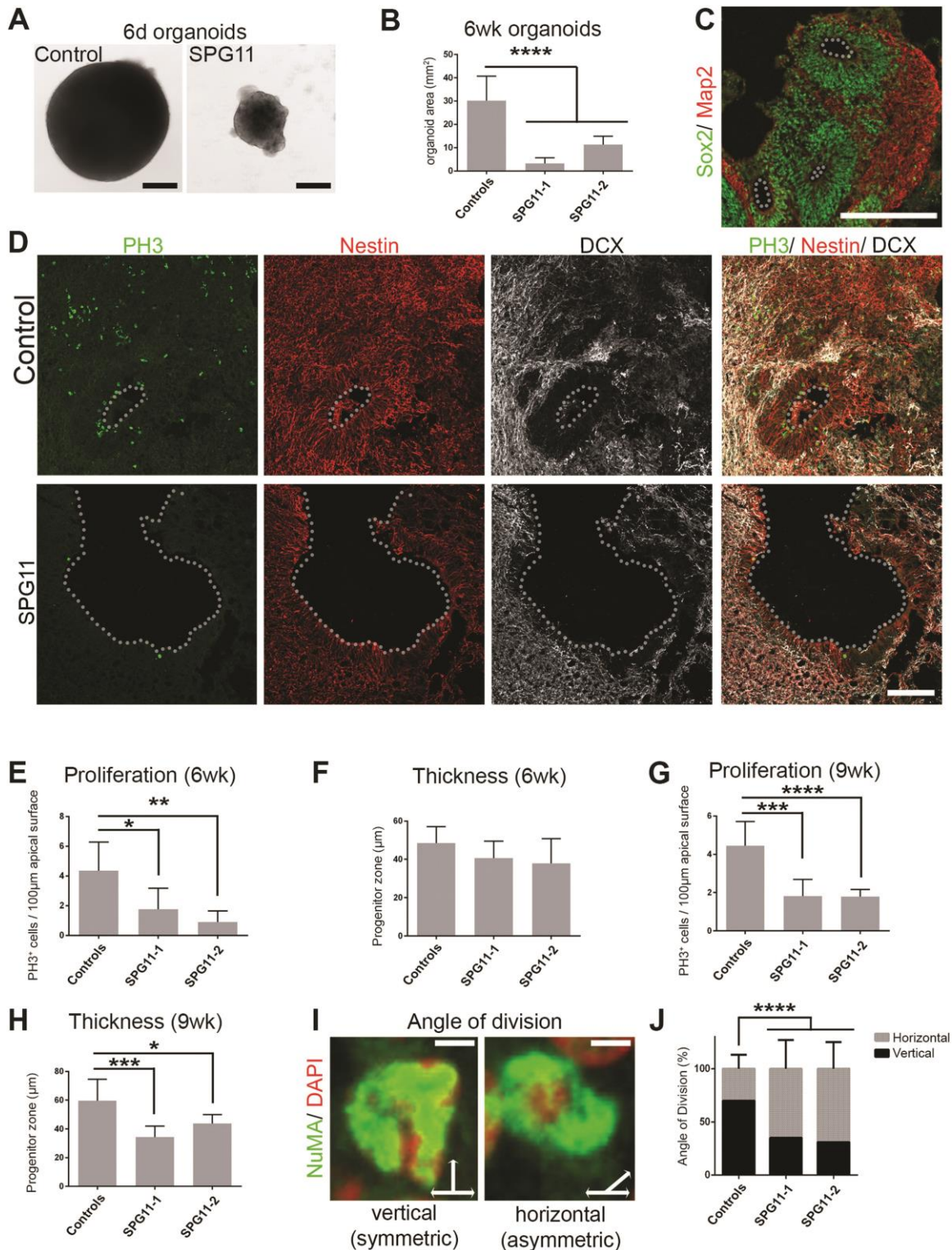


Figure 1. Altered size and self-renewal pattern in SPG11 organoids. (A) Representative bright field images of 6-day-old cerebral organoids generated from SPG11- and control-iPSCs. (B) Significant decrease in total organoid size in SPG11 at 6 weeks (**** $P < 0.0001$; $n \geq 9$ organoids per group). (C) Control cerebral organoids with apical progenitor zones (Sox2+, green) and basal neurons (Map2+, red). (D) Cerebral organoids from control- and SPG11-iPSCs, cultured for 9 weeks. PH3 (green): proliferating cells, nestin (red): NPCs, DCX (grey): neuroblasts. Apical surface indicated by dotted lines. Quantification of (E–H) PH3⁺-cells in the progenitor zone per 100 µm apical surface length, progenitor zone thickness (µm) of 6-week-old (E, F) and 9-week-old (F, H) organoids, respectively (* $P < 0.05$, ** $P < 0.01$, *** $P < 0.001$, **** $P < 0.0001$; $n \geq 5$ organoids per group). (I) Orientation of NuMA+ cells (green): horizontal and vertical divisions (micrographs exemplify angle of division). Nuclei labeled with DAPI (red). (J) Percentage of NuMA+ cells undergoing horizontal and vertical division at the ventricle wall of 6-week-old organoids (**** $P < 0.0001$; $n \geq 200$ cells per group). Controls were grouped in (B), (E–J). All data: mean \pm SD. Scale bars: 200 µm in (A), (C), (D), 5 µm in (I).

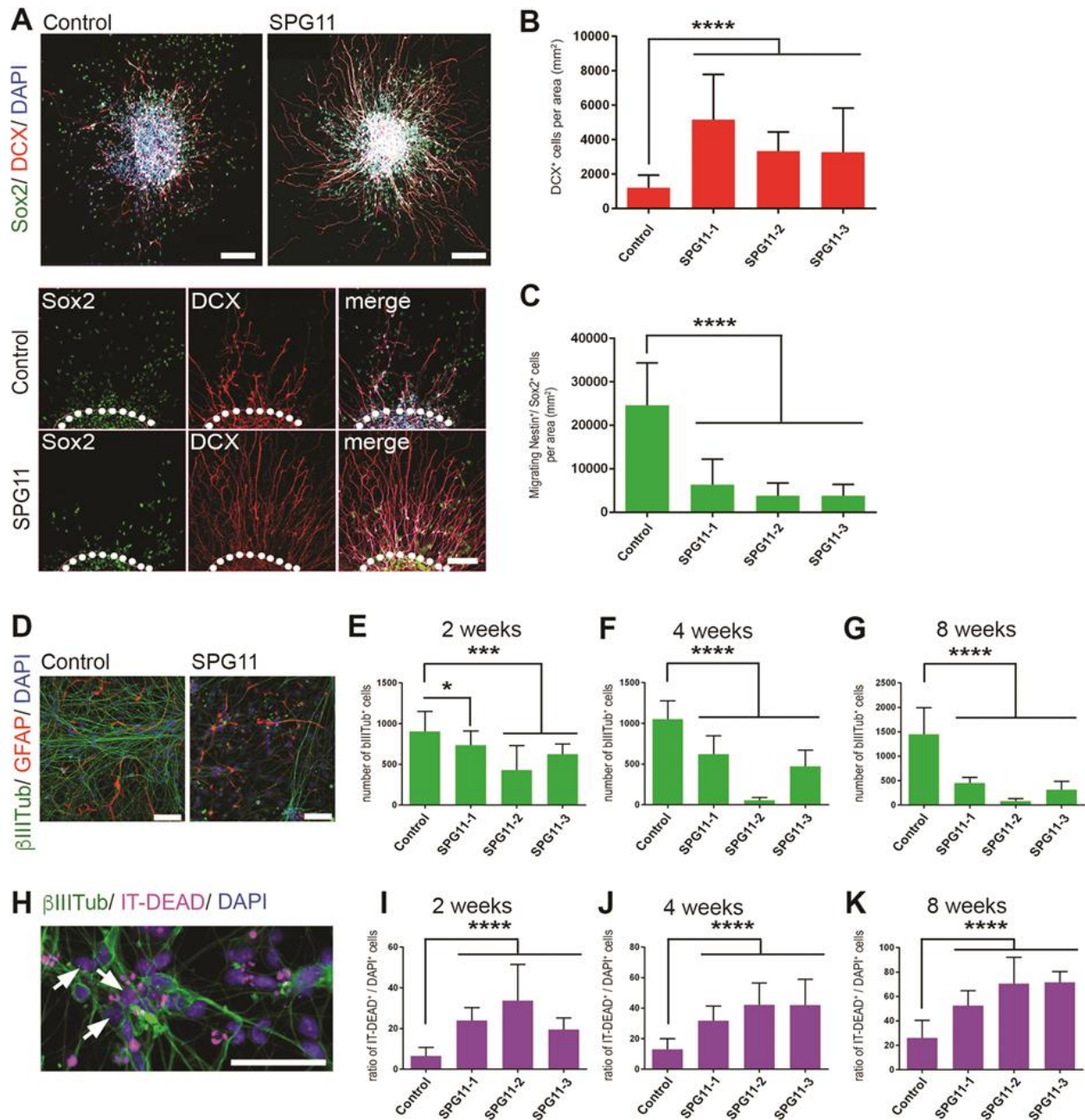


Figure 2. SPG11-NPCs undergo premature neurogenesis. (A) NPC spheres from controls and SPG11 patients; NPCs (green) and neuroblasts (red) were labeled with antiSox2 and anti-DCX, respectively. (B, C) Quantification of migrating DCX⁺- and Sox2⁺-cells in relation to the area of the assessed spheres (dotted lines: borders of the analyzed area; **** P < 0.0001 for all comparisons of control versus SPG11-1, SPG11-2, and SPG11-3; n ≥ 24 spheres per group). (D) Neuronal differentiation of NPCs, labeled for the neuronal marker βIIIITubulin (βIIIITub; green), the astrocyte marker GFAP (red), and DAPI (blue). (E–G) The numbers of βIIIITub⁺-cells are significantly decreased in SPG11 patients' lines at 2, 4 and 8 weeks of differentiation when compared to control (*P < 0.05, **P < 0.001, ****P < 0.0001; n ≥ 10 per group). (H) Neuronal differentiation of NPCs, labeled for βIIIITub (green) and the cell death dye IT-DEAD (magenta), DAPI (blue). Arrows indicate dead neurons. (I–K) Significantly increased numbers of dead cells in SPG11 cortical cultures at 2 (I), 4 (J) and 8 (K) weeks in culture (****P < 0.0001 for all comparisons of control versus SPG11-1, SPG11-2, and SPG11-3; n ≥ 26 per group). All data: mean ± SD. Scale bars: 200 μm [overview (A)] and 50 μm [magnification (A), (D) and (H)].

and fluorescent images every 8 and 160 min, respectively. The temporal analysis showed significantly reduced division rounds per clone in SPG11-NPCs (Supplementary Material, Fig. S1F and G) and delineated that SPG11-NPCs need more time to complete a full cell cycle (Supplementary Material, Fig. S1H).

Premature neurogenesis in SPG11-NPCs

To evaluate changes in migration and neuronal differentiation in NPCs, we analyzed neural stem cell (Sox2/Nestin) and neuroblast markers (DCX) in NPCs growing in spherical structures under mitogenic culture conditions as neurospheres (3). When

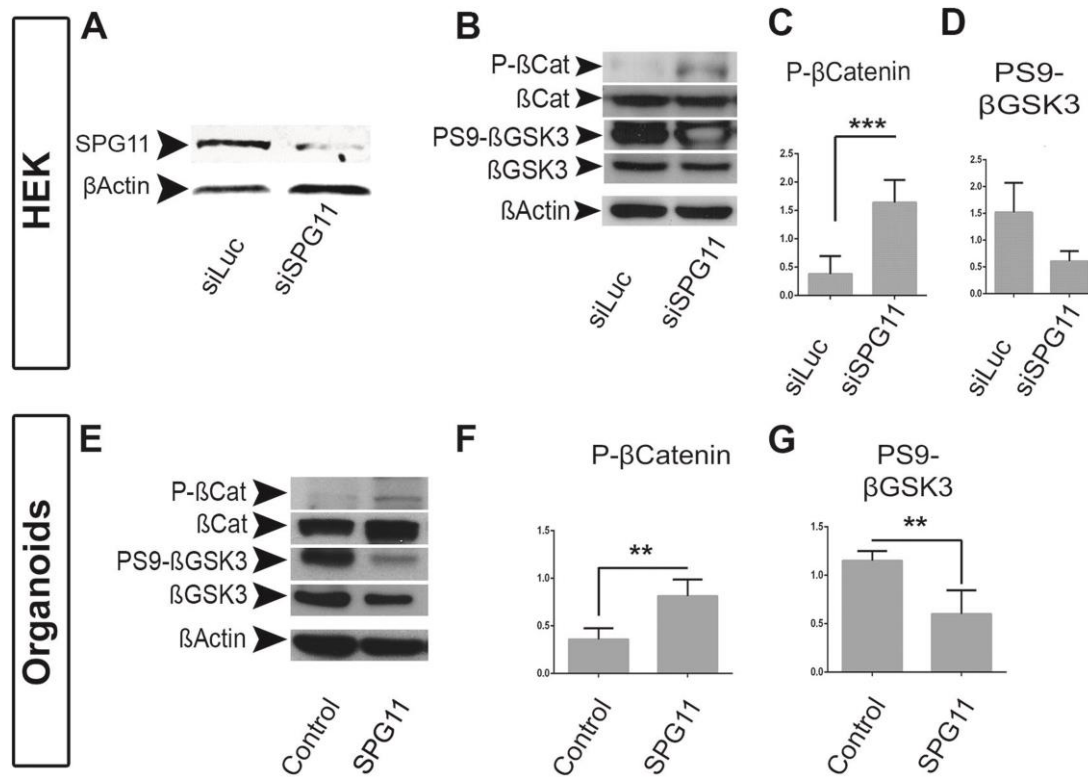


Figure 3. GSK3 overactivation in SPG11. (A–E) HEK cells transfected with control siRNA (siLuc) and siRNA against spatacsin (siSPG11). β -Actin served as loading control. (A) Demonstration of spatacsin knockdown in HEK cells upon siSPG11 transfection, but not siLuc transfection. (B) Western blots of hyperphosphorylated β Cat (P- β Cat), total β Cat, inactivated (PS9- β GSK3) and total β GSK3. (C) Quantification of P- β Cat. Data were related to total β Cat (** P < 0.001; n = 3). (D) Quantification of PS9- β GSK3, related to total β GSK3 (no significant change; n = 3). (E) Western blots of protein preparations of untreated control- and SPG11-organoids, blotted for the same proteins as in (B). (F) Quantification of P- β Cat in control- and SPG11-organoids. Data were related to total β Cat (** P < 0.01; n = 3). (G) PS9- β GSK3 in control- and SPG11-organoids. Data were related to total β GSK3 (** P < 0.01; n = 3). All data: mean \pm SD.

quantifying cells migrating out from the sphere borders 48 h after plating, significantly more DCX+ cells were present in the SPG11 groups, indicating an increased number of migrating neuroblasts (Fig. 2A and B). As expected, the number of Sox2-positive NPCs was significantly reduced in SPG11, while no GFAP-positive cells were present (Fig. 2A and C; Supplementary Material, Fig. S2A). This indicates an increase of migrating neuroblasts at the expense of NPCs, which is in line with the shift in division towards an asymmetric pattern in organoids.

To test if premature neurogenesis, associated with the dysfunction of *SPG11*, implies a decrease in the total number of neurons, we induced neuronal differentiation in SPG11-NPCs. Compared to controls, SPG11-NPCs differentiated for 2, 4 and 8 weeks showed a severe reduction of neurons (Fig. 2D–G) and significantly increased rates of cell death (Fig. 2H–K). The number of GFAP-positive astrocytes was unchanged in weeks 2 and 4. There was a significant increase in GFAP-positive astrocytes at week 8 (Supplementary Material, Fig. S2B).

Partners for the modulation of neurogenesis in spatacsinopathies

SiRNA-mediated knockdown of *SPG11* was performed to model SPATACSIN loss of function in HEK cells (Fig. 3A). P- β Cat levels were significantly increased upon SPG11-siRNA transfection when compared to control luciferase-siRNA transfection (Fig. 3B and C). β GSK3 activity is regulated by phosphorylation at specific sites and phosphorylation of serine-9 (PS9- β GSK3) results in

inactivation (16). In *SPG11*-silenced cells, despite a trend, the inactivated form of β GSK3 (PS9- β GSK3) was unaltered (Fig. 3D). Since this result might have been influenced by the cell type (HEK cells) used for the analysis and to proceed towards the crucial step of translating these findings into precision medicine, knowledge about the biochemical changes in complex neural models is essential. We thus analyzed components of the GSK3/ β Cat pathway in SPG11 organoids. Dysregulation of β GSK3 was also observed in SPG11 organoids, i.e. P- β Cat levels were increased and PS9- β GSK3 levels were significantly decreased (Fig. 3E–G).

Phosphorylated cAMP response element-binding protein (pCREB) is a key factor in the regulation of neurogenesis (12) and previous studies described a direct interaction between pCREB and three amino acids in β GSK3 (17). We therefore investigated, if activated CREB (Supplementary Material, Fig. S3A and B) is altered in SPG11-NPCs. We found a significant increase in SPG11-NPCs, indicative of increased transcription of neurogenic genes (20). These findings imply that premature activation of neurogenesis in SPG11 was driven by a concomitant repression of proliferative pathways of the Wnt/ β Cat system.

Modulation of the GSK3/ β -catenin pathway rescues SPG11 phenotypes

In a first step, we investigated how the premature neurogenesis phenotype in SPG11 can be rescued. We first tested in SPG11- and

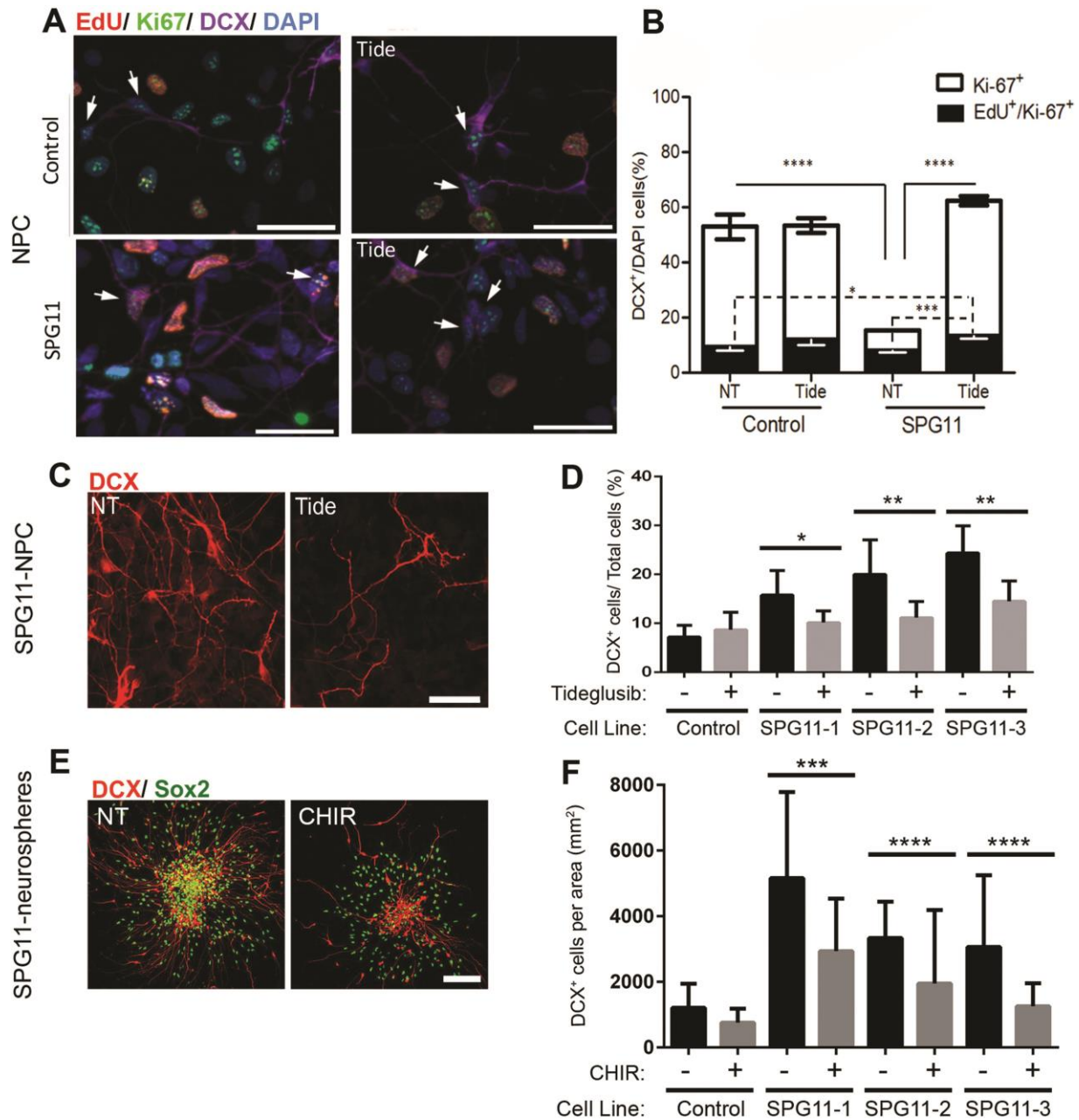


Figure 4. Rescue of premature neurogenesis in SPG11-NPCs. (A) Images of untreated (left) and tide-treated (right) control- and SPG11-NPCs. The cells were stained for EdU (orange), Ki-67 (green) and DCX (purple). Proliferating cells are indicated with arrows. (B) Quantification of the percentage of Ki-67-positive cells out of DCX-positive cells, with representation of the subpopulation of EdU/Ki-67/DCX-positive cells within the proliferative population of neuroblasts (DCX+). (C) Images of SPG11-NPCs, untreated (NT) or treated with tideglusib (Tide) and stained for DCX (red). (D) Quantification of the percentage of neuroblasts (DCX+) in relation to the total number of cells. Three control NPC lines (grouped) and SPG11-NPC lines (SPG11-1 and SPG11-2, SPG11-3, respectively) were analyzed ($n \geq 20$ per condition). (E) Non-treated (NT) and CHIR-treated neurospheres generated from SPG11-NPCs, labeled with DCX (red) and Sox2 (green). (F) Quantification of DCX+ cells in NT or CHIR-treated spheres per mm^2 ($n \geq 20$ per condition). * $P < 0.05$; ** $P < 0.01$; *** $P < 0.001$; **** $P < 0.0001$. Data in (D), (F): mean \pm SD; data in (B): mean \pm SEM. Scale bars: 50 μm .

control-NPCs whether overexpression of SPATACSIN was able to rescue premature neurogenesis. Overexpression of SPATACSIN reduced the number of DCX+ cells in SPG11-NPCs under proliferating conditions (Supplementary Material, Fig. S3C–E), indicating that restoration of SPATACSIN levels can revert the phenotype. To further examine proliferation of SPG11 neuroblasts, we labeled NPCs with EdU 1 h before harvesting (paradigm: Supplementary Material, Fig. S4B). We then counted

EdU/Ki67/ DCX-positive cells within the total population of Ki67/DCX double positive cells. While the percentage of total Ki-67/DCX double positive cells was decreased in SPG11 neurons, there was no significant difference in the EdU-positive subpopulation of the proliferating neuroblasts (EdU/Ki-67/DCX positive cells; Fig. 4A and B).

We next asked whether the observed phenotype can be rescued by manipulation of the βGSK3 pathway. For this aim

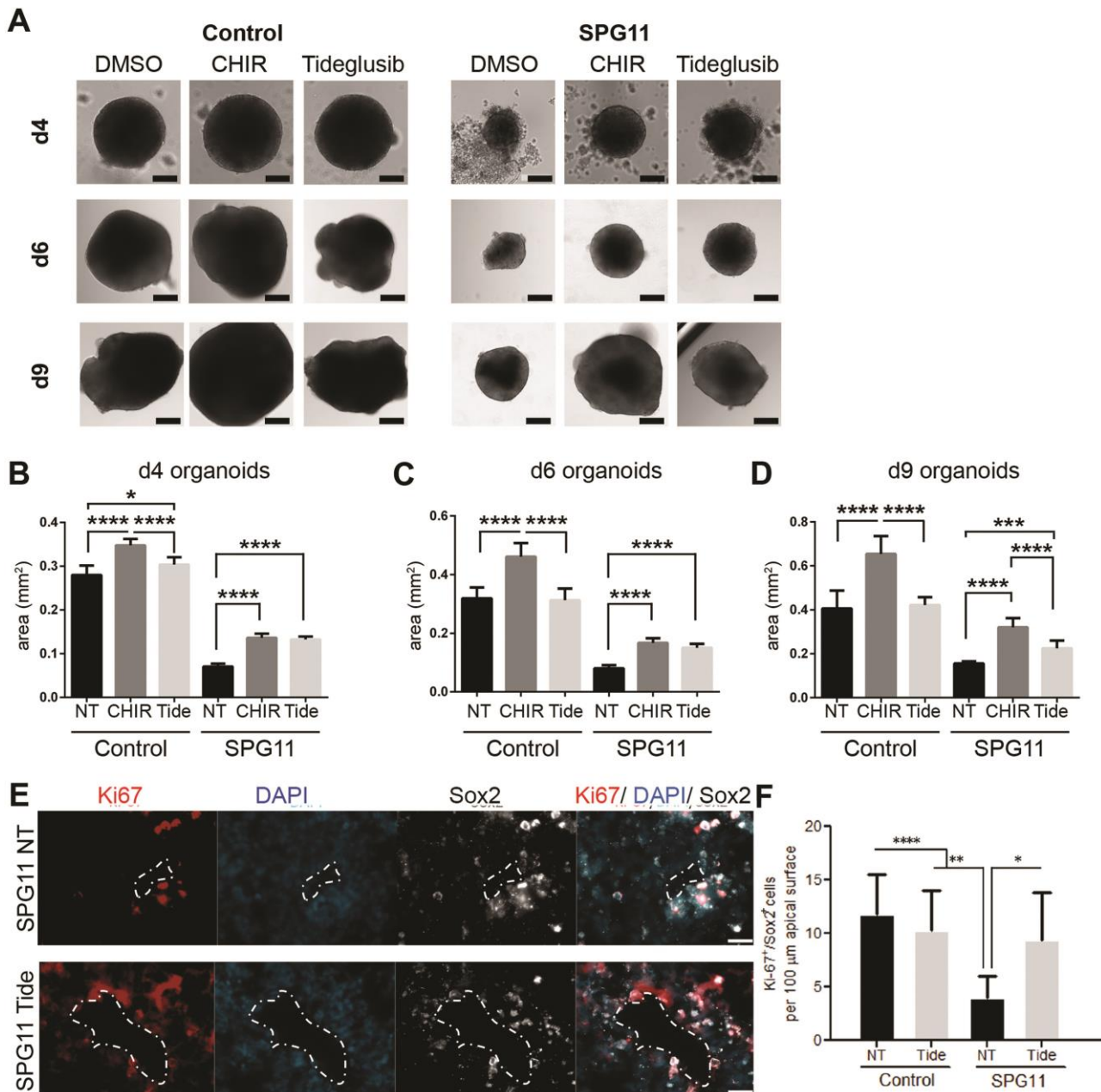


Figure 5. Rescue of SPG11 phenotypes in organoids. (A) Bright field images of control- and SPG11-organoids, NT or treated with CHIR or Tide, at 4, 6 and 9 days in culture. (B–D) Quantification of organoid size at day 4, 6 and 9 for the respective groups. (E) Organoids (40d) stained for Ki-67 (red) and Sox2 (white). (F) Quantification of 40d organoid proliferation (treated according to the paradigm in Supplementary Material, Fig. S4D; * $P < 0.05$, ** $P < 0.01$, *** $P < 0.001$, **** $P < 0.0001$; (A–C): $n \geq 9$ organoids per condition; E–F: $n \geq 3$). All data: mean \pm SD. Scale bars: 200 μ m in (A); 20 μ m in (E).

we employed compounds that specifically inhibit β GSK3, an FDA-approved tideglusib and CHIR. We found that tideglusib was able to increase the number of proliferating neuroblasts in SPG11. (Fig. 4A and B). Interestingly, tideglusib or CHIR treatment reduced the premature generation of neuroblasts in SPG11-NPCs (Fig. 4C and D) and in neurosphere model, respectively (Fig. 4E and F; paradigms Supplementary Material, Fig. S4). In summary, in addition to the rescue of SPATACSIN loss of function by overexpression, also pharmacological inhibition of β GSK3 decreased neuroblast numbers and thus attenuated premature neurogenesis in SPG11-NPCs.

When treating organoids with CHIR or tideglusib (paradigm Supplementary Material, Fig.S4D), SPG11 organoids significantly increased in size compared to untreated controls (Fig. 5A–D). We conclude that decreased organoid size in SPG11 is partially rescued by β GSK3 inhibition. CHIR had effects on both control and SPG11-organoid sizes. Interestingly, tideglusib specifically increased the size of SPG11 organoids, but did not influence organoid size of controls. Moreover, the significantly lower amount of Ki-67+/Sox2+ cells at the apical surface of SPG11 organoids compared to controls was rescued by tideglusib treatment (Fig. 5E and F). This indicates that tideglusib might be a potent compound for SPG11 in 3D structures.

Discussion

We employed iPSC-derived multidimensional neuronal cultures of SPG11 patients to demonstrate that disruption of SPATACSIN leads to impaired self-renewal of cortical NPCs, resulting in premature neurogenesis due to an increase in asymmetric versus symmetric division and consequently a progressively reduced survival of neurons. The addition of an FDA-approved β GSK3 modulator (tideglusib) increased organoid size in SPG11.

Although animal models have provided insights into SPG11, specifically early onset pathologies are inconsistent; a previously published *SPG11*-null mouse, generated by inserting a gene-trap cassette in the first exon of the *SPG11* gene, exclusively showed late-onset motor impairments, together with a massive loss of neurons in the cortex and cerebellum of old mice (39). In contrast, the disruption of *SPG11* by introduction of a stop codon in exon 32, mimicking the most frequent mutation observed in SPG11 patients, resulted in early cognitive deficits, together with abnormal callosal projections and neuronal death in the cortex of mutant mice (2). This considerable variability reflects the need for alternative strategies to decipher the function of spatacsin in human models.

The invention of generating iPSCs opened the unique possibility of modeling disease phenotypes in a human cellular system (38). iPSC-derived 3D neuronal models, so-called cerebral organoids, mimic fetal development and hold great promise of providing the spatial and temporal solution for elucidating disease mechanisms (5,18). Our findings parallel cellular neurodevelopmental phenotypes recently described in human cerebral organoids of severe lissencephalies such as the Miller–Dieker syndrome (1) or other microcephalies (18). Changes at the NPC stage may represent the cellular phenotype of cortical atrophy observed in SPG11 patients. Traditionally considered as a neurodegenerative disease with juvenile onset, cortical MRIs of SPG11 patients evidenced early reductions of grey matter volumes (37). These imaging studies were complemented by the *post-mortem* finding of severe neuronal loss in the frontal cortex of SPG11 patients (10). Specifically, TCC and childhood onset atrophy of the cortex, combined with early onset cognitive impairment might be characteristic of early childhood onset in SPG11 patients. Our finding that dysfunction of *SPG11* interferes with the development of iPSC-derived brain organoids is in line with early cortical atrophy diagnosed in the patients included in this study (15). Our data thus support the hypothesis of an additional neurodevelopmental phenotype in SPG11-HSP.

Our results in SPG11 iPSC-derived neural models suggest a reduced rate of symmetric division of NPCs, a higher proportion of proliferative neuroblasts and defects in the germinal zone of organoids, which ultimately result in premature neurogenesis (Fig. 5G). More specifically, we observe defects at two distinct stages. First of all, SPG11-NPCs present with longer cell cycle, which is complemented by increased asymmetric division rate, resulting in increased number of neuroblasts, or premature neurogenesis. For instance, rodent models revealed interplay between the duration of the cell cycle and the initiation and the total period of neurogenesis (4). A prolonged duration of mitosis was previously connected to premature neuronal differentiation of radial glia cells and an increase in apoptotic cells in a murine model of mago homolog, exon junction complex core component *Magoh* (33). Likewise, in humans, disease-causing mutations have helped to identify molecular mechanisms of cell cycle and neurogenesis regulation. For example, the *protocadherin 19* gene, mutated in intellectual disability, modulates neurogenesis via excessively

prolonged mitosis of progenitors (9). Second, at neuroblast stage, there are less proliferating cells, possibly due to premature differentiation. Overall, the combination of these defects culminated in defective SPG11 neurons (Supplementary Material, Fig. S6).

SPATACSIN was previously linked to a significant decrease of axon-related genes and neurite complexity (32). Activated GSK3 is implicated in neurogenesis, promoting the degradation of β Cat and the activation of an array of transcription factors like CREB, but also in glutamate-induced neuronal death (8). Therefore, our results point out that the dysfunction of SPATACSIN impairs the delicate balance of the GSK3 signaling system. The activation of GSK3, in turn, significantly contributes to changes in NPC proliferation, neurogenesis and neuronal maturation (11). Our previous observations in SPG11-NPCs indicated impaired β Cat signaling in SPG11-NPC that could be rescued by administration of specific β GSK3 inhibitors (25). We took advantage of this knowledge in order to assess whether the same observations are present also in the neurosphere and cerebral organoids models. Along this line, two different GSK3 inhibitors (CHIR and tideglusib) reversed neurodevelopmental defects in SPG11 cortical cultures, and organoids. Tideglusib, an FDA-approved drug, improved cognitive function in mild Alzheimer's Disease (19) and is currently in phase II clinical studies for adolescents with autism spectrum disorder and myotonic dystrophy (clinicaltrials.gov). Tideglusib therefore appeals as a promising compound based on its specificity in blocking β GSK3, which is the isoform distinctively implicated in proliferation/neurogenesis tasks, and thereby rescuing SPG11 neurodevelopmental phenotypes. Furthermore, since the blockade of GSK3 also activates lysosomal/autophagy pathways (30), tideglusib might also attenuate aberrant accumulation of membranous bodies associated with dysfunction of *SPG11* (35).

Our previous study indicated the beneficial effect of β GSK3 inhibition on NPCs. Here, for the first time we link SPG11/SPATACSIN in their roles for the Wnt/ β Cat pathway in a 3D brain organoid system. By confirming the potency of tideglusib in a complex, human brain organoid system we emphasize the clinical relevance of the compound.

In addition, our findings are the first report to decipher impaired cortical neurogenesis in SPG11-HSP. We provide a rigorous spatial and temporal analysis of the related pathology in 2D and 3D systems. Alterations of the natural ratio of cell divisions and proliferation rate are tightly linked to the observed morphological changes of brain organoids. These observations are crucial for the understanding of disease etiology and contribute a novel aspect for clinical intervention.

Experimental procedures

SPG11 patients and controls

Three patients (UKERi6O6-R1, UKERi4AA-R1 and UKERiK22-R1, described as SPG11-1, SPG11-2 and SPG11-3) and two controls (UKERi1JF-R1 and UKERi1E4-R1) were included. Patients were described in detail previously (15). The underlying Institutional Review Board approval (Nr. 4120: *Generierung von humanen neuronalen Modellen bei neurodegenerativen Erkrankungen*) and informed consent were obtained at the movement disorder clinic at the Department of Molecular Neurology, Universitätsklinikum Erlangen (Erlangen, Germany).

IPSC-derived neuronal model

IPSCs were reprogrammed from fibroblasts using Yamanaka's retroviral transduction (two iPSC lines per individual). The lines were maintained and controlled for pluripotency as previously described (14). From every individual, two independent NPC lines and respective neurons were generated using an embryoid body (EB)/rosette protocol (14) and further differentiated into neurons.

Multidimensional cultures

Cerebral organoids were generated from iPSC as previously described (18). For control lines, EBs were generated from 9000 cells each. For patient lines, EBs were generated from 9000 and 18 000 cells with no visible difference in size or development. Two control- and two SPG11-iPSC lines (SPG11-1 and SPG11-2) were analyzed. Controls were grouped. Cerebral organoids were cultured for 40 to 61 days (6 and 9 weeks) at 37°C under 5% CO₂ and atmospheric oxygen. For the rescue experiment, control- and SPG11 organoids were treated with 1 µM of the GSK3 blockers CHIR99021 and tideglusib and kept in culture for 40 to 60 days (6 and 9 weeks). Compounds were replaced every 2–3 days (Supplementary Material, Fig. S4D).

For the neurosphere assay (3), NPCs were kept in suspension in 96 well ultra-low attachment plates (Corning, Amsterdam, the Netherlands) for 72 h at a density of 5×10^4 cells/cm² under proliferative conditions. For the analysis of NPC migration, neurospheres grew attached to polyornithine/laminin (Invitrogen, Carlsbad, California, United States) coated coverslips for 48 h (Fig. 2A). Spheres generated from six SPG11-NPC lines (SPG11-1, SPG11-2 and SPG11-3) were compared to controls.

Time-lapse video microscopy

Control- and SPG11-NPCs were infected with a pEF1-GFP lentivirus. Time-lapse assays were performed for 6 days under mitogenic conditions. Time-lapses and single-cell tracking (29) of SPG11- and control-NPCs were performed with a cell observer (Zeiss Jena, Germany) at 37°C and 5% CO₂. Phase contrast and fluorescent images were acquired every 8 and 160 min respectively using a 20× phase contrast microscopy objective (Zeiss), an AxioCam HRm camera and Zeiss AxioVision 4.7 software (Zeiss). Time-lapses were assembled using ImageJ whereas single-cell tracking was carried out using a self-written computer program (TTT). Per every assessed NPC line, at least 40–50 videos were analyzed and 50 single cells tracked. Time-lapse analyses were evaluated from two control- and three SPG11NPC lines (SPG11-1, SPG11-2 and SPG11-3). Control NPC lines were grouped.

Statistical analysis

Immunofluorescence analyses, neurite measurement, protein expression and phosphorylation were statistically analyzed using Prism (GraphPad, San Diego, California, United States). Unless indicated otherwise, all data are shown as mean ± SD. Statistical analysis was carried out employing the Student's *t* test for unpaired variables (two-tailed) and one-way *analysis of variance* followed by Bonferroni multiple comparison tests when three or more groups were compared. *P*-values < 0.05 were considered significant.

Detailed information on the transfection of human cells and details for immunofluorescence, protein sample preparation and western blot assays are listed in the supplemental methods.

Supplementary Material

Supplementary Material is available at *HMG* online.

Acknowledgements

This work is dedicated to our patients, whom we have been following up for more than 15 years now, controls and is *in memoriam* of Anne Wahlig. We thank Professor Chichung Lie, Timucin Öztürk, Dr Iryna Prots, Holger Wend and Dr Marisa Karow for excellent support and critical input.

Conflict of Interest statement. None declared.

Funding

Tom-Wahlig Foundation Advanced Fellowship; German Federal Ministry of Education and Research (BMBF: 01GQ113, 01GM1520A, 01EK1609B); Deutsche Forschungsgemeinschaft (GRK2162 to M.R., T.P., J.W., B.W., CA 1205/2-1 to S.C.); Interdisciplinary Centre for Clinical Research (University Hospital Erlangen; N3 to B.W., J52 to M.R.); Bavarian Ministry of Education and Culture, Science and the Arts in the framework of the Bavarian Research Network for Molecular Biosystems (BioSysNet); Bavarian Network for induced pluripotent stem cells (ForIPS).

Author contributions

F.P.B., I.Y.B., S.C. and B.W. participated in the conceptualization. F.P.B., I.Y.B., T.P., W.F., A.S., H.M., S.C. and B.W. conceived the methodology. F.P.B., I.Y.B., T.P., W.F., A.S. and D.G. performed the investigation. F.P.B., I.Y.B., M.R., T.P., J.W., S.C. and B.W. wrote and edited the manuscript and figures.

References

- Bershteyn, M., Nowakowski, T.J., Pollen, A.A., Di Lullo, E., Nene, A., Wynshaw-Boris, A. and Kriegstein, A.R. (2017) Human iPSC-derived cerebral organoids model cellular features of lissencephaly and reveal prolonged mitosis of outer radial glia. *Cell Stem Cell*, 20, 435–449. doi:10.1016/j.stem.2016.12.007
- Branchu, J., Boutry, M., Sourd, L., Depp, M., Leone, C., Corriger, A., Vallucci, M., Esteves, T., Matusiak, R., Dumont, M. *et al.* (2017) Loss of spatascin function alters lysosomal lipid clearance leading to upper and lower motor neuron degeneration. *Neurobiol. Dis.*, 102, 21–37. doi:10.1016/j.nbd.2017.02.007
- Brennand, K., Savas, J.N., Kim, Y., Tran, N., Simone, A., Hashimoto-Torii, K., Beaumont, K.G., Kim, H.J., Topol, A., Ladrán, I. *et al.* (2015) Phenotypic differences in hiPSC NPCs derived from patients with schizophrenia. *Mol. Psychiatry*, 20, 361–368. doi:10.1038/mp.2014.22
- Calegari, F., Haubensak, W., Haffner, C. and Huttner, W.B. (2005) Selective lengthening of the cell cycle in the neurogenic subpopulation of neural progenitor cells during mouse brain development. *J. Neurosci.*, 25, 6533–6538. doi:10.1523/JNEUROSCI.0778-05.2005
- Camp, J.G., Badsha, F., Florio, M., Kanton, S., Gerber, T., Wilsch-Bräuninger, M., Lewitus, E., Sykes, A., Hevers, W., Lancaster, M. *et al.* (2015) Human cerebral organoids recapitulate gene expression programs of fetal neocortex development. *Proc. Natl. Acad. Sci. U. S. A.*, 112, 15672–15677. doi:10.1073/pnas.1520760112

6. Chailangkarn, T., Trujillo, C.A., Freitas, B.C., Hrvoj-Mihic, B., Herai, R.H., Yu, D.X., Brown, T.T., Marchetto, M.C., Bardy, C., McHenry, L. *et al.* (2016) A human neurodevelopmental model for Williams syndrome. *Nature*, 536, 338–343. doi:10.1016/j.neuroimage.2010.06.010.
7. Chang, J., Lee, S. and Blackstone, C. (2014) Spastic paraplegia proteins spastizin and spatacsin mediate autophagic lysosome reformation. *J. Clin. Invest.*, 124, 5249–5262. doi:10.1172/JCI77598DS1.
8. Chuang, D.-M., Wang, Z. and Chiu, C.-T. (2011) GSK3 as a target for lithium-induced neuroprotection against excitotoxicity in neuronal cultures and animal models of ischemic stroke. *Front. Mol. Neurosci.*, 4, 15. doi:10.3389/fnmol.2011.00015.
9. Compagnucci, C., Petrini, S., Higurashi, N., Trivisano, M., Specchio, N., Hirose, S., Bertini, E. and Terracciano, A. (2015) Characterizing PCDH19 in human induced pluripotent stem cells (iPSCs) and iPSC-derived developing neurons: emerging role of a protein involved in controlling polarity during neurogenesis. *Oncotarget*, 6, 26804–26813. doi:10.18632/oncotarget.5757.
10. Denora, P.S., Smets, K., Zolfanelli, F., Ceuterick-de Groote, C., Casali, C., Deconinck, T., Sieben, A., Gonzales, M., Züchner, S., Darios, F. *et al.* (2016) Motor neuron degeneration in spastic paraplegia 11 mimics amyotrophic lateral sclerosis lesions. *Brain*, 139, 1723–1734. doi:10.1093/brain/aww061.
11. Duan, X., Chang, J.H., Ge, S., Faulkner, R.L., Kim, J.Y., Kitabatake, Y., Liu, X.-B., Yang, C.-H., Jordan, J.D., Ma, D.K. *et al.* (2007) Disrupted-in-schizophrenia 1 regulates integration of newly generated neurons in the adult brain. *Cell*, 130, 1146–1158. doi:10.1016/j.cell.2007.07.010.
12. Faigle, R. and Song, S. (2013) Signaling mechanisms regulating adult neural stem cells and neurogenesis. *Biochim. Biophys. Acta.*, 1830, 2435–2448. doi:10.1016/j.bbagen.2012.09.002.
13. Götz, M. and Huttner, W.B. (2005) The cell biology of neurogenesis. *Nat. Rev. Mol. Cell Biol.*, 6, 777–788. doi:10.1038/nrm1739.
14. Havlicek, S., Kohl, Z., Mishra, H.K., Prots, I., Eberhardt, E., Denguir, N., Wend, H., Plötz, S., Boyer, L., Marchetto, M.C.N. *et al.* (2014) Gene dosage-dependent rescue of HSP neurite defects in SPG4 patients' neurons. *Hum. Mol. Genet.*, 23, 2527–2541. doi:10.1093/hmg/ddt644.
15. Hehr, U., Bauer, P., Winner, B., Schüle, R., Olmez, A., Koehler, W., Uyanik, G., Engel, A., Lenz, D., Seibel, A. *et al.* (2007) Long-term course and mutational spectrum of spatacsin-linked spastic paraplegia. *Ann. Neurol.*, 62, 656–665. doi:10.1002/ana.21310.
16. Hur, E.M. and Zhou, F.Q. (2010) GSK3 signalling in neural development. *Nat. Rev. Neurosci.*, 11, 539–551.
17. Ilouz, R., Kowalsman, N., Eisenstein, M. and Eldar-Finkelman, H. (2006) Identification of novel glycogen synthase kinase-3beta substrate-interacting residues suggests a common mechanism for substrate recognition. *J. Biol. Chem.*, 281, 30621–30630.
18. Lancaster, M.A., Renner, M., Martin, C.-A., Wenzel, D., Bicknell, L.S., Hurles, M.E., Homfray, T., Penninger, J.M., Jackson, A.P. and Knoblich, J.A. (2013) Cerebral organoids model human brain development and microcephaly. *Nature*, 501, 373–379. doi:10.1038/nature12517.
19. Lovestone, S., Boada, M., Dubois, B., Hüll, M., Rinne, J.O., Huppertz, H.-J., Calero, M., Andrés, M.V., Gómez-Carrillo, B., León, T., del Ser, T. and ARGO investigators (2015) A phase II trial of tideglusib in Alzheimer's disease. *J. Alzheimers Dis.*, 45, 75–88. doi:10.3233/JAD-141959.
20. Mao, Y., Ge, X., Frank, C.L., Madison, J.M., Koehler, A.N., Doud, M.K., Tassa, C., Berry, E.M., Soda, T., Singh, K.K. *et al.* (2009) Disrupted in schizophrenia 1 regulates neuronal progenitor proliferation via modulation of GSK3beta/beta-catenin signaling. *Cell*, 136, 1017–1031. doi:10.1016/j.cell.2008.12.044.
21. Mansour, A.A., Gonçalves, J.T., Bloyd, C.W., Li, H., Fernandes, S., Quang, D., Johnston, S., Parylak S.L., Jin, X., Gage, F.H. (2018) An in vivo model of functional and vascularized human brain organoids. *Nat. Biotechnol.*, 36, 432–441. doi:10.1038/nbt.4127.
22. Marchetto, M.C., Belinson, H., Tian, Y., Freitas, B.C., Fu, C., Vadodaria, K., Beltrao-Braga, P., Trujillo, C.A., Mendes, A.P.D., Padmanabhan, K. *et al.* (2017) Altered proliferation and networks in neural cells derived from idiopathic autistic individuals. *Mol. Psychiatry*, 22, 820–835. doi:10.1038/mp.2016.95.
23. Marchetto, M.C.N., Carromeu, C., Acab, A., Yu, D., Yeo, G.W., Mu, Y., Chen, G., Gage, F.H. and Muotri, A.R. (2010) A model for neural development and treatment of Rett syndrome using human induced pluripotent stem cells. *Cell*, 143, 527–539. doi:10.1016/j.cell.2010.10.016.
24. Mariani, J., Coppola, G., Zhang, P., Abyzov, A., Provini, L., Tomasini, L., Amenduni, M., Szekeley, A., Palejev, D., Wilson, M. *et al.* (2015) FOXP1-dependent dysregulation of GABA/glutamate neuron differentiation in autism spectrum disorders. *Cell*, 162, 375–390. doi:10.1016/j.cell.2015.06.034.
25. Mishra, H.K., Prots, I., Havlicek, S., Kohl, Z., Pérez-Brangulí, F., Boerstler, T., Anneser, L., Minakaki, G., Wend, H., Hampl, M. *et al.* (2016) GSK3β-dependent dysregulation of neurodevelopment in SPG11-patient induced pluripotent stem cell model. *Ann. Neurol.*, 79, 826–840. doi:10.1111/j.1471-4159.2007.05194.x.
26. Montecchiani, C., Pedace, L., Lo Giudice, T., Casella, A., Mearini, M., Gaudiello, F., Pedroso, J.L., Terracciano, C., Caltagirone, C., Massa, R. *et al.* (2015) ALS5/SPG11/KIAA1840 mutations cause autosomal recessive axonal Charcot-Marie-Tooth disease. *Brain*, 139, 73–85. doi:10.1093/brain/aww320.
27. Noctor, S.C., Martínez-Cerdeño, V., Ivic, L. and Kriegstein, A.R. (2004) Cortical neurons arise in symmetric and asymmetric division zones and migrate through specific phases. *Nat. Neurosci.*, 7, 136–144. doi:10.1038/nn1172.
28. Orlacchio, A., Babalini, C., Borreca, A., Patrono, C., Massa, R., Basaran, S., Munhoz, R.P., Rogueva, E.A., St George-Hyslop, P.H., Bernardi, G. and Kawarai, T. (2010) SPATACSIN mutations cause autosomal recessive juvenile amyotrophic lateral sclerosis. *Brain*, 133, 591–598. doi:10.1093/brain/awp325.
29. Ortega, F., Berninger, B. and Costa, M.R. (2013) Primary culture and live imaging of adult neural stem cells and their progeny. *Methods Mol. Biol.*, 1052, 1–11. doi:10.1007/7651_2013_22.
30. Parr, C., Carzaniga, R., Gentleman, S.M., Van Leuven, F., Walter, J. and Sastre, M. (2012) Glycogen synthase kinase 3 inhibition promotes lysosomal biogenesis and autophagic degradation of the amyloid-β precursor protein. *Mol. Cell Biol.*, 32, 4410–4418. doi:10.1128/MCB.00930-12.
31. Pensato, V., Castellotti, B., Gellera, C., Pareyson, D., Ciano, C., Nanetti, L., Salsano, P., Piscoquito, G., Sarto, E., Eoli, M. *et al.* (2014) Overlapping phenotypes in complex spastic paraplegias SPG11, SPG15, SPG35 and SPG48. *Brain*, 137, 1907–1920.
32. Pérez-Brangulí, F., Mishra, H.K., Prots, I., Havlicek, S., Kohl, Z., Saul, D., Rummel, C., Dorca-Arevalo, J., Regensburger, M., Graef, D. *et al.* (2014) Dysfunction of spatacsin leads to axonal pathology in SPG11-linked hereditary spastic paraplegia. *Hum. Mol. Genet.*, 23, 4859–4874. doi:10.1093/hmg/ddu200.

33. Pilaz, L.-J. and Silver, D.L. (2015) Post-transcriptional regulation in corticogenesis: how RNA-binding proteins help build the brain. *Wiley Interdiscip. Rev. RNA*, 6, 501–515. doi:10.1002/wrna.1289.
34. Qian, X., Nguyen, H.N., Song, M.M., Hadiono, C., Ogden, S.C., Hammack, C., Yao, B., Hamersky, G.R., Jacob, F., Zhong, C. *et al.* (2016) Brain-region-specific organoids using minibioreactors for modeling ZIKV exposure. *Cell*, 165, 1238–1254. doi:10.1016/j.cell.2016.04.032.
35. Renvoisé, B., Chang, J., Singh, R., Yonekawa, S., FitzGibbon, E.J., Mankodi, A., Vanderver, A., Schindler, A., Toro, C., Gahl, W.A. *et al.* (2014) Lysosomal abnormalities in hereditary spastic paraplegia types SPG15 and SPG11. *Ann. Clin. Transl. Neurol.*, 1, 379–389. doi:10.1002/acn3.64.
36. Stevanin, G., Santorelli, F.M., Azzedine, H., Coutinho, P., Chomilier, J., Denora, P.S., Martin, E., Ouvrard-Hernandez, A.-M., Tessa, A., Bouslam, N. *et al.* (2007) Mutations in SPG11, encoding spatacsin, are a major cause of spastic paraplegia with thin corpus callosum. *Nat. Genet.*, 39, 366–372. doi:10.1038/ng1980.
37. Stromillo, M.L., Malandrini, A., Dotti, M.T., Battaglini, M., Borgogni, F., Tessa, A., Storti, E., Denora, P.S., Santorelli, F.M., Gaudiano, C. *et al.* (2011) Structural and metabolic damage in brains of patients with SPG11-related spastic paraplegia as detected by quantitative MRI. *J. Neurol.*, 258, 2240–2247. doi:10.1007/s00415-011-6106-x.
38. Takahashi, K., Tanabe, K., Ohnuki, M., Narita, M., Ichisaka, T., Tomoda, K. and Yamanaka, S. (2007) Induction of pluripotent stem cells from adult human fibroblasts by defined factors. *Cell*, 131, 861–872. doi:10.1016/j.cell.2007.11.019
39. Varga, R.-E., Khundadze, M., Damme, M., Nietzsche, S., Hoffmann, B., Stauber, T., Koch, N., Hennings, J.C., Franzka, P., Huebner, A.K. *et al.* (2015) In vivo evidence for lysosome depletion and impaired autophagic clearance in hereditary spastic paraplegia type SPG11. *PLoS Genet.*, 11, e1005454. doi:10.1371/journal.pgen.1005454.

Human SPG11 cerebral organoids reveal cortical neurogenesis impairment

Authors

Francesc Perez-Branguli^{1,‡,*}, **Isabel Y Buchsbaum**^{2,3,‡}, Tatyana Pozner^{1,‡}, Martin Regensburger^{1,4}, Wenqiang Fan⁶, Annika Schray¹, Tom Borstler¹, Himanshu Mishra¹, Daniela Graf¹, Zacharias Kohl^{5,8}, Jurgen Winkler^{5,8}, Benedikt Berninger^{6,7}, Silvia Cappello^{2,*} and Beate Winner^{1,8,*},†

Supplemental figures:

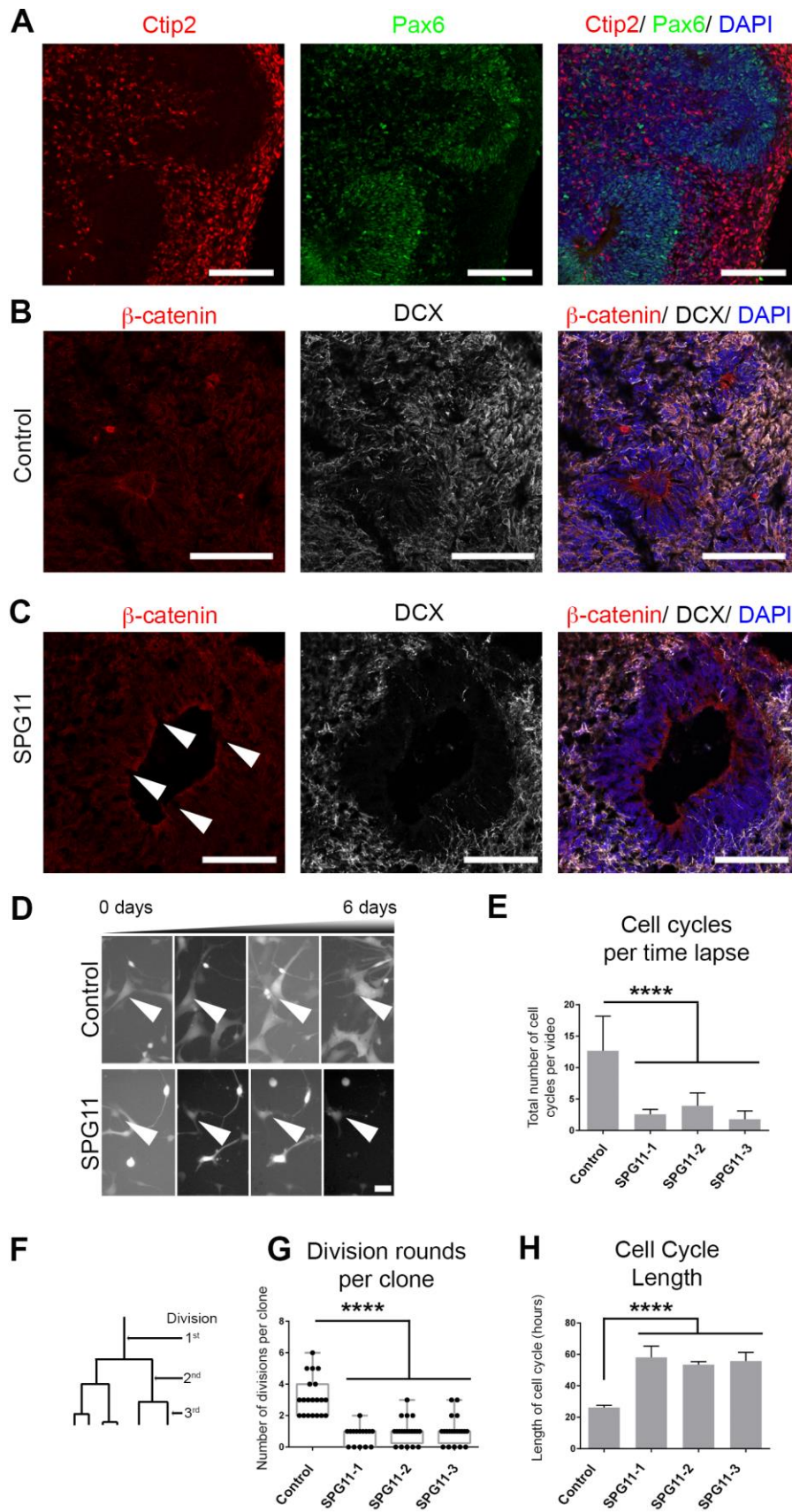


Fig. S1. Altered ventricle structure and cell cycle dynamics in SPG11 organoids. Related to Fig. 1. **(A)** Staining for Ctip2 (red) indicating cortical differentiation in control organoids, separated from the basal localization of PAX6-positive cells (green) close to the lumina. **(B, C)** β -catenin staining (red) shows that apico-basal polarity is correctly established but the apical border of the proliferative zone (arrowheads) is less clearly defined in 9 weeks old SPG11 organoids (C) compared to controls (B) Scale bars=100 μ m. **(D-H)** 6-day time lapse analysis of control- and SPG11-NPCs expressing GFP. **(D)** Visual representation of single cells of control and SPG11 cortical NPCs (arrows) over time. Scale bar=10 μ m. **(E)** Total numbers of cell cycles per assessed time-lapse. **(F)** Scheme of division round quantification of single NPCs. **(G)** Number of division rounds of single clones. **(H)** Length of each cell cycle in single clones. All data are presented as mean \pm SD. Two-way ANOVA and Bonferroni's adjustment for multiple comparisons were performed; ****P <0.0001 for comparison of Controls vs. SPG11-1, SPG11-2, and SPG11-3, respectively (n \geq 200 cells per condition).

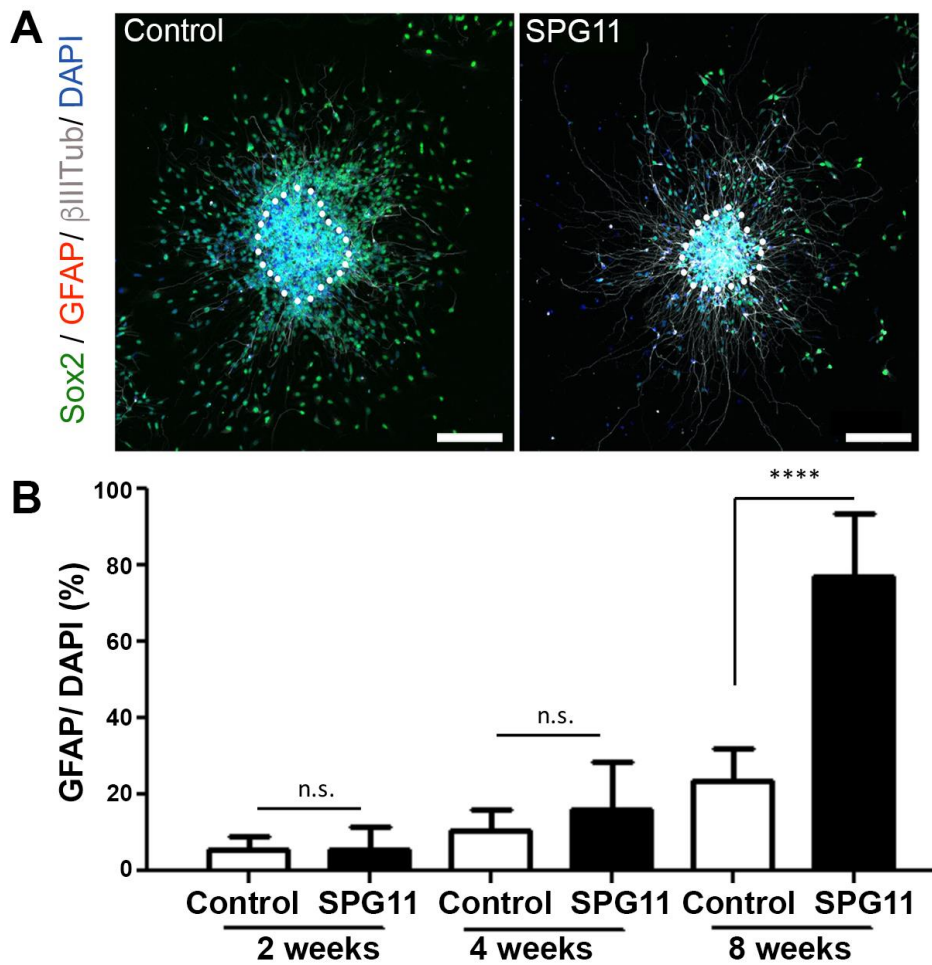


Fig. S2. Astrocytes in SPG11 and control neurospheres and NPCs. Related to Fig. 2. **(A)** Absence of GFAP labeled astrocytes in neurospheres generated from controls and SPG11 patients (SPG11). Neurospheres were labelled with the neural stem cell marker Sox2 (green), the astrocyte marker GFAP (red) and the neuronal marker β III Tubulin (β III Tub, grey). Scale bars=200 μ m. **(B)** Neuronal cultures of SPG11 and controls differentiated for 2, 4, and 8 weeks. The % of GFAP within the culture is not significantly different at 2 and 4 weeks, but there is a significant increase in the portion of GFAP positive cells at 8 weeks in the SPG11 group **** $P < 0.0001$. Data: mean \pm SD.

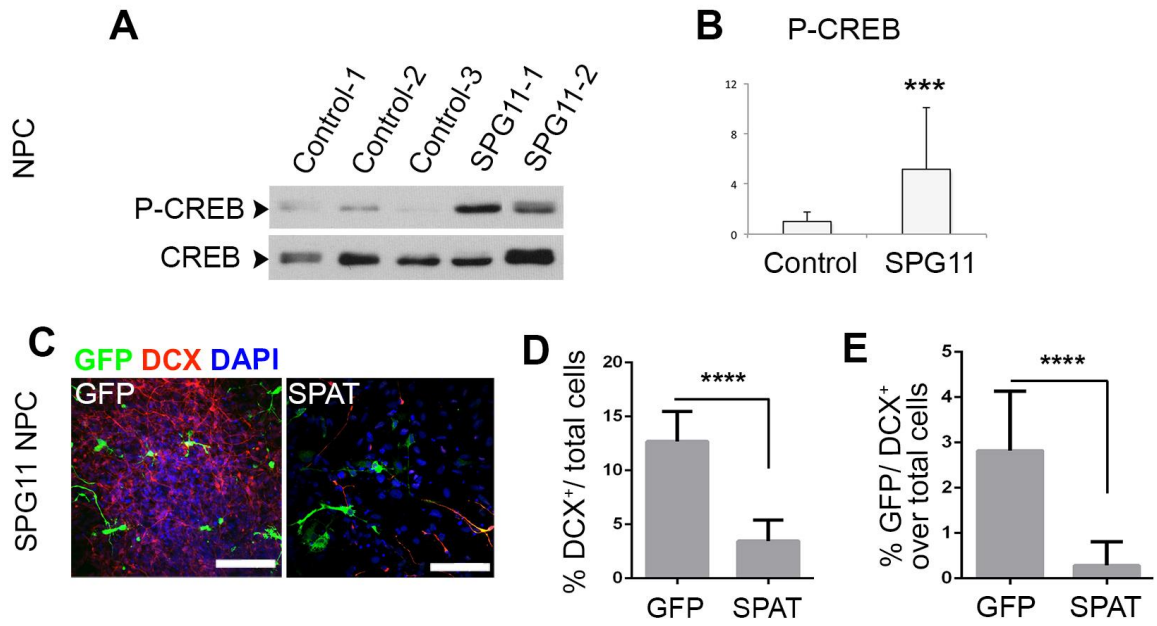


Fig. S3. Spatacsin mediated impairments in SPG11-NPCs. (A) Western Blot of the nuclear (nuc) fraction of NPCs for phosphorylated CREB (P-CREB) and total CREB. (B) Quantification of the ratio of P-CREB over CREB (related to Fig.3; *** $P < 0.001$; $n = 3$; means \pm SD). (C, D) DCX⁺-cells (red) in SPG11-NPCs transfected with GFP or GFP-spatacsin (SPAT). (D) Quantification of DCX⁺-cells (ratio of DCX⁺/DAPI⁺, ** $n = 4$ transfections, each with 10 images). (E) Quantification of DCX/DAPI double positive cells over all (DAPI⁺) cells ($n = 4$ transfections, each with 10 images). Scale bars=200 μ m.

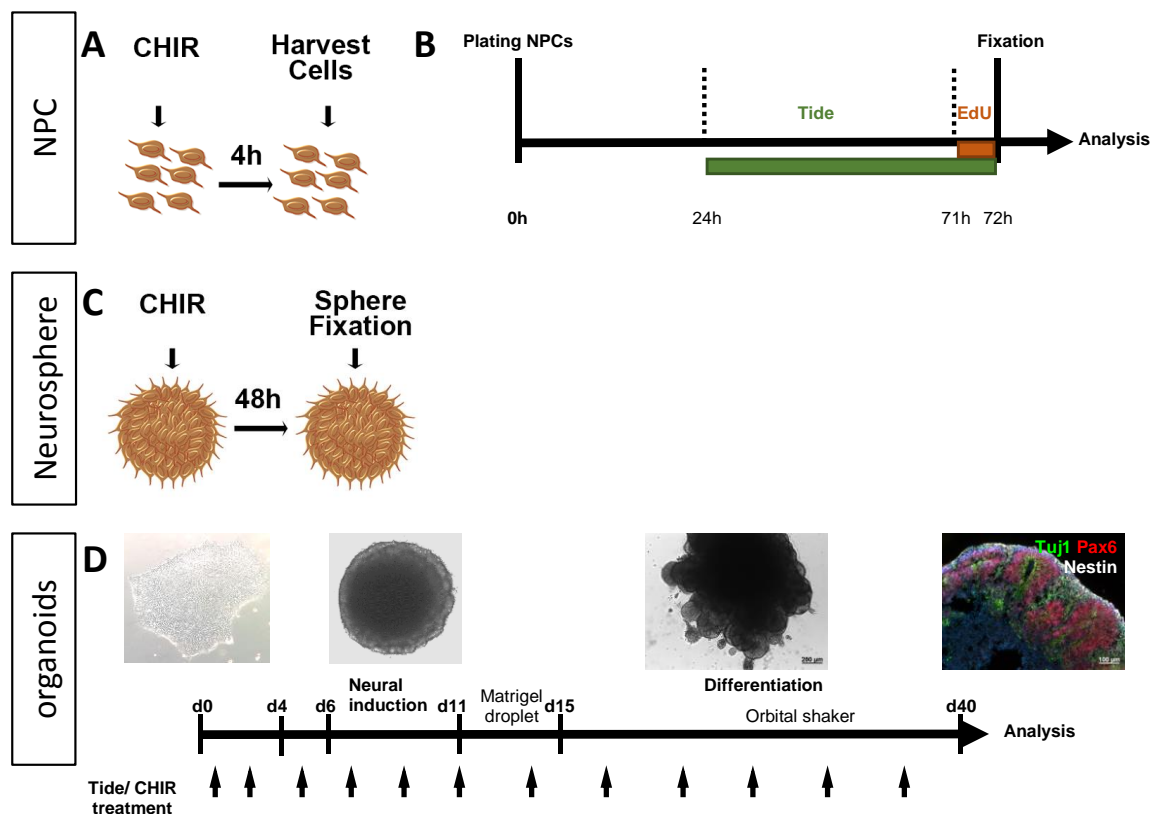


Fig. S4. Paradigms of rescue strategies of premature neurogenesis in SPG11. (A) NPC-derived NPCs. **(B)** Paradigm for Tide treatment and addition of EdU (Fig 4E, F). **(C)** Neurospheres were treated with CHIR for 48h. **(D)** For organoid treatment, compounds were added to culture medium at 1 μ M concentration from plating of cells during the formation of embryoid bodies until fixation; medium including compounds was changed every 2-3 days (every 2 days after plating and every 3 days from embedding in Matrigel).

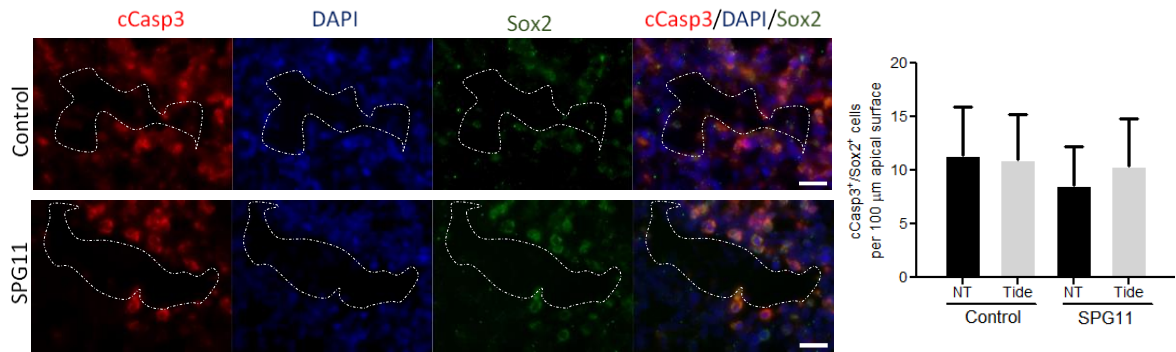


Fig. S5. Cell death in SPG11 and control organoids. Co-staining for cleaved caspase-3 (cCASP3; red) and Sox2 (green) positive cells within the apical surface of ventricular zones. Scale bar=20 μ M. Quantification of the cCasp3⁺/Sox2⁺ in 3 ventricular structures of organoids (n=3 per condition) reveals no significance difference between controls and SPG11 patients. Additionally, Tide treatment has no significant effect on cell death. All data are presented as mean \pm SD. One-way ANOVA and Bonferroni's adjustment for multiple comparisons were performed.

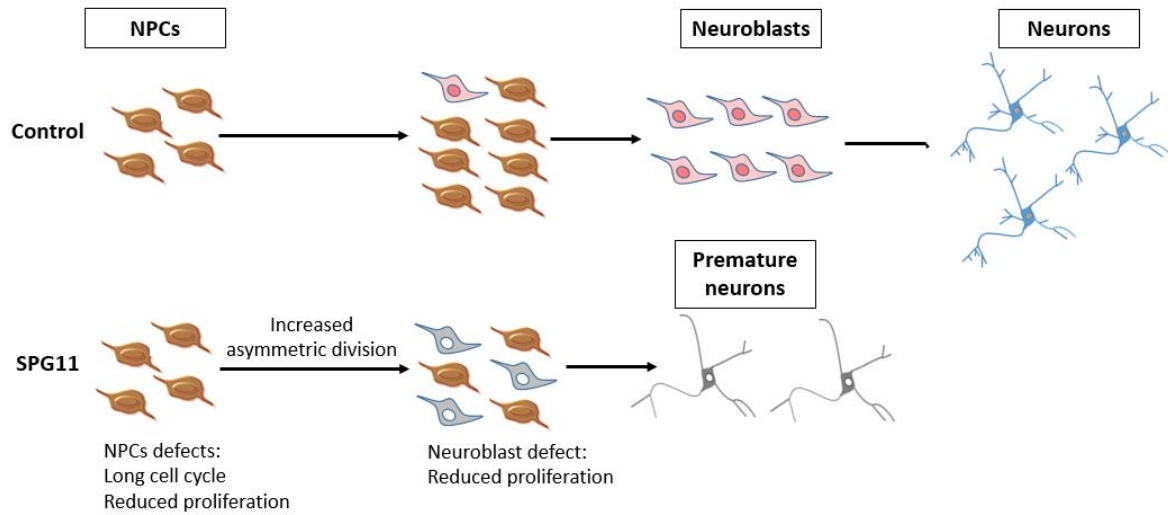


Fig. S6. Schematic representation of premature neurogenesis observed in SPG11. Compared to controls, SPG11 iPSCs derived NPCs have longer cell cycle, reduced proliferation and increased level of asymmetric divisions, leading to increased number of neuroblasts that exhibit proliferation defects. Overall, the impairments lead to premature neurons.

Supplemental Table 1

Antibody	Host	Exp. used	Concentration	Company
anti- β Catenin (clone H-102)	rabbit polyclonal	IB/IF	1:500	Santa Cruz
anti-NuMA	rabbit polyclonal	IF	1:500	Abcam
anti-GSK3 (clone 4G-1E)	mouse monoclonal	IB	1:500	Millipore
anti- β Actin (1:1000)	mouse monoclonal	IB	1:2000	Sigma-Aldrich
anti-H2A (Histone 2A, clone JBW301)	mouse monoclonal	IB	1:1000	Millipore
anti-HA (Hemagglutinin tag, clone HA.C5)	mouse monoclonal	IB/IF	1:1000	Abcam
anti-GFP	rabbit polyclonal	IB/ IF	1:1000	ThermoFisher
anti- β III Tubulin (TUBB3)	rabbit monoclonal	IF	1:1000	BioLegend
anti- β III Tubulin (TUBB3)	mouse monoclonal	IF	1:1000	BioLegend
anti-Glial fibrillary acidic protein	rabbit monoclonal	IF	1:1000	Millipore
anti-Nestin (clone 10C2)	mouse monoclonal	IF	1:1000	Millipore
anti-Sox2 (clone D6D9)	rabbit monoclonal	IF	1:400	Cell Signaling
anti-DCX (clone C-18)	goat polyclonal	IF	1:200	Santa Cruz
anti-Sox2 (clone Y-17)	goat polyclonal	IF/IHC	1:200	Santa Cruz
anti-Ctip2 (clone 25B6)	rat monoclonal	IF	1:500	Abcam
anti- β -catenin (clone14)	mouse IgG1 monoclonal	IHC	1:500	BD Biosciences
anti-doublecortin	guinea pig polyclonal	IHC	1:2000	Millipore
anti-Nestin (clone 10C2)	mouse IgG1 monoclonal	IHC	1:200	Millipore
anti-phospho-Histone H3 (Ser10)	rabbit polyclonal	IHC	1:500	Millipore
anti-cleaved caspase 3	Rabbit polyclonal	IHC	1:300	Cell Signaling
anti-Ki67	Mouse monoclonal	IF/IHC	1:300	BD Biosciences

Table S1. Antibodies used in this study. Related to Methods. Legend: Immunoblotting (IB), Immunofluorescence (IF), Immunohistochemistry of organoids (IHC).**Supplemental experimental procedures***Transfection of human cell lines*

Human embryonic kidney 293 (HEK) cells were cultured according to manufacturer's instructions and transfected with the respective constructs using polyethylenimine (PEI) as previously described (Perez-Branguli et al., 2014). Control and SPG11 NPCs were transfected with plasmids expressing GFP or GFP-spatacsin (SPAT) by employing Lipofectamin-LTX (Invitrogen) according to manufacturer's instructions. 0.5 μ g of DNA per transfection was used.

Immunofluorescence (IF)

HEK cells, NPCs, neurospheres, and forebrain cultures were fixed in 4 % paraformaldehyde (PFA) for 10-30 min at room temperature (RT). After several rinses with phosphate buffered saline (PBS), cultures were pre-incubated for 60 min at RT in immunofluorescence buffer [IFB: PBS supplemented with 0.1 % Triton X-100 (PBST) and 3-5 % normal donkey serum] for 60 min at RT, followed by overnight (ON) incubation at

4 °C with primary antibodies diluted in IFB. EdU detection procedure was conducted according to the user manual (BCK-EdU555; baseclick, GmbH).

Organoids were fixed in 4 % PFA on a shaker for 4h at 4 °C and then cryoprotected in PBS supplemented with 30 % sucrose at 4 °C ON. Organoids were embedded in Cryostor™ CS 10 Cryopreservation Medium (Sigma-Aldrich) and cut at 16 µm thickness. For IF, primary antibodies were diluted in blocking solution (BS: PBS supplemented with 10 % normal goat serum and 0.5 % Triton® X-100) at 4 °C ON. For cleaved-caspase 3 (cCasp3) an additional step of permeabilization within acetic acid and ethanol solution (1:2 ratio) was added prior to blocking.

All rinses were performed using PBST. Incubation with respective fluorescent secondary antibodies diluted in PBS was performed for 60 min at RT. Dead cells were detected by incubating unfixed iPSC-derived forebrain cultures with 100 nM IT-DEAD for 30 min at 37 °C. After several washes with PBS, samples were mounted for further microscopic analysis. All IFs were visualized using a Zeiss inverted fluorescent Apotome.2, a confocal LSM-780 microscope (Carl Zeiss) or a confocal TCS-SP8 microscope (Leica).

Protein sample preparation

For the protein analysis, NPC lines were harvested and washed twice in cold PBS buffer, gently resuspended in cold hypotonic buffer (20 mM Tris pH 7.4, 10 mM NaCl, 3 mM MgCl₂ supplemented with protease and phosphatase inhibitors) and incubated on ice for 15 min. After adding 10 % NP40, homogenates were centrifuged for 15 min at 3000 rpm at 4°C to separate supernatant 1 (S1; cytosolic fraction) from pellet 1 (P1; nuclear pellet). P1s were resuspended in cold homogenization buffer (HB: 100 mM Tris pH 7.4, 1 mM EDTA, 100 mM NaCl, 1 % Triton X-100, supplemented with protease and phosphatase inhibitors) and incubated on ice for 30 min, and afterwards centrifuged at 14000 rpm for 30 min at 4°C. Supernatants (S2; nuclear fraction) were collected.

Transfected HEK cells were resuspended in HB, incubated on ice for 30 min and centrifuged at 14000 rpm for 30 min at 4°C. Resulting supernatants (total protein extract) were harvested.

Immunoblotting (IB)

20 µg to 50 µg of total protein were separated by SDS-PAGE and blotted onto nitrocellulose (NC) or PVDF membranes. Primary antibodies were incubated ON at 4°C in Tris buffered saline and 0.1 % Tween-20 (TBSTB) supplemented with 3 % bovine serum albumin (BSA). After several washes with TBST, blots were incubated with secondary antibodies conjugated to horseradish peroxidase (HRP) and developed by chemical luminescence.

Measurements and analysis

To analyze migration in neurospheres, numbers of migrating cells (cells located in the "migrating area" outside of dotted lines in Fig. 2A) were normalized by the area of seeded neurospheres (core of the spheres outlined in Fig. 2A). Migration was studied in untreated neurospheres and in neurospheres chronically treated with 3µM CHIR99021. Migration rates were analyzed using ImageJ (<http://imagej.nih.gov/ij/>). 20 to 50 spheres

per experimental condition and NPC line were analyzed. Likewise, the number of neurons and dead cells in forebrain 2D cultures derived from iPSC of SPG11 patients and controls were analyzed as previously described (Perez-Branguli et al., 2014).

Organoid area and organoid progenitor zone thickness were measured using ImageJ. At least 3 organoids per experimental condition were assessed. To analyze the number of dividing cells in the progenitor zone of organoids, the number of PH3⁺ and Ki-67⁺/Sox2⁺ cells was normalized to the length of the apical surface of ventricle-like structures (shown per 100 μ m). Multiple ventricles per organoid were analyzed.

Angle of division of dividing cells labeled with anti-NuMa at the germinal wall of ventricles of organoids was analyzed using the tools “angle measurement” and “area measurement” included in AxioVision (Zeiss). Cells with a division angle between 0-45 degrees were classified as cells dividing asymmetrically (horizontal; Fig 1J), while cells with division angles between 45-90 degrees were considered as cells dividing symmetrically (vertical; Fig 1J). 10 to 20 cells per image, and at least 20 randomly taken images per experimental condition were analyzed.

For the investigation of β GSK3 signaling pathway in SPG11-NPCs, we compared protein extracts from untreated NPCs and NPCs treated with 3 μ M CHIR99021 for 4 hours at 37 °C. Protein expression and phosphorylation were evaluated by dividing the signal intensity of each protein of interest by the signal intensity of housekeeping markers and pan-proteins respectively. At least 3 independent experiments were analyzed. Protein evaluation was carried out using ImageJ.

Immunohistochemistry and pharmacological compounds

Nuclei were counterstained with DAPI (1:5,000). CHIR99021 was obtained from R&D Technologies, Tideglusib from Selleck-Chem, (Houston, TX) and auto-fluorescent reagent IT-DEAD from Invitrogen. pGFP-Spatacsin and siRNAs sequences to knock down SPG11 (Sigma-Aldrich) have been described previously (Perez-Branguli et al., 2014; Murmu et al., 2011).

3. FICD ACTIVITY AND AMPYLATION REMODELLING MODULATE HUMAN NEUROGENESIS.

3.1. CITATION

This manuscript is currently under revision in *Nature Communications*.

Running title:

“FICD activity and AMPylation remodelling modulate human neurogenesis.”

Pavel Kielkowski^{1,+}, **Isabel Y. Buchsbaum**^{2,3+}, Volker C. Kirsch¹, Nina C. Bach¹, Micha Drukker⁴, Silvia Cappello^{2,3*}, Stephan A. Sieber^{1*}

¹Department of Chemistry, Technical University of Munich, Garching, Germany.

²Max Planck Institute of Psychiatry, Munich, Germany.

³Graduate School of Systemic Neurosciences, Ludwig-Maximilians-University Munich, Planegg, Germany

⁴Helmholtz Center, Munich, Germany

+ These authors contributed equally to this work.

* To whom correspondence shall be addressed: stephan.sieber@tum.de,
silvia_cappello@psych.mpg.de

3.2. AUTHOR CONTRIBUTIONS

S.A.S. and P.K. conceived of the project. P.K., I.Y.B., S.C. and S.A.S. designed the experiments. P.K. and I.Y.B. performed the experiments. P.K. synthesized the probes, conducted chemical-proteomic experiments, data analysis and *in vitro* assays. I.Y.B. cultured the fibroblasts, neuroblastoma cells, iPSCs, NPCs, and neurons, performed all KD and OX experiments and analysis on COs, fluorescent imaging, qPCR, and STRING. V.C.K. performed the metabolomics experiments. N.C.B. set up the MS methods and helped with MS data analysis. M.D. generated and provided iPSC. P.K., I.Y.B., S.C. and S.A.S. wrote the manuscript.

FICD activity and AMPylation remodelling modulate human neurogenesis.

Pavel Kielkowski¹⁺, Isabel Y. Buchsbaum^{2,3+}, Volker C. Kirsch¹, Nina C. Bach¹, Micha Drukker⁴, Silvia Cappello^{2,3*}, Stephan A. Sieber^{1*}

Posttranslational modification (PTM) of proteins represents an important cellular mechanism for controlling diverse functions such as signalling, localisation or protein-protein interactions¹. AMPylation (also termed adenylylation) has recently been discovered as a prevalent PTM for regulating protein activity². In human cells AMPylation has been exclusively studied with the FICD protein³⁻⁵. Here we investigate the role of AMPylation in human neurogenesis by introducing a cell-permeable propargyl adenosine pronucleotide probe to infiltrate cellular AMPylation pathways and report distinct modifications in intact cancer cell lines, human-derived stem cells, neural progenitor cells (NPCs), neurons and cerebral organoids (COs) via LC-MS/MS as well as imaging methods. A total of 162 AMP modified proteins were identified. FICD-dependent AMPylation remodelling accelerates differentiation of neural progenitor cells into mature neurons in COs, demonstrating a so far unknown trigger of human neurogenesis.

Introduction of protein PTMs is a tightly controlled and almost ubiquitous process that often modulates critical protein function. PTMs such as tyrosination, acetylation and neddylation are known to play a crucial role in the development of the nervous system and in particular of neurons by broadening the diversity of the tubulin and microtubule proteoforms^{6, 7}.

AMPylation was first discovered in *Escherichia coli* as regulator of glutamine synthetase activity⁸. Later, it was found that bacterial effectors from *Vibrio parahaemolyticus* and *Histophilus somni* AMPylate Rho guanosine triphosphatases (GTPases) in human host cells^{9,10}. These bacterial effectors contain highly conserved Fic (filamentation induced by cAMP) domains, which catalyse the transfer of AMP onto a serine, threonine or tyrosine residue of a substrate protein (Fig. 1a). Approximately 3,000 members of this family are known to contain the conserved HXFX(D/E)GNRXXR sequence motif throughout all domains of life¹¹. Despite their abundance in bacteria, only one human protein AMPylator containing the signature Fic

¹ Department of Chemistry, Technical University of Munich, Garching, Germany.

² Max Planck Institute of Psychiatry, Munich, Germany.

³ Graduate School of Systemic Neurosciences, Ludwig-Maximilians-University Munich, Planegg, Germany

⁴ Helmholtz Center, Munich, Germany

+ These authors contributed equally to this work.

* To whom correspondence shall be addressed: stephan.sieber@tum.de,
silvia_cappello@psych.mpg.de

domain termed FICD (also known as Huntingtin yeast partner E, HYPE) has been discovered¹¹. Structural and biochemical studies with FICD have revealed that its activity is tightly regulated and controlled by an autoinhibitory loop. Mutation of E234 to glycine overrides autoinhibition and results in a constitutively activated enzyme¹¹; the mutant form H363 to alanine is catalytically inactive³. One known substrate of FICD is HSPA5, which is a chaperone located in the endoplasmic reticulum (ER) and master regulator of the unfolded protein response (UPR)³⁻⁵. Recent data show that FICD regulates the ATPase activity of HSPA5 and its interactions with unfolded proteins but the exact function is not yet clear¹². However, it was found that the HSPA5 AMPylation associates with changes in neuronal fitness in *drosophila*¹³⁻¹⁶.

Just recently, the highly conserved pseudokinase selenoprotein-O (SelO) was found to possess AMP transferase activity in eukaryotic cells¹⁷. Pseudokinases account for about 10% of the human kinome but lack the characteristic active site residues and hence their function is largely unknown. However, their putative AMPylation activity is pointing to a possibly larger number of AMPylated proteins in human cells.

Lately, *N*⁶-propargyl adenosine-5'-O-triphosphate (*N*⁶pATP)-derived probes have been applied to profile substrates of AMPylation in cell lysate¹⁸⁻²⁰. Nevertheless, the most pressing, unaddressed challenge in discovering the function of AMPylation is the global analysis of AMPylated substrates under physiological conditions inside living cells. Particularly, ATP-derived probes suffer from restricted uptake of the charged nucleotides as well as competition with high endogenous ATP levels. Thus, new concepts are urgently needed to unravel the function of AMPylation in eukaryotic cells. Here we present a chemical-proteomic approach for identification of protein AMPylation in living cells using a pronucleotide probe and uncover FICD-dependent AMPylation remodelling responsible for acceleration of neuronal differentiation in cerebral organoids (COs).

Results

6-Propargyl adenosine pronucleotide reports on protein AMPylation. To approach the challenge of identifying AMPylated proteins *in situ*, we selected a phosphoramidate pronucleotide strategy (Fig. 1a, b)²¹. This delivery method not only enhances the probes' cell membrane permeability but also bypasses the first phosphorylation of the nucleoside analogue by kinases. Based on these considerations, we designed and synthesized a *N*⁶-propargyl adenosine phosphoramidate pronucleotide (**pro-N6pA**, Fig. S1). We initiated our investigations with metabolomics experiments to determine **pro-N6pA** *in situ* metabolic activation to the corresponding **N6pATP**. A maximum concentration is reached 8 hours after **pro-N6pA** addition and it is maintained for at least 24 hours (Fig. S2). For the subsequent analysis of AMPylated proteins we treated living (intact) HeLa cells with **pro-N6pA** (100 μ M in DMSO) or dimethylsulfoxide (DMSO). Subsequent click-chemistry to a rhodamine-biotin-azide tag, enrichment on avidin beads and SDS-PAGE analysis via in-gel fluorescence detection revealed several distinct protein bands in the soluble fraction (Fig. 1c). Next, we performed quantitative proteome profiling in HeLa cells²². Enriched proteins were trypsin digested and resulting peptides were either isotopically marked by dimethyl labelling (DiMe) prior to LC-MS/MS measurement or analysed directly using label-free quantification (LFQ)

(Fig. 1d)^{23,24}. Comparing **pro-N6pA** labelling (Fig. 1e) with parent *N*⁶-propargyl adenosine (**N6pA**, Fig. 1f, Fig. S3) yielded a larger number of significantly enriched proteins with the pronucleotide. Using **pro-N6pA**, a diverse group of 19 proteins were identified in HeLa cells, including the known FICD substrate HSPA5 (Fig. 1e, Table S1). Immunoprecipitation of the two selected proteins PFKP and PPME1 from the probe treated HeLa cells followed by click reaction with rhodamine-azide tag confirmed incorporation of the probe into these proteins (Fig. S3).

Although the *N*⁶-propargyl ATP analogue could, in principle, serve as precursor for ADP-ribosylation²⁵, our controls indicate that ADP-ribosylation is not a major route. ADP-ribosylation is usually induced by stress conditions e.g. by addition of hydrogen peroxide to the cells' media²⁶. First, HeLa cells were pre-treated with poly(ADP-ribose)polymerases (PARP) inhibitors 4-aminobenzamide (4-ABA) or olaparib (Ola) prior to **pro-N6pA** labelling. For both PARP inhibitors no influence on labelling intensity was observed based on in-gel fluorescence analysis (Fig. S3). In addition, MS-based chemical-proteomic experiments with Ola and **pro-N6pA** treated cells confirmed no changes in AMPylation (Fig. 1g and Table S2). Second, only two of our identified AMPylated proteins in HeLa cells (HIST1H2AH, RPS10) matched known ADP-ribosylated proteins (Fig. S3)²⁷. Known ADP-ribosylated proteins were excluded as potential hits in the following experiments (Table S3).

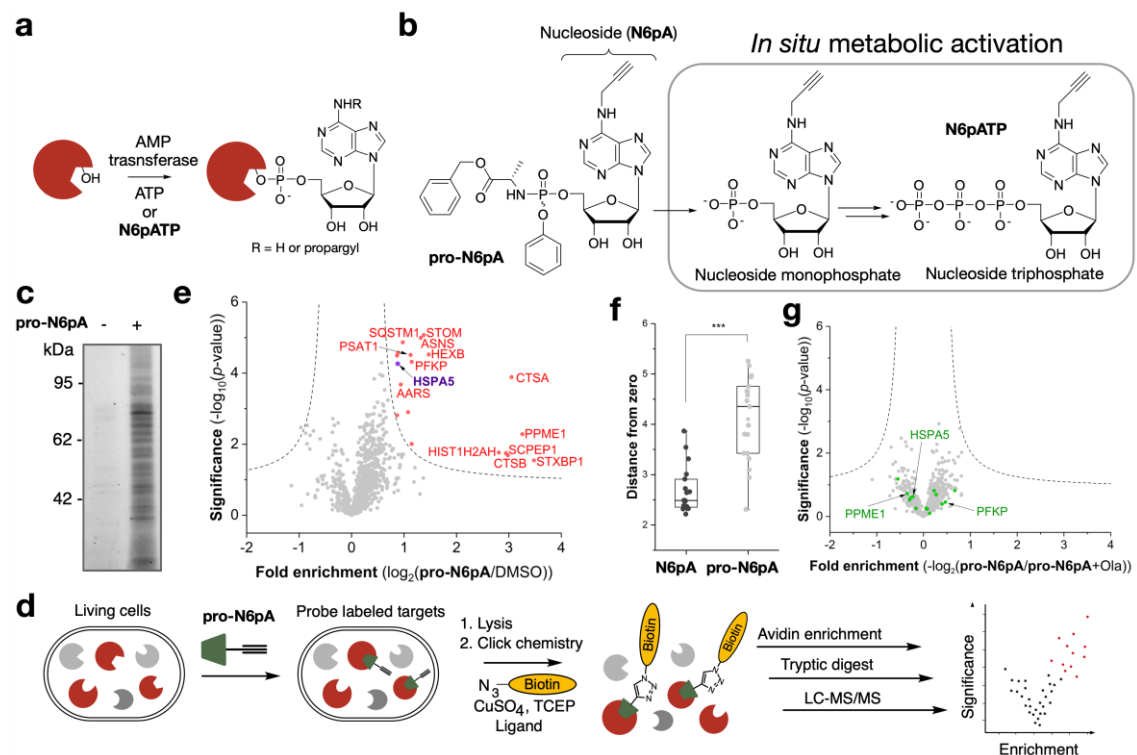


Figure 1 | Pronucleotide probe reveals AMPylation of diverse proteins in HeLa cells. a, AMPylation on Ser, Thr or Tyr. **b**, Scheme of the pronucleotide probe **pro-N6pA** and parent adenosine derivative (**N6pA**) and its *in situ* activation. **c**, SDS-PAGE with in-gel fluorescence scanning showing *in situ* HeLa cell labelling by **pro-N6pA** compared to control (DMSO). **d**, Schematic representation of the chemical-proteomic approach used for *in situ* identification of AMPylated proteins. **e**, Volcano plot of fold-enrichment in HeLa cells by **pro-N6pA** labelling

compared to DMSO versus significance upon two-sample *t*-test (FDR 0.05, s0 0.3; *n* = 12). **f**, Box plot representing comparison of labelling efficiency of pronucleotide **pro-N6pA** (light grey, *n* = 12) and parent nucleoside **N6pA** (black, *n* = 11); Squares represent the mean of the distances to zero for enriched proteins, lines represent the median of the distances to zero and whiskers stand for min and max values. Statistical significance was calculated with two-tailed Student's *t*-test; ****P* < 0.001. **g**, Volcano plot of fold-enrichment by **pro-N6pA** labelling compared to probe and Ola treated HeLa cells versus significance upon two-sample *t*-test (FDR 0.05, s0 0.3; *n* = 8). Green circles represent proteins identified as AMPylated in HeLa cells.

AMPylation of cathepsin B inhibits its peptidase activity *in vitro*. In order to validate our approach in more detail we have employed an azide-TEV-cleavable-biotin linker during the pull-down procedure to identify the corresponding AMPylation sites of modification via MS/MS (Fig. 2a, b)²⁸. We were able to directly analyse AMPylated peptides on three different cysteine cathepsin proteases CTSB (S104 and S107), CTSC (S254) and CTSL (S137) (Fig. S4 and S5). All of the AMPylation sites were located on serine residues within the conserved sequence surrounding the catalytically active cysteine (Fig. 2c), suggesting that the bulky AMP modification might obstruct the binding of the peptide substrates and thus inhibit protease activity²⁹. To determine whether FICD is the AMPylator of these cathepsins, we used an *in vitro* peptidase activity assay and found that cathepsin B is indeed inhibited upon FICD (wild-type (wt) or E234A mutant) treatment and did not observe any inhibition without the addition of ATP (Fig. 2d, Fig. S4). The direct measurement of AMPylation sites in CTSB (S104,107) *in vitro* was restricted by preparation of the recombinant double mutant CTSB which did not fold into the active protein, likely due to the mutation of the crucial amino acid residues within the conserved active site. Moreover, the TEV-linker based enrichment of modified peptides was performed with other cell types used in this study and three additional sites on MYH9, RAI14 and AASS (on Thr, Ser and Tyr residues respectively) were detected (Table S4). Of note, the MS-based identification of AMPylated sites in living cells is limited by the endogenous degree of modification. We thus assume that site identifications of proteins with lower AMP abundance are challenged by the detection limit. Here, previous trials in cell lysates using an active recombinant FICD E234G mutant yielded a complementary set of proteins likely due to an increased degree of modification (Fig. S6 and Table S5)²⁰.

Chemical-proteomics profiling shows cell type dependent AMPylation pattern and in part independency of FICD. We performed proteome profiling in three different cancer cell lines, HeLa, A549 and SH-SY5Y, which revealed a total of 58 significantly enriched proteins, of which 38 were contributed solely from the latter neuroblastoma cells (Fig. 3a, Fig. S7). Overall, AMPylated proteins identified here are involved in diverse metabolic pathways including a widely conserved key regulator of glycolysis ATP-dependent 6-phosphofructokinase (PFKP)³⁰, proteolysis (CTSA, CTSB)³¹, regulation of PTMs (PPME1)³² and UPR (HSPA5 and SQSTM1)³³. Intriguingly, only PFKP was found to be AMPylated in all three cell lines, which otherwise exhibited unique AMPylation patterns.

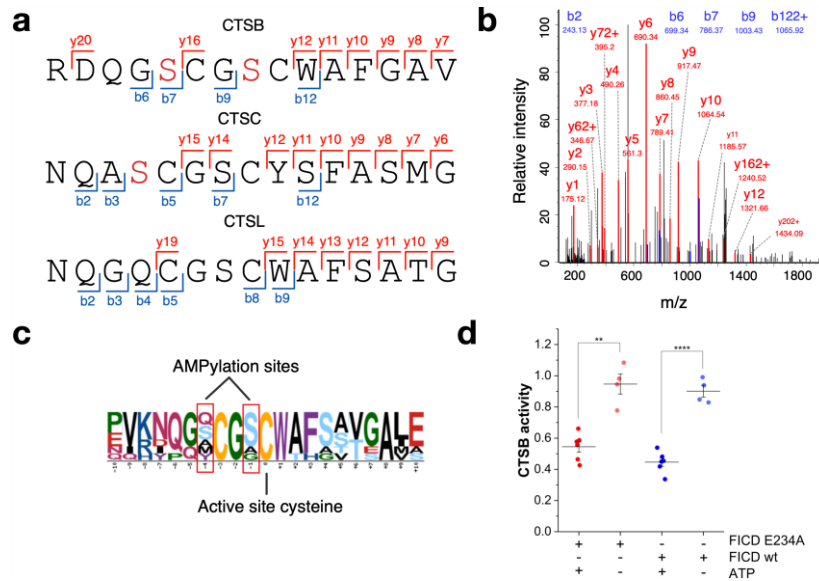


Figure 2 | CTSB peptidase activity is inhibited by FICD catalysed AMPylation. **a**, Identified AMPylation sites on serine residues (red) of cathepsins B, C and L using **pro-N6pA** in HeLa cells. **b**, Exemplary MS/MS spectrum (MaxQuant) for the CTSB AMPylation site identification on S107 (see Fig. S4 and S5). **c**, Amino acid motif surrounding the active site cysteine of cysteine cathepsins. **d**, *In vitro* peptidase assay of CTSB activity after incubation with wt FICD or E234A mutant and with or without ATP for 6 h. Normalized to CTSB activity without FICD protein. Lines represent the mean and whiskers stand for 25th and 75th percentile. Two-tailed Student's *t*-test; ***P* < 0.01, *****P* < 0.0001.

To directly dissect the descent of AMPylated proteins from FICD we compared the AMPylation levels of proteins in probe treated HeLa cells comprising FICD knockdown, wt FICD overexpression (OX) and activated FICD E234G OX (Fig. 3b, Fig. S8 and Table S6). Interestingly, HSPA5 is a clear FICD-dependent responder where AMPylation is significantly upregulated in FICD E234G OX and downregulated in wt FICD OX, which is also known to perform de-AMPylation⁵. Remarkably, while all previous studies have been carried out *in vitro*¹⁸⁻²⁰, we here independently confirm this data by the first *in situ* experiments. A direct *in situ* interaction is further corroborated by MS-based pulldown experiments of wt FICD and FICD E234G in the presence of a chemical crosslinker which revealed HSPA5 together with other sets of proteins as interacting partners, while proteins like SQSTM1, PFKP and PPME1 were not enriched and thus considered as not interacting with FICD (Fig. 3c)³⁴. Of note, FICD E234G revealed a more pronounced interaction with HSPA5, confirming our OX studies (Fig. S9 and Table S7). GO term analysis of the overlapping interacting partners indicated a link to basal metabolism (Fig. 3d). With HSPA5 as a validated candidate we moved on and analysed other AMPylated proteins. The set of hits including PPME1, PFKP and SQSTM1 exhibited no significant changes in AMPylation levels upon FICD KD and OX, suggesting an FICD-independent mode of AMPylation (Fig. 3b) for which the origin of the AMP transfer could not be fully deduced. Given the recent discovery of an additional AMPylating enzyme also in eukaryotic cells it is likely that the other proteins detected here descent from a yet undiscovered AMPylator(s)¹⁷.

Next, proteome profiling under endoplasmic reticulum (ER) stress conditions was performed to determine whether modifications are altered as previously reported for thapsigargin (Tg)-treated cells⁵. Only a slight increase in AMPylated HSPA5 was observed in HeLa and A549 cells. Normalization of the AMPylation upon Tg-treatment to the increased levels of the HSPA5 expression in HeLa shows overall decrease of the AMPylation on HSPA5⁵. Despite the moderate impact of ER stress on AMPylation in these cells, we found 145 dysregulated proteins in SH-SY5Y neuroblastoma cells (Fig. S7). The high amount of AMPylated proteins in SH-SY5Y under baseline and ER stress conditions indicates that AMPylation may have a specific role in the nervous system.

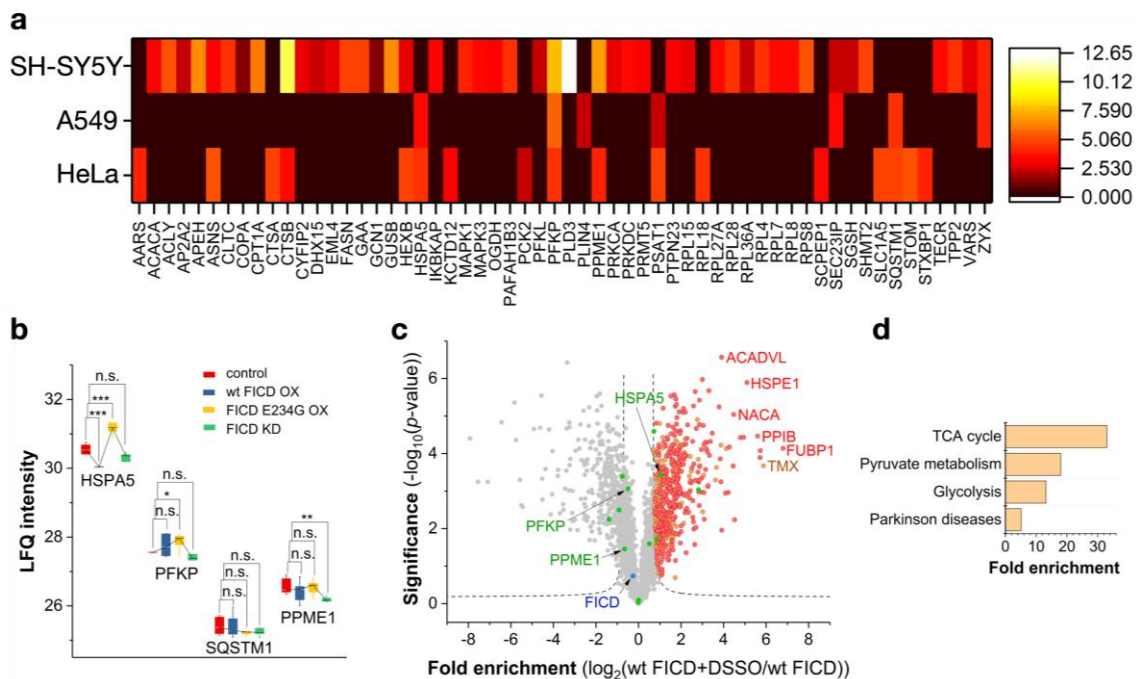


Figure 3 | AMPylation in cancer cell lines, FICD-dependent AMPylation and FICD-interacting proteins. **a**, Heatmap representation of enriched proteins identified in cancer cell lines. Colour represents distance to zero of enriched proteins from respective volcano plot (FDR 0.05, s_0 0.3; $n = 8$ or 9). **b**, Changes in AMPylation on selected proteins (those identified in HeLa cells from Fig. 1e) upon FICD overexpression (OX) or siRNA-mediated knock-down in (KD) HeLa cells. Statistical significance was tested using two-tailed Student's t-test; * $P < 0.05$ ** $P < 0.01$, *** $P < 0.001$. **c**, Volcano plot representing FICD interacting proteins identified in the pull-down experiment of his tag labelled FICD and DSSO cross-linking reagent (FDR 0.01; s_0 1.5; $n = 3$). Green circles represent proteins identified as AMPylated in HeLa cells. Red circles represent hits overlapping with parallel experiment with FICD E234G mutant. Orange circles are hits enriched only with wt FICD. **d**, Panther Pathways enriched from FICD-interacting proteins, cut-off FDR 0.05.

Chemical-proteomics profiling reveals remodelling of AMPylation during neuronal differentiation. The large number of hits in neuroblastoma cells (Fig. 3a) indicates a specific importance of AMPylation in neural cells. To study AMPylation in a

model system of developing neurons, neural progenitor cells (NPCs) and neurons were generated from human induced pluripotent stem cells (iPSCs, Fig. S10)³⁵. Successively, iPSCs, NPCs and neurons were each treated with **pro-N6pA** and the enriched proteins were analysed via LFQ LC-MS/MS (Fig. 4a, Fig. S11 and S12 and Table S1 and S9). While PFKP was AMPylated in both the proliferating cell lines and neurons, the proteins CTSB, PSAT1 and PPME1 were only AMPylated in proliferating cells. Importantly, neurons exhibited the largest number of significantly and differentially AMPylated proteins (55 total), including transport proteins (KIF21A, KIF5C, MYH3, MYH7, MYH8) and cytoskeletal proteins (TUBB, TUBB2B, TUBB3B, TUBB4B, MAP2) (Fig. 4a). This is of particular interest as the cytoskeletal remodelling, which is required for neuronal polarisation, migration, and proper axon guidance, is a highly dynamic processes precisely regulated by several PTMs on tubulin and microtubules - and AMPylation may indeed be an additional one (Fig. S13)^{6,7,36,37}. AMPylation remodelling could be involved in the process of cell type specification and differentiation from iPSCs through NPCs to neurons, with cellular proteins undergoing substantial de- and re-AMPylation following an hourglass-like model (Fig. 4b, Fig. S11)^{2,3,20}. Further, parallel chemical-proteomics studies of AMPylation under ER stress induced by Tg in iPSCs, NPCs and neurons showed distinct responses ranging from a strong change of AMPylation on several proteins in iPSCs over mild alterations in NPCs to an obvious upregulation on two proteins (HSPA5 and SQSTM1) in neurons (Fig. S11).

To specify if the observed AMPylation in neurons is common for differentiated postmitotic cells we performed chemical profiling in fibroblasts (Fig. 4c, Fig. S14). Analysis of the enriched proteins revealed similarities with tested cancer cells and proliferating cell types. Most significantly enriched proteins included HSPA5, CTSB, PFKP and PPME1, all common to the proliferating cells. This highlights a distinct AMPylation remodelling in neurons.

GO term analysis of AMPylated proteins found in all screened cell types using the Panther Pathway tool displayed enrichment of basal metabolism such as TCA cycle and glycolysis as well as neuronal specific pathways including cytoskeletal regulation by Rho-GTPase and FGF signalling. Interestingly, pathways marking neurodegenerative diseases, e.g. Alzheimer, the disease-amyloid secretase pathway and Huntingtin disease were identified as well (Fig. 4d).

FICD and AMPylated proteins have different cellular localisations. The chemical-proteomic results were corroborated by fluorescence imaging of probe-treated HeLa, iPSCs, NPCs and neurons (Fig. 5, Fig. S15 and Table S8). In order to rule out signals derived from *N*⁶-propargyladenosine nucleotide incorporation into RNAs (e.g. in polyA tails of mRNA)³⁸, we performed a control experiment in which the RNA of the fixed cells was digested with different concentrations of RNase prior to click-chemistry and as positive control of the RNase digest 5-ethynyl uridine (5-EU) stained RNAs were degraded in parallel to **pro-N6pA** labelling. Indeed, we observed only a slight decrease in overall cell staining by **pro-N6pA** rather than disappearance of the bright AMPylation spots, while we observed a strong decrease in 5-EU labelling (Fig. S16).

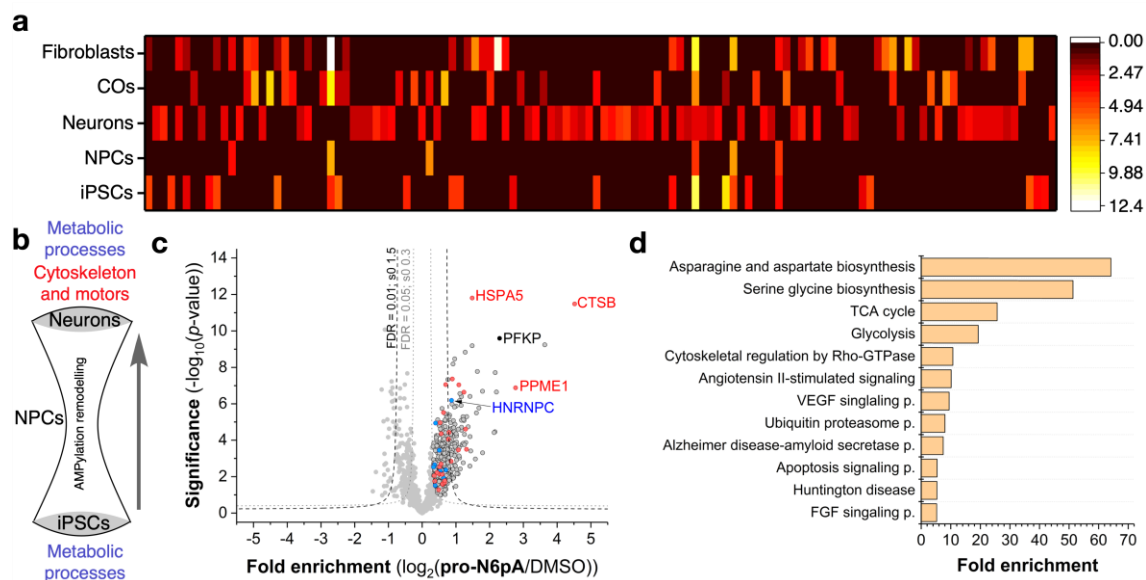


Figure 4 | AMPylation remodelling is specific for the development of the neuronal cells. a, Heatmap representation of enriched proteins identified in different cell types and COs. Color represents distance to zero of enriched proteins from respective volcano plot (FDR 0.05, s0 0.3; $n = 8$ or 9). **b**, The hourglass model of AMPylation remodelling hypothesises a complete de- and re-AMPylation in the process of neuronal differentiation: from a high number of AMPylated proteins in proliferative iPSCs, most of which are involved in metabolic processes and possess catalytic activity, differentiating cells pass through a state of very sparse AMPylation as NPCs, with final neuronal differentiation resulting in neuronal identity with a high number of newly and uniquely AMPylated proteins which are enriched in metabolic functions on the one hand and in cytoskeletal and molecular motor functions on the other hand. **c**, Volcano plot of fold-enrichment by **pro-N6pA** labelling compared to DMSO versus significance upon two-sample t-test (FDR 0.05, s0 0.3; $n = 9$) in fibroblasts. Red circles represent proteins identified AMPylated in proliferating cell types while blue circles stand for overlap with hits in neurons. **d**, Panther Pathways enriched within the identified AMPylated proteins in all tested cell types, cut-off FDR 0.05.

Given that the cellular localisation of FICD and AMPylated proteins might play an important functional role, we combined click chemistry with rhodamine-azide for intracellular probe visualisation with immunohistochemistry (IHC) for FICD and various cellular markers: PDI for rough endoplasmic reticulum, GM130 for Golgi complex, TUBB3 for total neuronal microtubule cytoskeleton, MAP2 for neuronal dendrites, phospho-TAU for neuronal axons, and DAPI to visualize nuclei (Fig. 5, Fig. S15). Staining performed in HeLa cells revealed that AMPylated proteins are enriched in the nucleus, additional small spots were found in the cytoplasm partially overlapping with the ER. As expected, FICD is localized in the ER but also present in the cytoplasm and nucleus (Fig. 5a). On the contrary, in NPCs AMPylation strictly localized next to the rough ER and in the nucleus, while FICD is ubiquitously distributed (Fig. 5b, c). In neurons, AMPylation was observed in nucleus and to a lesser extent in neurites, including MAP2+ dendrites and phospho-TAU+ axons (Fig. 5d-g). Here, FICD is localized in the nucleus, cytoplasm as well as ER (Fig. 5d). Finally, fibroblasts showed another specific localisation pattern with AMPylation accumulated around the nucleus

and its' complete absence inside, while FICD is homogenously spread across the cells (Fig. S15). Differences in localisation of FICD and AMPylated proteins support the presence of additional AMP transferases with complementary cellular distribution.

Decrease of FICD levels in *in vitro* neural model systems reveals a role of FICD-dependent AMPylation remodelling in neuronal differentiation. To understand if FICD-mediated AMPylation plays a role in neuronal differentiation, we utilized both NPC-to-neuron differentiation and the recently developed 3-dimensional human cerebral organoids (COs)^{39,40}. COs contain areas which closely resemble the structure and organisation of the germinal zones of developing human neocortex (Fig. S17)⁴¹. Treatment of COs with **pro-N6pA** and subsequent analysis via LFQ LC-MS/MS confirmed the AMPylation of PFKP, found in all cell types, and CTSB, another prevalent target in other studied cell lines (Fig. 4a and Fig. S5 and S12). Analysis of the significantly enriched proteins using a STRING database revealed that several proteins are located in extracellular space (Fig. S13). Interestingly, visualization of the **pro-N6pA** probe-treated COs via click-chemistry with rhodamine-azide revealed strongest fluorescence in the neuronal layer (Fig. 5i, j and Fig. S15), which is in line with the highest number of AMPylated proteins identified in neurons (Fig. 4a).

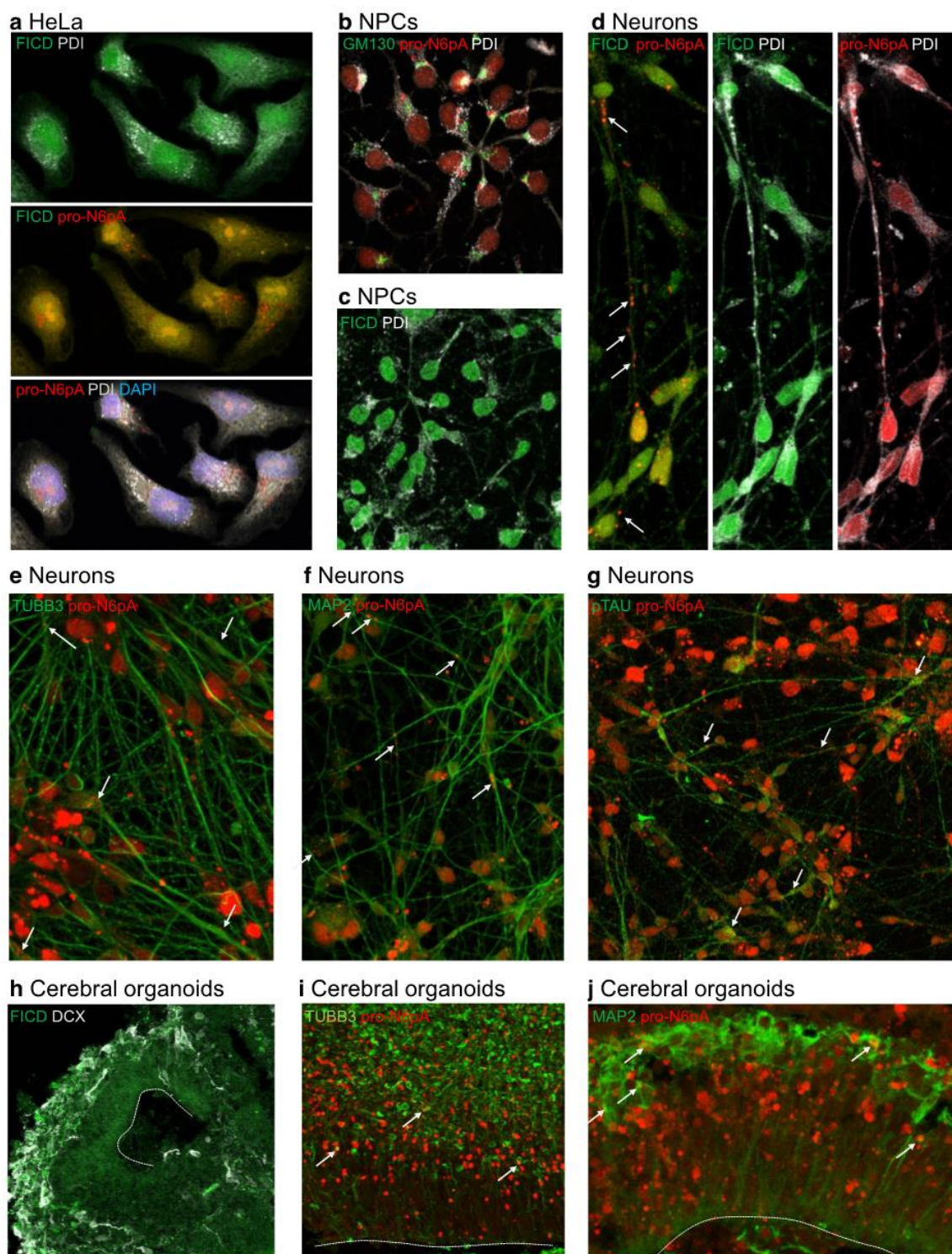


Figure 5 | Characterization of intracellular FICD and probe localisation in HeLa (a), NPCs (b, c), neurons (d-g) and cerebral organoids (h-j). Click chemistry of **pro-N6pA** with rhodamine-azide and immunohistochemical stainings. **a**, HeLa cells contain big nuclear (DAPI – blue) clusters of AMPylated proteins (pro-N6pA, red) and additional, small cytoplasmic spots of probe localisation. FICD colocalises with rough ER (PDI – white) and is present both in nucleus and cytoplasm. FICD rarely colocalises with probe-containing proteins. **b**, In NPCs, probe-containing AMPylated proteins (pro-N6pA, red) localize mostly to ER and only rarely with Golgi (GM130, green) with additional small nuclear and cytoplasmic clusters. **c**, FICD localizes to the

ER, nucleus, and the cytoplasm including short processes of NPCs. **d**, In differentiated neurons, clusters of AMPylated proteins localise to nucleus and processes (white arrows), both inside and outside rough ER, partly overlapping with FICD. FICD also localises to nucleus and cytosol including neuronal processes and only partly to ER. **e**, Pro-N6pA partly colocalises with the TUBB3+ neuronal cytoskeleton (green, white arrows), with TUBB3 being identified as AMPylation target in neurons. **f**, AMPylated proteins can be found both in neuronal dendrites (MAP2+, green, white arrows indicating colocalisation; also identified as neuronal AMPylation target) and **g**, in axons (phosphoTAU+, green, white arrows for colocalisation). **h**, In cerebral organoids, FICD (green) is enriched in the DCX+ neuronal layer (white), which is in line with qPCR data from 2D in vitro generated NPCs and neurons (Fig. S18). **i**, **j**, AMPylated proteins are enriched right below and within the neuronal layer (TUBB3+ and MAP2+, green) and include TUBB3 (**g**, white arrows indicating colocalisation) and MAP2 (**h**, white arrows indicating colocalisation). See also Fig. S15.

To examine the function of AMPylation in neurogenesis and neuronal differentiation in more detail, we first characterized the expression of FICD in NPCs, neurons, neuroblastoma cells and COs and found a clear enrichment of FICD in the neurites of neurons, SH-SY5Y and in the neuronal layer of COs compared to the progenitor zone (Fig. 5d, h; Fig. S15). Results of imaging were paralleled by qPCR studies demonstrating higher baseline expression levels of FICD in neurons compared to iPSCs and NPCs (Fig. S18). We knocked down FICD levels (Fig. S19) in NPCs differentiating to neurons (Fig. 6a, b) and found a significant increase in transfected cells that remain in cell cycle (KI67+) (Fig. 6a). This result suggested a potential role of FICD-mediated AMPylation in neurogenesis. We then performed down- or upregulation of FICD expression in ventricle-like germinal zones of 50 days old COs by electroporation, as this model system better resembles the 3-dimensional organization of the developing brain. Only apical radial glia cells (aRGs), which are bipolar neural stem cells that will subsequently give rise to intermediate progenitors and neurons directly, are capable of taking up the vectors via their apical process to the ventricle-like lumen (Fig. 6c). To assess if FICD-mediated AMPylation has a function in neurogenesis during development, COs were analysed 7 (Fig. 6 and 7, Fig. S20) and 14 days post-electroporation (dpe) (Fig. S21). Cortical-like germinal zones were defined by immunohistochemical (IHC) analysis using PAX6 as a marker for dorsal aRGs (Fig. 6d, Fig. 7b) with mitotic cells labelled for PH3 (Fig. 6e, Fig. S20). The position and number of neurons was analysed by IHC using two different markers for mature neurons: MAP2, a microtubule-associated protein which is enriched in neuronal dendrites (Fig. 7c, Fig. S20) and the nuclear marker NEUN (Fig. 6g, Fig. 7d). Most of miRNA-transfected (GFP+) cells (FICD KD) were positive for PAX6 (Fig. 6d) 7 dpe. The proportion of mitotic PH3+GFP+ cells was significantly increased (Fig. 6e, f) at the expense of neurons, as shown by the significantly reduced number of NEUN+GFP+ cells (Fig. 6g, h).

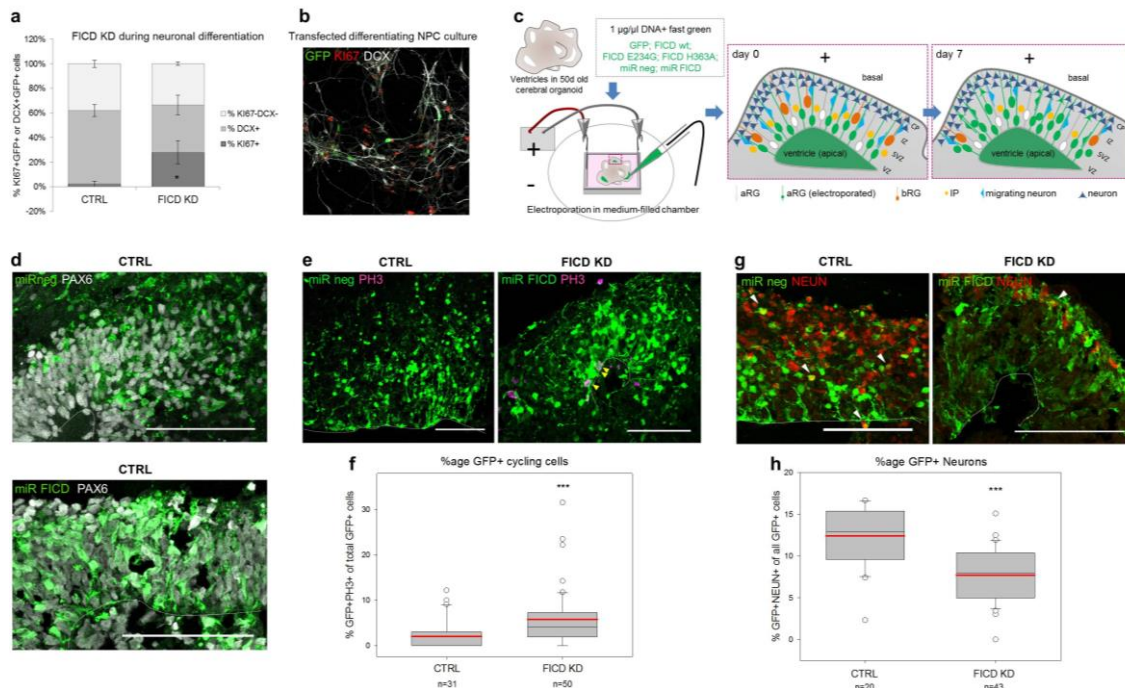


Figure 6 | AMPylation remodelling in differentiating neurons and cerebral organoids by downregulation of FICD levels keeps cells in a cycling state. **a**, FICD knockdown (KD) in neural progenitors (NPCs) differentiating to neurons inhibits cells from cell cycle exit. NPCs were transfected with miRNAs targeting FICD (Fig. S19) and cultured under differentiating conditions for 7 days. IHC stainings for the proliferation marker KI67+ and the early neuronal marker doublecortin (DCX) showed that FICD KD leads to a significant increase in KI67+ compared to control, while the amount of generated neurons tends to be decreased (analysis of 3 coverslips/condition with at least 20 transfected cells each; two-tailed Student's *t*-test: KI67+: * $P < 0.05$; DCX+: $P = 0.068$). **b**, Example image of transfected and IHC stained culture with transfected cells (GFP+) in green, proliferating cells (KI67+) in red and differentiating neurons (DCX+) in white. **c**, Scheme showing the electroporation of DNA into ventricle-like structures of cerebral organoids (COs) and the organisation of different cell types within the germinal zone. DNA (constructs are listed; supplemented with fast green for visualisation) is injected into the lumen and taken up by aRG via their apical processes. The transfected construct can be found in IPs and neurons upon differentiation of transfected aRG (green, 7 days post electroporation (dpe)) (VZ = ventricular zone, SVZ = subventricular zone, IZ = intermediate zone, CP = cortical plate; aRG = apical radial glia, bRG = basal radial glia, IP = intermediate progenitor). **d**, Upon acute miRNA-mediated KD of FICD in ventricles of COs (50d+7), most GFP+ cells (green) have aRG identity (PAX6+, white). **e**, **f**, FICD KD leads to an increased number of cycling progenitors (**e**, IHC staining for PH3+ cells in M-Phase. GFP+ PH3+ cells marked by yellow arrowheads; **f**, Quantification of GFP+ PH3+ progenitor cells 7 dpe). **g**, **h**, aRG transfected with FICD-targeting miRNAs differentiate less to neurons (**g**, IHC staining for neuronal nuclei marker NEUN, red; GFP-positive neurons shown by white arrowheads; **h**, Quantification of GFP+ neurons 7 dpe shows significant decrease upon FICD knockdown). **d**, **e**, **g**, 50+7d old organoids; electroporated cells and their progeny shown in green; Scalebar = 50 μ m, dotted line = apical surface. **f**, **h**, 1n = 1 electroporated germinal zone; box plot: mean (red line), median (black line), box represents 25th and 75th percentiles, whiskers extend to 10th and 90th percentiles, all outliers are shown; Significance was tested using Kruskal-Wallis One-way ANOVA on Ranks and Dunn's Pairwise Multiple Comparison (** $P < 0.001$). See also Fig. S19 for miRNA validation, Fig. S17 for characterisation of COs, and Fig. S20 for analysis of MAP+ neuronal processes upon FICD KD in COs.

Forced expression of FICD wt and E234G *in vitro* leads to an increased neuronal differentiation. Conversely, when electroporating vectors carrying wt FICD, activated FICD E234G mutant or catalytically inactive FICD H363A mutant into ventricles of 50 days old COs, those transfected with FICD wt or E234G showed an increase and redistribution in fluorescent signal upon **pro-N6pA** treatment indicating a remodelling of AMPylation upon FICD overexpression (Fig. 7a), while there were no changes in distribution or intensity of the signal upon OX of FICD H363A used as a control (Fig. S20). Despite the lack of obvious changes in differentiation with the FICD H363A control we cannot exclude other cellular processes to be affected by this methodology. Similar increase in fluorescent signal was observed in **pro-N6pA** treated SH-SY5Y cells upon transfection with wt FICD and FICD E234G mutant (Fig. S22). The opposite was the case upon FICD KD in CO ventricles (Fig. S20). Upon FICD wt or E234G OX in COs, progenitor zones had regions sparse in PAX6+ cells (Fig. 7b). At the same time, MAP2+ neurites increasingly invaded these progenitor zones 7 dpe (Fig. 7c, blue arrowheads; S20) and 14 dpe (Fig. S21), which was not the case upon control or FICD H363A electroporation (Fig. 7c), nor upon FICD KD (Fig. S20). Interestingly, both the E234G mutant and wt FICD-transfected aRGs gave rise to a significantly higher number of neurons compared to H363A inactive mutant or control already at 7 dpe (Fig. 7e, f), which was consistent also at 14 dpe (Fig. S21).

Thus, FICD may regulate the transition from neural progenitors to neurons. The direct comparison to catalytically inactive FICD H363A, showing no difference to control condition, demonstrates the importance of FICD catalytic activity in proper progenitor cell cycle exit and neuronal differentiation. These results suggest that remodelling of AMPylation may play a role in neuronal differentiation during human brain development. However, it remains to be investigated whether the specific AMPylation/de-AMPylation activity on HSPA5 and subsequent changes in the UPR are responsible for modulation of the neuronal differentiation, which would be supported by the known connection between UPR and brain development.⁴² Alternatively, the synergistic action of AMPylation on cytoskeletal protein targets and associated changes in cellular polarization as described for MAP6 palmitoylation could be responsible for these effects.⁴³

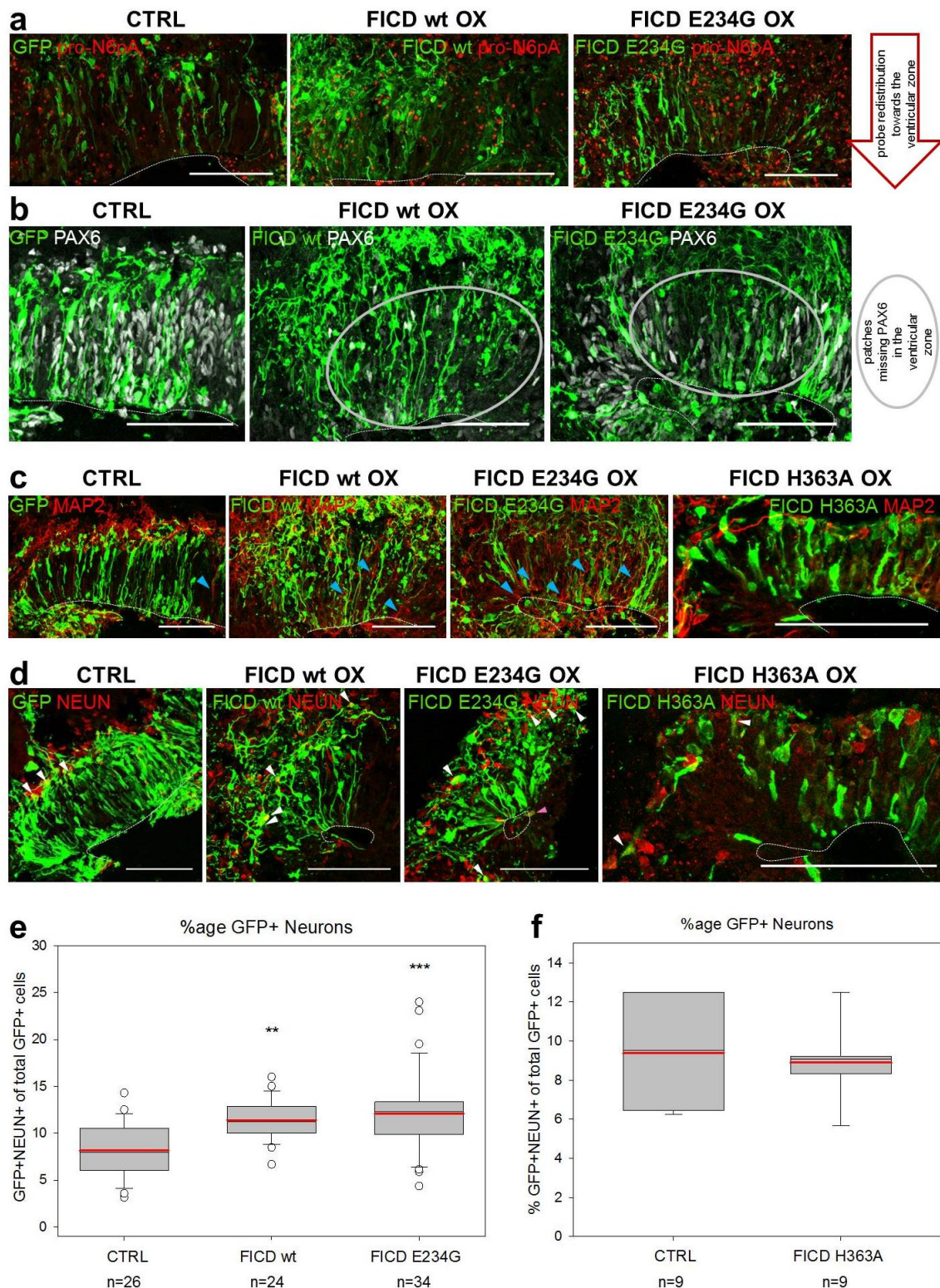


Figure 7 | AMPylation remodelling in cerebral organoids by FICD overexpression increases neuronal differentiation. FICD wt, E234G and H363A were overexpressed in 50d old cerebral organoids (COs, see Fig. 6c for electroporation scheme) and sections were analysed 7 days later by immunohistochemistry (IHC). **a**, Acute overexpression (OX) of FICD wt and E234G (green) in ventricles of COs (50+7d) leads to remodelling of AMPylation, visualised by the redistribution of fluorescence labelling using pro-N6pA (red). **b**, Germinal zones rich in

cells overexpressing FICD wt or E234G (green) show patchy “holes” lacking PAX6+ dorsal NPCs (grey) in their ventricular zone (VZ) (indicated by grey circle). **c**, Upon FICD wt and E234G OX, MAP2+ neuronal processes (red) increasingly extend into the VZ (blue arrowheads), which does not occur upon control and FICD H363A OX. **d, e**, RGs overexpressing FICD wt or E234G show increased differentiation to neurons compared to control. (**d**, IHC staining for nuclei of differentiated neurons (NEUN, red; GFP+ neurons shown by white arrowheads, GFP+ neuron in the progenitor zone by blue arrowhead. **e**, Quantification of GFP+ neurons shows significant increase upon FICD wt or E234G OX). **f**, OX of the catalytically inactive FICD H363A does not lead to an increase in GFP+ neurons. **a, b, c, d**, 50+7d old organoids; electroporated cells and their progeny shown in green; Scalebar = 50 μ m, dotted line = apical surface. **e, f**, 1n=1 electroporated germinal zone; box plot: mean (red line), median (black line), box represents 25th and 75th percentiles, whiskers extend to 10th and 90th percentiles, all outliers are shown; significance was tested using Kruskal-Wallis One-way ANOVA on Ranks and Dunn’s Pairwise Multiple Comparison (** $P < 0.01$; *** $P < 0.001$). See also Fig. S20 for analysis of PH3+ progenitors upon FICD wt/E234G/H363A OX in COs and for scoring of MAP2+ progenitor cells intruding the VZ upon FICD KD or FICD wt/E234G/H363A OX in COs.

Discussion

Our **pro-N6pA** phosphoramidate probe design facilitated *in situ* identification of 162 potentially AMPylated proteins in different cell types and uncovered FICD as a modulator of neuronal differentiation. We successfully identified FICD dependent AMPylation as exemplified on HSPA5 and FICD independent AMPylation as shown for other proteins like PFKP, PPME and SQSTM1. FICD is the only known human AMPylator and all previous studies utilize this enzyme for deciphering substrates *in vitro*. Our *in situ* approach is global and does not only depend on FICD. Thus FICD-independent AMPylation supports the existence of additional AMP transferases such as an emerging group of pseudokinases which were identified as AMPylators in eukaryotic cells¹⁷. Moreover, our *in situ* profiling allowed to screen AMPylation remodelling during neuronal development from iPSCs in 2D and 3D *in vitro* approaches, connecting biological implications of FICD dependent AMPylation/de-AMPylation with human brain development: Acute KD of FICD in differentiating neurons (2D) and cerebral organoids (3D) kept cells in a cycling state, while OX of the only known human AMPylating enzyme was shown to drive the differentiation of NPCs to neurons in cerebral organoids. The subtle but always significant dysregulation of neurogenesis resulting from FICD OX and KD may be caused by impaired AMPylation remodelling, influencing catalytic activity of metabolic enzymes or stability of cytoskeletal proteins. The remarkable number of AMPylated targets identified altogether in NPCs, neurons and COs indicates a synergistic influence in fine-tuning neurogenesis, but it is not trivial to pinpoint the function of each target protein individually, leaving the precise molecular mechanism unresolved. Furthermore, alternation of the neuronal differentiation process might be influenced as well through the AMPylation of HSPA5 and successive changes in UPR.¹⁶

Our study highlights both the promises and challenges of using chemical-proteomics for identification of protein PTMs. Although we have successfully identified a large group of AMPylated proteins in various cell types and elucidated its functional

implications, the method itself yielded rather low rate of identified sites needed for biochemical testing of the AMPylation function *in vitro*. Although we were able to identify seven sites and show that this PTM can inhibit target protein activity, as exemplified by CTSB, the abundance of AMPylation likely limits *in situ* detection. Future studies will thus focus on methods to quantify AMPylation levels and fine-tune enrichment and MS-based detection procedures. Interestingly, taking together both approaches of chemical-proteomics and fluorescence imaging utilizing the **pro-N6pA** probe suggests a cell type-specific AMPylation pattern. This is a combination of the particular AMPylated proteins and their intracellular localisation in a certain cell type. For example, postmitotic fibroblasts exhibit highly enriched proteins shared with the proliferating cell lines, but their subcellular localisation is very distinct from the localisation in the cycling cells. Aside the dependence of AMPylation on the cell type, we have shown with the example of thapsigargin-induced ER stress that the prevalent environmental condition can affect AMPylation.

With these features, we believe our method will lead to discovery of new functions for protein AMPylation beyond neuronal development e.g. in stem cell differentiation, unfolded protein response or regulation of complex network of cysteine cathepsins.

References

1. Aebersold, R. et al. How many human proteoforms are there? *Nat. Chem. Biol.* **14**, 206–214 (2018).
2. Casey, A. K. & Orth, K. Enzymes Involved in AMPylation and deAMPylation. *Chem. Rev.* **118**, 1199-1215 (2017).
3. Sanyal, A. et al. A Novel Link between Fic (Filamentation Induced by cAMP)-mediated Adenylation/AMPylation and the Unfolded Protein Response. *J. Biol. Chem.* **290**, 8482–8499 (2015).
4. Preissler, S. et al. AMPylation matches BiP activity to client protein load in the endoplasmic reticulum. *Elife* **4**, e12621 (2015).
5. Preissler, S., Rato, C., Perera, L., Saudek, V. & Ron, D. FICD acts bifunctionally to AMPylate and de-AMPylate the endoplasmic reticulum chaperone BiP. *Nat. Struct. Mol. Biol.* **24**, 23–29 (2017).
6. Song, Y. & Brady, S. Post-translational modifications of tubulin: pathways to functional diversity of microtubules. *Trends in Cell Biology* **25**, 125–136 (2015).
7. Vogl, A. M. et al. Neddylation inhibition impairs spine development, destabilizes synapses and deteriorates cognition. *Nature neuroscience* **18**, 239 (2015).
8. Kingdon, H. S., Shapiro, B. N. & Stadtman, E. R. Regulation of glutamine synthetase, VIII. ATP: Glutamine synthetase adenylyltransferase, an enzyme that catalyzes alterations in the regulatory properties of glutamine synthetase. *Proc. Natl. Acad. Sci. U.S.A.* **58**, 1703–1710 (1967).
9. Yarbrough, M. et al. AMPylation of Rho GTPases by Vibrio VopS Disrupts Effector Binding and Downstream Signaling. *Science* **323**, 269–272 (2009).
10. Worby, C. A. et al. The fic domain: regulation of cell signaling by adenylation. *Mol. Cell* **34**, 93–103 (2009).
11. Engel, P. et al. Adenylation control by intra- or intermolecular active-site obstruction in Fic proteins. *Nature* **482**, 107–110 (2012).
12. Preissler, S. et al. AMPylation targets the rate-limiting step of BiP's ATPase cycle for its functional inactivation. *Elife* **6**, e29428 (2017).
13. Rahman, M. et al. Visual neurotransmission in *Drosophila* requires expression of Fic in glial capitate projections. *Nat Neurosci* **15**, 871–875 (2012).
14. Ham, H. et al. Unfolded protein response-regulated *Drosophila* Fic (dFic) protein reversibly AMPylates BiP Chaperone during Endoplasmic reticulum Homeostasis. *J. Biol. Chem.* **289**, 36059–36069 (2014).
15. Casey, A. et al. Fic-mediated deAMPylation is not dependent on homodimerization and rescues toxic AMPylation in flies. *J Biol Chem* **292**, 21193–21204 (2017).
16. Moehlman, A., Casey, A., Servage, K., Orth, K. & Krämer, H. Adaptation to constant light requires Fic-mediated AMPylation of BiP to protect against reversible photoreceptor degeneration. *Elife* **7**, e38752 (2018).

17. Sreelatha, A. et al. Protein AMPylation by an evolutionarily conserved pseudokinase. *Cell* **175**, 1–13, (2018).
18. Grammel, M., Luong, P., Orth, K. & Hang, H. A Chemical Reporter for Protein AMPylation. *J. Am. Chem. Soc.* **133**, 17103–17105 (2011).
19. Broncel, M., Serwa, R. & Tate, E. A New Chemical Handle for Protein AMPylation at the Host–Pathogen Interface. *ChemBioChem* **13**, 183–185 (2012).
20. Broncel, M., Serwa, R., Bunney, T., Katan, M. & Tate, E. Global Profiling of Huntingtin-associated protein E (HYPE)-Mediated AMPylation through a Chemical Proteomic Approach. *Mol. Cell Proteom.* **15**, 715–725 (2016).
21. Mehellou, Y., Rattan, H. S. & Balzarini, J. The ProTide Prodrug Technology: From the Concept to the Clinic. *J. Med. Chem.* **61**, 2211–2226 (2018).
22. Evans, M. & Cravatt, B. Mechanism-Based Profiling of Enzyme Families. *Chem. Rev.* **106**, 3279–3301 (2006).
23. Boersema, P., Raijmakers, R., Lemeer, S., Mohammed, S. & Heck, A. Multiplex peptide stable isotope dimethyl labelling for quantitative proteomics *Nat. Protoc.* **4**, 484–494 (2009).
24. Cox, J. et al. Accurate proteome-wide label-free quantification by delayed normalization and maximal peptide ratio extraction, termed MaxLFQ. *Mol. Cell. Proteom.* **13**, 2513–2526 (2014).
25. Westcott, N., Fernandez, J., Molina, H. & Hang, H. Chemical proteomics reveals ADP-ribosylation of small GTPases during oxidative stress. *Nat. Chem. Biol.* **13**, 302–308 (2017).
26. Daniels, C., Ong, S.-E. & Leung, A. The Promise of Proteomics for the Study of ADP-Ribosylation. *Mol. Cell* **58**, 911–924 (2015).
27. Gibson, B. et al. Chemical genetic discovery of PARP targets reveals a role for PARP-1 in transcription elongation. *Science* **353**, 45–50, (2016).
28. Backus, K. M. et al. Proteome-wide covalent ligand discovery in native biological systems. *Nature* **534**, 570–4 (2016).
29. Stoka, V., Turk, V. & Turk, B. Lysosomal cathepsins and their regulation in aging and neurodegeneration. *Ageing Res. Rev.* **32**, 22–37 (2016).
30. Agostini et al. Metabolic reprogramming during neuronal differentiation. *Cell Death Differ.* **23**, 1502–1514 (2016).
31. Olson, O. & Joyce, J. Cysteine cathepsin proteases: regulators of cancer progression and therapeutic response. *Nat. Rev. Cancer* **15**, 712–29 (2015).
32. Xing, Y. et al. Structural Mechanism of Demethylation and Inactivation of Protein Phosphatase 2A. *Cell* **133**, 154–163 (2008)..
33. Wang, M. & Kaufman, R. Protein misfolding in the endoplasmic reticulum as a conduit to human disease. *Nature* **529**, 326–335 (2016).

34. Fux, A., Korotkov, V. S., Schenider, M., Antes, I. & Sieber, S. A. Chemical cross-linking enables drafting ClpXP proximity maps and taking snapshots of in situ interaction networks *Cell Chem. Biol.* DOI: 10.1016/j.chembiol.2018.10.007, (2018).
35. Boyer, L., Campbell, B., Larkin, S., Mu, Y. & Gage, F. Dopaminergic differentiation of human pluripotent cells. *Cur. Prot. Stem Cell Biol.* **22**, 1H.6.1–1H.6.11. (2012).
36. Liu, N. *et al.* Proteomic Profiling and Functional Characterization of Multiple Post-Translational Modifications of Tubulin. *J. Proteom. Res.* 14,3292–3304 (2015).
37. Gascón, S., Masserdotti, G., Russo, G. & Götz, M. Direct Neuronal Reprogramming: Achievements, Hurdles, and New Roads to Success. *Cell Stem Cell* **21**, 18–34 (2017).
38. Nainar, S. *et al.* Metabolic Incorporation of Azide Functionality into Cellular RNA. *ChemBioChem* **17**, 2149–2152 (2016).
39. Camp, G. *et al.* Human cerebral organoids recapitulate gene expression programs of fetal neocortex development. *Proc. Natl. Acad. Sci. U.S.A.* **51**, 15672–15677 (2015).
40. Quadrato, G. *et al.* Cell diversity and network dynamics in photosensitive human brain organoids. *Nature* **545**, 48–53 (2017).
41. Lancaster, M. *et al.* Cerebral organoids model human brain development and microcephaly. *Nature* **501**, 373–379 (2013).
42. Martínez, G., Khatiwada, S., Costa-Mattioli, M. & Hetz, C. ER Proteostasis Control of Neuronal Physiology and Synaptic Function. *Trends Neurosci.* **41**, 610–624, (2018).
43. Tortosa, E. *et al.* Dynamic palmitoylation targets MAP6 to the axon to promote microtubule stabilization during neuronal polarization. *Neuron* **94**, 809–825. e7 (2017).

Supplementary Information

Acknowledgements This work was supported by the European Research Council (ERC) consolidator grant (725085 - CHEMMINE), SFB749 and Alexander von Humboldt fellowship to P.K. We thank to A. Itzen for helpful suggestions and providing us with recombinant FICDs and B. F. Cravatt for providing us with the azide-TEV-cleavable-biotin linker. S. M. Hacker and A. Hoegl for manuscript proofreading, and T. Öztürk and G. Giorgio for technical assistance.

Author Contribution S.A.S. and P.K. conceived of the project. P.K., I.Y.B., S.C. and S.A.S. designed the experiments. P.K. and I.Y.B. performed the experiments. P.K. synthesized the probes, conducted chemical-proteomic experiments, data analysis and *in vitro* assays. I.Y.B. cultured the fibroblasts, neuroblastoma cells, iPSCs, NPCs, and

neurons, performed all KD and OX experiments and analysis on COs, fluorescent imaging, qPCR, and STRING. V.C.K. performed the metabolomics experiments. N.C.B. set up the MS methods and helped with MS data analysis. M.D. generated and provided iPSC. P.K., I.Y.B., S.C. and S.A.S. wrote the manuscript.

Author Information

Reviewer Information

METHODS

Synthesis. The nucleoside (*N*⁶-propargyl adenosine, **N6pA**) and the rhodamine-biotin-azide tags were synthesized as described previously^{44,45}. Synthesis of the phosphoramidate probe **pro-N6pA** is described in the Supplementary Information following a methodology described previously⁴⁶. Chemical identity and samples purity were established using NMR, HRMS and HPLC analysis.

Cell lines. Human epitheloid cervix carcinoma cells (HeLa, CCL-2) and human lung carcinoma cells (A549) were cultivated in high glucose Dulbeccos's Modified Eagle's Medium (DMEM) supplemented with 10% (v/v) fetal bovine serum (FBS) and 2 mM l-glutamine. Cells were grown under a humidified atmosphere at 37 °C and 5% CO₂. Cells were seeded into 6 cm diameter dishes and grown to 80-90% confluency. Human neuroblastoma cells SH-SY5Y (CRL-226) were cultivated in DMEM/F12 1:1 media supplemented with 10% (v/v) FBS.

Chemical-proteomics. Cells were treated with the probes at 80-90% confluency (*n* represents number of cell culture dishes). Culture medium was removed and the cells or COs were labelled in fresh media containing 100µM **N6pA** or 100µM **pro-N6pA** (both stocks 100mM in DMSO) for 16 h at 37 °C in cells incubator. Subsequent cell lysis, click chemistry, avidin beads enrichment and MS sample preparation were performed as described previously^{22-24,47}. A total amount of 500 µg (HeLa, A549, SH-SY5Y or COs) or 250 µg (iPSCs, NPCs, neurons) of proteins in lysate was used for each MS sample preparation. For details see Supplementary Information.

Site identifications. Site identification experiments were performed in HeLa and SH-SY5Y cells and COs. Cells or COs were cultivated and treated with **pro-N6pA**. After the cells lysis and protein concentration measurement, 3.6 and 16 mg of HeLa or 6 mg of SH-SY5Y or 8 mg of CO protein lysates were used for further MS sample preparations. The protocol used for enrichment and digest with TEV-cleavable linker was adapted from ref. 28. For details see Supplementary Information.

Mass Spectrometry. Nanoflow LC-MS/MS analysis was performed with an UltiMate 3,000 Nano HPLC system coupled to an Orbitrap Fusion or Q Exactive Plus (*Thermo Fisher Scientific*). Fragments were generated using higher-energy collisional dissociation (HCD) and detected in the ion trap at a rapid scan rate. Raw files were

analysed using MaxQuant software with the Andromeda search engine. Searches were performed against the Uniprot database for Homo sapiens (taxon identifier: 9606, 7th July 2015, including isoforms). At least two unique peptides were required for protein identification. False discovery rate determination was carried out using a decoy database and thresholds were set to 1 % FDR both at peptide-spectrum match and at protein levels. For AMPylation site identification spectra were searched for AMP conjugated with TEV tag (+694.2700) and only one unique or razor peptide was required. For details of MS measurement and data analysis see Supplementary Information and Tables S1, S4 and S9.

In vitro CTSB activity assay. Cathepsin B (CTSB, 0.4 $\mu\text{g}/\mu\text{L}$, *R&D Systems*) was diluted in activation buffer (25 mM MES, 5 mM DTT, pH 5.0) to 10 $\mu\text{g}/\text{mL}$ and incubated at 25 °C for 25 min. The activated CTSB was further diluted to 2 $\mu\text{g}/\text{mL}$ in AMPylation buffer (20 mM HEPES, 100 mM NaCl, 5 mM MgCl_2 , 1 mM DTT, 0.1 mg/mL BSA, pH 7.5) and supplemented with 100 μM ATP, 2.8 μM wt FICD or FICD E234G mutant (gift from A. Itzen, TUM) or ddH₂O and incubated at 25 °C for 0 – 6 h. Subsequently, 3 μL of the mixture was used in 57 μL assay buffer (25 mM MES, 10 μM Z-Arg-Arg-7-amido-4-methylcoumarin hydrochloride (*Sigma*), pH 5.0) in 96-well plate and the fluorescent intensity was read by TECAN 200M Pro after 20 min using 380 nm and 460 nm as excitation and emission wavelengths.

iPSC culture. Induced pluripotent stem cells reprogrammed from fibroblasts (for reprogramming see Supplementary Information) were cultured at 37 °C, 5 % CO₂ and ambient oxygen level on Geltrex coated plates (*Thermo Fisher Scientific*) in mTeSR1 medium (*StemCell Technologies*) with daily medium change. For passaging, iPSC colonies were washed with PBS and incubated with StemPro Accutase Cell Dissociation Reagent (A1110501, *Life Technologies*) diluted 1:4 in PBS for 3 minutes. Pieces of colonies were washed off with DMEM/F12, collected by 5 min centrifugation at 300 x g and resuspended in mTeSR1 supplemented with 10 μM Rock inhibitor Y-27632(2HCl) (72304, *StemCell Technologies*) for the first day.

Generation of neural progenitor cells (NPCs) and neurons from iPSCs. Neural progenitors were generated as described previously³⁵ with the following modifications. Embryoid bodies (EBs) were generated from feeder-free iPSCs by incubating colonies with Collagenase Type IV (7909, *StemCell Technologies*) for 10 min, followed by washing with DMEM/F12, manual disruption and scraping with a cell lifter (3008, *Corning Life Sciences*). Resulting pieces of colonies were plated in suspension in Neural Induction Medium (NIM) consisting of DMEM/F12+Hepes (31330095, *Life Technologies*) with 1x N2 and B27 supplements (without vitamin A, *Thermo Fisher*) with medium change every other day. Resulting NPCs were passaged using Accutase (*StemCell Technologies*) and split at a maximum ratio of 1:4. NPCs were only used for up to seven passages. For differentiation to neurons, single NPCs were plated at a density of 10⁴ cells/cm² on Polyornithine/Laminin plates and cultured in NPM for 1 more day to reach about 30% cell density. Afterwards, medium was changed to Neuronal Differentiation Medium NDM (NIM containing 20 ng/mL BDNF (248-BD, *R&D Systems*))

and 20 ng/mL GDNF (212-GD, *R&D Systems*) and cells were differentiated for 40 days with medium change every 5 days.

Cerebral organoids. Cerebral organoids were generated starting from 9,000 single iPS cells/well as previously described⁴⁰. Organoids were cultured in 10 cm dishes on an orbital shaker at 37 °C, 5% CO₂ and ambient oxygen level with medium changes twice a week. Organoids were electroporated at 50 days after plating (see *Electroporation of cerebral organoids*) and analysed 7 and 14 dpe. For immunostaining, 16 µm sections of organoids were prepared using a cryotome. For analysis 7 dpe, 24-34 different ventricles in 7-12 organoids from 2 independent batches were analysed per construct. For 14 days, 4 organoids per construct with altogether 13-21 electroporated ventricles per construct were analysed.

Generation and validation of microRNAs targeting FICD: MicroRNAs (miRNAs) targeting FICD were generated using the BLOCK-iT system from Invitrogen (Thermo Fisher, Waltham, MA, USA). MiRNA sequences were determined using Invitrogens RNAi design tool <https://rnaidesigner.thermofisher.com/rnaiexpress/setOption.do?designOption=mirnapid=1961720787891316464>, accessed on December 6th, 2017, with the NCBI Reference Sequence NM_007076.2 as seed sequence. Three miRNA sequences were chosen and ordered as oligonucleotides from Sigma. FICD miRNA oligonucleotides were annealed and ligated into a GFP-containing entry vector pENTR-GW/EmGFP-miR using T4 DNA Ligase (Thermo Fisher, Waltham, MA, USA). Subsequently, the miRNA sequences were cloned into the pCAG-GS destination vector using the Gateway system (Thermo Fisher). The resulting miRNA expression plasmids were sequenced, the knockdown efficiency was validated in Hela cells via qPCR and Westernblot and the most efficient construct was used for NPC transfection and for electroporation of COs (Fig. S19, Fig. 6).

Oligo Name	Sequence (5' to 3')
miR FICD_top	TGCTGAATGCTCTTCCACAACCTCCAGTTTTGGCCACTGACTGACTGGGAGTTGGAAGAGCATT
miR FICD_bottom	CCTGAATGCTCTTCCACAACCTCCAGTCAGTCAGTGGCCAAAACCTGGGAGTTGTGGAAGAGCATTC

Transfection of differentiating NPCs. For transfection of differentiating NPCs, 10⁴ cells/cm² were plated on Polyornithine/Laminin-coated coverslips in 24-well plates. After one day in NPM (see *Generation of neural progenitor cells (NPCs) and neurons from iPSCs*), medium was changed to growth-factor free NIM (see *Generation of neural progenitor cells (NPCs) and neurons from iPSCs*.) to generate differentiating conditions. 4 days after plating, NPCs were transfected with 500 ng DNA/well following Lipofectamine® 3000 protocol (*Thermofisher*) and continuously cultured in NIM with medium change every other day. Cells were fixed 7 days post transfection with 4 % PFA for 20min at RT and processed by immunohistochemistry.

Electroporation of cerebral organoids. For electroporation (see scheme in Fig. 6c), cerebral organoids were kept in NDM+A without antibiotics. The organoids were placed in an electroporation chamber (*Harvard Apparatus*) and pCMV-SPORT6 plasmid with FICD wt, FICD E234G (gift from A. Itzen, TUM), or FICD H363A plus pCAG-IRES-GFP

(FICD to GFP ratio 2:1), GFP only as overexpression control, miRNA against FICD (or scrambled miRNA negative control) in pCAG-GS at a concentration of 1 $\mu\text{g}/\mu\text{l}$, supplemented with fast green for visualization, was injected into ventricle-like cavities at several positions per organoid. Electroporation was performed with an ECM830 electroporation device (*Harvard Apparatus*) by subjecting the organoids to a 1 second interval with 5 pulses of 50 ms duration at 80mV.

Immunohistochemistry: Frozen organoid sections were thawed to rt for 20 min and then rehydrated in PBS for 5 min. For nuclear antigens, an antigen retrieval step (HIER) was performed in which the sections were boiled in 0.01M citric buffer pH 6 for 1 min at 720 Watt and an additional 10 min at 120 W. Slides were then left to cool down for 20 min. Half of the citric buffer was replaced by H₂O, slides were incubated for another 10 min and then washed in PBS. Subsequently, a postfixation step of 10 min was carried out with 4 % PFA in PBS. Then, the sections were permeabilized using 0.1 % Triton X100 in PBS for 5 min. After permeabilization, sections were blocked at rt for at least 1 h with 10 % Normal Goat Serum in 0.1 % Tween in PBS. The primary antibody (Table S11 in Supplementary information) in blocking solution was then incubated overnight at 4 °C. Following several washes with 0.1 % Tween in PBS, sections were incubated with 1:1,000 dilutions of Alexa Fluor-conjugated secondary antibodies (*Life Technologies*) in blocking solution for at least 1h at rt, using 0.1 $\mu\text{g}/\text{ml}$ 4,6-diamidino-2-phenylindole (DAPI, *Sigma Aldrich*) to counterstain nuclei. Finally, sections were washed again several times with 0.1 % Tween in PBS and mounted with Aqua Polymount (18606, *Polysciences*). Sections were visualized using a Leica SP8 confocal laser scanning microscope. Cells were cultured on round coverslips (13 mm diameter, *VWR*) in 24 well plates, washed with PBS and fixed with 4 % PFA in PBS for 15 min at rt. HIER, permeabilization, blocking and staining were carried out as described for the organoid sections.

Cell quantifications. For quantification of GFP⁺ mitotic cells or neurons upon NPC transfection or in electroporated CO ventricles, all GFP⁺PH3⁺, GFP⁺Ki67⁺, GFP⁺DCX⁺, and GFP⁺NEUN⁺ cells were counted using the cell counter plugin in Fiji⁴⁸. Double positive cells were normalized to the total number of GFP⁺ cells.

Statistics. Statistical analysis of the MaxQuant result table proteinGroups.txt (Table S2) was done with Perseus 1.5.1.6. Putative contaminants and reverse hits were removed. Dimethyl-labelling ratios or normalized LFQ intensities were log₂-transformed, hits with less than 3 valid values in each group were removed and -log₁₀(*p*-values) were obtained by a two-sided one sample Student's *t*-test over replicates with the initial significance level of *p* = 0.05 adjustment by the multiple testing correction method of Benjamini and Hochberg (FDR = 0.05), the -log₁₀ of *p*-values were plotted against the log₂ of geometric mean of ratios "heavy"/"light" (H/L) for dimethyl labelling or by volcano plot function for LFQ. Distance from zero was calculated from significance and fold enrichments from respective volcano plot as $d = \sqrt{(\text{fold enrichment})^2 + (\text{significance})^2}$. Venn diagrams were generated with a drawing tool at <http://bioinfogp.cnb.csic.es/tools/venny/> using gene names as a key. All graphs were processed in Microsoft Excel or OriginPro 2017. Statistics for qPCR data

and quantifications of immunohistochemical stainings in cells and COs was performed in SigmaPlot (Version 13.0; Systat Software, San Jose, CA) using Kruskal-Wallis ANOVA on Ranks with Dunn's Pairwise Multiple Comparison. For NPC transfection, 3 coverslips with at least 20 transfected cells each were analysed. For COs, 2-4 batches of organoids were analysed for each construct (Data shown with n = total number of electroporated ventricles analysed per construct).

Data availability. The mass spectrometry proteomics data have been deposited to the ProteomeXchange Consortium via the PRIDE partner repository with the dataset identifier PXD012118 reviewer account detail, username: reviewer94371@ebi.ac.uk password: 2i1CmPOu.

44. Jiang, H. *et al.* Mechanism-Based Small Molecule Probes for Labeling CD38 on Live Cells. *J. Am. Chem. Soc.* **131**, 1658–1659 (2009).
45. Eirich, J. *et al.* Pretubulysin derived probes as novel tools for monitoring the microtubule network via activity-based protein profiling and fluorescence microscopy. *Mol. Biosyst.* **8**, 2067-2075 (2012).
46. Deduras, M. *et al.* The application of phosphoramidate proside technology to acyclovir confers anti-HIV inhibition. *J. Med. Chem.* **52**, 5520–5530 (2009).
47. Speers, A. E. & Cravatt, B. F. Activity Based Protein Profiling (ABPP) and Click Chemistry (CC)-ABPP by MudPIT Mass Spectrometry. *Current protocols in chemical biology* **1**, 29–41 (2009).
48. Schindelin, J. *et al.* Fiji: an open-source platform for biological-image analysis. *Nat. Methods* **7**, 676–682 (2012).

SUPPLEMENTARY INFORMATION

FICD activity and AMPylation remodelling modulate human neurogenesis.

Pavel Kielkowski, Isabel Y. Buchsbaum, Volker C. Kirsch, Nina C. Bach, Micha Drukker, Silvia Cappello, Stephan A. Sieber

CONTENTS

- (A) Supplementary Figures
- (B) Structures and synthesis
- (C) Biological methods
- (D) NMR spectra
- (E) References

(A) Supplementary Figures

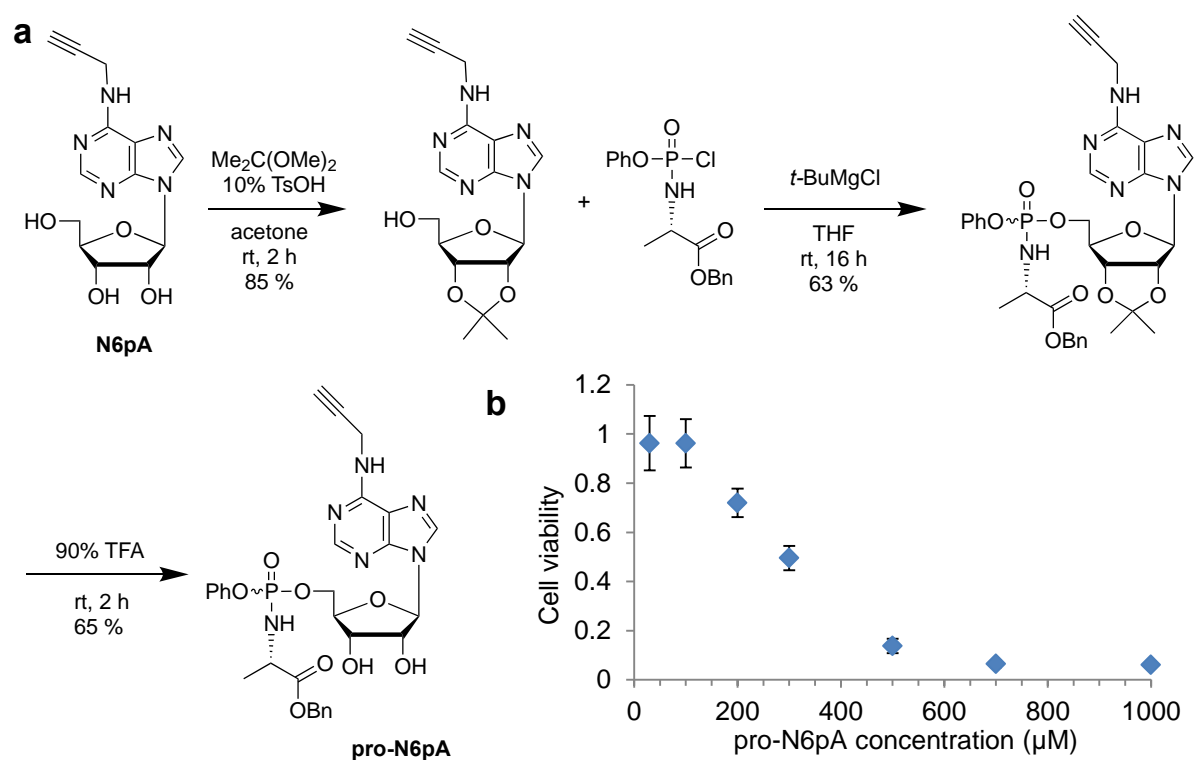


Figure S1 | Synthesis and cytotoxicity of pro-N6pA. **a**, Synthetic approach to pronucleotide probe. **b**, Cytotoxicity MTT assay of **pro-N6pA** probe. Dots represent the means of four replicates with standard deviation.

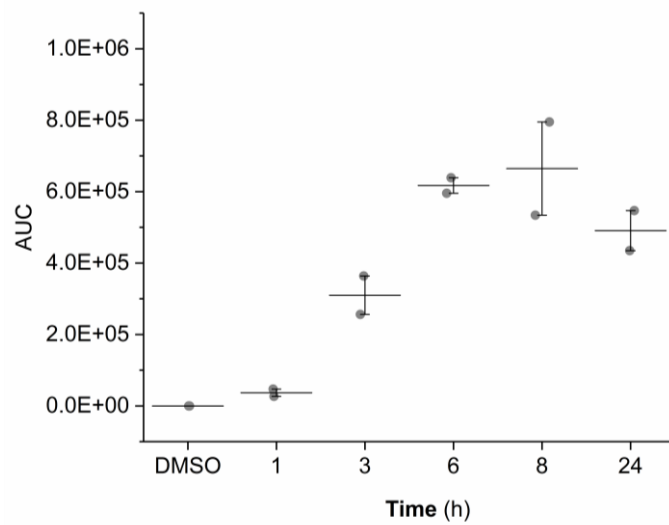


Figure S2 | *In situ* metabolic activation of the pro-N6pA probe to N6pATP. HeLa cells were treated with 100 μ M pro-N6pA for indicated period of time. Horizontal represent the mean of the duplicates.

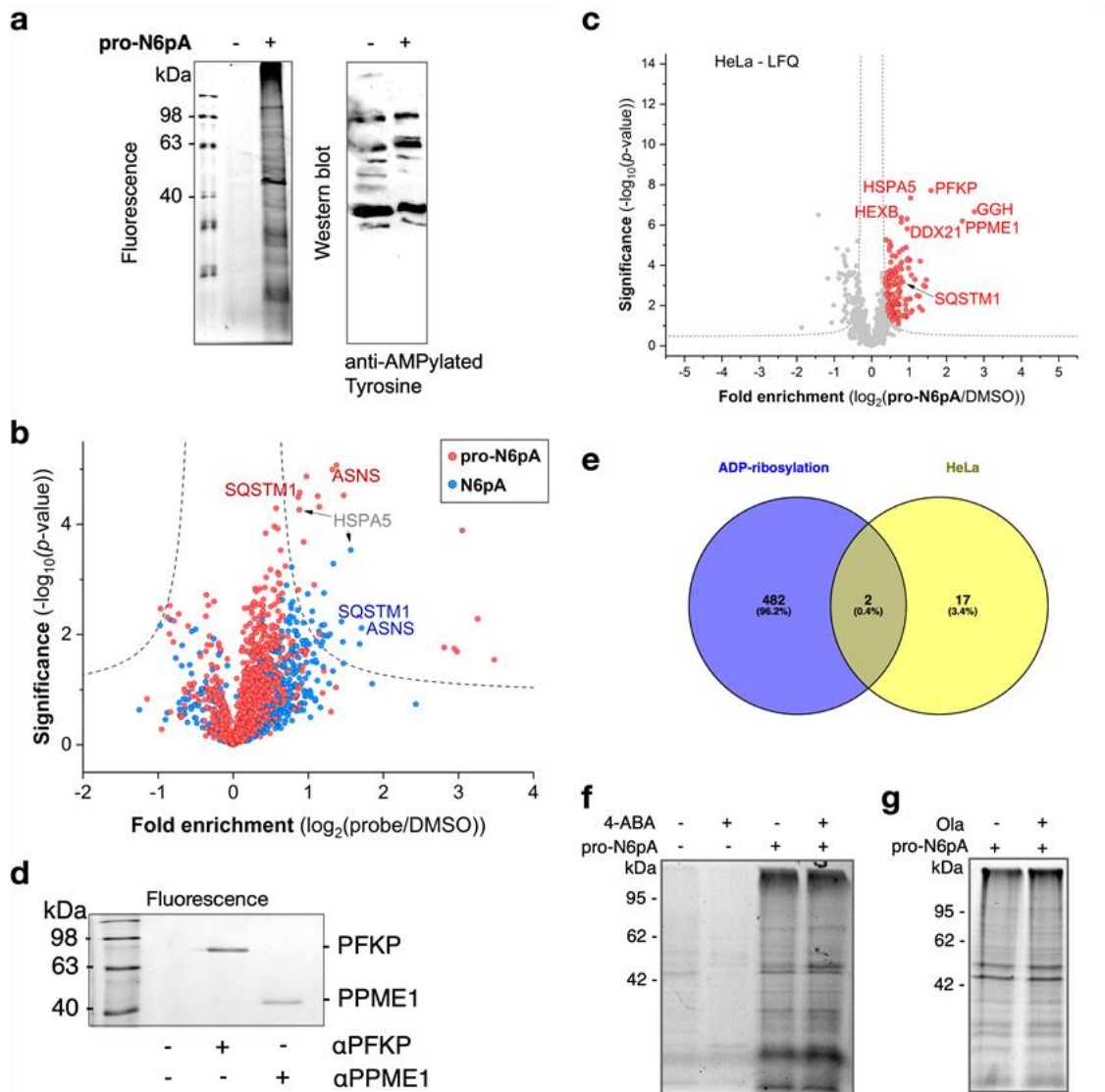


Figure S3 | Validation of phosphoramidate pronucleotide probe pro-N6pA as probe for cellular AMPylation. **a**, Direct comparison of the pro-N6pA labelling in HeLa cells with immunostaining of the western blot using anti-AMPylated tyrosine antibody. **b**, Volcano plot visualization of fold-enrichment using pro-N6pA or parent nucleoside (N6pA) compared to DMSO (control) versus significance upon performing a two-sample *t*-test (FDR 0.05, *s*₀ 0.3; *n* = 12 (pro-N6pA) or 11 (N6pA)). Pro-N6pA or N6pA treatment with 100 μM probe, 16 h incubation. **c**, Volcano plot visualising the pro-N6pA identified targets using LFQ method in HeLa cells. **d**, Fluorescence SDS-PAGE showing immunoprecipitated PFKP and PPME1 from pro-N6pA treated HeLa cells. Immunoprecipitated proteins were labelled via click-chemistry with rhodamine-azide. **e**, Venn plot representing overlap of known ADP-ribosylated proteins and hits identified by pro-N6pA probe in HeLa cells. **f**, Inhibition of poly(ADP-ribose) polymerases by pre-treatment of the HeLa cells with 20 mM 4-aminobenzamide (4-ABA) for 2 h before addition of pro-N6pA. **g**, Inhibition of poly(ADP-ribose) polymerases by pre-treatment of the HeLa cells with 10 μM Olaparib (Ola) for 2 h before addition of pro-N6pA.

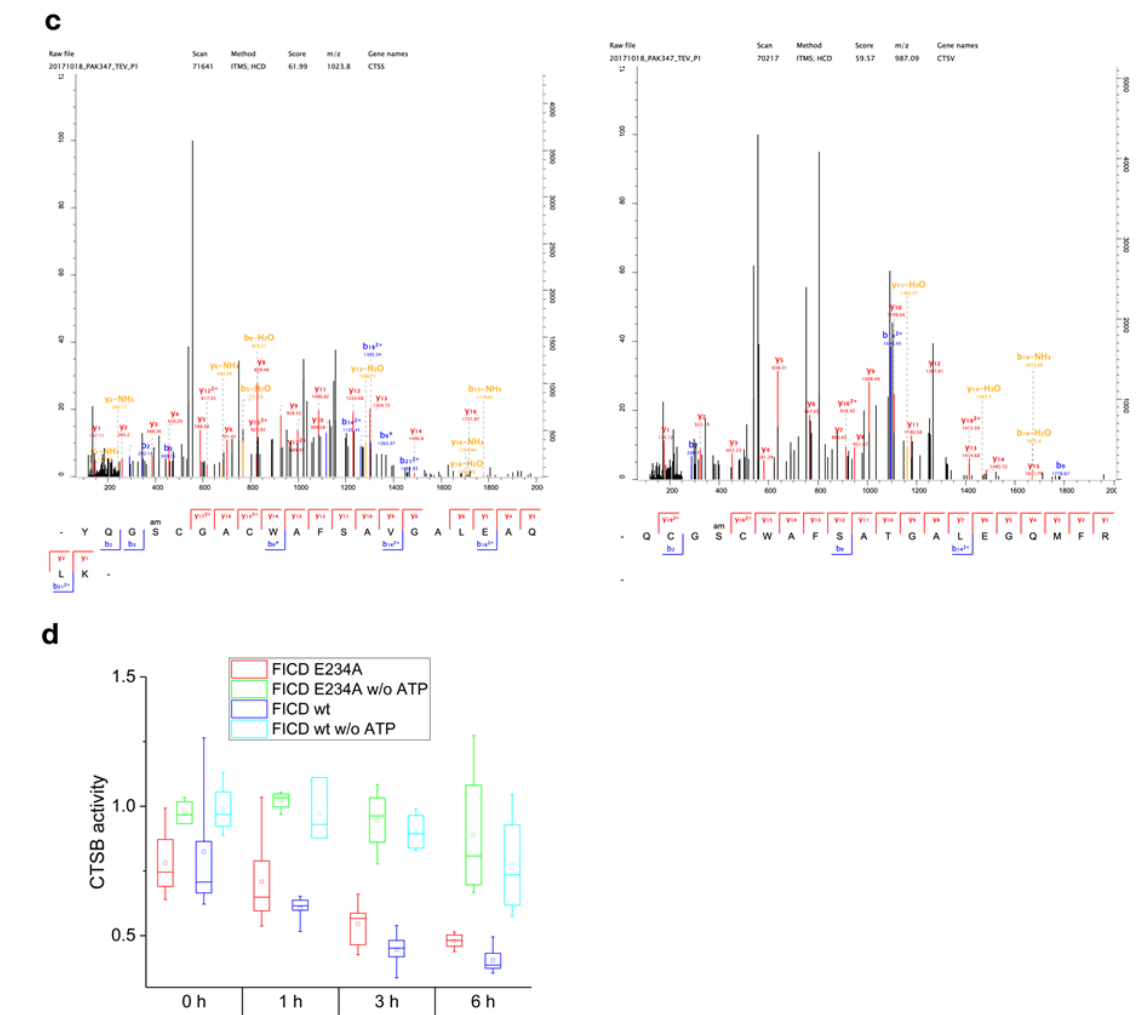


Figure S4 | AMPylation site identification on cathepsins in HeLa cells and inhibition of CTSSB activity upon AMPylation by FICD. **a**, Scheme of site identification using the TEV-cleavable-linker. **b**, MS/MS spectra (MaxQuant) for the CTSSB, CTSC and CTSL AMPylation site identification. CTSC AMPylation site was identified by two MS/MS scans with PEP scores 0.0224 and 0.0168. Additional sites on cathepsins were identified in SH-SY5Y cells and COs (Table S4). **c**, MS/MS spectra (MaxQuant) for the CTSS and CTSV identified in COs. **d**, *In vitro* CTSSB peptidase activity upon incubation with wt FICD or E234A mutant at 25 °C for 0 – 6 h with or without ATP (0.1 mM). Boxes represent 25-75 percentile, whiskers stand for min and max values, square is mean value and line is median.

Figure S5 | AMPylation sites identified in SH-SY5Y cells and cerebral organoids.
a, MS/MS spectra (MaxQuant) for the CTSB, CTSL AMPylation sites from SH-SY5Y cells. **b**, Cathepsins CTSV, CTSS AMPylation sites identified in cerebral organoids. **c**, Cathepsins CTSB, CTSC AMPylation sites identified in cerebral organoids (Table S4).

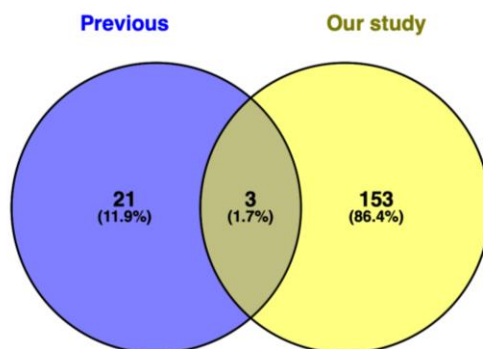


Figure S6 | Comparison of proteins identified in previous studies¹⁶ and our study.

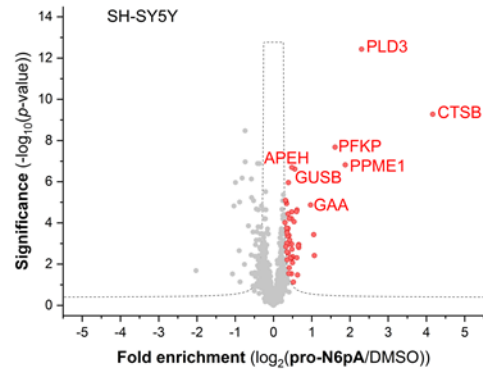
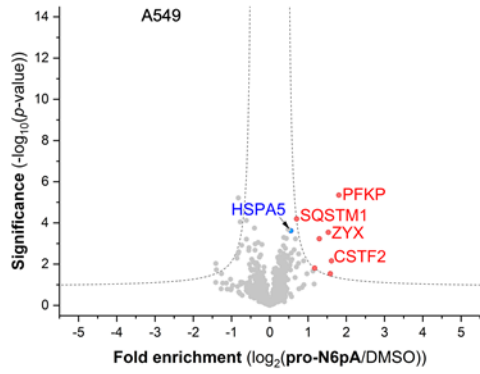
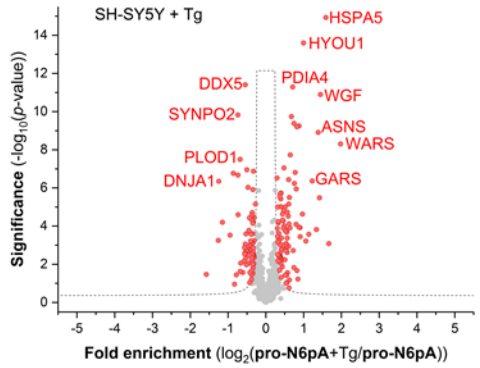
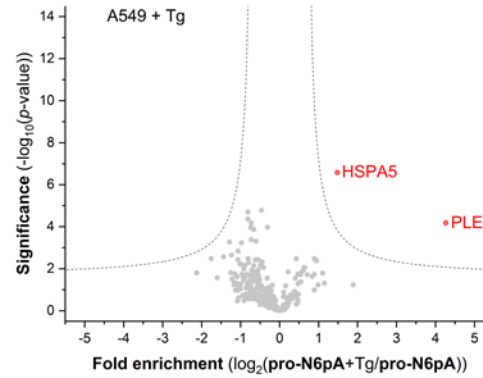
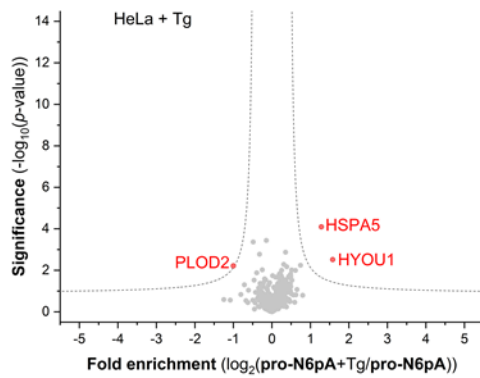
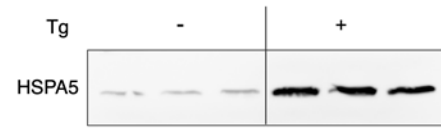
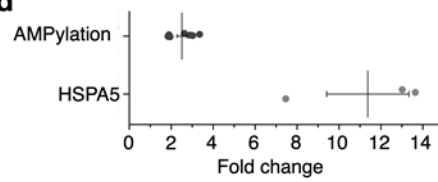
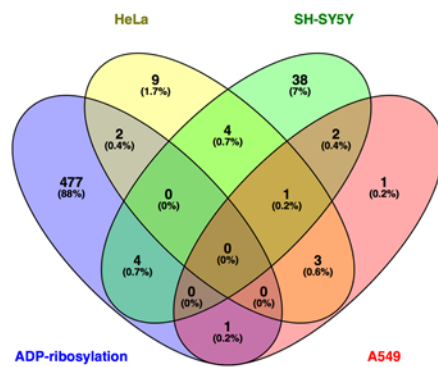
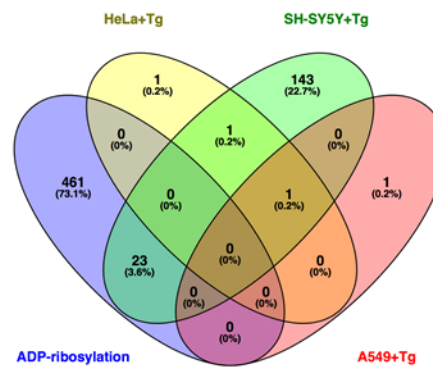
a**b****c****d****e****f**

Figure S7 | AMPylation is dependent on cell type and changes upon ER stress induction. **a, b**, Pro-N6pA 100 μ M probe, 16 h incubation. Complete list of the proteins identified by chemical-proteomic experiments is in Table S1 and S9. **a**, Volcano plot visualizations of fold-enrichment using pro-N6pA compared to DMSO *versus* significance upon performing a two-sample *t*-test (FDR 0.05, s_0 0.3; $n = 8$) from *in situ* labelling of A549 and SH-SY5Y cells. The MS intensities were quantified in A549 via DiMe, in SH-SY5Y via LFQ. **b**, Volcano plot visualizations of fold-enrichment using pro-N6pA upon Tg treatment (1 μ g/mL, 24 h) compared to pro-N6pA treated cells *versus* significance upon performing a two-sample *t*-test (FDR 0.05, s_0 0.3; $n = 8$ or 7 (HeLa + Tg)) from *in situ* labelling of HeLa, A549 and SH-SY5Y cells. The MS intensities were quantified in HeLa + Tg via DiMe, in A549 and SH-SY5Y via LFQ. **c**, Immunoblot of endogenous HSPA5 levels in HeLa cells without or with Tg treatment (1 μ g/mL, 24 h). **d**, Graph representation of fold change in AMPylation and HSPA5 expression levels after Tg treatment based on normalized MS intensities (MaxQuant) and immunoblot analysis, respectively. **e, f**, Venn diagrams show minor overlap of known ADP-ribosylated proteins with identified AMPylated proteins in different cell lines with or without induction of ER stress by Tg.

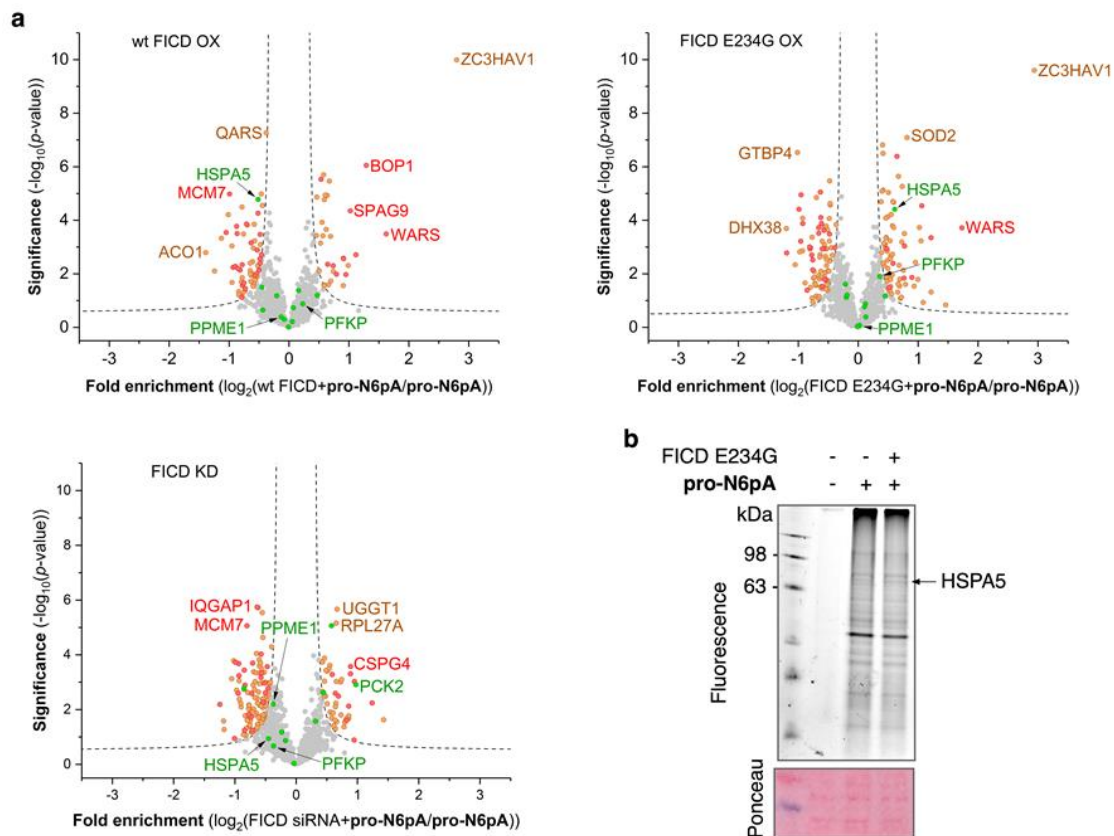


Figure S8 | Volcano plots of FICD overexpression and knockdown in HeLa cells. **a**, Volcano plot of fold-enrichment by pro-N6pA in HeLa transfected with FICD or siRNA compared to pro-N6pA treated cells *versus* significance upon performing a two-sample *t*-test (FDR 0.05, s_0 0.3; $n = 8$). Green dots represent proteins identified as

AMPylated in HeLa cells. Red dots represent proteins which overlap for the presented three volcano plots. Orange dots represent other significantly enriched proteins see Table S6. **b**, Overexpression of FICD E234G in HeLa cells. In-gel analysis of the labelling with pro-N6pA probe.

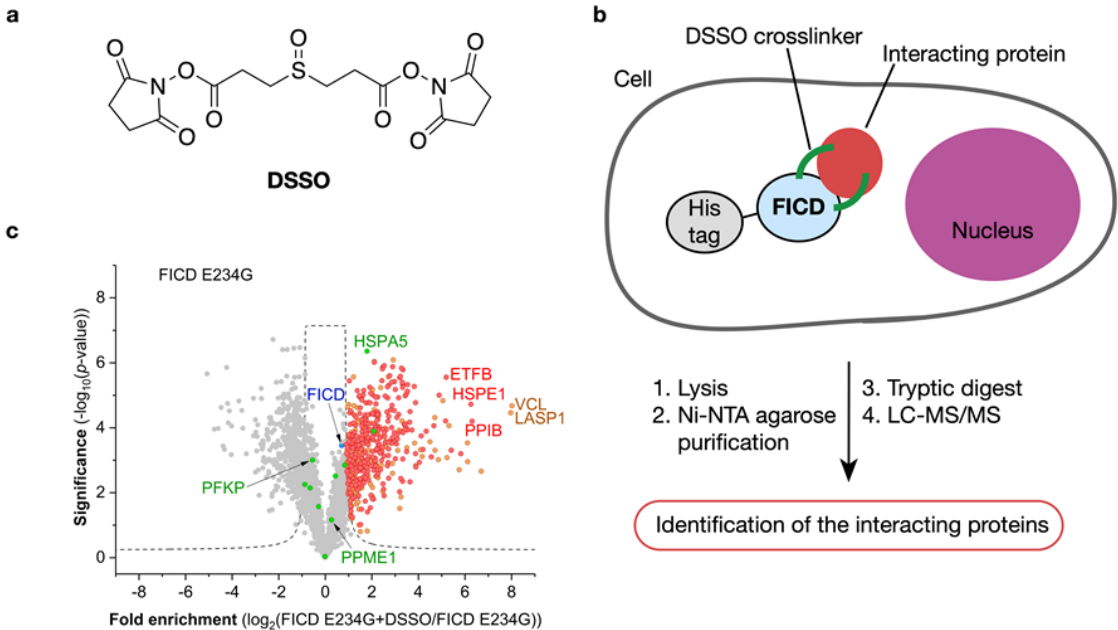


Figure S9 | Pull-down of FICD interacting proteins using DSSO crosslinker. **a**, Structure of the DSSO crosslinker. **b**, Workflow of identification of the FICD interacting proteins using the DSSO crosslinker. **c**, Volcano plot representing FICD E234G enriched proteins from HeLa cells. Green dots represent the proteins found AMPylated in HeLa cells (FDR 0.01; s_0 1.5; $n = 3$). Red dots represent proteins which were significantly enriched in the parallel experiment with the wt FICD. Orange dots represent proteins significantly enriched only in this experiment see Table S7.

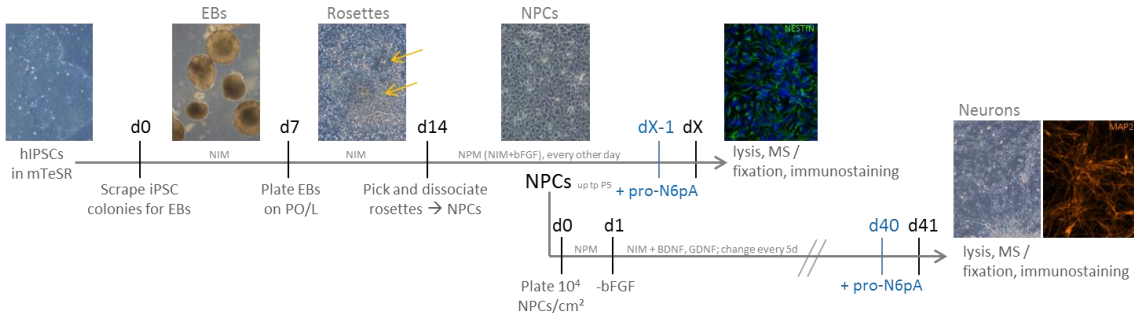


Figure S10 | NPCs and neuron preparation. Timeline for generation of Neural progenitor cells (NPCs) and neurons (according to ref. 31) and their treatment with pro-N6pA (neural rosettes: yellow arrows; hIPSCs = human induced pluripotent stem cells; EBs = embryoid bodies; PO/L = poly-ornithine-laminin coated plates; NIM = neural induction medium; NPM = neural progenitor medium).

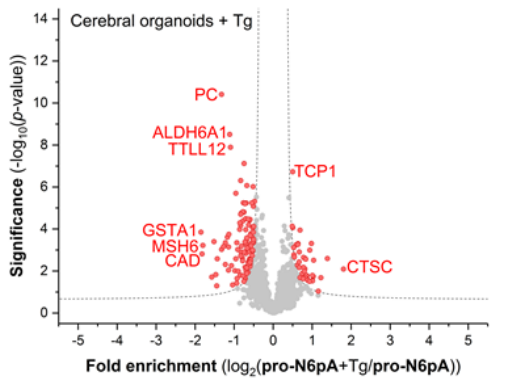
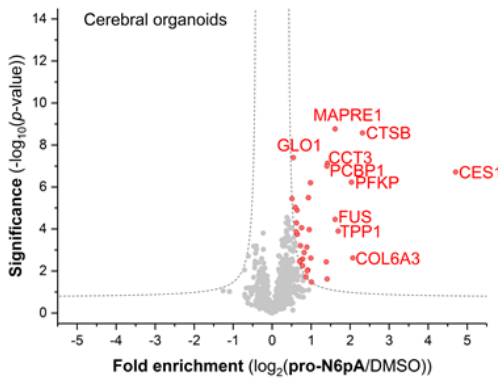
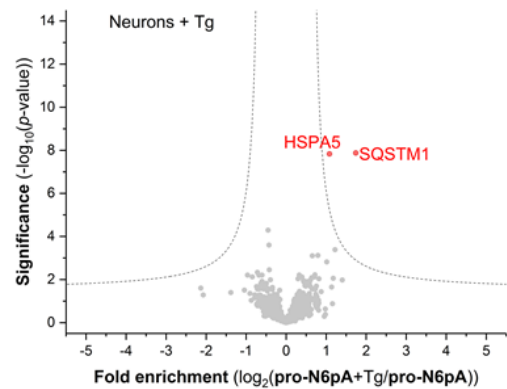
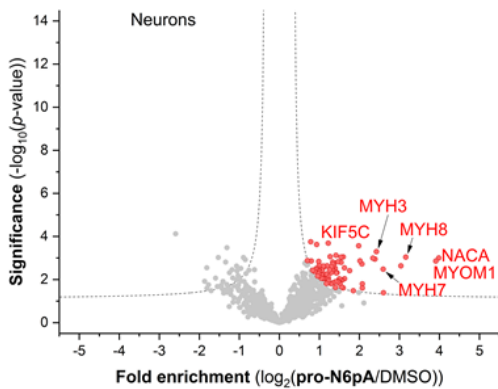
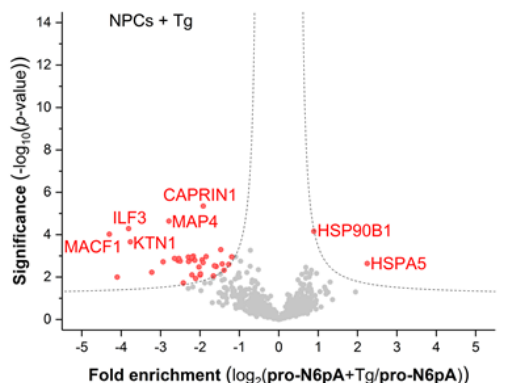
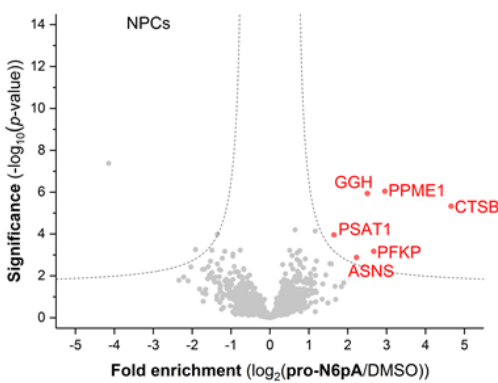
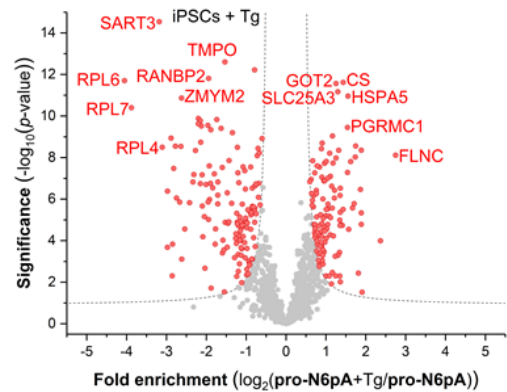
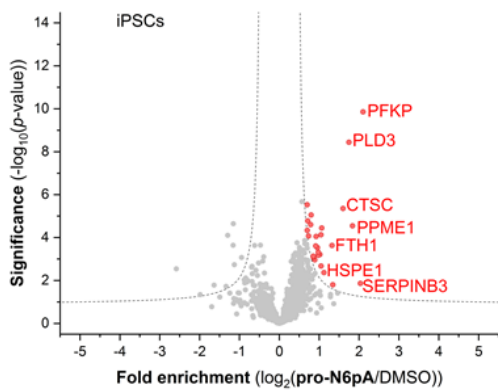


Figure S11 | Neurons show specific AMPylation of cytoskeletal and motor proteins. a, Volcano plot visualizations of fold-enrichment using pro-N6pA with or without Tg treatment (1 $\mu\text{g}/\text{mL}$, 24 h) compared to DMSO or pro-N6pA treated cells versus significance upon performing a two-sample *t*-test (FDR 0.05, s0 0.3; $n = 9$) from *in vitro* labelling of iPSCs, NPCs, neurons and COs.

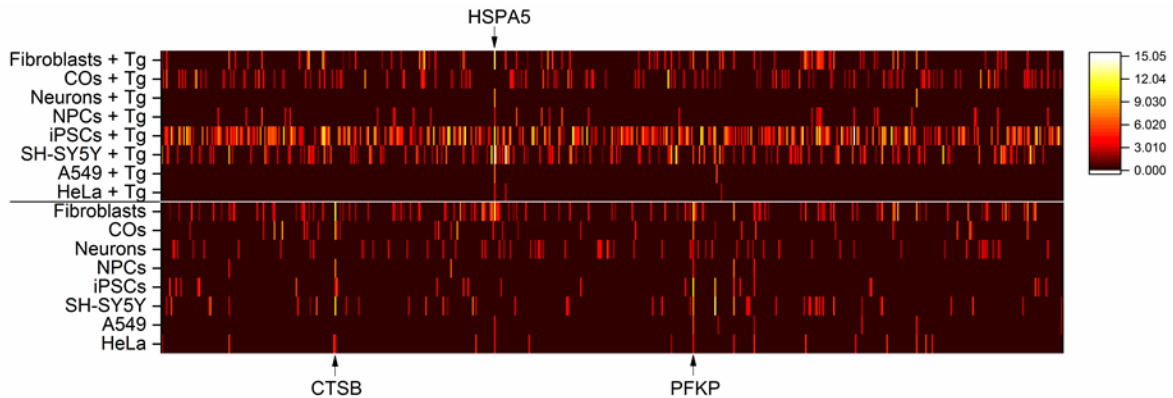


Figure S12 | Heat map summarising the data from all tested cell lines. a, Heatmap representation of enriched proteins identified in different cell types and COs; Colour represents the proteins' distance from zero of enriched proteins from respective volcano plot (FDR 0.05, s0 0.3; $n = 7 - 9$). Table S1, S9.

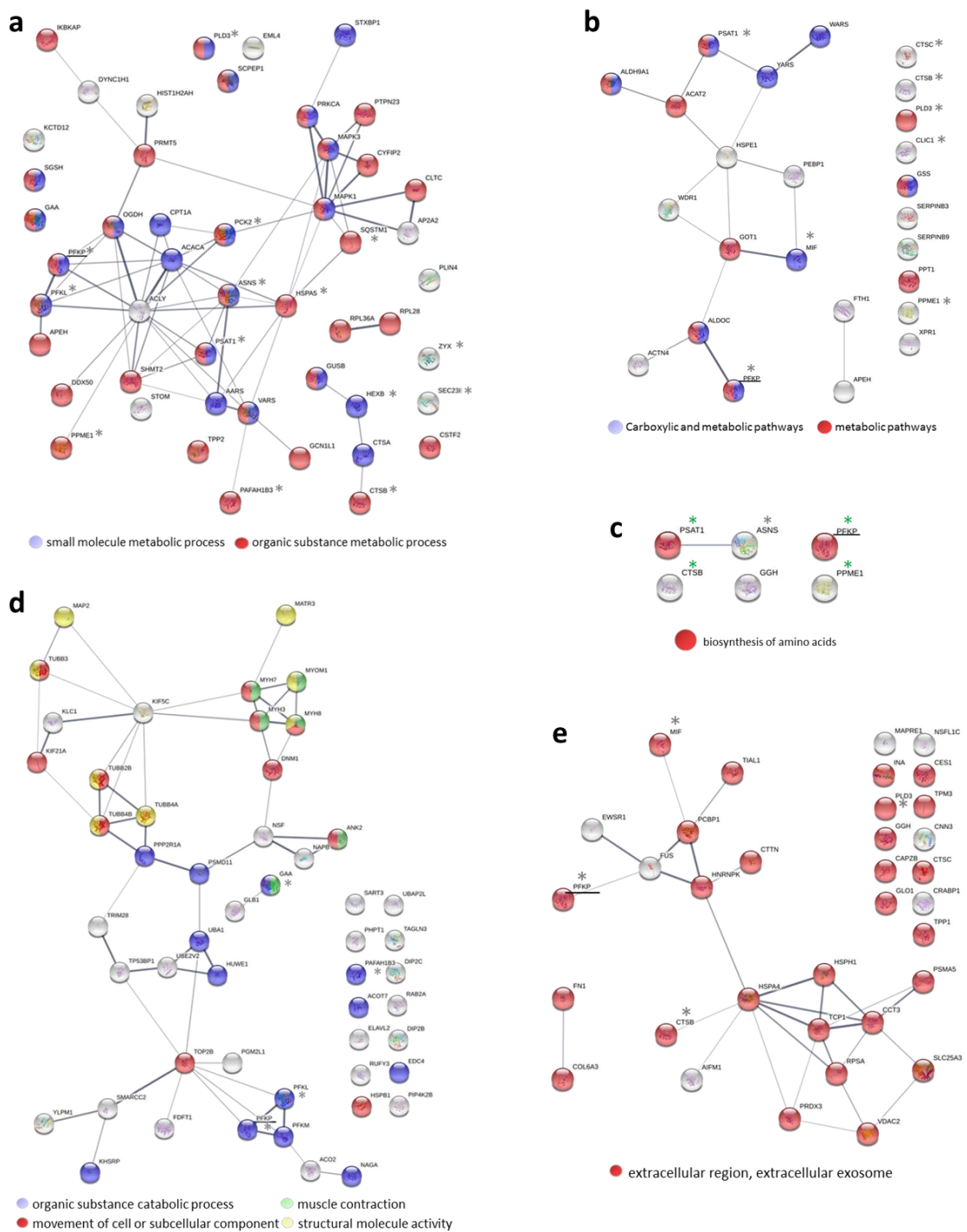


Figure S13 | Network and GO Term Analysis of AMPylated Proteins. Network analysis of AMPylated (and not ADP-ribosylated) hits in cancer lines (a), iPSCs (b), NPCs (c), neurons (d), and COs (e) with examples of enriched GO Terms highlighted in different colours and stars marking recurrent hits (PFKP underlined as only hit found in all analysed cell types; green stars for hits in NPCs already present in iPSCs). Network Analysis was performed in STRING.db. See also Table S10.

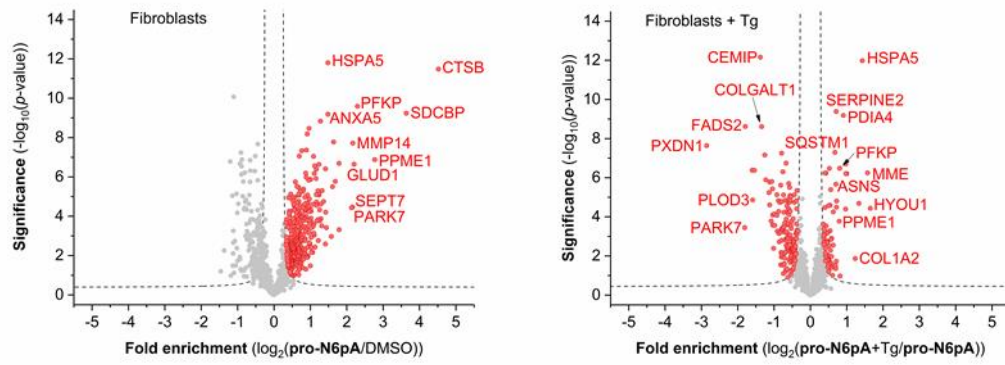


Figure S14 | Fibroblasts chemical proteomics. Volcano plot of fold-enrichment in fibroblasts by **pro-N6pA** labelling compared to DMSO or **pro-N6pA + Tg** versus significance upon two-sample *t*-test (FDR 0.05; s_0 0.3; $n = 9$).

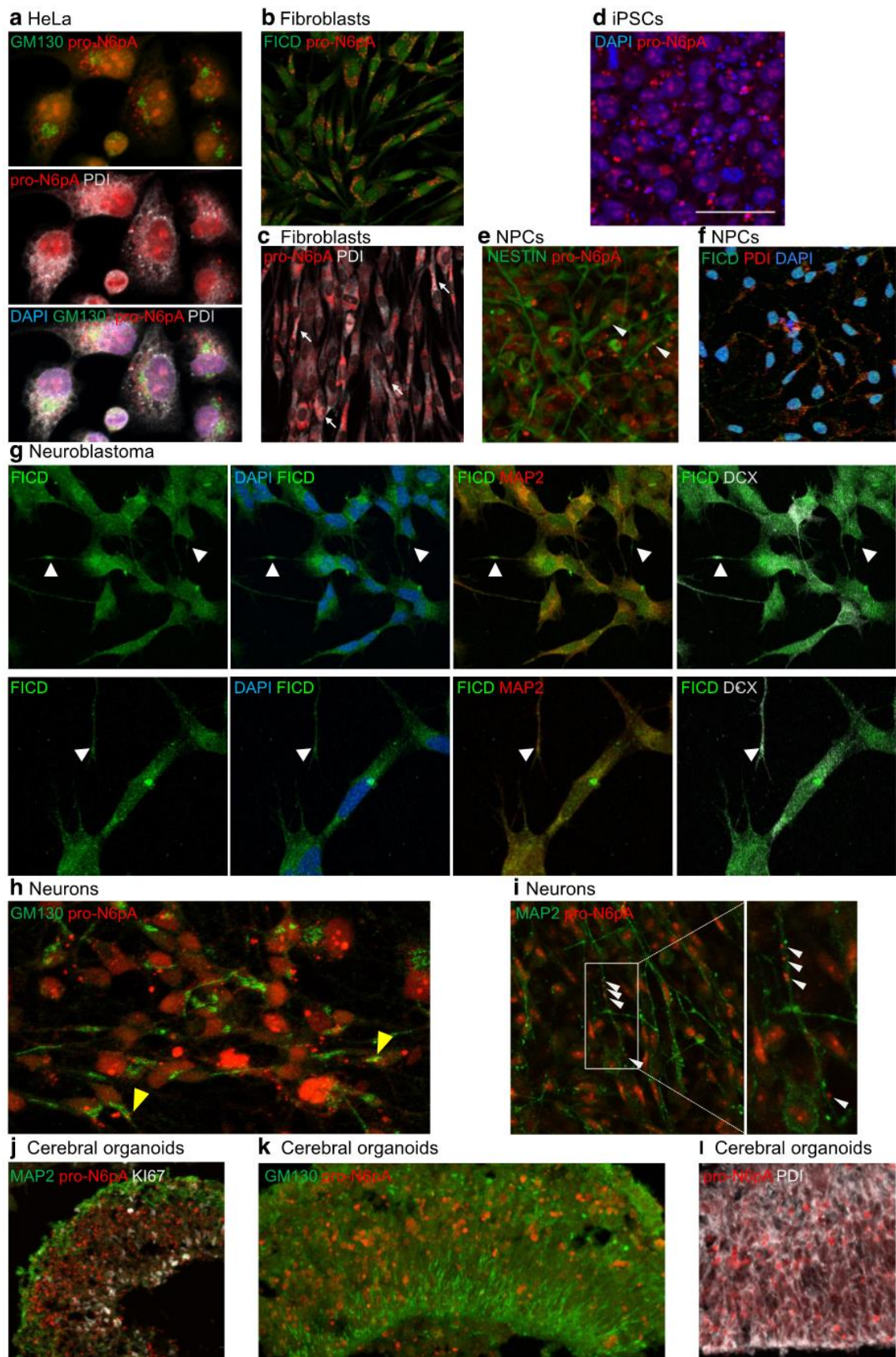


Figure S15 | Characterization of intracellular FICD and probe localisation in HeLa, fibroblasts, iPSCs, NPCs, neuroblastoma, neurons and cerebral organoids. **a**, AMPylated proteins (red) localise to the nucleus and rough ER (PDI, white) in HeLa, but not to cis-Golgi (GM130, green). **b**, In fibroblasts, FICD (green) is localised in the nucleus and cytoplasm, including processes. AMPylated proteins (red; b, c) accumulate in the perinuclear area, including ER (PDI, white, white arrows). **c**, with additional probe localisation to the processes, while the nucleus is free of probe signal. **d**, In iPSCs, AMPylated proteins form nuclear clusters similar to those in HeLa. **e**, Probe localises to NESTIN+ (green) processes (white arrowheads) in NPCs. **f**, FICD (green) is both in the nucleus and in processes of NPCs, partly colocalising with rough ER (PDI, red). **g**, IHC of FICD in SH-SY5Y neuroblastoma cells overlaid with DAPI, DCX and MAP2 markers reveals FICD localisation in cytoplasm and neurites (white arrowheads). **h**, Probe rarely localises to Golgi (GM130, green) in neurons (yellow arrowheads). **i**, Additional example showing the localisation of AMPylated proteins in MAP2+ (green) neuronal processes (white arrowheads). **j-l**, In cerebral organoids, AMPylated proteins accumulate basally, below and within the neuronal layer (MAP2+, green, j), with some degree of colocalisation with Golgi (GM130, green; k) and more with ER (PDI, white; l).

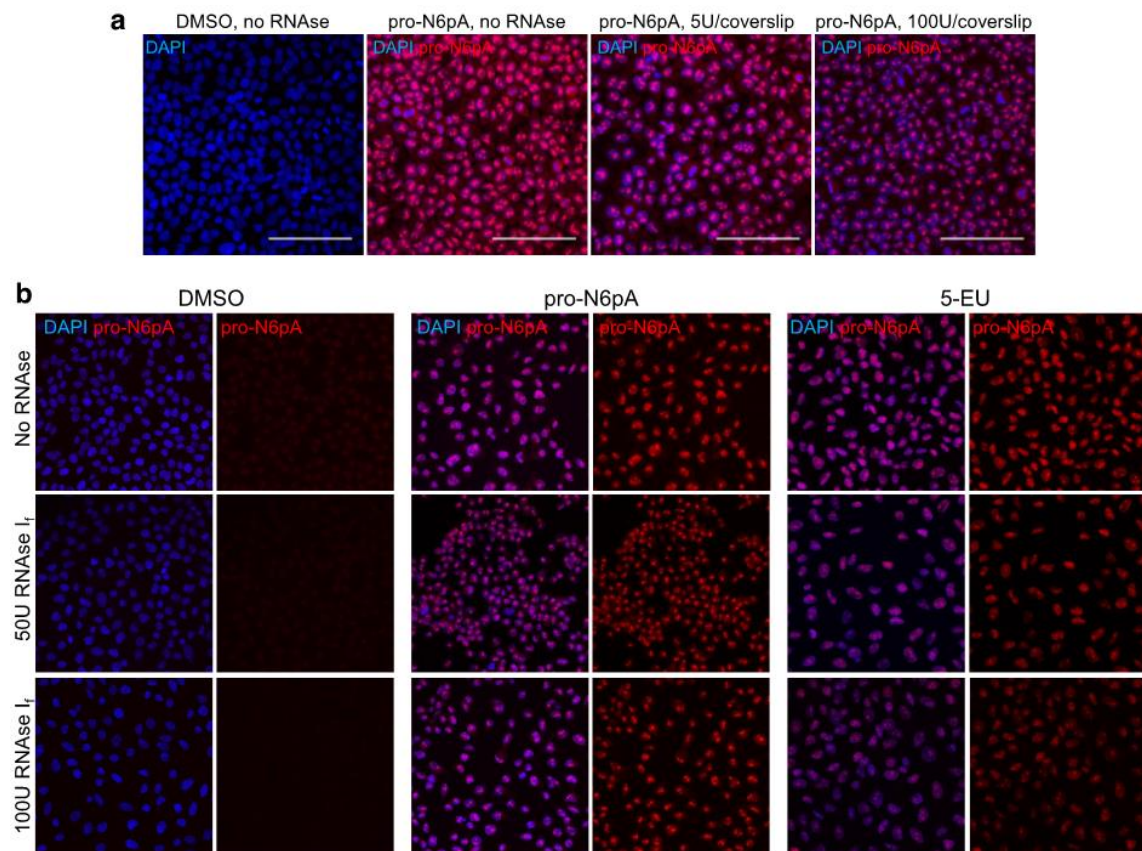


Figure S16 | pro-N6pA is specifically incorporated into proteins. RNase treatment of cells cultured with pro-N6pA or 5-EU demonstrates that pro-N6pA is only to a small

extent incorporated into RNAs. **a**, HeLa cells were grown on coverslips in 24-well plates and incubated with 100 μ M pro-N6pA for 16 h before PFA-fixation. Prior to addition of rhodamine-azide by click reaction, they were treated with different amounts of RNase I_f (5U or 100U of RNase per one well). The dotted pattern of localisation of the probe seems to be specific to the proteins it was incorporated in (Scalebar = 100 μ m). **b**, 5-EU signal strongly vanishes with RNase I_f treatment, whereas pro-N6pA staining does not.

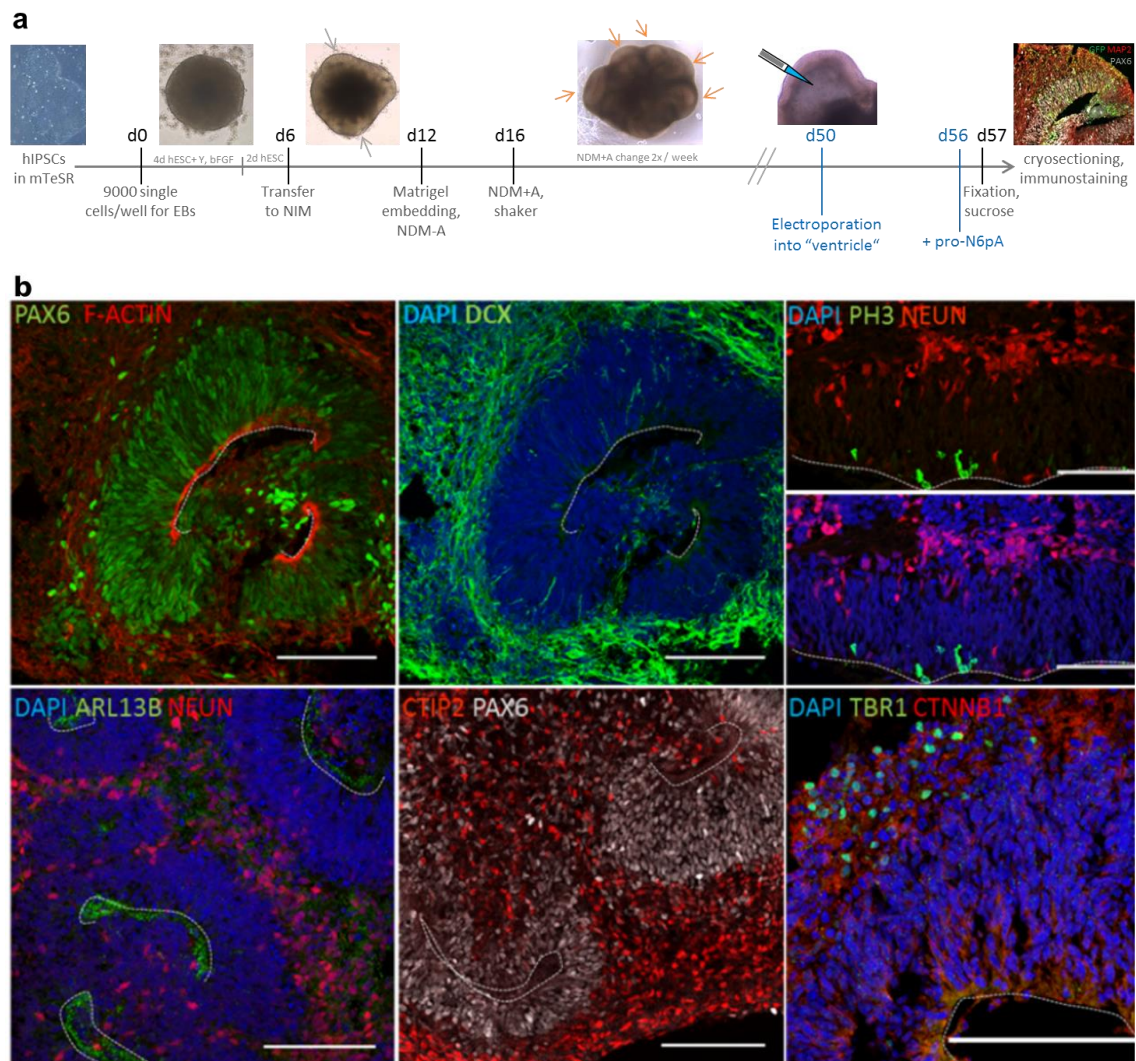


Figure S17 | Cerebral organoid preparation and characterization. **a**, Timeline for generation of cerebral organoids and their treatment with pro-N6pA (according to ref. 35), early neuroectoderm: grey arrows; expanded neuroepithelium: orange arrows; (EBs: embryoid bodies; hESC: low bFGF human embryonic stem cell medium; NIM: neural induction medium; Y: Rock inhibitor Y-27632; bFGF: basis fibroblast growth factor FGF-2; NDM: neural differentiation medium; +/- A: B27 supplement with or without vitamin A). **b**, Generation of cerebral organoids containing germinal zones comprised of different cell types that arise during dorsal cortical development. The progenitor zone, consisting of proliferative (e.g. PH3⁺ for M-phase) PAX6⁺ radial glia is

apically delineated by ARL13B⁺ primary cilia of radial glia, pointing into the ventricle-like lumen, and by apical junctions containing F-ACTIN and CTNNB1. Radial glia give rise to neuroblasts (DCX⁺) that migrate basally, where they differentiate fully to become NEUN⁺ neurons. The neocortical layers form in an inside-out manner with TBR1⁺ and CTIP2⁺ deep-layer projection neurons being generated first (Immunostainings of cerebral organoids cultured for 55-60 days, apical surface indicated by dotted line, Scalebar = 100 μ m).

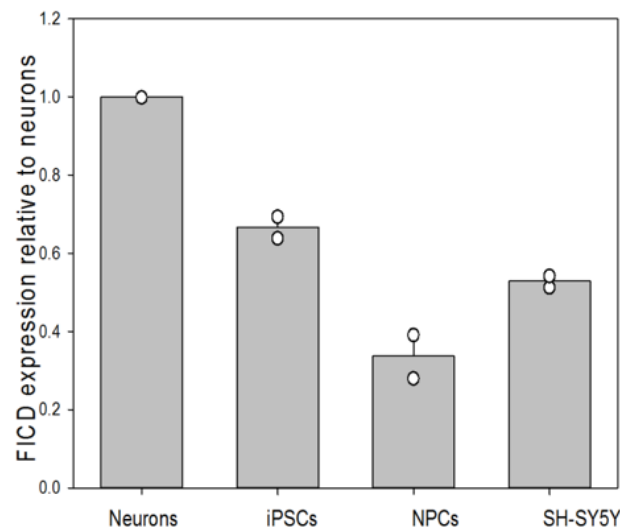


Figure S18 | Neurons exhibit higher expression levels of FICD. qPCR based analysis of FICD expression in different cell types confirms highest level in neurons. Error bars represent standard deviation.

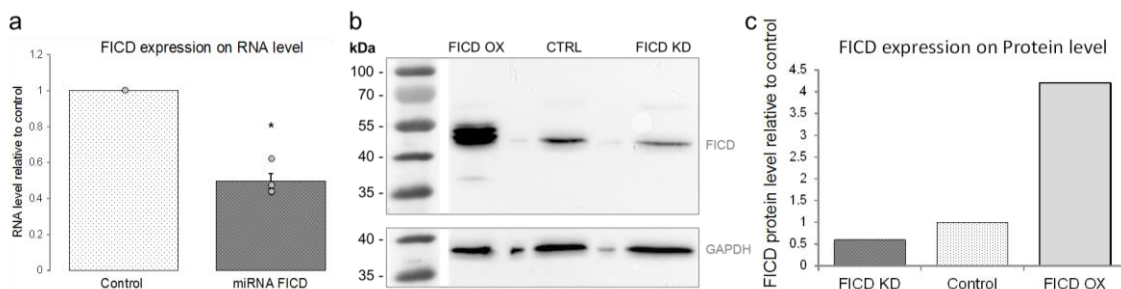


Figure S19 | Validation of miRNAs targeting FICD. miRNAs were generated following the BLOCK-iTTM Pol II miR RNAi Expression Vector Kits protocol by Invitrogen. Validation in HeLa via qPCR (a) and Westernblot (b, c) showed a knockdown efficiency to 50% of the control expression level both for RNA and protein (a: * $P=0.029$).

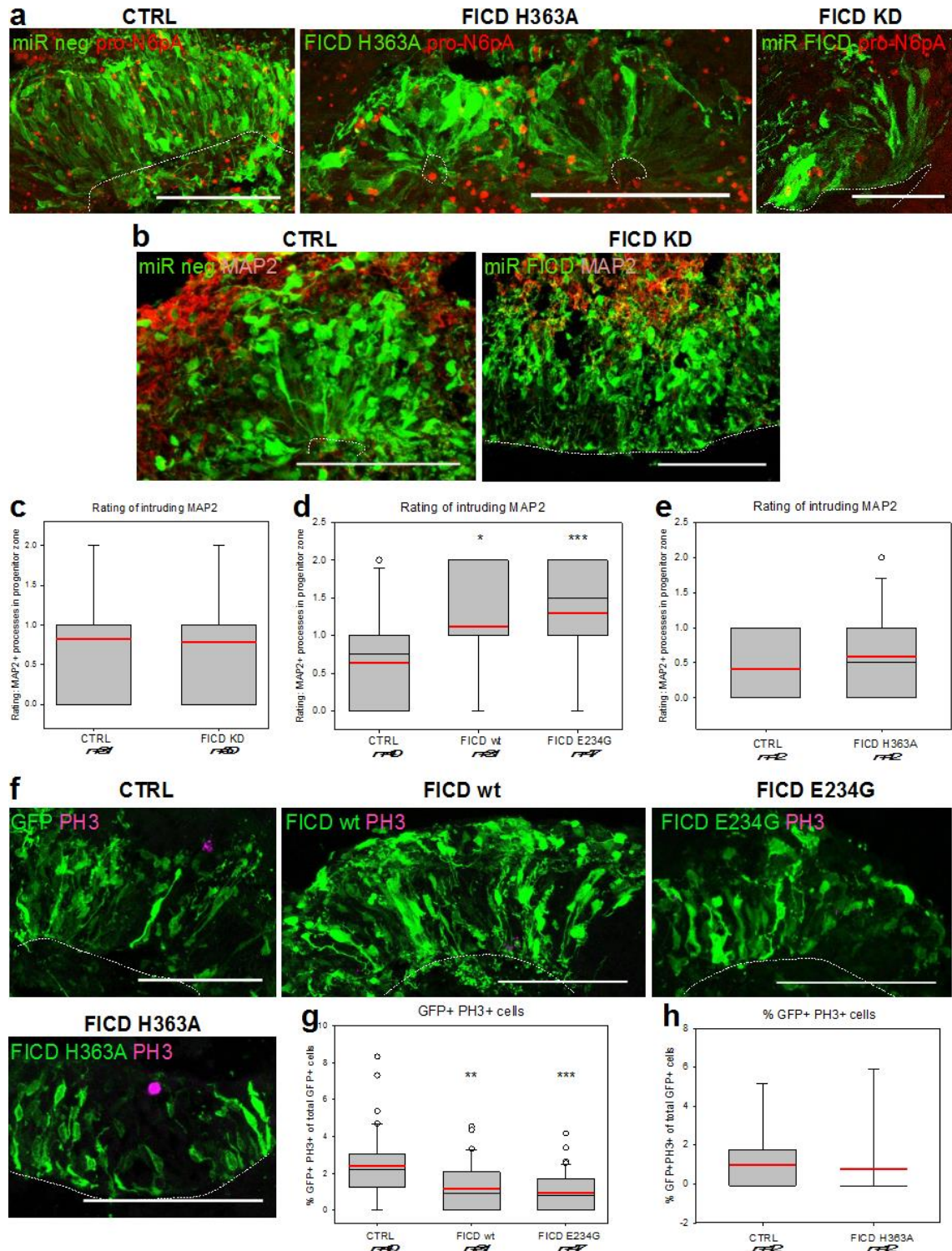


Figure S20 | pro-N6pA signal and MAP2+ processes in COs upon FICD KD, rating of MAP2 intrusion, and mitotic cells upon FICD OX. **a**, Click chemistry (red) in electroporated COs shows no difference in probe distribution in the case of catalytically inactive FICD H363A, but a decrease in signal upon FICD KD (transfected cells shown in green). **b**, IHC shows that MAP2+ neuronal processes (red) do not intrude the progenitor zone in COs upon FICD KD. **c**, **d**, **e**, Rating of intrusion of MAP2+ neuronal processes into the progenitor zone of COs electroporated with constructs for FICD KD

(**c**), FICD wt or E234G OX (**d**) or FICD H363A (**e**) shows increase upon FICD wt and E234G OX, but no change for KD and inactive FICD H363A. (Looking at IHC staining for MAP2, each ventricle was rated concerning the amount of neuronal processes inside the progenitor zone as 0 = none, 1 = few, 2 = many.) **f**, Example images of IHC for PH3+ mitotic cells (magenta) upon FICD wt/E234G/H363A OX in COs. **g**, **h**, Quantification of PH3+ electroporated (GFP+) cells in germinal zones of COs electroporated with FICD wt or E234G (**g**) or H363A (**h**) shows significant decrease when wt or activated FICD is overexpressed, but no change for H363A. Electroporated organoids were analysed at 50d+7. **a**, **b**, **f**, electroporated cells and their progeny are shown in green; Scalebar = 50 μ m; dotted line = apical surface. **c**, **d**, **e**, **g**, **h**, 1n = 1 electroporated germinal zone; box plot: mean (red line), median (black line), box represents 25th and 75th percentiles, whiskers extend to 10th and 90th percentiles, all outliers are shown; significance was tested using Kruskal-Wallis One-way ANOVA on Ranks and Dunn's Pairwise Multiple Comparison (* $P < 0.05$; ** $P < 0.01$; *** $P < 0.001$).

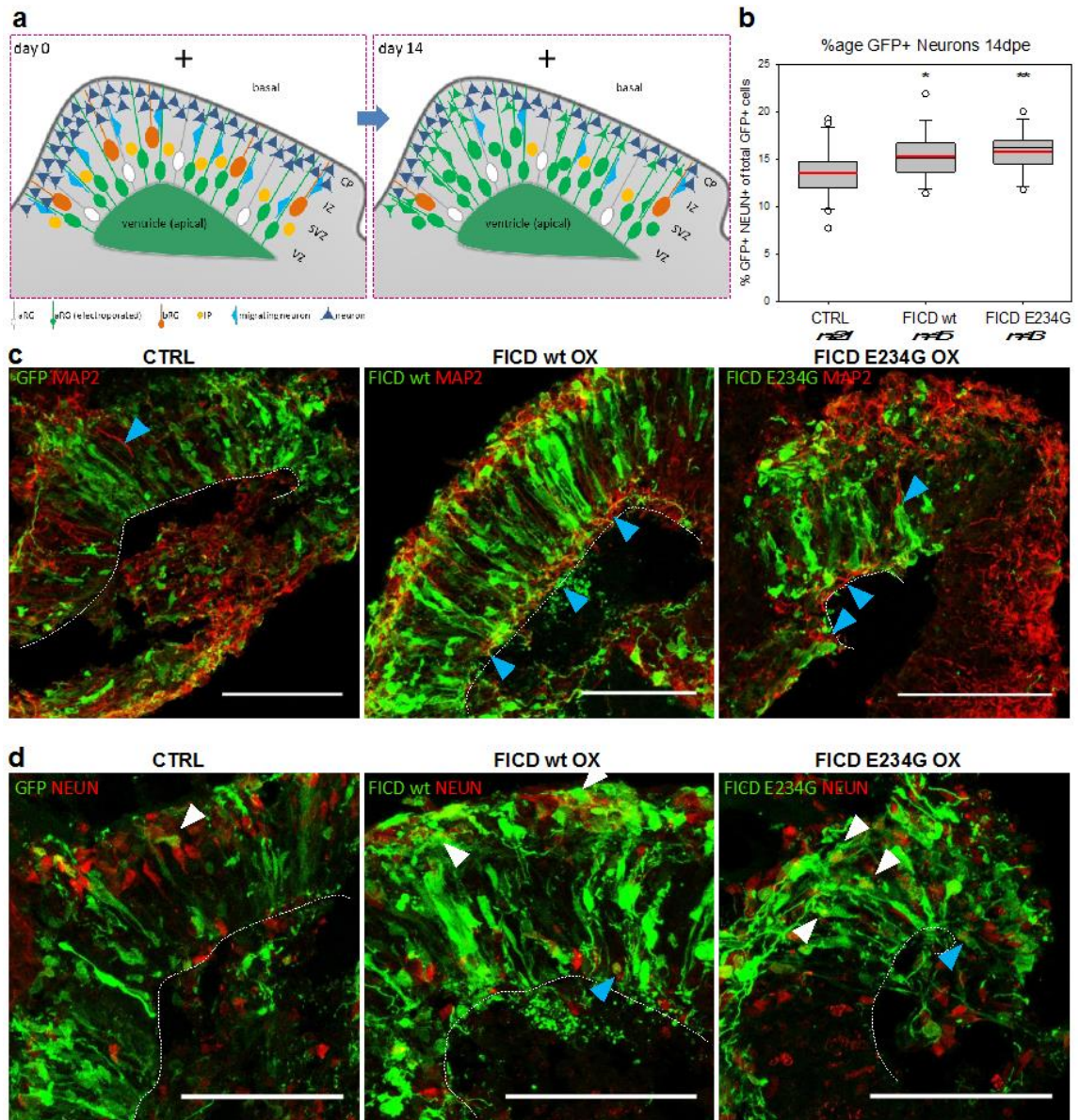


Figure S21 | Overexpression of FICD in radial glia accelerates neurogenesis. a, Scheme showing electroporated cells in CO germinal zone at day 0 and day 14: Over 14 days culture after electroporation, transfected (green) radial glia cells give rise to more differentiated cell types (green IPs, immature migrating neurons and differentiated neurons on day 14). **b,** Quantification of GFP⁺ neurons 14 dpe shows natural increase in GFP⁺ neurons over time (higher percentage than 7 dpe) and a significant increase in neuronal differentiation upon overexpression of FICD wt or E234G compared to control. **c,** Immunohistochemical (IHC) staining for electroporated cells (green) and neuronal dendrites (MAP2, red) shows neuronal processes in the progenitor zone. **d,** Immunostaining of electroporated cells (GFP, green) and nuclei of differentiated neurons (NEUN, red). **a, e, f,** Scalebar = 50 μ m, dotted line = apical surface; **b, d,** Box plots: mean (red line), median (black line); box represents 25th and 75th percentiles, whiskers extend to 10th and 90th percentiles, all outliers are shown; significance was tested using Kruskal-Wallis One-way ANOVA on Ranks and Dunn's Pairwise Multiple Comparison (* $P < 0.05$; ** $P < 0.01$; *** $P < 0.001$).

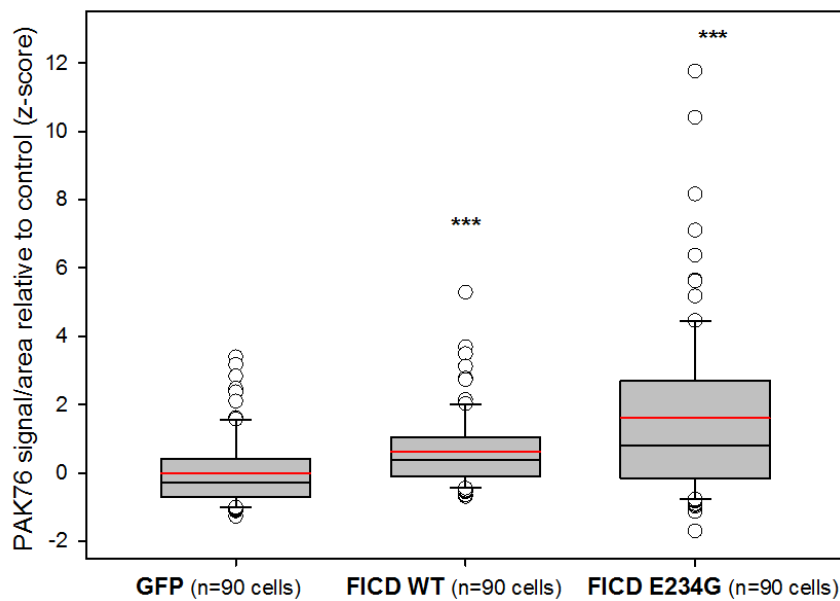


Figure S22 | pro-N6pA signal upon FICD overexpression in SH-SY5Y cells.

Transfection of SH-SY5Y cells with overexpression construct vs. GFP (3 μ g DNA per 1 Mio. cells), plating on 3 separate coverslips per condition. Pro-N6pA treatment for the last 16 h of culture. Fixation 48h post-transfection, followed by click-chemistry and nuclear counterstaining with DAPI. AMPylation signal was measured using Fiji, selecting transfected GFP+ cells and normalising to their area. Mean (red line), median (black line), box represents 25th and 75th percentiles, whiskers extend to 10th and 90th percentiles, all outliers are shown. One-tailed Student's *t*-test. ****P* < 0.001.

Cytotoxicity. Cytotoxicity of pro-N6pA and N6pA was measured by MTT assay. The IC_{50} of pro-N6pA is 300 μ M and IC_{50} of N6pA is above 1 mM. pro-N6pA low cytotoxicity makes it suitable for the use in high concentrations for cell treatment (Fig. S1).

Immunoprecipitation of PFKP and PPME1. In order to further corroborate the efficiency of incorporation of pro-N6pA probe as a protein PTM, the PFKP and PPME1 proteins identified in HeLa cells were immunoprecipitated from pro-N6pA treated HeLa cell lysates and after the click-chemistry with rhodamine-azide and SDS-PAGE, in-gel fluorescence was scanned showing strong labelling at 85 kDa (PFKP) and 42 kDa (PPME1) while no signal was observed in control sample (without antibody) (Fig. S3).

Cell type dependent changes in AMPylation during endoplasmic reticulum stress. Proteome profiling under endoplasmic reticulum (ER) stress was performed to determine whether modifications are altered as a result of HSPA5 upregulation, as previously reported for thapsigargin (Tg)-treated HEK293T cells³. Surprisingly, only a slight increase in AMPylated HSPA5 was observed in HeLa and A549 cells. Despite the moderate impact of ER stress on AMPylation in these cells, we found 145 dysregulated proteins in SH-SY5Y (Fig. S7 and S12). This further corroborated the role of AMPylation in neuronal-like cells. Further, Tg induced ER stress in iPSCs, NPCs and neurons results in very distinguished changes in AMPylation (Fig. S11), with strong response in iPSCs and only two proteins were influenced in neurons.

Site identifications on cathepsins in SH-SY5Y cells and cerebral organoids. In addition to the AMPylated serines identified on cathepsins in HeLa cells (Fig. 2 and Fig. S4) we confirmed the AMPylation on CTSB (S104 and S107) and CTSL (S137) also in SH-SY5Y cells (Fig. S5) and found two new sites on CTSV (S137) and CTSS (S135) in COs, the CTSB (S107) and CTSC (S254) AMPylation sites were confirmed (Fig. S5). See Table S4 for complete characterization. We used similarly to previous site identifications approach employing the TEV-cleavable linker (Fig. S4).

HSPA5 is AMPylated on T518 in U2OS cells. In addition to the identified AMPylation sites on cathepsins using biotin-TEV-cleavable linker we have searched by MaxQuant MS spectra measured in ref. 42. These were acquired to identify the protein ADP-ribosylation sites in bone osteosarcoma epithelial cells (U2OS) on Orbitrap Fusion using a combination of higher-energy collision-induced dissociation (HCD) and electron transfer dissociation (ETD) acquisition. The ETD ion source was triggered by adenine diagnostic peak (136.062 Da). Since both ADP-ribosylated and AMPylated peptides contain the adenine base this setup inherently leads to the raw MS spectres which include also an intact AMPylated peptides. The MaxQuant search for AMPylated peptides (+329.052 Da) revealed HSPA5 AMPylation on T518. This corroborates the findings by *Preissler et al.* (ref. 4 and 5).

ADP-ribosylation exclusion. MS raw files obtained from site identification experiments using the TEV-cleavable linker were searched for potential ADP-ribosylation (+906.2786) on the amino acids EDSTR. However, none of the identified ADP-ribosylation sites was included as a hit in the chemical-proteomic pull-down

experiments. A reference list of ADP-ribosylated proteins was adopted from ref. 23 and can be found in Table S3. To exclude experimental incorporation of the pro-N6pA probe into ADP-ribosylation we have pre-treated HeLa cells with poly(ADP-ribose)polymerases (PARP) inhibitors 4-aminobenzamide (4-ABA) or olaparib (Ola) before the pro-N6pA labelling, similarly reported in ref. 10. For both PARP inhibitors we have not observed any influence on labelling intensity or change in labelling pattern thus concluding that majority of the labelling yield from the AMPylation (Fig. S3).

Protein interaction and GO term analysis. In order to understand if AMPylation plays a role in the regulation of specific biological processes or pathways, network and GO term analysis was performed using STRING.db⁴³. Resulting networks for AMPylation targets identified in cancer cell lines and iPSCs have significantly more interactions than expected (cancer cell lines: PPI enrichment p -value $P = 0.00028$; iPSCs $P = 1.7 \cdot 10^{-5}$ and are significantly enriched for proteins with metabolic function (Table S1). In NPCs, there is only an enrichment for a single KEGG pathway (“biosynthesis of amino acids”) and the number of targets is very low. Their differentiation to neurons results in a state with a high number of AMPylated proteins again, which are different from those in pluripotent stem cells and NPCs and build a strongly interacting network (PPI enrichment p -value $P = 0.000124$). This network is, in addition to a new set of proteins involved in metabolic processes, significantly enriched for proteins with cytoskeletal and motor function (Table S10). Interestingly, these proteins are known to be important for neuronal development and function and have been shown to be modified by multiple other PTMs. Looking at AMPylated targets in iPSCs, NPCs and neurons, it becomes clear that during neuronal differentiation, cellular proteins undergo a process of complete remodelling of AMPylation that resembles an hourglass (Fig. 4b and Fig. S13): of many targets in iPSCs hardly any are left in NPCs and differentiation to mature neurons goes along with AMPylation of a big and unique group of new target proteins. As expected, additional targets were found in the more heterogeneous and complex COs. Thus, AMPylation of proteins known to play a role in neuronal development and function could represent one additional level of fine tuning and regulating cortical development.

Overexpression of wt FICD and E234G mutant in SH-SY5Y cells. In order to quantify AMPylation upon different levels of FICD, wt FICD and E234G mutant were overexpressed in SH-SY5Y neuroblastoma cells. We observed a significant increase of AMPylation in SH-SY5Y cells upon transfection with wt FICD and FICD E234G mutant proteins (Fig. S22).

(B) Structures and synthesis

General methods. Reagents and solvents were purchased from commercial suppliers (*Sigma-Aldrich Co. LLC*, *Thermo Fisher Scientific Inc.*, *Merck KGaA*, *TCI Europe GmbH*, *Fluorochem Ltd.* and *Alfa Aesar GmbH*) and used without further purification. HPLC-grade solvents or anhydrous solvents (max. 0.01 % water content, stored over molecular sieve under an argon atmosphere, *Sigma-Aldrich Co. LLC*) were used for all reactions. All experiments were monitored by analytical thin layer chromatography (TLC). TLC was performed on pre-coated silica gel plates (60 F-254, 0.25 mm, *Merck KGaA*) with detection by UV ($\lambda = 254$ and/or 366 nm) and/or by colouration using a potassium permanganate (KMnO_4) stain and subsequent heat treatment. Flash chromatography was performed on silica gel 60 (0.035 – 0.070 mm, mesh 60 Å, *Merck KGaA*) with the indicated eluent. ^1H , proton-decoupled ^{13}C and proton-decoupled ^{31}P NMR spectra were recorded on a *Bruker Avance III HD 300* (300 MHz), a *Bruker Avance I 360* (360 MHz) or a *Bruker Avance III HD* (500 MHz) at 298 K. Chemical shifts are reported in delta (δ) units in parts per million (ppm) relative to distinguished solvent signals. The following abbreviations are used for the assignment of the signals: s – singlet, d – doublet, t – triplet, q – quartet, m – multiplet. Coupling constants J are given in Hertz [Hz]. HR-MS spectra were recorded in the ESI mode on a Thermo Scientific LTQ-FT Ultra (FT-ICR-MS) coupled with an UltiMate 3000 HPLC system (*Thermo Fisher Scientific Inc.*).

4-(Prop-2-yn-1-ylamino)-7-(2',3'-O-isopropylidene- β -D-ribofuranosyl)-1H-purine.

After suspending N^6 -propargyl-adenosine (106 mg, 0.506 mmol) in acetone (13.0 mL), 2,2-dimethoxypropane (0.620 mL, 5.06 mmol) was added. Then *p*-toluenesulfonic acid monohydrate (1.61 g, 8.47 mmol) was added and the mixture was stirred for two hours at room temperature. The reaction was stopped with aqueous NaHCO_3 (24 mL), extracted with EtOAc (3x30 mL) and the combined organic phases were dried over Na_2SO_4 and filtered. The solvents were removed under reduced pressure and the residue was purified by column chromatography on silica gel (2% \rightarrow 5% MeOH in DCM) to give the product as a pale yellow solid (149 mg, 85 %). Spectral analysis was in good accordance with the literature⁴⁴.

Phenyl(benzyloxy-L-alaninyl)phosphorochloridate⁴⁵. Anhydrous triethylamine (264 μL , 1.896 mmol) was added dropwise to a stirred solution of the phenyl dichlorophosphate (142 μL , 0.948 mmol) and the L-alanine benzyl ester *p*-toluenesulfonate salt (333 mg, 0.948 mmol) in anhydrous DCM (4 mL) at -78 °C. Following the addition, the reaction mixture was stirred at room temperature for 1 h. After this period the solvent was removed under reduced pressure and the residue triturated with anhydrous THF. The precipitate was filtered and the solution was concentrated to give a colourless oil. The crude product was used for the next step.

4-(Prop-2-yn-1-ylamino)-7-(2',3'-O-isopropylidene- β -D-ribofuranosyl)-1H-purine 5'-O-[phenyl(benzyloxy-L-alaninyl)]phosphate. Protected N^6 -propargyl-adenosine (89 mg, 0.26 mmol) was dissolved in THF (3 ml). Solution of *t*BuMgCl in THF (1M, 0.52 ml, 0.52 mmol) was added drop-wise and the reaction mixture was stirred for 15 minutes.

Then solution of a phenyl(benzyloxy-L-alaninyl)phosphorochloridate (228 mg, 0.64 mmol) in THF (3 ml) was added and the reaction mixture was stirred overnight at room temperature. Reaction was quenched by saturated NH_4Cl solution (1 ml) and mixture was extracted with EtOAc and water. Organic layer was dried over Na_2SO_4 , filtered and evaporated under reduced pressure. Crude product was purified using column chromatography on silica gel (10% HEX in EtOAc) protected phosphoramidate (100 mg, 63 %) was obtained as colourless oil (mixture of diastereoisomers ~1:1). ^1H NMR (300 MHz, CDCl_3) δ 8.43 (s, 1H), 8.41 (s, 1H), 7.94 (s, 1H), 7.91 (s, 1H), 7.37 – 6.97 (m, 20H), 6.38 (bs, 2H), 6.09 (d, $J = 5.3$ Hz, 1H), 6.08 (d, $J = 5.3$ Hz, 1H), 5.37 (dd, $J = 6.3, 2.3$ Hz, 1H), 5.16 – 4.99 (m, 4H), 4.92 (dd, $J = 6.3, 2.6$ Hz, 1H), 4.53 – 4.38 (m, 6H), 4.37 – 4.19 (m, 4H), 4.09 – 3.91 (m, 4H), 2.35 – 2.17 (m, 2H), 1.62 – 1.57 (m, 6H), 1.41 – 1.16 (m, 12H). ^{13}C NMR (75 MHz, CDCl_3) δ 153.21, 139.71, 139.45, 129.74, 128.74, 128.58, 128.31, 128.25, 125.09, 125.03, 120.27, 120.21, 120.15, 120.08, 114.50, 91.62, 91.15, 85.70, 85.60, 84.37, 84.30, 81.57, 81.41, 80.15, 77.58, 77.36, 77.16, 76.74, 71.71, 71.65, 67.32, 66.48, 66.41, 50.51, 50.33, 27.26, 27.17, 25.47, 25.30, 21.08, 20.90. ^{31}P NMR (121 MHz, CDCl_3) δ 2.56, 2.45. MS (ESI⁺): m/z (%): 663.18 (100). $[\text{M} + \text{H}]^+$. HRMS (ESI⁺): m/z $[\text{M} + \text{H}]^+$ calculated for $\text{C}_{32}\text{H}_{36}\text{N}_6\text{O}_8\text{P}^+$: 663.23323; found 663.23219.

4-(Prop-2-yn-1-ylamino)-7-(β -D-ribofuranosyl)-1H-purine 5'-O-[phenyl(benzyloxy-L-alaninyl)]phosphate. Protected phosphoramidate (100 mg, 0.15 mmol) was dissolved in 90% aqueous TFA (2 ml) and stirred for 2 h at room temperature. Then the solvent was repeatedly co-evaporated with methanol under reduced pressure. Product was purified using column chromatography on silica gel (10% MeOH in DCM). Several co-evaporations with chloroform gave phosphoramidate PRO-N6PA (61 mg, 65 %) as a white solid (mixture of diastereoisomers ~1:1). ^1H NMR (500 MHz, MeOD) δ 8.26 (s, 2H), 8.20 (s, 1H), 8.17 (s, 1H), 7.32 – 7.20 (m, 14H), 7.19 – 7.10 (m, 6H), 6.00 (m, 2H), 5.11 – 4.99 (m, 4H), 4.63 – 4.57 (m, 2H), 4.40 – 4.31 (m, 8H), 4.31 – 4.23 (m, 2H), 4.22 – 4.18 (m, 2H), 2.58 (t, $J = 2.5$ Hz, 2H), 1.33 – 1.19 (m, 6H). ^{13}C NMR (126 MHz, MeOD) δ 173.42, 173.39, 173.22, 173.18, 152.47, 152.43, 150.66, 150.61, 139.46, 139.41, 135.82, 135.74, 129.35, 128.14, 127.87, 127.84, 124.78, 120.03, 119.99, 119.93, 119.63, 88.52, 82.95, 82.91, 82.88, 82.84, 79.75, 73.96, 70.86, 70.14, 70.02, 66.53, 66.51, 66.12, 66.08, 65.69, 65.65, 50.26, 50.14, 19.01, 18.96, 18.85, 18.79. ^{31}P NMR (121 MHz, MeOD) δ 3.89, 3.64. MS (ESI⁺): m/z (%): 623.25 (100) $[\text{M} + \text{H}]^+$. HRMS (ESI⁺): m/z $[\text{M} + \text{H}]^+$ calculated for $\text{C}_{29}\text{H}_{32}\text{N}_6\text{O}_8\text{P}^+$: 623.20193; found 623.20224.

(C) Biological methods

Metabolomics samples preparation. Samples were prepared according to protocol from Matano *et al.* with minor changes⁴⁶. Cells were seeded in 60 mm cell culture dishes (approx. 800,000 cells/dish) till 90% confluency. Media was removed, cells washed with 3 mL PBS and incubated with 8 mL media, supplemented with **pro-N6pA** in DMSO (100 μ M final conc.) or DMSO respectively. After the particular incubation times, cells were washed twice with 2 mL warm PBS and twice with 2 mL water (LC-MS grade, *Fisher Chemical*). Subsequently 4 mL of cold quenching solution (ACN:MeOH:H₂O 2:2:1 incl. 0.5M FA, -20°C) was added, cells detached by scraping and transferred to falcons. Washing and quenching of cells was completed in 1-2 min. Cell lysis was carried out by sonication (30s, Sonorex RK 100, *Badelin*) while cooling followed by incubation on ice (15 min) prior to snap-freezing in liquid nitrogen. Samples were freeze-dried until complete dryness and stored at -80°C until day of measurement. For MS-analysis dried samples were dissolved in 20 μ L water (LC-MS grade, *Fisher Chemical*), centrifuged (21000 x g, 10 min, 4°C) and transferred into LC-MS vials. A pooled sample was prepared from all samples for column equilibration

Metabolomics sample measurement and evaluation. Metabolic profiling and MS/MS analysis was carried out on an Ultimate 3000 RSLC system (*Thermo Scientific*) coupled to an LTQ Orbitrap XL mass spectrometer (*Thermo Scientific*). Chromatographic separation was performed using a SeQuant® ZIC®-pHILIC (250 x 2.1 mm, 5 μ m, 100 Å) (Merck Millipore) at 40 °C. Gradient elution was carried out with 5 mM NH₄OAc (LC-MS grade, *Fisher Chemical*) in 100% H₂O (LC-MS grade, *Fisher Chemical*) (A) and 5 mM NH₄OAc in 95% ACN (LC-MS grade, *Fisher Chemical*) (B). After 5 min pre-equilibration with 98% B, samples were eluted with a linear gradient from 98% to 53% B over 20 min at a flow rate of 250 μ L/min followed by a 9 min washing step with 5% B and re-equilibration with 98% B for 4 min. Mass spectrometric measurements were accomplished in HESI- mode (H-ESI-II probe, *Thermo Scientific*) with following source parameters: capillary voltage 4.5 kV, tube lens -110 V, vaporizer temperature 80 °C, sheath gas 30 l/h, aux gas 10 l/h, capillary voltage -60 V and capillary temperature 275 °C. Parent ions of interest (**N6pATP** m/z = 544.00) was isolated (Isolation width 0.5 m/z) at 60,000 resolution in the orbitrap in profile mode and subjected to collision-induced dissociation (normalized collision energy 45 V) in the SRM mode and most intense daughter ion (**N6pATP** m/z = 446.03) isolated (SIM width 5 m/z) at a resolution of 7,500 in the orbitrap and used for quantification. Retention time, exact mass and MS/MS spectra of quantified compound were matched to an authentic synthetic standard. Prior to measurement, 15 pooled quality control (QC) samples were injected to equilibrate the column. In order to take into account metabolic degradation over time, the sample order was randomized. Data were processed with Xcalibur 2.2 SP1.48 Quan Browser (*Thermo Scientific*) using the Genesis algorithm for peak detection and manual integration mode. Peak detection was carried out with the following track peak parameters: Genesis Peak Detection: Highest Peak, Minimum peak height (S/N) = 3.0. Intensities of the corresponding daughter ion was extracted

and plotted for each time point. (Experiments were carried out in two biological replicates).

Cytotoxicity assay. Human epitheloid cervix carcinoma cells (HeLa) cultivated in high glucose Dulbeccos's Modified Eagle's Medium supplemented with 10% (v/v) fetal bovine serum and 2 mM L-glutamine were seeded at a density of 5,000 cells per well (100 μ L of a solution of 50,000 cells/mL) in a transparent, flat-bottom 96-well plate. Cells were grown over night in a humidified atmosphere at 37 °C and 5% CO₂. The next day the medium was removed and replaced by fresh medium supplemented with 1000, 700, 500, 300, 200, 100 or 30 μ M pro-N6pA or N6pA or 1% (v/v) DMSO as a control. The cells were incubated for 24 h. To determine metabolic activity of the cells, 20 μ L of 3-(4,5-dimethyl-2-thiazolyl)-2,5-diphenyl-2H-tetrazolium bromide solution (MTT, 5 mg/mL in PBS) were added to each well. The cells were incubated for 4 h. The medium was completely removed and the formazan crystals were resuspended in 200 μ L DMSO and absorbance at 570 nm and at a reference wavelength of 630 nm was determined in an infinite F200 pro plate reader (*Tecan*). All data points were measured in triplicate. The data was normalized with respect to the DMSO control.

Protein concentration. Protein concentrations were determined by bicinchoninic acid assay (BCA, *Carl Roth GmbH + Co.*).

Probe treatment, click-chemistry and enrichment. Cells (6-cm dishes) were treated with the probes at 80-90% confluency. Culture medium was removed and the cells or COs were labelled in fresh media containing 100 μ M pro-N6pA or 100 μ M N6pA (both stocks 100mM in DMSO) for 16 h at 37 °C in cells incubator. Subsequent cell lysis was done in 1 mL ice cold lysis buffer (1% (v/v) NP40, 1% (w/v) sodium deoxycholate and 1 tablet protease inhibitor (cComplete™, Mini, EDTA-free protease inhibitor cocktail, *Roche*) in 10 mL PBS) while mechanically detached by scraping and subsequently transferred into an eppendorf tube or by ultrasonication at 40 % intensity for 10 s. Lysis was done for 30 min at 4 °C while rotating. Insoluble fraction was pelletized (10 min, 14,000 g, 4 °C) and protein concentration was determined by BCA. To 500 μ g (HeLa, A549, SH-SY5Y cells, COs and fibroblasts) or 250 μ g (iPSCs, NPCs, neurons) of a protein lysate in total volume of 970 μ L 0.2% (w/v) SDS in PBS 10 μ L 5-rhodmamine-azide (10 mM in DMSO, *Jena Bioscience*; in-gel analysis) or 10 μ L azide-PEG₃-biotin (10 mM in DMSO, *Jena Bioscience*; for MS samples), 10 μ L Tris(2-carboxyethyl)phosphine (TCEP) (53 mM in ddH₂O) and 1.2 μ L tris(benzyltriazolylmethyl)amine (TBTA) (83.5 mM in DMSO) were added. Samples were gently vortexed and the click reaction was initiated by the addition of 20 μ L CuSO₄ solution (50 mM in ddH₂O). The mixture was incubated at 25 °C for 1.5 h. Afterwards proteins were precipitated by addition of 4 mL acetone and incubation overnight at -20 °C. The protein pellet was harvested by centrifugation at 9,000 g for 15 min at 4 °C and washed twice with 1 mL of ice cold methanol. Proteins were reconstituted in 500 μ L 0.2% (w/v) SDS in PBS, the remaining not soluble particles were spun down at 9,000 g for 5 min and resulting supernatant was loaded onto the beads and incubated at 25 °C for 1.5 h while rotating. The 50 μ L of avidin-agarose beads (*Sigma-Aldrich*) were washed in advance thrice with 1 mL 0.2% (w/v) SDS in

PBS. Afterwards through the enrichment protocol, the beads were always spun at 400 g, 25 °C, for 2 min. Beads were subsequently washed thrice with 1 mL 0.2% (w/v) SDS in PBS, twice with 1 mL 6 M urea in ddH₂O and thrice with 1 mL PBS.

Endoplasmic reticulum stress induction. For induction of unfolded protein response, cells or COs were treated with 100µM pro-N6pA for 16 h, then the media was exchanged with fresh media containing 100µM pro-N6pA and 1 µg/mL thapsigargin (stock 10 mg/mL in DMSO) and incubated for 24 h.

4-aminobenzamide (4-ABA) and Olaparib (Ola) poly(ADP-ribose) polymerases inhibition. In HeLa (6-cm dishes) cells 2 h before addition of the pro-N6pA probe 4 µL of 10M 4-ABA or 2 µL 10mM Ola (both stock solutions in DMSO) were added to the 2 mL of the fresh culture media, after two hours 2 µL of 100mM pro-N6pA was added and incubated for 16 h. Subsequent cell lysis was done in 1 mL ice cold lysis buffer (1% (v/v) NP40, 1% (w/v) sodium deoxycholate and 1 tablet protease inhibitor (cOmplete™, Mini, EDTA-free protease inhibitor cocktail, Roche) in PBS) while mechanically detached by scraping and subsequently transferred into an eppendorf tube or by ultrasonication at 40 % intensity for 10 s. Lysis was done for 30 min at 4 °C while rotating. Insoluble fraction was pelletized (10 min, 14,000 g, 4 °C) and protein concentration was determined by BCA. To 200 µg of a protein lysate in total volume of 200 µL 0.2% (w/v) SDS in PBS 2 µL 5-rhodmamine-azide (10 mM in DMSO, Jena Bioscience; in-gel analysis) 2 µL Tris(2-carboxyethyl)phosphine (TCEP) (53 mM in ddH₂O) and 0.24 µL tris(benzyltriazolylmethyl)amine (TBTA) (83.5 mM in DMSO) were added. Samples were gently vortexed and the click reaction was initiated by the addition of 4 µL CuSO₄ solution (50 mM in ddH₂O). The mixture was incubated at 25 °C for 1.5 h. Afterwards proteins were precipitated by addition of 900 µl acetone and incubation 1 h at -20 °C. The protein pellet was harvested by centrifugation at 9,000 g for 15 min at 4 °C and washed once with 500 µl of ice cold methanol. Finally, it was dissolved in 50 µL of gel loading buffer (4% SDS, 20% glycerol, 10% 2-mercaptoethanol, 0.004% bromphenol blue in 125mM Tris-HCl, pH 6.8) and loaded on a 12.5% SDS-PAGE.

Chemical-proteomic samples preparation. Cells were treated with Olaparib and pro-N6pA probe in a same way as for in-gel analysis, but it was continued with click reaction with azide-PEG₃-biotin and continued with enrichment as described above.

In-gel analysis. Enriched rhodamine-tagged proteins were released from the beads with 50 µL of gel loading buffer (4% SDS, 20% glycerol, 10% 2-mercaptoethanol, 0.004% bromphenol blue in 125mM Tris-HCl, pH 6.8) and loaded on a 12.5% SDS-PAGE. After electrophoretic separation, fluorescently labelled proteins were visualized using a Fujifilm LAS-4000 equipped with a Fujifilm Fujinon VR43LMD3 lens and a 575DF20 filter (Fujifilm) operated in Cy3 fluorescence detection mode.

Chemical-proteomics. Enriched proteins were on beads digested in 200 µL digestion buffer (20 mM HEPES, pH 7.5, 7 M urea, 2 M thiourea). Proteins were reduced (0.2 µL 1 M DTT, 45 min, 25 °C) and alkylated (2 µL, 30 min, 25 °C, in the dark). The alkylation reaction was quenched by addition of 0.8 µL 1M DTT and incubation for 30 min at 25

°C. Proteins were pre-digested with 1 μ L LysC (*Wako*) at 25 °C for 4 h. 600 μ L 50 mM TEAB buffer was added and the proteins were digested overnight with 1.5 μ L sequencing grade trypsin (0.5 mg/mL, Promega) at 37 °C. The following day the beads were settled and the supernatant was acidified with 10 μ L formic acid to a pH of 2 – 3. Peptides were desalted and on-column dimethyl labelled using 50 mg SepPak C18 cartridges (*Waters Corp.*) on a vacuum manifold. The cartridges were equilibrated with 1 mL acetonitrile, 1 mL 80% acetonitrile and 3 mL 0.5% formic acid. The samples were loaded on the cartridges and subsequently washed with 5 mL 0.5% formic acid. Peptides were labelled with either 5 mL labelling buffer “light” (90 mM sodium phosphate, pH 7.5, 30 mM NaBH₃CN, 0.2% CH₂O) or 5 mL labelling buffer “heavy” (90 mM sodium phosphate, pH 7.5, 30 mM NaBD₃CN, 0.2% ¹³CDO). Cartridges were subsequently washed with 2 mL 0.5% formic acid. The peptides were eluted with two times 200 μ L 80% acetonitrile, 0.5% formic acid. DMSO and probe-treated samples were combined and dried by lyophilization. Peptides were reconstituted in 30 μ L 1% (v/v) formic acid, prepared for mass spectrometry by filtering through a membrane filter (Ultrafree-MC and –LC, Durapore PVDF-0.22 μ m, *Merck Millipore*) and transferred into mass vials. For label-free quantification (LFQ) samples were prepared as above without the use of labelling solutions “light” and “heavy” and subsequent washing with 3 mL 0.5% formic acid. Samples were not combined. Experiments were conducted in 7 to 12 replicates. Label switch was used for dimethyl-labelling samples.

Site identification using TEV-cleavable linker. HeLa, SH-SY5Y or COs lysates in total volume of 2 mL 0.2% (w/v) SDS in PBS were supplemented with 20 μ L azide-TEV-biotin (10 mM in DMSO, gift from B. F. Cravatt laboratory)¹¹, 20 μ L TCEP (53 mM in ddH₂O) and 2.5 μ L TBTA (83.5 mM in DMSO). Samples were gently vortexed and the click reaction was initiated by the addition of 40 μ L CuSO₄ solution (50 mM in ddH₂O). The mixture was incubated at 25 °C for 1.5 h. Afterwards, proteins were precipitated in 18 mL acetone at -20 °C overnight. Protein pellet washing, enrichment and on-beads trypsin digest was done as described above using 100 μ L of avidin-beads slurry and digestion buffer without the thiourea. After the overnight incubation with trypsin, the beads were transferred onto the membrane filter (Ultrafree-MC and –LC, Durapore PVDF-0.22 μ m, *Merck Millipore*) and spun down at 1,000 g for 1 min. The flow through was processed as described above for trypsin digest. Beads loaded on a membrane filter were washed twice with 50 μ L of ddH₂O, thrice with 600 μ L PBS and thrice with 600 μ L ddH₂O. Beads were resuspended in 150 μ L TEV buffer (141 μ L of ddH₂O, 7.5 μ L 20xTEV buffer supplied by manufacturer, 1.5 μ L of 100 μ M DTT) and transferred from the membrane filter into eppendorf tube. Beads were spun down at 400 g for 2 min and supernatant was removed. Beads were resuspended in 150 μ L of TEV buffer and incubated with agitation at 29 °C with 5 μ L of AcTEV protease (10 U/ μ L, *Invitrogen*) overnight. The suspension was transferred onto the membrane filter and spun down at 1,000 g for 1 min, beads were further washed twice with 50 μ L of ddH₂O. Flow through was collected and after addition of 4 μ L of formic acid it was desalted on stage tips (double C₁₈ layer, Empore disc-C18, 47MM, *Agilent Technologies*). Stage tips were equilibrated with 70 μ L acetonitrile, spun at 1,000 g for 2 min, then samples were loaded and spun at 1,000 g for 5 min. Stage tips were washed thrice with 70 μ L 0.5% formic acid and TEV cleaved proteins eluted with two

portions 30 μ L of 80% acetonitrile and 0.5% formic acid. Samples were combined and dried by lyophilization. Peptides were reconstituted in 30 μ L 1% (v/v) formic acid, prepared for mass spectrometry by filtering through a membrane filter (Ultrafree-MC and -LC, Durapore PVDF-0.22 μ m, *Merck Millipore*) and transferred into mass vials.

DSSO crosslinking. HeLa cells were cultivated in 15 cm dishes and transfected with pCMV-SPORT6 plasmid with FICD wt or FICD E234G with GGGGS sequence connected to 6 x HIS tag at C-terminus. Cells were supplemented with 15 mL fresh DMEM media and transfected using 8 μ L Lipofectamine®2000 (*Thermo Fisher Scientific*) and 16 μ g of the pCMV-SPORT6 respective plasmid in 2 mL of the Opti-MEM™ (*Gibco*™) media according to manufacturer protocol. Cells were incubated for 36 h then washed twice with 3 mL PBS, scraped into the 1 mL PBS containing 2 mM DSSO crosslinker (20 μ L of 100 mM DSSO stock in DMSO) and incubated at 37 °C for 1 h. Crosslinking reaction was stopped by addition of 0.5 mL 50 mM Tris pH 8.0. Cells were harvested at 600 rpm for 5 min and washed twice with 0.5 mL ice cold PBS and lysed in 1 mL ice cold lysis buffer (1% (v/v) NP40, 1% (w/v) sodium deoxycholate and 1 tablet protease inhibitor (cOmplete™, Mini, EDTA-free protease inhibitor cocktail, *Roche*) in 10 mL PBS). Lysis was done for 30 min at 4 °C while rotating. Insoluble fraction was pelletized (10 min, 14,000 g, 4 °C), supernatant was transferred to prewashed (3 x 1 mL of lysis buffer) Ni-NTA agarose (200 μ L of beads slurry, *QIAGEN*) and incubated at 4 °C for 2 h. The beads were spun down at 2,000 rpm and supernatant was removed, beads were resuspended in 600 μ L mL high salt wash buffer (25 mM Tris pH 8.0, 500 mM NaCl, 20 mM imidazol) and transferred on filter columns (Pierce® centrifuge columns), washed twice with 600 μ L mL wash buffer (25 mM Tris pH 8.0, 150 mM NaCl, 80 mM imidazol). Beads were resuspended in 600 μ L of PBS and transferred into 1.5 eppendorf tube, spin down at 2,000 rpm and supernatant was removed. Enriched proteins were digested as described above for chemical-proteomics experiments and identified using LC-MS/MS as described below.

Mass Spectrometry. MS analysis was either performed on an Orbitrap Fusion or an Q Exactive Plus instrument coupled to an Ultimate3000 Nano-HPLC via an electrospray easy source (all *Thermo Fisher Scientific*). Samples were loaded on a 2 cm PepMap RSLC C18 trap column (particles 3 μ m, 100A, inner diameter 75 μ m, *Thermo Fisher Scientific*) with 0.1% TFA and separated on a 50 cm PepMap RSLC C18 column (particles 2 μ m, 100A, inner diameter 75 μ m, *Thermo Fisher Scientific*) constantly heated at 50 °C. The gradient was run from 5-32% acetonitrile, 0.1% formic acid during a 152 min method (7 min 5%, 105 min to 22%, 10 min to 32%, 10 min to 90%, 10 min wash at 90%, 10 min equilibration at 5%) at a flow rate of 300 nL/min. For measurements of chemical-proteomic samples on the fusion instrument survey scans (m/z 300-1,500) were acquired in the orbitrap with a resolution of 120,000 at m/z 200 and the maximum injection time set to 50 ms (target value 2e5). Most intense ions of charge states 2-7 were selected for fragmentation with high-energy collisional dissociation at a collision energy of 30%. The instrument was operated in top speed mode and spectra acquired in the ion trap with the maximum injection time set to 50 ms (target value 1e4). The option to inject ions for all available parallelizable time was enabled. Dynamic exclusion of sequenced peptides was set to 60 s. Real-time mass

calibration was based on internally generated fluoranthene ions. Data were acquired using Xcalibur software version 3.0sp2 (*Thermo Fisher Scientific*).

Binding site identifications of AMPylated peptides were performed on the fusion instrument with slightly changed parameters. The scan range for survey scans in the orbitrap was changed to 300-1,700 with an AGC target value of 4e5. HCD fragmentation was performed at a collision energy of 27% and spectra first acquired in the ion trap with a maximum injection time of 30 ms and an AGC target value of 2e4. Peptides with targeted masses of m/z 501.28, 251.14 and 167.76 (adenine_TEV singly, doubly and triply charged), as well as m/z 615.31, 308.16 and 205.77 (adenosine_TEV singly, doubly and triply charged) were further selected for ETD fragmentation while highest charge states were prioritized. ETD fragmentation scans were acquired in the orbitrap with a resolution of 30,000, a maximum injection time of 1,000 and an AGC target value of 2e5.

For measurements of chemical-proteomic samples on the Q Exactive Plus instrument survey scans (m/z 300-1,500) were acquired in the orbitrap with a resolution of 70,000 at m/z 200 and the maximum injection time set to 80 ms (target value 3e6). Data dependent HCD fragmentation scans of the 12 most intense ions of the survey scans were acquired in the orbitrap at a resolution of 17,500, maximum injection time of 50 ms as well as minimum and maximum AGC targets of 5e3 and 5e4, respectively. The isolation window was set to 1.6 m/z. Unassigned and singly charged ions were excluded for measurement and the dynamic exclusion of peptides enabled for 60 s. The lock-mass ion 445.12002 from ambient air was used for real-time mass calibration on the Q Exactive Plus. Data were acquired using Xcalibur software version 3.1sp3 (*Thermo Fisher Scientific*).

Quick change point mutation. Quick change point mutation of FICD H363A was performed using following primers

5'-CCGTTGCCATCAATGAAAGGGGCGATGTAAACGAGTTTATAATG- 3'
and 5'-CATTATAAACTCGTTTACATCGCCCCTTTCATTGATGGCAACGG- 3'
and pCMV-SPORT6 with wt FICD as a template. PCR reaction mixture contained 5xPhusion buffer 10 µL, 10 mM dNTPs 1 µL, 10 µM each primer 0.75 µL, template 50 ng 1 µL, ddH₂O 32 µL, DMSO 4 µL and Phusion polymerase (*NEB*) 0.5 µL. PCR cycle (initial denaturation 98 °C, 3 min then 25 cycles of 95 °C 45 s, 65 °C 30 s, 72 °C 3 min; final elongation at 72 °C for 5 min). Template was digested using DpnI (8 µL of PCR mixture, 10xCutSmart buffer (*NEB*) 1 µL and DpnI (*NEB*) 1 µL) at 37 °C for 4 h. Resulting plasmid was amplified in *E. coli* XL1 blue. Identity of the isolated plasmid was verified by sequencing.

Cloning of FICD with C-terminal 6xhis tag. To construct the pCMV-SPORT6 plasmid containing FICD gene with C-terminal GGGGSHHHHHH tag. The FICD gene was extended in PCR using following primers

5'-GACTTACACTAGTCCAGATGCTCATACCAATGGCTTC- 3'
and
5'-
GTATCTACCCTCAGGACAGCCTTTGTCACTGAGGATTTCTAATGATGGTGGTGATG
GTGAGAGCCTCCACCCCGGGCTTCACAGGAAGC- 3'.

PCR reaction mixture contained 5xPhusion buffer 4 μ L, 10 mM dNTPs 0.4 μ L, 10 μ M each primer 1 μ L, template 50 ng 0.2 μ L, ddH₂O 13.2 μ L and Phusion polymerase (*NEB*) 0.2 μ L. PCR cycle (initial denaturation 98 °C, 1 min then 25 cycles of 98 °C 20 s, 72 °C 1 min; final elongation at 72 °C for 5 min). Next, PCR product was separated and isolated from the 1 % agarose gel by gel extraction and 30 μ L of it was digested in 10xCutSmart buffer (*NEB*), SpeI HF 1 μ L (*NEB*) and Bsu36I 1 μ L (*NEB*) supplied with 13 μ L ddH₂O at 37 °C for 1 h. The resulting mixture was separated on 1 % agarose gel and desired digested DNA fragment was extracted from a gel (Gel Extraction Kit, *OMEGA bio-tek*). Ligation into pCMV-SPORT6 plasmid was performed using 2xQuick ligase buffer (*NEB*) digested pCMV-SPORT6 empty plasmid 3.5 μ L (32 ng) and PCR product 6 μ L (19.2 ng) and Quick ligase 1 μ L (*NEB*) incubated at rt for 5 min and transformed into *E. coli* XI1 blue. Identity of the isolated plasmid was verified by sequencing.

ADP-ribosylation. The reference list of ADP-ribosylated proteins was taken from ref. 23. In total, it includes 484 proteins identified as ADP-ribosylated by PARP-1, PARP-2 or PARP-3 with known site of modification (Table S3). All presented heatmaps and summaries of AMPylated proteins are without the AMPylation-ADP-ribosylation overlapping proteins.

Immunoprecipitation-click-chemistry. HeLa cells were cultivated in 15 cm dishes and treated with 100 μ M pro-N6pA (13 μ L 100mM in DMSO) for 16 h as described above. Cells were washed twice with 3 mL ice cold PBS and lysed in 1mL ice cold IP lysis buffer (50mM Tris HCl, pH 8; 250mM NaCl; 1% NP-40, 5mM EDTA, with protease inhibitors) while mechanically detached by scraping. Lysis was done for 30 min at 4 °C while rotating. Insoluble fraction was pelletized (10 min, 14,000 g, 4 °C). Protein lysates (3.5 - 4 mg) from pro-N6pA or DMSO treated cells were incubated with 10 μ L of primary antibodies (anti-PFKP (rabbit) or anti-PPME1 (rabbit) both 1 mg/mL, *Bethyl laboratories Inc.*) at 4 °C with gentle agitation overnight. Beads were spun at 400 g, 4 °C for 2 min. Approximately 70 μ L Pierce Protein A/G agarose beads slurry (*Thermo Scientific*) was washed twice with 0.5 mL ice-cold IP lysis buffer, added to the lysates and incubated at 4 °C for 4 hours with gentle agitation. The beads were washed thrice with 0.5 mL of ice cold IP lysis buffer, then twice with ice cold IP wash buffer (50 mM Tris/HCl pH 8.5, 75 mM KCl) and finally resuspended in 97 μ L of PBS supplied with 1 μ L 5-rhodamine-azide (10 mM in DMSO, *Carl Roth GmbH + Co. KG*), 1 μ L TCEP (53 mM in ddH₂O) and 0.2 μ L TBTA (83.5 mM in DMSO). The click-reaction mixture was incubated at 25 °C for 1.5 h with agitation, supernatant was removed and 20 μ L of gel loading buffer was added to the beads slurry. Immunoprecipitated proteins were released from the beads into the gel loading buffer at 95 °C for 5 min and separated on 12.5% SDS PAGE. In-gel fluorescence was scanned as described above.

Immunoblot analysis. SDS-PAGE separated proteins were blotted on a methanol-activated PVDF membrane for 1 h at 22 V (blotting buffer: 48 mM Tris, 39 mM glycine, 0.0375% SDS, 20% methanol) using a Bio-Rad Trans-Blot SD semi-dry transfer cell setup. The membrane was then blocked in blocking buffer (5% milk powder in PBS with 0.5% Tween-20), washed and incubated with primary antibody (Supplementary

Table 11) (diluted 1:1,000 in blocking buffer) for 16 h at 4 °C. The membrane was washed thrice 10 min in 0.5% Tween-20 in PBS, and then incubated with secondary antibody (goat anti-rabbit IgG-HRP (Santa Cruz), diluted 1:10,000 in blocking buffer) at 25 °C for 1 h. The membrane was washed again with 0.5% Tween-20 in PBS and subsequently incubated in ECL (Bio-Rad) and imaged using a Fujifilm LAS-4000 equipped with a Fujifilm Fujinon VR43LMD3 lens and chemoluminescence detection mode.

Table S11 | Antibodies used in immunohistochemistry and immunoprecipitations

Antigen	Dilution	Vendor	Catalog #
AMPylated Tyrosine	1:1000	Merck	ABS184
ARL13B	1:200	Proteintech	17711-1-AP
CTIP2	1:500	Abcam	ab18465
Doublecortin (DCX)	1:2,000	Merck Millipore	ab2253
F-Actin (Phalloidin)	1:40	Thermo Fisher	A12381
FICD	1:100	Sigma	HPA021390
GFP	1:1,000	Aves Lab	GFP-1020
GM130	1:500	GeneTex	GTX130351
HSPA5	1:1,000	Abcam	ab21685
KI67	1:100	Dako	M7248
MAP2	1:500	Sigma Aldrich	M4403
NESTIN	1:200	Millipore	MAB5326
NEUN	1:500	Merck Millipore	MAB377
PAX6	1:500	Biolegend	PRB-278p
PDI	1:500	Abcam	ab2792
PFKP	1:100	Bethyl Lab. Inc.	A304-283A
PH3	1:500	Millipore	06-570
Phospho-TAU (Ser202, Thr205)	1:500	Thermo Fisher	MN1020
PPME1	1:100	Bethyl Lab. Inc.	A304-762A
TBR1	1:500	Abcam	ab31940
β-Catenin	1:500	BD Biosciences	610154

Transfection of SH-SY5Y cells by nucleofection. SH-SY5Y cells were grown to 80 % confluency, washed with PBS, dissociated to single cells with 0.05 % trypsin-EDTA and counted. Per construct, 1 mio. cells were resuspended in 100 µl nucleofection buffer (50 mM HEPES, 90 mM Na₃PO₄, 5 mM KCl, 0.15 mM CaCl₂) and 2 µg pCMV-

SPORT6 plasmid containing wt FICD or FICD E234G mutant (gift from A. Itzen, TUM) and 1 μ g of pCAG-IRES-GFP or 3 μ g of only pCAG-IRES-GFP (control) was added. The suspension was filled into an aluminium electrode cuvette and exposed to program G00.04 in an Amaxa II Nucleofector (Lonza). Sequentially, 30,000 cells/well were plated on coverslips in a 24-well-plate in triplicates. Transfected cells were cultured for 48 h before analysis by click-reaction with rhodamine-azide for quantification of AMPylation.

Probe staining of fixed cells. Cells and organoids were cultured with medium containing 100 μ M pro-N6pA or 1:1,000 dilution of DMSO for 16 h prior to fixation. PFA-fixed cells on coverslips and thawed, rehydrated organoid sections were permeabilized using 0.1 % Triton X100 in PBS for 5 min. Then they were incubated with click-chemistry staining mix (10 μ M rhodamine-azide, 1 mM CuSO₄, 10 mM freshly prepared sodium ascorbate in PBS) at rt for 2 h in the dark, followed by several washes with PBS⁴⁷. For nuclear counterstaining only, cells or sections were incubated with 0.1 μ g/mL DAPI in PBS for 15 min. For co-staining by immunohistochemistry, 10 min postfixation with 4 % PFA in PBS was performed after the click-reaction with rhodamine azide, followed by the immunohistochemistry protocol (see above).

qPCR of FICD mRNA levels. Cells were washed and scraped with cold PBS and the pellet was lysed in QIAzol® Lysis Reagent (#79306, Qiagen). RNA was extracted using RNA Clean & Concentrator Kit (#R1015, Zymo Research) and cDNA was synthesised from 1 μ g RNA each using SuperScript III reverse transcriptase (#18080-044, Thermo Fisher) with Oligo(dT)₁₂₋₁₈ primers (#18418012, Thermo Fisher) according to the manufacturer's protocol. Subsequently, qPCR was performed in triplicates on a LightCycler® 480 II (Roche) using the LightCycler® 480 SYBR Green I Master (#04707516001, Roche) with the following reaction mix: 1 μ L of each primer (5 μ M), SYBR Green I Master 5 μ L, H₂O 2 μ L and 1 μ L of cDNA. The primer sequences were the following for FICD: 5'-GCGGTTGGGGTTCTGAC- 3' and 5'-TGAAGCCATTGGTATGAGCA- 3' and for GAPDH: 5'-AATCCCATCACCATCTTCCAGGA- 3' and 5'-TGGACTCCACGACGTACTIONCAG- 3'. PCR cycle (initial denaturation 95 °C, 10 min then 45 cycles of 95 °C 10 s, 60 °C 10 s and 72 °C 10 s) with melting curve 95 °C to 65 °C with 15s per step. C_p values were determined from the second derivative maximum of the amplification curve and fold expression was calculated using the $\Delta\Delta C_p$ method.

Quantification of AMPylation upon FICD overexpression. The transfected and probe-treated cells were fixed with 4 % PFA, followed by click-reaction and counterstaining of GFP and of nuclei with DAPI as described above. Confocal images were taken at 3 positions per coverslip. For quantification of AMPylation, using Fiji, the outline of individual GFP⁺ cells were drawn and then the rhodamine signal was measured and normalised to cell size (area). Results are shown for $n = 90$ cells per condition, normalised to GFP⁺ control.

Reprogramming of fibroblasts to induced pluripotent stem cells (iPSCs). Human iPSCs were prepared by reprogramming newborn foreskin fibroblasts (CRL-2522,

ATCC). As feeders 2.5×10^5 NuFF3-RQ IRR human newborn foreskin fibroblasts (GSC-3404, GlobalStem) were seeded per well of a 6-well tissue culture dish with advanced MEM (12491015, Thermo Fisher Scientific) supplemented with 5% HyClone Fetal Bovine Serum (SV30160.03HI, GE Healthcare), 1% MEM NEAA and GlutaMAX (11140050; 35050061 Thermo Fisher Scientific). On day 1, a newborn foreskin fibroblast culture of 70-80% confluency was dissociated using 0.25% Trypsin-EDTA (25200056, Life Technologies), counted and seeded on the pre-plated NuFF3-RQ cells at two densities: 2×10^4 and 4×10^4 cells/well. On day 2, the medium was changed to Pluriton Reprogramming Medium (00-0070, Stemgent) supplemented with 500 ng/ml carrier-free B18R Recombinant Protein (03-0017, Stemgent). On days 3-18, a cocktail of modified mRNAs (mmRNAs) was transfected daily. For that, *OCT4*, *SOX2*, *LIN28A*, *CMYC*, and *KLF4* mmRNAs at a 3:1:1:1:1 stoichiometric ratio in Opti-MEM I Reduced Serum Medium (13778150, Thermo Fisher Scientific) in a total volume of 105 μ l was combined with a mix of 92 μ l Opti-MEM I Reduced Serum Medium and 13 μ l Lipofectamine RNAiMAX Transfection Reagent (31985062, Thermo Fisher Scientific) after an incubation at RT for 15 min. Cells were transfected for 4hrs, washed and fresh reprogramming medium supplemented with B18R was added to the cultures. The mmRNAs were provided by the RNA CORE unit of the Houston Methodist Hospital and contained the following modifications: 5-Methyl CTP, a 150 nt poly-A tail, ARCA cap and Pseudo-UTP. Already 5 days after the first transfection, initial morphological changes became apparent, and first induced pluripotent stem cell (iPSC) colonies appeared by day 12-15. On day 16, the medium was changed to STEMPRO hESC SFM (A1000701, Thermo Fisher Scientific) for five days. Afterwards, the iPSC colonies were harvested after 40min incubation at 37°C with 2mg/ml Collagenase Type IV (17104019, Thermo Fisher Scientific) solution in DMEM/F12 (31331093, Thermo Fisher Scientific). The iPSCs were plated on γ -irradiated mouse embryonic fibroblasts (MEFs) and grown in STEMPRO hESC SFM for 10 additional passages. Then the iPSCs were adapted to a feeder-free culture system, using mTeSR1 (05850, StemCell Technologies) and plates coated with LDEV-Free Geltrex (A1413302, Thermo Fisher Scientific).

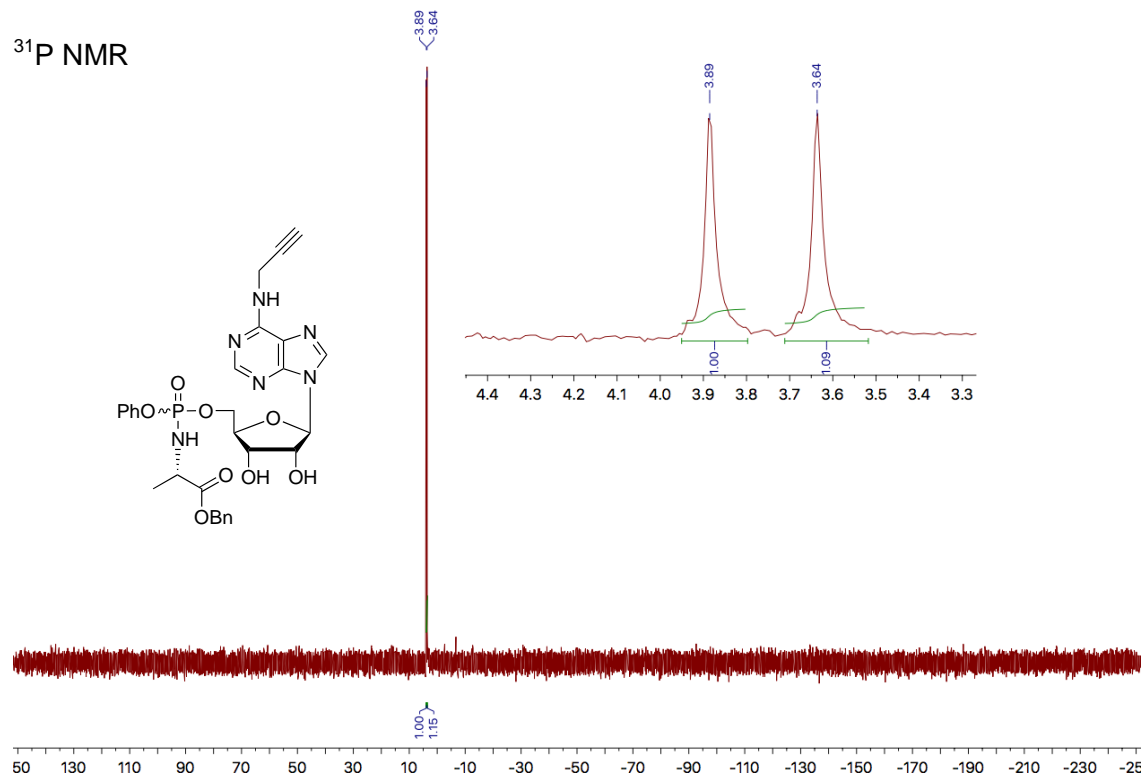
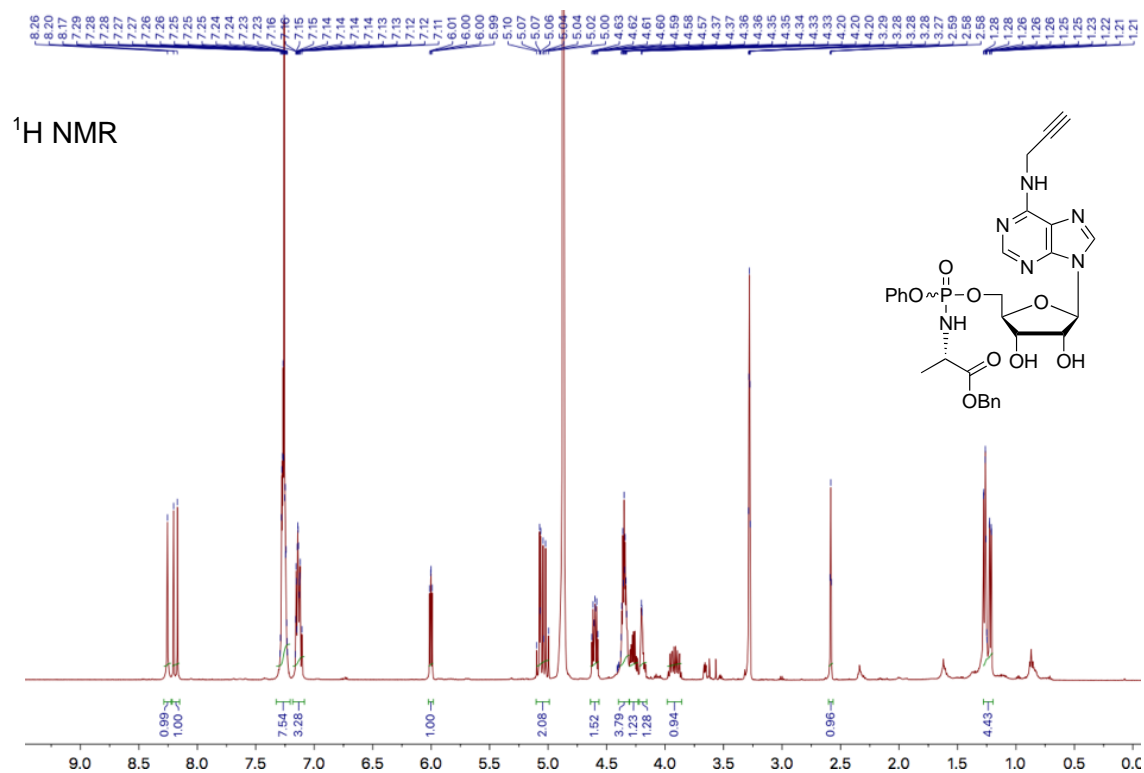
pro-N6pA / 5-Ethynyl-uridine and RNase treatment. In order to exclude incorporation of pro-N6pA into RNAs³⁴, HeLa cells were grown on coverslips in 24-well-plates. For the last 16 h of culture prior to PFA fixation, they were incubated with the pro-N6pA probe (100 μ M = 1:1,000 from stock), DMSO (1:1,000) or 5-ethynyl-uridine (5-EU; 1 mM = 1:100 from stock in H₂O) in medium. The fixed cells were treated with different amounts of RNase I_f prior to probe staining by click-chemistry (Figure S16): Cells were permeabilized applying 0.3 % Triton X100 in PBS for 5 min and the incubated with 5 to 100 U/coverslip RNase I_f (M0243S, New England Biolabs; unspecific RNase cleaving both purine and pyrimidine residues) in 1 x NEB3 buffer for 30 min or 2h at 37 °C (Figure S16) . NEB3 without RNase served as control. After the RNase treatment the fixed cells were washed thrice with PBS.

Rating of MAP2+ neuronal processes intruding the progenitor zone in COs. After IHC for GFP (to identify electroporated germinal zones) and MAP2 (for neuronal dendrites), combined with DAPI for nuclear counterstain, confocal laser scanning

images were acquired. A rating system was applied to categorize ventricles according to invading MAP2 processes within the progenitor zone, recognized in the DAPI channel as cell-dense zone lining the ventricle-like lumen, with the grading: 0 = no invading processes, 1 = few invading processes, 2 = a lot of invading processes. Every one ventricle was taken as n.

GO Term and Network Analysis using STRING.db. STRING database was used to perform Network and GO Term Analysis of AMPylated proteins identified in the different cell lines⁴³. Proteins overlapping with ADP-ribosylation were excluded. Network nodes represent the AMPylated proteins. Network edges represent protein-protein association. Thickness of the network edges was chosen to indicate edge confidence, meaning strength of the data support for the shown interaction. Minimum required interaction score was set to 0.400. The Table S10 contains all GO Term analyses for the cell types. Networks with example GO Terms highlighted are shown for iPSCs, NPCs, neurons, and COs in Figure S13. Functional enrichments in each network were considered significant in case of a false discovery rate $FDR < 0.05$.

(D) NMR spectra



(E) References

42. Bonfiglio, J. *et al.* Serine ADP-Ribosylation Depends on HPF1. *Mol Cell* **65**, 932–940 (2017).
43. Szklarczyk, D. *et al.* The STRING database in 2017: quality-controlled protein-protein association networks, made broadly accessible. *Nucleic acids research* **45**, D362–D368 (2017).
44. Ramadan, M., Bremner-Hay, N., Carlson, S., Comstock, L. Synthesis and evaluation of *N*⁶-substituted azide- and alkyne-bearing *N*-mustard analogs of S-adenosyl-l-methionine *Tetrahedron* **70**, 5291–5297 (2014).
45. Quintiliani, M. *et al.* Design, synthesis and biological evaluation of 2'-deoxy-2',2'-difluoro-5-halouridine phosphoramidate ProTides. *Bioorganic Medicinal Chem* **19**,4338–4345 (2011).
46. Martano, G. *et al.* Fast sampling method for mammalian cell metabolic analyses using liquid chromatography-mass spectrometry. *Nature protocols* **10**, 1–11 (2014).
47. Neef, A. & Luedtke, N. Dynamic metabolic labeling of DNA in vivo with arabinosyl nucleosides. *Proc. National. Acad. Sci.* **108**, 20404–20409 (2011).

Supplementary Tables

The Supplementary Tables of this study have been deposited online in the “Nextcloud Bio II” LMU data cloud.

4. *ECE2* REGULATES NEUROGENESIS AND NEURONAL MIGRATION DURING HUMAN CORTICAL DEVELOPMENT

4.1. CITATION

This manuscript is under revision in *EMBO Reports*.

Running title:

“ECE2 regulates Neurogenesis and Neuronal Migration during Human Cortical Development”

Isabel Y. Buchsbaum^{1,2}, Pavel Kielkowski³, Grazia Giorgio^{1,2}, Adam C. O’Neill⁴, Rossella di Giaimo^{1,5}, Christina Kyrousi¹, Shahryar Khattak⁶, Stephan A. Sieber³, Stephen P. Robertson⁴ and Silvia Cappello^{1,\$}

¹Max Planck Institute of Psychiatry, Munich, Germany

²Graduate School of Systemic Neurosciences, Ludwig-Maximilians-University Munich, Planegg, Germany

³Department of Chemistry, Chair of Organic Chemistry II, Center for Integrated Protein Science (CIPSM), Technische Universität München, Garching, Germany

⁴Department of Women's and Children's Health, University of Otago, Dunedin, New Zealand

⁵University of Naples Federico II Naples, Italy

⁶DFG Center for Regenerative Therapies, Dresden (CRTD), Technische Universität Dresden, Dresden, Germany

^{\$}Correspondence may be addressed to: silvia_cappello@psych.mpg.de

4.2. AUTHOR CONTRIBUTIONS

Conceptualization:	I.Y.B. and S.C.
Methodology:	I.Y.B., P.K., G.G., R.D.G., C.K., A.C.O.
Investigation:	C.K., A.C.O., R.D.G.
Resources:	S.K., S.P.R., and S.C.
Writing Original Draft:	I.Y.B.
Writing Review & Editing:	I.Y.B., A.O.N., S.P.R. and S.C.
Supervision:	S.C.
Funding Acquisition:	S.P.R. and S.C.

ECE2 regulates Neurogenesis and Neuronal Migration during Human Cortical Development

Isabel Y. Buchsbaum^{1,2}, Pavel Kielkowski³, Grazia Giorgio^{1,2}, Adam C. O'Neill⁴, Rossella di Giaimo^{1,5}, Christina Kyrousi¹, Shahryar Khattak⁶, Stephan A. Sieber³, Stephen P. Robertson⁴ and Silvia Cappello^{1,§}

¹Max Planck Institute of Psychiatry, Munich, Germany

²Graduate School of Systemic Neurosciences, Ludwig-Maximilians-University Munich, Planegg, Germany

³Department of Chemistry, Chair of Organic Chemistry II, Center for Integrated Protein Science (CIPSM), Technische Universität München, Garching, Germany

⁴Department of Women's and Children's Health, University of Otago, Dunedin, New Zealand

⁵University of Naples Federico II Naples, Italy

⁶DFG Center for Regenerative Therapies, Dresden (CRTD), Technische Universität Dresden, Dresden, Germany

[§]Correspondence may be addressed to: silvia_cappello@psych.mpg.de

Abstract

During embryonic development, the cerebral cortex is equipped with excitatory projection neurons that migrate in organized layers. Periventricular heterotopia (PH) is a rare disorder in which a subpopulation of new-born projection neurons fails to initiate their radial migration to the cortex, ultimately resulting in bands or nodules of grey matter lining the lateral ventricles. Although a number of genes have been implicated in its cause, currently they only satisfactorily explain the pathogenesis of the condition for 50% of patients. Complicating novel gene discovery is the extreme genetic heterogeneity recently described to underly its cause. Here, we study the neurodevelopmental role of *endothelin-converting-enzyme-2* (*ECE2*) for which two biallelic variants have been identified in two separate patients with PH. Our results show that manipulation of *ECE2* levels in human cerebral organoids and in the developing mouse cortex leads to ectopic localization of neural progenitors and neurons. We uncover the role of *ECE2* in neurogenesis and, mechanistically, we identify its involvement in the generation and secretion of extracellular matrix proteins in addition to cytoskeleton and adhesion.

Introduction

Mammalian neocortical development occurs through a highly complex series of processes including neural progenitor proliferation, migration of new-born neurons towards the future cortical plate (CP), and their terminal maturation and integration into neuronal networks [1,2]. Neuroepithelial cells give rise to apical radial glia (aRG), bipolar neural stem cells of the ventricular zone (VZ) spanning the thickness of the developing cortex, which can self-renew to increase the size of the neural progenitor cell (NPC) pool and differentiate to produce basal progenitors (BPs) - including intermediate progenitor cells (IPCs) and basal radial glia (bRG) - or neurons directly [1,3,4]. Newly generated projection neurons acquire a bipolar morphology and use the basal processes of RG as a scaffold for their radial migration towards the developing CP [5].

The widespread occurrence of malformations during cortical development underscores the importance of this tightly controlled process of events. One of the most common neuronal migration disorders (NMDs) is periventricular nodular heterotopia (PH) [6]. PH is characterized by a subset of cortical neurons failing to initiate radial migration towards the CP and instead remaining as nodules at the apical, ventricular surface where they were generated. Patients with PH can present with intellectual disability and epilepsy [3]. Bands or nodules of grey matter in contact with the normotopic overlying or further distant cortex may represent the source of epileptogenic activity in patient brains, although clinical presentations are highly heterogeneous [7,8].

Known molecular causes of the failure of neurons to migrate include an intrinsic disruption in the cytoskeleton of neurons (cell-autonomous mechanism), or a disruption in the RG scaffold that they use for their radial migration (non-cell-autonomous mechanism) [9-13]. Until recently, variants in only a handful of genes have been shown to cause PH. These include X-linked *FLNA* [14-17] as the most frequent cause, rare biallelic variants in *ARFGEF2* [15,18-22], *MCPH1* [23], *FAT4* [10,13,24], *DCHS1* [10,13], and *INTS8* [25] as cause for recessive forms of PH. *De novo* or inherited variants in *NEDD4L* [26] or *MAP1B* [27] also cause heterozygous forms of the disorder. Recently, high throughput analysis of patients with PH has revealed extreme genetic heterogeneity including single nucleotide and copy number variants [27-39]. Functional analyses have delivered supportive evidence for the potential for further candidate genes to be causative, with some of them implicating a role for bRG cell dysfunction in its pathogenesis [29].

In this study, we combined human induced pluripotent stem cell (iPSC)-based 2D and 3D *in vitro* models [31,32] with acute *in vivo* manipulation of gene expression in the developing mouse cortex [33] to characterize the role of endothelin-converting-enzyme-2 (*ECE2*) in cortical development, for which two patients with PH have been identified with rare biallelic variants [27]. The applicability of cerebral organoids (COs) [32] to model different aspects of PH and explore the role of novel candidate causative genes in human cortical development has been shown in several recent studies [13,28,29]. We identified a role for *ECE2* both in RG polarity and morphology, as well as in neuronal migration and differentiation. Proteome analysis of genome-engineered *ECE2* knockout (KO) iPSC-derived cerebral organoids revealed an additional function in the production and secretion of components of the extracellular matrix (ECM) and additionally suggest an involvement of *ECE2* in protein phosphorylation.

Results and Discussion

Identification of ECE2 as candidate gene for periventricular heterotopia (PH)

Recent trio-based exome sequencing studies have indicated considerable genetic heterogeneity underlying PH, complicating the identification of causative genes given the large mutational landscape [27]. To aid novel disease gene identification we sought to functionally complement such large-scale sequencing efforts with evidence obtained from both *in vivo* and *in vitro* model systems. Using data obtained from a recent study in which 202 individuals with PH were subject to whole exome sequencing using a trio based strategy, we designed functional experiments for genes within this cohort with rare (minor allele frequency MAF<0.005) biallelic variants identified in two or more individual patients. Applying these criteria on this dataset, we identified three candidate genes – *ECE2*, *GPR98* and *PRPN13* (**Table EV1**). As a further filter, we limited our analysis to

genes whose biallelic variants were assigned as potentially deleterious by any one of four *in silico* prediction programs (Materials and Methods). Under this framework, only one gene – *ECE2* – remained.

ECE2, encoding for endothelin-converting-enzyme-2 [27], is a metallopeptidase that has previously been associated with non-classical production of neuropeptides [34,35], removal of intracellular amyloid- β in Alzheimer's disease [36,37], and its knockout in mouse leads to deficits in spatial learning and memory acquisition [38]. The function of this gene in the developing cortex, however, has not been described. The two patients with PH had biallelic missense variants in this gene that were *in silico* predicted to be deleterious. Patient 1 (see example MRI images in **Figure 1A**) has two variants in *ECE2*, each inherited from a separate parent (c.655C>G, p.Arg219Gly; and c.2253, p.Arg752Trp; RefSeq [NM_001037324.2](#)). Patient 2 is homozygous for a missense variant in this locus (c.2239T>A, p.Ser747Thr; RefSeq [NM_001037324.2](#)) (**Table EV1**).

***ECE2* is enriched in human neurons**

In order to verify that *ECE2* is expressed in human iPSCs-derived models, we started with characterization of *ECE2* expression in these model systems and we detected higher *ECE2* expression in neurons compared to NPCs using qRT-PCR (**Figure 1B**). This was confirmed by the online database libd (<http://stemcell.libd.org/scb/>) [39], containing publically available RNA sequencing data from different stages of neuronal differentiation from 13 iPSC lines to neurons (**Figure 1C**). Additionally, *in situ* hybridisation (ISH) for *ECE2*, performed in 50 days old COs, confirmed higher levels in the cortical plate-like zone (CP') than in the ventricular-like zone (VZ') (**Figure 1D**). Immunohistochemical (IHC) analysis for *ECE2* also demonstrated higher levels in the CP' (colocalising with MAP2+ neurons) than in phospho-VIMENTIN+ (pVIM+) RG located in the VZ' of COs, although an enrichment at the apical surface was also evident (**Figure 1E**). Human iPSC-derived *in vitro* model systems are thus suitable tools to manipulate and study the role of *ECE2* in the developing cortex.

Knockdown of ECE2 leads to accumulation of neurons in the VZ of COs

ECE2 was enriched within neurons, thus to unravel the potential function of this protein in these cells we performed acute knockdown (KD) of *ECE2* in human COs. To this end, miRNAs targeting the peptidase were injected into the ventricle-like lumen of 50 days old COs prior to electroporation (**Figure 1F**). GFP+ transfected aRGs and their progeny were analysed 7 days post electroporation (7dpe). At this stage, due to the organisation of COs into separated zones containing progenitors and neurons, changes in morphology, cell fate and migration can be analysed at once. Interestingly, a significant increase in differentiated NEUN+ neurons were ectopically located within the VZ' after *ECE2* KD compared to control, mimicking the neuroanatomical anomalies observed in patients with PH (**Figures 1G-I**). Interestingly, most ectopically located neurons were not electroporated (NEUN+GFP-), but they were localised in close proximity of transfected aRGs, suggesting a non-cell-autonomous function of *ECE2* in neuronal migration. These electroporated aRGs had often lost their attachment to the apical surface (arrows in **Figure 1H**), hinting at a defect in aRG morphology and consequent delamination upon *ECE2* KD. This morphological change of transfected aRGs is already visible 4 dpe upon *ECE2* KD in COs (**Figure EV1C**) and suggests a role of *ECE2* in aRG and adherens junction integrity as suggested from its enrichment at the apical surface.

Inhibition of ECE2 activity changes the dynamics of neuronal migration in vitro

To assess if the enzymatic function of ECE2 is also directly involved in neuronal migration, timelapse imaging of young migrating neurons was performed upon inhibition of ECE2 activity. To this end, NPCs were cultured under differentiating conditions in the presence or absence of Phosphoramidon (Phos) (scheme in **Figure 1J**). This compound was shown to inhibit the function of ECE2 at low concentrations of 1 μ M [40]. Young neurons cultured in the presence or absence of Phos were imaged over 17 hours with several parameters, such as speed of migration, resting timepoints and tortuosity being analysed (**Figure 1K**). After inhibition of ECE2 activity, neurons migrated significantly more slowly, rested more often and migrated in a more tortuous path compared to control neurons. Thus, the activity of ECE2 is required for normal neuronal dynamics, suggesting an additional cell-autonomous function of ECE2 directly in neuronal migration. Taken together, this data supports a role of *ECE2* in the developing human brain.

Acute KD of Ece2 in the developing mouse cortex leads to ectopic rosettes and nodules

In order to reveal the role of *Ece2* in the developing cerebral cortex *in vivo*, acute KD of this gene's expression was performed by *in utero* electroporation (IUE) of miRNAs targeting *Ece2* in the ventricles of the developing telencephalon of mice at embryonic day 13 (E13). Brains were then analysed 1 dpe (E14) and 3 dpe (E16).

The distribution of the GFP+ electroporated cells was analysed 1dpe by dividing the developing cortex in 5 equal bins, bin1 corresponds to apical side while bin5 to pial side of the cortex. Upon *Ece2* KD, significantly more transfected (GFP+) cells localised to bin2 (**Figure 2A**). Ectopic, basally located Pax6+ progenitors were identified which, compared to control, tended to localise more to bin2 than bin1 (**Figures 2B, C** and **Figure EV2A**) and were also positive for the active cell cycle markers Ki67 and phospho-Vimentin (**Figures EV2B, C**), with reduced apical Arl13b (**Figure EV 2G**). This redistribution of Pax6+ progenitors was not met with a significant change in neuron localisation 1 dpe, although some ectopic neurons were detectable at this early stage with a trend to increased localisation to bin3, and not bins4 and 5 as per the control (**Figures EV 2D-F**). Interestingly, ectopic progenitors were often not transfected (GFP-, **Figure 2C**), indicating that – similarly to the results found in COs – non-cell-autonomous mechanisms may contribute to this redistribution of cortical progenitors. Similarly, the morphology of transfected aRG was changed to a less radial and bipolar shape (**Figure 2A, Figures EV 2B, G**).

Analysis 3 dpe (E13-E16) revealed ectopic clusters, containing delaminated non-transfected Pax6+ (**Figure 2D**) and Ki67+ progenitors (**Figure EV2H**), accumulating in the parenchyma around an Arl13b+ area, surrounded by thickened processes of transfected cells (**Figures 2E, F**). In contrast, we often found a reduction in apical Arl13b and β -catenin (CTNNB1) in the electroporation site (**Figures 2E, G**). Altogether, these data suggest the delamination of cells from the apical surface (Arl13b+) and the formation of “rosettes” at more basal positions upon *Ece2* knockdown. Pax6- areas were also found in the progenitor zone underneath the ectopic rosette both at 1 dpe and at 3dpe (circles in **Fig. 2B, D**), indicating that the delamination of radial progenitors may be the cause of the ectopic rosettes.

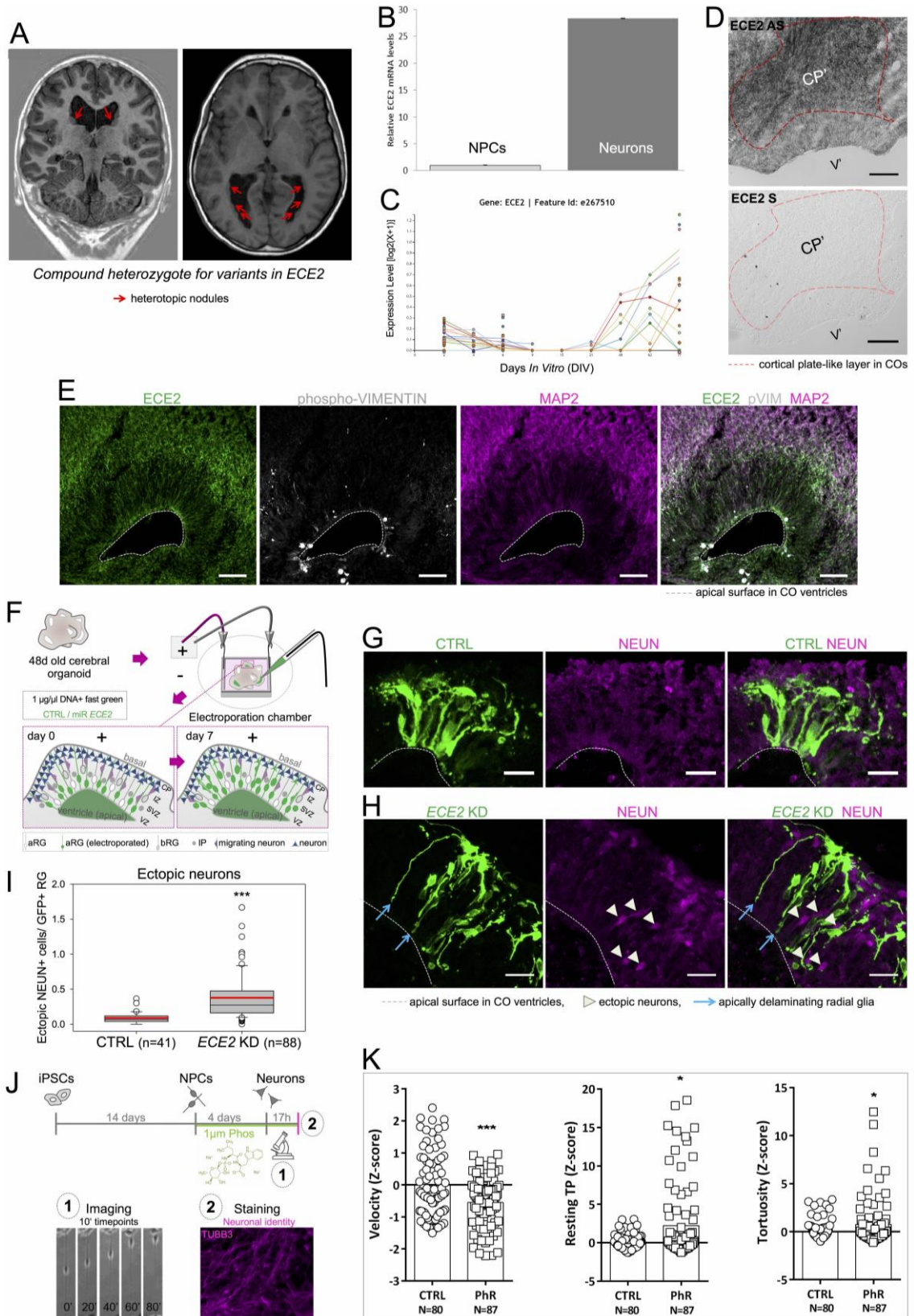


Figure 1: Neuronal mislocalisation and migration defects found in individuals with *ECE2* variants are recapitulated in iPSC-derived *in vitro* models. **A**, Coronal and axial brain MRI of the patient with compound heterozygote mutations in *ECE2* shows nodules of heterotopic neurons lining the lateral ventricles. **B-D**, *ECE2* expression on RNA level. **B**, qPCR of *in vitro* generated iPSC-derived NPCs vs. neurons shows higher *ECE2* RNA expression in neurons. **C**, RNA sequencing data of different stages of neuronal differentiation from iPSCs (<http://stemcell.libd.org/scb/>) [39]. **D**, *In situ* hybridisation for *ECE2* RNA in 50d old cerebral

organoids (COs) shows higher signal in the cortical plate-like zone (CP') (Scalebar=100 μ m). **E**, ECE2 expression on protein level. Immunohistochemistry (IHC) for ECE2 in 50d old COs shows accumulation in the CP' and at the apical surface (Scalebar=50 μ m). **F**, Scheme showing the electroporation of DNA into ventricles of COs and the organisation of different cell types within the germinal zone. DNA is injected into the ventricle-like lumen and taken up by aRG via their apical processes. 7 dpe, the transfected construct can be found in IPs and neurons upon differentiation of transfected aRG (green) (VZ' = ventricular zone, SVZ' = subventricular zone, IZ' = intermediate zone, CP' = cortical plate, aRG' = apical radial glia, bRG' = basal radial glia, IP' = intermediate progenitor). **G-H**, COs transfected with miRNAs targeting *ECE2* (KD) (**H**) or scrambled negative control (CTRL) and GFP (**G**) and analysed 7 days later reveal an increase in ectopic neurons upon *ECE2* KD (Transfected cells are shown in green, NEUN+ neuronal nuclei in magenta. d=day. Scalebar=25 μ m). **I**, Graph depicting the number of ectopically located NEUN+ cells in CTRL and KD electroporated COs. Data shown as box plot (mean = red line, median = black line, box represents 25th and 75th percentiles, whiskers extend to 10th and 90th percentiles, all outliers are shown; n=number of ventricles analysed; *** $P < 0.001$ in Kruskal-Wallis One Way ANOVA on Ranks and Dunn's Pairwise Multiple Comparison). **J**, Scheme depicting the experimental setup of neuronal differentiation and timelapse imaging under treatment with the *ECE2*-inhibitor phosphoramidon (Phos) [40]. **K**, Graphs showing different parameters of neuronal migration dynamics, tracked via live imaging. Upon *ECE2* inhibition, significant decrease in velocity, increase in resting TP and increase in tortuosity are observed. Data shown as z-scores (CTRL = DMSO control; PhR = Phosphoramidon; Resting TP = Resting timepoints; N=number of individual neurons analysed from 2 batches; Resting TP: * $P=0.024$; tortuosity: * $P=0.035$, *** $P < 0.001$ in 2-tailed Chi-Square test). See also **Figure EV1**.

Ectopic rosettes were surrounded by clusters of (mostly non-transfected) ectopic neurons, with both deep and superficial layer identities, often forming "nodules" (**Figures 2H, I** and **Figure EV 2H**). Moreover, single neurons were also more frequently localised to the apical surface of the lateral ventricles after *Ece2* knockdown compared to control cortices (**Figure 2H**). At both analysed time points, ectopic rosettes and nodules contained almost exclusively non-transfected cells, but were surrounded by GFP+ processes of transfected cells (**Figures 2E, F**). We consistently observed defects in the position and morphology of progenitors and neurons in all brains, but the severity of the phenotype strongly depended on the size and position of the electroporated area. Upon acute KD of *Ece2*, we identified significantly more ventricles with reduced Pax6 in the electroporation site, more ectopic rosettes and nodules, more ectopic Arl13b+/ β -catenin apical surfaces and a reduction in apical Arl13b and β -catenin (**Figure 2J**).

Therefore, similar to our results with KD of *ECE2* in COs, we could recapitulate some features of the patients' PH phenotype in the developing mouse cortex *in vivo*. We suggest that the PH-like disruption originated from a delamination of progenitor cells, followed by the formation of subapical clusters of progenitors that possibly generate the ectopic neurons found in their proximity. Also at this stage, ectopic rosettes and nodules consisted almost exclusively of non-transfected cells, highlighting again the non-cell-autonomous nature of the PH.

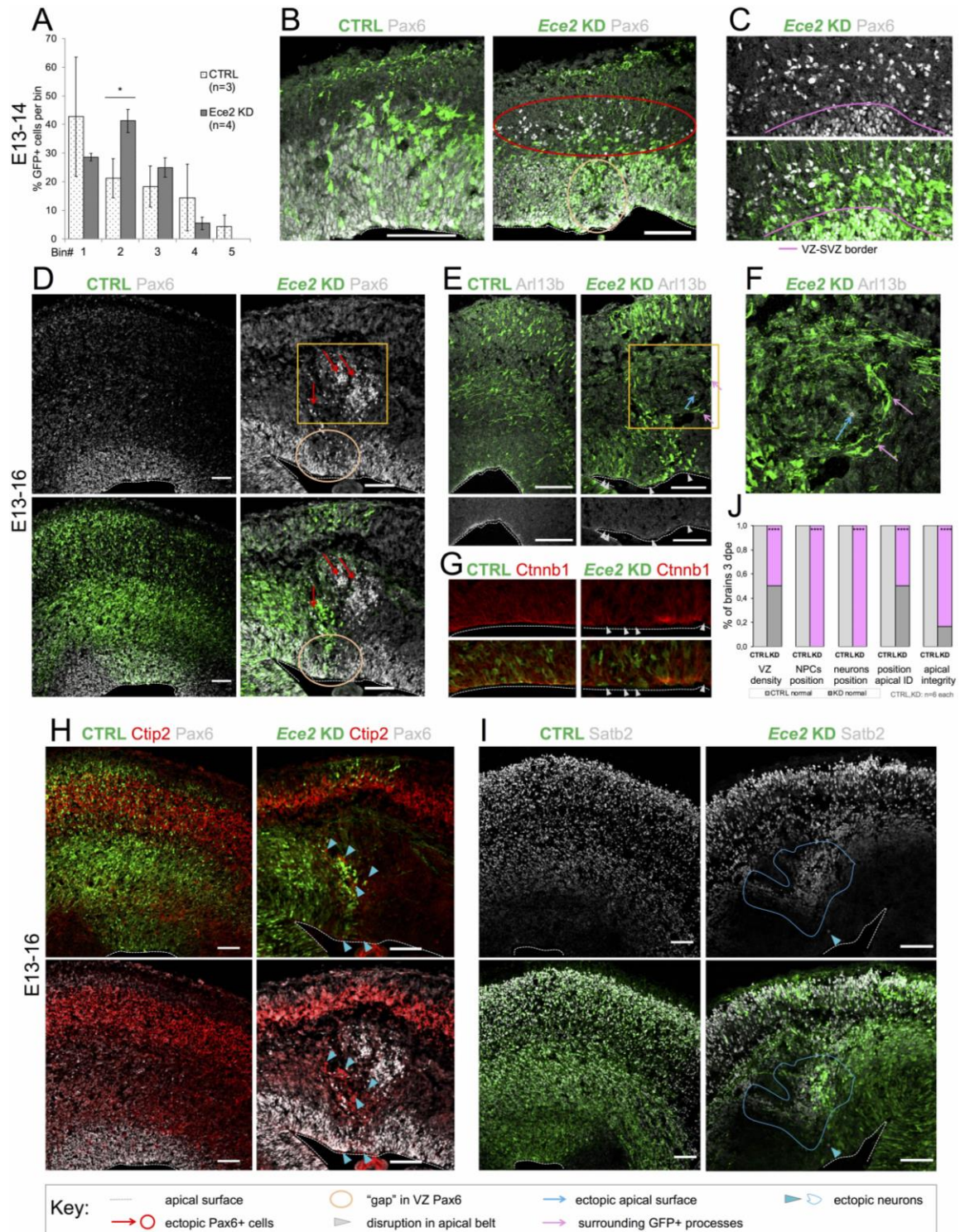


Figure 2: Acute *Ece2* KD in the developing mouse cortex causes ectopic rosettes and nodules. **A**, Quantification of distribution of GFP+ transfected cell 1dpe upon CTRL and *Ece2* KD by IUE (n=3 CTRL and 4 *Ece2* KD brains; * $P=0.044$ in One-way ANOVA and Tukey's Multiple Pairwise Comparison; data shown as mean \pm SEM). **B-C**, *Ece2* KD leads to ectopic non-transfected Pax6+ progenitors 1 dpe (E13-E14). **B**, IHC staining of GFP (transfected cells) and Pax6 1 dpe showing ectopic Pax6+ progenitors and a reduction in their apical localisation. **C**, High magnification images of GFP and Pax6 showing ectopic progenitors are mostly not transfected. **D-J**, E13-16 *Ece2* KD. **D**, GFP+Pax6+ progenitors delaminate upon *Ece2* KD, leaving behind a region free of Pax6+ cells in the VZ (circle) and forming ectopic rosettes (box). **E**, **G**, Reduction in apical Arl13b and β -catenin in the electroporation site indicates loss of apical belt integrity and disruption of apico-basal polarity upon *Ece2* KD. **F**, Inside the nodule, which is surrounded by thickened

GFP+ processes, Arl13b staining shows the formation of an ectopic apical surface (enlargement of boxed area from D and E). **H**, Deep layer and **I**, upper layer neurons localise next to ectopic rosettes, forming nodules of ectopic neurons. **J**, Quantification at 3 dpe, counting the proportion of brains with reduced density of Pax6 in the VZ, ectopic progenitors or neurons, and changes in apico-basal polarity (including ectopic apical surface formation and reduction in apically localised apical markers; n=6 brains per condition; Exact binomial test: **** $P < 0.0001$). Scalebars in A-I=100 μ m. See also **Figure EV2**.

Manipulation of ECE2 levels and activity reveal a role of ECE2 in cell fate determination

To address the functional role of ECE2 in human cells, two parallel approaches were taken: COs were treated with the ECE2 inhibitor Phos prior to IHC or Fluorescence-Activated Cell Sorting (FACS) analysis (scheme in **Figure 3A**, **Figures 3B-D**, **Figures EV 3B-D**) and *ECE2* KO iPSCs and COs were generated and analysed (**Figures 3E-J** and **Figures EV 3E-J**).

Chronic treatment (21 days) of 60 days old COs with Phos, which did not increase cell death as revealed by cleaved Caspase-3 staining (**Figure EV 3A**), lead to a change in the cellular composition: FACS analysis of neural progenitors (SSEA1 and BLBP sorted cells) and of neurons (MAP2 sorted cells) revealed an increase in neural progenitor cells (**Figures 3B, C**) and a reduction in neurons (**Figure 3D**) (see **Figure EV 3B** for the gating strategy).

CRISPR/Cas9-mediated genome editing in iPSCs resulted in a frameshift and premature STOP codon in one allele and fusion of first half of exon 3 and second half of exon 4 due to the loss of 80 AA in the second allele. The absence of *ECE2* mRNA in *ECE2* KO iPSCs (**Figure EV 3E**) was confirmed by qPCR (**Figure 3F**). COs were generated from *ECE2* KO and the isogenic control iPSCs [32]. An initial delay in differentiation was visible, with a later emergence of neuroepithelial tissue in the *ECE2* KO COs (**Figure EV 3E**), without a significant difference in CO size compared to control (**Figure EV3F**). *ECE2* KO COs generated normal cortical-like regions (**Figure 3E**), indicating that *ECE2* deficiency is still permissive for the first steps of neurodevelopment.

60d old COs were analysed by FACS using the progenitor marker PAX6, the mitotic marker PH3 and the neuronal marker DCX (see **Figure EV3G** for the gating strategy). Similarly to the above described findings for ECE2 inhibition, the proportion of progenitors was increased (**Figures 3G, H**) and that of neurons was decreased (**Figure 3I**) in *ECE2* KO COs compared to control. This change in cellular proportions was also confirmed by IHC, where we found that the number of PH3+ cycling progenitor cells (normalized by the length of apical surface) was significantly increased in germinal zones of *ECE2* KO COs (**Figures EV3H, I**), whereas the thickness of the MAP2+ neuronal layer was decreased (**Figure EV3J**). The higher expression of ECE2 in neurons may be required for neuronal differentiation.

Altogether, both chronic enzymatic inhibition and the permanent KO of *ECE2* in COs lead to changes in the proportions of progenitor and differentiated cells, demonstrating a role for ECE2 in neurogenesis.

Further exploiting the spatial organisation and separation of progenitor and CP-like zones in COs, we identified ectopic neurons within these COs in the VZ' after *ECE2* KO. Some MAP2+ neuronal processes are present throughout the progenitor zone in KO COs and even though these structures were also observed in control COs, there is a clear

significant increase in brain-like regions with progenitor zones containing neuronal cell bodies upon *ECE2* KO, with a concomitant decrease of normally organised ventricles in the KO condition (**Figures 3J, K**). The malpositioning of neurons characterizing the brains of patients with PH is thus partially recapitulated both after acute *ECE2* KD and in *ECE2* KO COs.

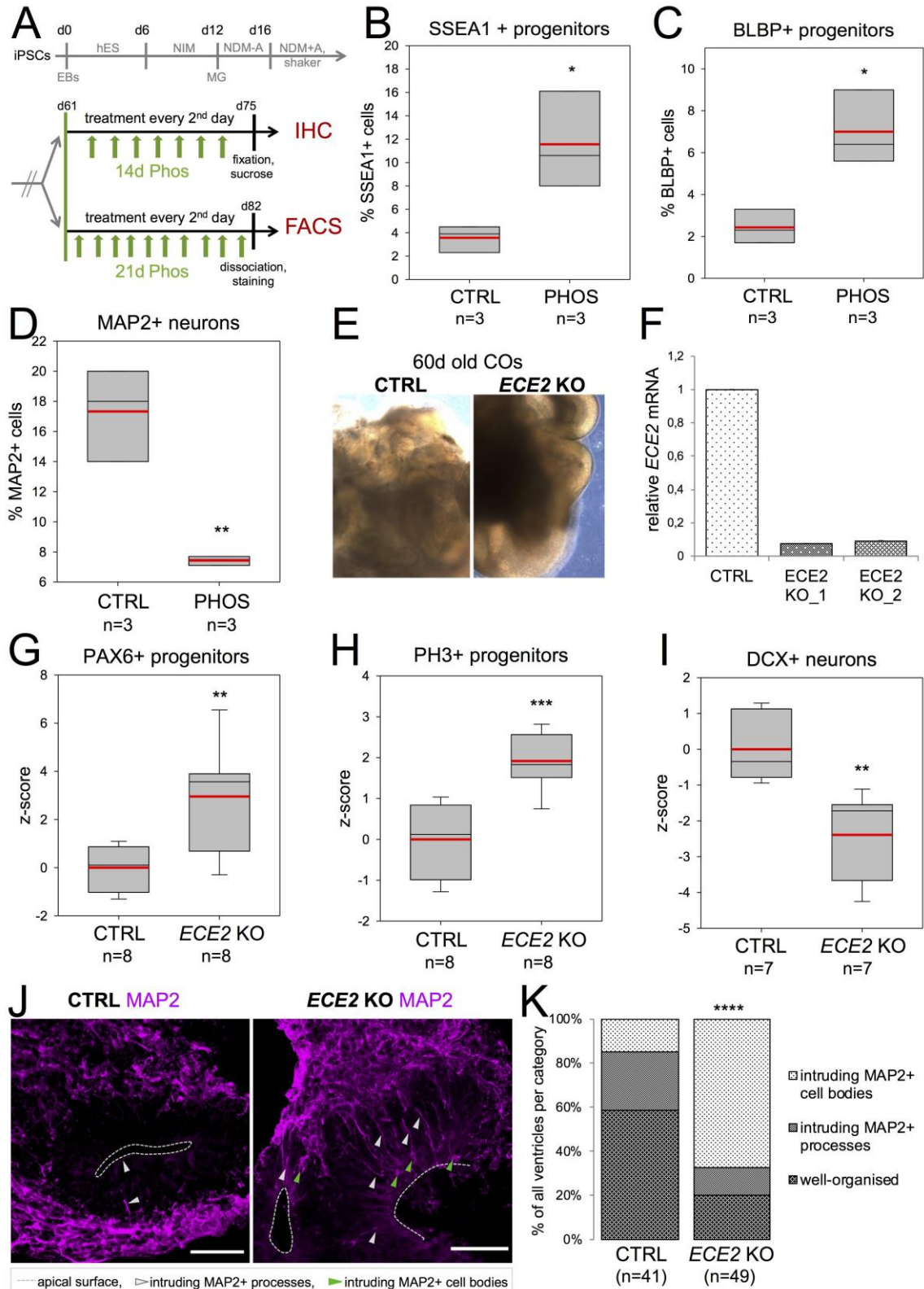


Figure 3: ECE2 inhibition and KO cause a change in cell fate and neuronal positioning in COs. **A**, Scheme depicting the timeline of chronic Phos treatment in COs prior to IHC or FACS analysis (hES, NIM, NDM-/A: media for CO generation, see Methods). **B, C**, FACS analysis of Phos-treated COs shows an increase in neural progenitors. **D**, FACS analysis of Phos-treated COs reveals a decrease in neurons. Data shown as z-scores. (Box plots: mean=red line, median=black line, box represents 25th and 75th percentiles, whiskers extend to 10th and 90th percentiles, all outliers are shown; B-D: * $P < 0.05$; ** $P < 0.01$ in One Way ANOVA and Tukey's Pairwise Multiple Comparison). **E**, Brightfield images of 60d old CTRL and *ECE2* KO COs show normal formation of neuroepithelial structures. **F**, qPCR confirms absence of *ECE2* mRNA in 2 clones of *ECE2* KO iPSCs (Data shown as mean \pm SEM from triplicates). **G-I**, FACS analysis of 60d old *ECE2* KO COs reveals an increase in progenitors (**G, H**) and decrease in neurons (**I**) (n=7-8 samples of 3 pooled organoids each from 3 different batches; ** $P < 0.01$; *** $P < 0.001$ in One Way ANOVA and Tukey Pairwise Multiple Comparison). **J, K**, In *ECE2* KO COs, more ventricles are disorganised in terms of neuronal localisation as revealed from MAP2+ cell bodies in the progenitor zone (n=number of ventricles from 2 independent batches; two-tailed Mann Whitney U ($U = 458$) and chi-square test: $\chi^2_{(2)}=25.42$, **** $P < 0.0001$). See also **Figure EV3**.

***ECE2* inhibition and KO leads to changes in actin and microtubule cytoskeleton**

Due to the 3-dimensional organisation of germinal zones, COs represent a good system to analyse the cellular morphology, the integrity of cytoskeletal proteins and markers of apico-basal polarity after acute *ECE2* KD *in vitro* and *in vivo*.

Cytoskeletal dynamics and apico-basal polarity are essential both for the integrity of the RG scaffold used by locomoting excitatory neurons and for neuronal polarisation and migration itself [41]. These were thus characterized both in *ECE2* KO and in Phos-treated COs (**Figure 4**) to assess a possible involvement of *ECE2*.

A significant increase in thickness of the filamentous actin (F-Actin) enriched apical adherens belt was detected in both COs treated with Phos for two weeks (**Figures 4A, B**) and in *ECE2* KO COs (**Figures 4C, D**). In addition, the apical F-Actin enriched honeycomb structure was also analysed. Here, we identified morphological alterations in the case of *ECE2* KO (**Figure 4E**) consistent with a loosening of the apical junctions. *ECE2* may thus directly or indirectly influence the regulation of the actin filament (re)organisation, contributing to the morphology and delamination of aRG in the developing cerebral cortex.

Next, we analysed the stability of microtubules as the second important component of the cytoskeleton. We used IHC for acetylated tubulin (ac-tub), which is enriched in stabilised microtubules [42]. IHC of ac-tub in Phos treated and *ECE2* KO COs revealed some normal germinal zones and some with a reduction and/or disorganisation in stabilised microtubules (**Figures 4F, H**). We quantified ventricles with normal ac-tub and reduced or disorganised VZ' structures to assess the extent of disruption. This displayed a significant reduction in ventricles with normal stabilised microtubule cytoskeletons after both *ECE2* inhibition and KO (**Figures 4G, I**).

We next assessed apico-basal polarity in Phos-treated and *ECE2* KO COs by IHC for ARL13B as a marker for the microtubule-based primary cilium that contacts the ventricular lumen in aRG. We found again some normal ventricles and some with reduced or totally absent localisation of ARL13B at the apical surface. The number of ventricles with normal ARL13B was significantly reduced (**Figures 4J-M**).

To further support our finding of reduction in apically localised ARL13B and to minimize artefacts due to cutting orientation of COs, we used iDisco [43] of Phos-treated whole COs.

Whole-mount IHC for ARL13B, tissue clearing and imaging of whole COs confirmed the reduction in apical ARL13B upon *ECE2* enzymatic inhibition (**Videos 1 and 2**). Interestingly, an involvement of primary cilium abnormalities in ectopic neuronal positioning was recently suggested [28], indicating that this may be a common mechanism underlying the etiology of PH.

We also analysed the levels of β -catenin, which is enriched at the apical adherens junctions, by WB and identified a trend towards a reduction in *ECE2* KO COs (**Figure EV4A, B**). This is similar to its reduction upon *Ece2* KD in the developing mouse cortex (**Figure 2G**) and in line with the delamination of aRG upon acute *ECE2* KD in COs (see **Figure 1I, Figure EV1C**).

Finally, to visualize aRG morphology upon *ECE2* KO, we electroporated GAP43-GFP plasmid into ventricle-like structures of CTRL and KO COs to label the membrane of transected aRG. Analysis 1dpe revealed that in *ECE2* KO COs, aRG can lose their apical attachment (which was still present during electroporation for take-up of the construct) or even completely lose their bipolar morphology (**Figure 4 N, O**). This finding further underscores the involvement of *ECE2* in RG morphological integrity.

Altogether, we identified changes in both the microtubule and actin cytoskeleton and in the polarity of aRG. Loss of apically localised cilia and reduction in the stability of the apical F-actin belt suggest aRG delamination and formation of ectopic rosettes. These ectopic progenitors don't in general lack apico-basal polarity (ectopic Arl13b) but lack bipolar morphology, possibly leading to a disorientation of the derived neurons, which can then form nodules.

Hence, our data suggest that *ECE2* directly or indirectly plays a role not only in neuronal migration and positioning, but also in cell fate, cytoskeletal organisation and apico-basal polarity of aRG. Despite the numerous processes that *ECE2* is involved in, the molecular role of *ECE2* – both causing cell-autonomous and non-cell-autonomous defects upon its disruption during neurogenesis – still remains undefined.

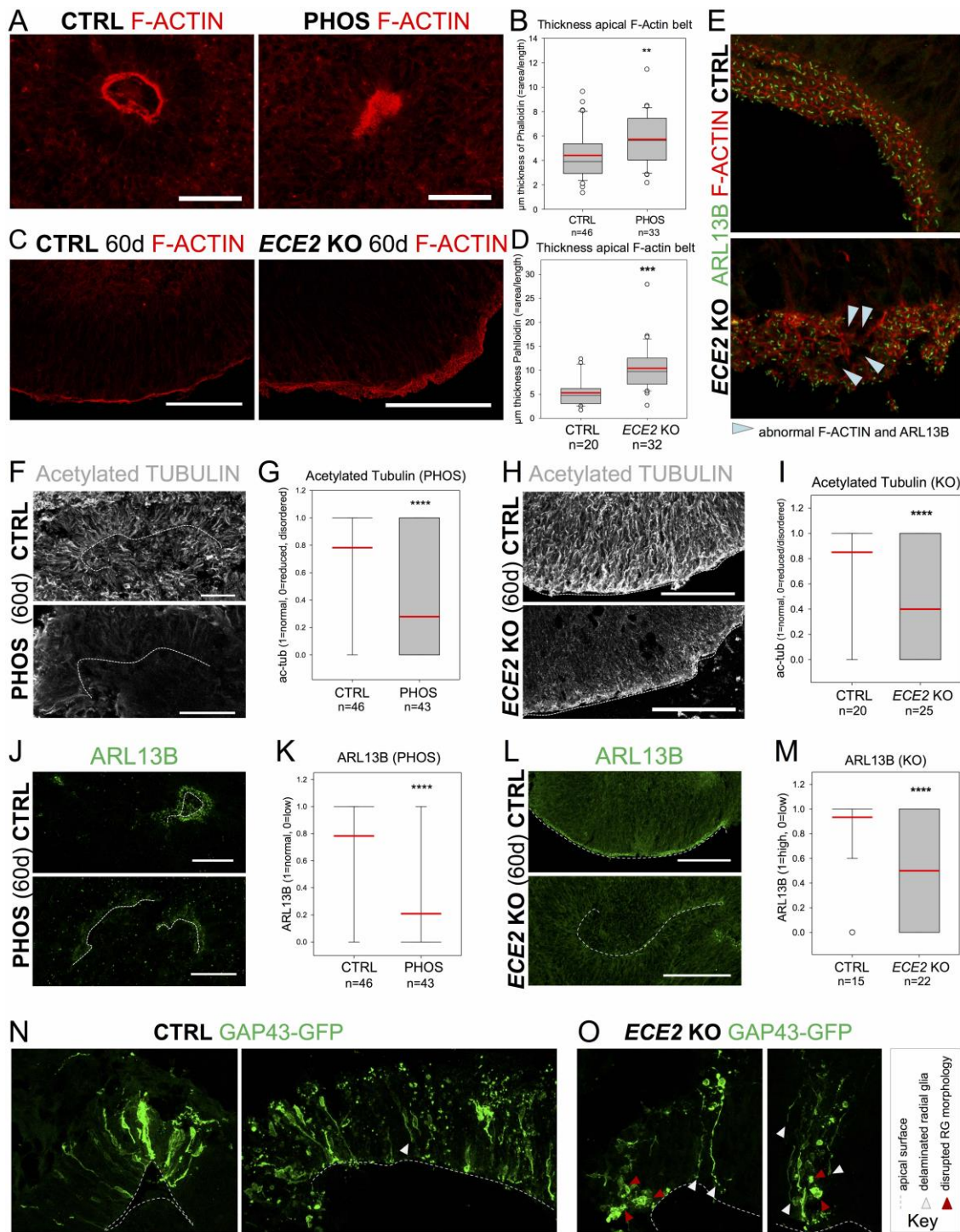


Figure 4: Cytoskeleton and apico-basal polarity are disrupted upon ECE2 inhibition and ECE2 KO. **A-D**, The thickness of the apical F-actin belt is increased in Phos-treated COs (**A, B**) and ECE2 KO COs (**C, D**). **A, C**, Example images of Phos and CTRL treated COs (**A**) and 60d old CTRL and ECE2 KO COs (**C**) with F-ACTIN labeled by AlexaFluor594-conjugated Phalloidin (**A**: Scalebar = 50 μ m, **C**: Scalebar = 100 μ m). **B, D**, The thickness of the F-Actin belt was assessed in Fiji [44] by measuring the area of F-actin and dividing by the length of apical surface (Box plots: mean=red line, median=black line, box represents 25th and 75th percentiles, whiskers extend to 10th and 90th percentiles, all outliers are shown; n=number of analysed ventricles in 2 batches; Kruskal-Wallis One Way ANOVA on Ranks and Dunn's Pariwise Multiple Comparison: ** $P=0.003$; *** $P < 0.001$). **E**, IHC for ARL13B and F-ACTIN in 60d old CTRL and ECE2 KO COs shows disruption of honeycomb-like structure of the apical adherens belt and of apico-basal polarity in terms of apically localised primary cilium. **F-I**, The microtubule cytoskeleton is changed upon

ECE2 inhibition (**F, G**) and KO (**H, I**). **F, H**, Example images of ac-tub IHC in CTRL vs. PHOS-treated (**F**) and CTRL vs. *ECE2* KO (**H**) COs (**F**: Scalebar = 50 μ m; **H**: Scalebar = 100 μ m). **G, I**, Quantification of ac-tub in ventricles of PHOS-treated (**G**) and *ECE2* KO (**I**) COs as normal ("1") or reduced/disordered ("0") shows significant reduction in normal ventricles (n=number of analysed ventricles in 2 batches; **** $P < 0.0001$ in exact binomial test). **J-M**, Apico-basal polarity is impaired upon ECE2 inhibition and KO as visible in example images of ARL13B IHC in CTRL vs. PHOS (**J**) and KO (**L**) COs (**J**: Scalebar = 50 μ m; **L**: Scalebar = 100 μ m). **K, M**, Quantification of germinal zones for normally high ("1") vs. reduced ("0") apical ARL13B reveals a reduction in normal ventricles in the absence of ECE2 (n=number of analysed ventricles from 2 batches; **** $P < 0.0001$ in exact binomial test). **N, O**, Analysis of CTRL and *ECE2* KO COs 1 dpe with GAP43-GFP reveals RG that delaminated and/or lost their bipolar morphology in the KO COs. See also **Figure EV4**.

Proteomics reveals ECE2 involvement in extracellular matrix production and integrity

To gain a deeper insight into the mechanisms underlying the observed phenotypes in *in vivo* and *in vitro* models, we performed whole proteome analysis of 60d old CTRL and *ECE2* KO COs. Mass Spectrometry-based proteomics has recently been used to compare trisomy 21 patient and control-derived COs and revealed 1) that the neurodevelopmental trajectory shown several times by scRNAseq [45-47] is also recapitulated on the protein level in COs, 2) a number of dysregulated proteins in trisomy 21, and 3) reversal of dysregulated proteins by drug treatment [48]. Here, quantitative proteome analysis of whole-organoid-lysate revealed a number of significantly up- and downregulated proteins upon *ECE2* KO (**Figure 5A** and **Table EV2**). These included upregulation of PAX6 and downregulation of MAP2, confirming FACS data from *ECE2* KO and Phos-treated COs (**Figure 3**). Additionally, the identified downregulated proteins included numerous proteins with functions that are highly relevant to cortical development and its disorders. **Figure 5B** illustrates a classification of all downregulated proteins into the following classes (see colour code in **Table EV3**) [49-51]. These included genes/proteins whose disruption is known to cause PH (e.g. FLNA [14-17]) or disorders of neurodevelopment. A number of additional microtubule and microtubule-associated proteins were also downregulated, strengthening our previous findings (**Figure 4**), as were additional actin-associated/-organizing proteins, such as ezrin and moesin, which are interactors of RHOA and FLNA (**Figure EV4C**). Decrease in phosphorylated ezrin, radiixin and moesin (pERM) was confirmed by WB of *ECE2* KO iPSCs (**Figures EV4D**). Some guidance and adhesion factors such as SLITs and FLRTs were downregulated in *ECE2* KO COs, similarly to other COs derived from patients with PH [13]. In the context of neuronal migration this is of relevance as differential expression of adhesion molecules such as FLRT1 and FLRT3 between future gyri and sulci was recently identified to influence the migration of cortical neurons, thereby regulating gyrification independantly of progenitor cell expansion [52].

In addition, a number of adhesion proteins were downregulated in *ECE2* KO organoids, which may explain the delamination of transfected RG observed upon acute KD in cerebral organoids and in the developing mouse cortex (**Figures 1 and 2**) and the reduction in apically localised β -catenin and ARL13B both *in vivo* (**Figures 2G-E, Figure EV2F**) and upon chronic ECE2 inhibition or KO in COs (**Figure 4J-M** and **Figure EV4A, B**).

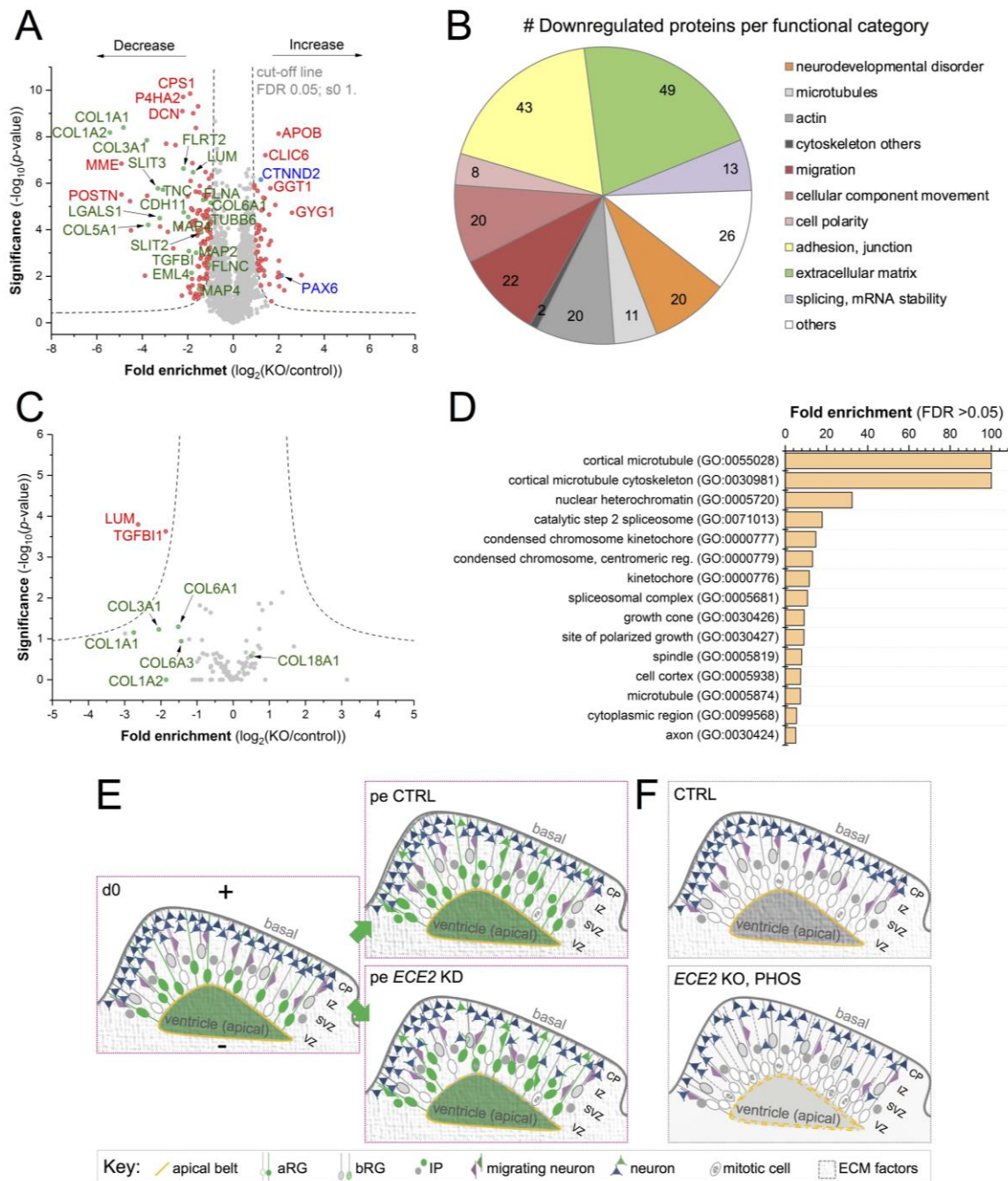


Figure 5: Proteomics reveal a role for ECE2 in ECM production and integrity. Volcano plot visualizes the proteomic analysis from 60d old CO lysates showing proteins with significantly lower and higher expression upon *ECE2* KO (n=3 batches of 60d old CTRL and *ECE2* KO COs; FDR 0.05; s_0 1; dashed lines indicating the cut-off). **B**, Pie chart with proteins downregulated in *ECE2* KO COs sorted by relevant categories (Number in the elements = number of proteins falling into each category, with numerous proteins falling into several ones) [49-51]. **C**, Volcano plot of MS of cell culture supernatant from 55d old CTRL and *ECE2* KO COs shows two significantly downregulated proteins in the secretome (n=3 batches of 60d old CTRL and *ECE2* KO COs; FDR 0.05; s_0 1; dashed lines indicating the cut-off). Non-significantly changed proteins of interest are highlighted in green below the cut-off curves. **D**, GO cellular component analysis of dysregulated phosphorylation sites (either found exclusively in CTRL or KO or up- or downregulated in *ECE2* KO COs relative to CTRL) identified in whole CO proteomic analysis. **E**, **F** Schemes summarizing identified phenotypes in *in vivo* and *in vitro* model systems upon acute *ECE2* KD (**E**) or chronic inhibition or KO (**F**) and thus the molecular action of ECE2 (Abbreviations: d = day, pe = post electroporation, VZ = ventricular zone, SVZ = subventricular zone, IZ = intermediate zone, CP =

cortical plate, aRG = apical radial glia, bRG = basal radial glia, IP = intermediate progenitor, ECM = extracellular matrix). See also **Figure EV4** and **Tables EV1-8**.

The largest group of downregulated proteins, however, consisted of ECM components and their receptors, e.g. laminins, lumican, decorin, and six different collagens (see **Figure 5B** and **Table EV3**), not surprisingly since we observed non cell-autonomous effects upon modulation of *ECE2* expression.

Analysis of protein-protein-interactions (PPI) of downregulated proteins, using String.db [51], showed an arrangement of downregulated proteins into a tightly interconnected network (**Figure EV4E**) and GO Term analysis [50,51] revealed an enrichment of proteins with functions that are highly relevant to cortical development, such as adhesion, polarity, and cytoskeleton (**Figure 5B**, **Table EV4**).

As *ECE2* is a protease localised in secretory vesicles [53], the cell culture supernatant of COs was also analysed by MS for differences in the “secretome” between *ECE2* KO and control COs. Two proteins were identified as significantly downregulated upon *ECE2* KO (see **Figure 5C**, **Table EV5**): Lumican and TGFBI, both collagen-binding proteins (**Table EV6**). Additionally, other collagens in the secretome of *ECE2* KO COs were somewhat decreased. These findings support the involvement of *ECE2* in ECM generation or regulation.

The ECM is implicated both in neuronal migration and differentiation as well as in cortical expansion and folding [54-56], with human-enriched ECM components contributing to inter-species differences such as in gyrification [57]. Here, the identified overrepresentation of ECM components among the downregulated proteins may explain the non-cell-autonomous nature of mechanism observed both in *in vitro* and in *in vivo* model systems.

Microtubule dynamics is regulated by different types of microtubule-associated proteins (MAPs), such as EML4, MAP2 and MAP4, which were downregulated in the proteome of *ECE2* KO COs. Additionally, posttranslational modifications (PTMs) of tubulins and MAPs influence microtubule stability, the interaction capability of MAPs, and microtubule-based transport [58]. To this end, we further investigated differentially phosphorylated protein sites from the whole proteome analysis between CTRL and *ECE2* KO COs (**Table EV7**). Strikingly, we detected differences in several proteins involved in apical adhesion, cytoskeletal and motor functions, with special enrichment of microtubule-related proteins among exclusive phosphorylation sites (**Table EV8**) and of actin cytoskeleton-related proteins among differentially phosphorylated sites (**Table EV9**) (**Figure 5D**). Our analysis of phospho-proteins suggests an additional role of *ECE2* in the regulation of the actin and microtubule cytoskeleton through PTMs such as phosphorylation.

Altogether, we studied the role of *ECE2* in brain development and identified *ECE2* as a promising novel candidate gene for PH, showing that *ECE2* controls apical adhesion, cytoskeleton dynamics and ECM composition.

Acknowledgements

Thanks to the families for their participation. We thank all members of the lab for fruitful discussions, Mariana Schröder and Mira Jakovcevski for help with statistical analysis and Timucin Öztürk and Bianca Schmid for technical support.

Author Contributions

Conceptualization, I.Y.B. and S.C.; Methodology, I.Y.B., P.K., G.G., R.D.G., C.K., A.C.O.; Investigation, C.K., A.C.O., R.D.G.; Resources, S.K., S.P.R., and S.C.; Writing Original Draft, I.Y.B.; Writing Review & Editing, I.Y.B., A.O.N., S.P.R. and S.C; Supervision, S.C.; Funding Acquisition, S.P.R. and S.C.

Declaration of Interests

The authors declare no competing interests.

Funding

This work was supported by funding the Max Planck Society (SC-IB-GG-RDG-CK), the Health Research Council of New Zealand and Curekids (AON-SR), the Graduate School of Systemic Neurosciences (IB), European Research Council (ERC) consolidator grant and CIPSM (SAS-PK).

Materials and Methods

Candidate gene prioritization. The recent trio-based whole exome sequencing study in patients with PH [27] was interrogated for genes with rare ($MAF < 0.005$) biallelic variants (homozygous recessive or compound heterozygote) in two or more patients. As outlined in Table S3 and S4 of this report [27], only three genes remained of interest - *ECE2*, *GPR98* and *PTPN13*. Note, although two separate homozygous recessive variants are identified for *SPEG*, they are all present within the same patient. As a further filter to identify a potential candidate gene for functional investigation, we restricted our analysis to any of these three genes whose variants in each individual were reported as potentially deleterious by one of four *in silico* prediction programs [59-62] (see **Table EV1**). Such prediction programs assess functional (i.e the resulting properties of the amino changes) and/or evolutionary properties (such as sequence conservation). Although such genic effects are not a proxy for disease association, any gene satisfying this criteria in this study would be prioritized for detailed functional investigation that further corroborates insight into the potential effect of the variants on gene function. Here, only one gene was prioritized – *ECE2*.

Reprogramming of fibroblasts to induced pluripotent stem cells. Human induced pluripotent stem cells (iPSCs) were obtained by reprogramming of foreskin fibroblasts as described before [28].

iPSC culture. iPSCs were cultured at 37 °C, 5 % CO₂ and ambient oxygen level on plates coated with Matrigel (*Corning*; diluted 1:100 in DMEM/F12+Glutamax, *Thermo Fisher Scientific*) in mTeSR1 medium (*StemCell Technologies*) with daily medium change. For passaging, iPSC colonies were washed with PBS and incubated with StemPro Accutase Cell Dissociation Reagent (#A1110501, *Life Technologies*) diluted 1:4

in PBS for 3 min. Detached pieces of colonies were collected by washing with DMEM/F12 and 5 min centrifugation at 300 x g. They were then resuspended in mTeSR1 supplemented with 10 μ M Rock inhibitor Y-27632(2HCl) (#72304, *StemCell Technologies*) for the first day with splitting ratios 1:3 – 1:6.

Generation of neural progenitor cells (NPCs) and neurons from iPSCs. Neural progenitors were generated as described previously [31] (**Figure EV 1A**) with some modifications. Embryoid bodies (EBs) were obtained by incubation of feeder-free iPSC colonies with Collagenase Type IV (#7909, *StemCell Technologies*) for 15 min, followed by washing with DMEM/F12, manual disruption and scraping with a cell lifter (3008, *Corning Life Sciences*). Resulting detached pieces of iPSC colonies were plated in suspension in Neural Induction Medium (NIM) consisting of DMEM/F12+Hepes (#31330095, *Life Technologies*) with 1x N2 and B27 supplements (without vitamin A, *Thermo Fisher*) with medium change every other day. EBs were plated on Polyornithine/Laminin plates after 1 week of suspension culture and after another week of culture in NIM, neural rosettes were picked and disrupted manually using a P20 tip. Resulting NPCs were cultured in NPM (NIM + 20 ng/ml basic fibroblast growth factor (bFGF/FGF-2), #100-18b-50, *Preprotech*) and passaged using Accutase (*StemCell Technologies*) splitting at a maximum ratio of 1:4. NPCs were only used for up to seven passages. For differentiation to neurons, single NPCs were plated at a density of 10^4 cells/cm² on Polyornithine/Laminin plates and cultured in NPM for 1 more day to reach about 30% cell density. Afterwards, medium was changed to Neuronal Differentiation Medium NDM (NIM containing 20 ng/mL BDNF (#248-BD, *R&D Systems*) and 20 ng/mL GDNF (#212-GD, *R&D Systems*)) and were differentiated for 20 days with medium change every 5 days.

Cerebral organoids. Cerebral organoids (COs) were generated starting from 9,000 single iPS cells/well as previously described [32] (**Figure EV 1B**) with the following alterations. Organoids were cultured in 10 cm dishes on a DOS-10L orbital shaker at 37 °C, 5% CO₂ and ambient oxygen level with medium changes twice a week. Organoids were electroporated at 50 days after plating (see *Electroporation of cerebral organoids* and **Figure 1G**) and analysed 4 and 7 days post electroporation (dpe). For immunostaining, 14 μ m sections of COs were prepared using a cryotome. For 7 dpe analysis, 41 (CTRL) and 88 (*ECE2* KD) different ventricles in a total of 17 (CTRL) and 25 (*ECE2* KD) organoids from 3 independent batches were analysed.

Generation and validation of microRNAs targeting *ECE2/Ece2*: MicroRNAs (miRNAs) targeting human or mouse *ECE2* were generated using the BLOCK-iT system from Invitrogen (*Thermo Fisher*). MiRNA sequences were determined using Invitrogen's RNAi design tool

<https://rnaidesigner.thermofisher.com/rnaiexpress/setOption.do?designOption=mirnapid=1961720787891316464>. Three miRNA sequences per species were chosen and ordered as oligonucleotides from Sigma. *ECE2*-targeting miRNA oligonucleotides were annealed and ligated into a GFP-containing entry vector pENTR-GW/EmGFP-miR containing the miRNA backbones using T4 DNA Ligase (*Thermo Fisher*), following the recommendations in the BLOCKiT system. Subsequently, the miRNA sequences (plus GFP) were cloned into the pCAG-GS destination vector using the Gateway system (*Thermo Fisher*) according to the manufacturer's recommendations. The resulting miRNA expression plasmids were sequenced using emGFP forward primer (5'-GGCATGGACGAGCTGTACAA-3'). The knockdown efficiency of the miRNAs were

tested via qPCR with validation of those targeting human *ECE2* in SH-SY5Y neuroblastoma cells and validation of those targeting mouse *Ece2* in P19 cells. The most efficient construct was used for neural progenitor transfection in COs by electroporation (see *Electroporation of Cerebral Organoids* and **Figure 1G**) and in the developing mouse cortex by in utero electroporation (see *In utero electroporation*). The following constructs were chosen. A miRNA with scrambled sequence (“miRneg”) was used as negative control:

Oligo name	Sequence(5' to 3')
miR <i>ECE2</i> top	TGCTGTAATGTTCCAACCACCAATCTGTTTTGGCCACTGACTGACAGATTGGTTGGAACATTA
miR <i>ECE2</i> bottom	CCTGTAATGTTCCAACCACCAATCTGTCTAGTCAGTGGCCAAAACAGATTGGTGGTTGGAACATTAC
miR <i>Ece2</i> top	TGCTGTCAATGAGGTCTCTAAGTGGCGTTTTGGCCACTGACTGACGCCACTTAGACCTCATTGA
miR <i>Ece2</i> bottom	CCTGTCAATGAGGTCTAAGTGGCGTCTAGTCAGTGGCCAAAACGCCACTTAGAGACCTCATTGAC
miRneg top	TGCTGAAATGTACTGCGGTGGAGACGTTTTGGCCACTGACTGACGTCTCCACGCAGTACATTTTCAGG
miRneg bottom	CCTGAAATGTACTGCGTGGAGACGTCAGTCAGTGGCCAAAACGTCTCCACGCAGTACATTTTCAGCA

Plasmid preparation. Small-scale plasmid preparation was carried out using the QIAprep Spin Miniprep Kit (*Qiagen*) and large-scale preparation with the Plasmid Maxi Kit (*Qiagen*) after transformation in Subcloning Efficiency™ DH5α™ Competent Cells (*Thermo Fisher*).

Electroporation of cerebral organoids. For transfection of aRG in germinal zones of COs by electroporation (see scheme in **Figure 1G**), COs were kept in NDM+A without antibiotics-antimycotics. The organoids were placed in an electroporation chamber (*Harvard Apparatus*) and miR*ECE2* or miRneg at a concentration of 1 µg/µl, supplemented with fast green (0.1%; *Sigma*) for visualization, was injected into ventricle-like cavities at several positions per organoid. Electroporation was performed with an ECM830 electroporation device (*Harvard Apparatus*) by subjecting the organoids to a 1 second interval with 5 pulses of 50 ms duration at 80mV. Medium was changed to antibiotics-containing NDM+A on the next day.

In utero electroporation. As approved by the Government of Upper Bavaria under the license number 55.2-1-54-2532-79-2016, pregnant C57BL/6 mice were used. They were weighed and anesthetized by intraperitoneal injection of saline solution containing fentanyl (0.05 mg per kg body weight), midazolam (5 mg per kg body weight) and medetomidine (0.5 mg per kg body weight) (Btm license number 4518395), and embryos were electroporated at E13 as described [63]. Plasmids were mixed with fast green (0.1%; *Sigma*) and injected at a final concentration of 1 µg/µl. After wound closure and sterilization, anesthesia was terminated by injection of buprenorphine (0.1 mg per kg body weight), atipamezole (2.5 mg per kg body weight) and flumazenil (0.5 mg per kg body weight). Brains were fixed 1dpe or 3dpe in 4% PFA for 4h (1 dpe) or overnight (3dpe) and were subsequently transferred to 30 % (w/v) sucrose in PBS for cryoprotection before embedding and freezing in OCT (*VWR*). For immunohistochemistry, 12 µm sections were prepared using a cryotome. For each experiment, at least 3 different mouse brains per condition were analyzed.

Analysis of cerebral organoids. For immunohistochemistry, cerebral organoids at the desired time point were washed with PBS and fixed in 4% formaldehyde (PFA) for 2 h at 4°C. They were then left in a 30% sucrose solution overnight at 4°C. After this, they were embedded in embedding molds with OCT (*VWR*), embedding 3-4 organoids per mold, and kept at -20°C until further processing. Frozen organoid samples were cut at a cryotome, preparing 14 µm sections.

Immunohistochemistry: Frozen organoid or mouse brain sections were thawed to RT for 20 min and then rehydrated in PBS for 5 min. For nuclear antigens, an antigen retrieval step (HIER) was performed, boiling the sections in 0.01M citric buffer (pH 6) for 1 min at 720 Watt and 10 min at 120 W. The slides were then left to cool down for 20 min. Half of the citric buffer was replaced by H₂O, slides were incubated for another 10 min and then washed in PBS. Subsequently, a postfixation step of 10 min was carried out with 4 % PFA in PBS. Then, the sections were permeabilized using 0.3 % Triton X100 in PBS for 5 min. After permeabilization, sections were blocked at RT for at least 1 h with 10 % Normal Goat Serum (#VEC-S-100, *Biozol*) and 3 % BSA (#A4503-50G, *Sigma-Aldrich*) in 0.1 % Tween in PBS. The primary antibody (see Table below) in blocking solution was then incubated overnight at 4 °C. Following several washes with 0.1 % Tween in PBS, sections were incubated with 1:1,000 dilutions of Alexa Fluor-conjugated secondary antibodies (*Life Technologies*) in blocking solution for at least 1h at RT, using 0.1 µg/ml 4,6-diamidino-2-phenylindole (DAPI, *Sigma Aldrich*) to counterstain nuclei. Finally, sections were washed again several times with 0.1 % Tween in PBS and mounted with Aqua Polymount (#18606, *Polysciences*). Sections were visualized using a Leica SP8 confocal laser scanning microscope. For immunohistochemistry of NPCs and neurons, cells were cultured on round coverslips (13 mm diameter, *VWR*) in 24 well plates, washed with PBS and fixed with 4 % PFA in PBS for 15 min at RT. For HIER, citric buffer was boiled, added to coverslips and left to cool down, while permeabilization, blocking and staining were carried out as described for the tissue sections.

Table: Primary antibodies.

Antigen	Dilution	Vendor	Catalog #
ARL13B	1:500	<i>Proteintech</i>	17711-1-AP
ACETYLATED TUBULIN	1:6,000	<i>Sigma- Aldrich</i>	T7451
BLBP	1:150	<i>Merck Millipore</i>	ABN14
CTNNB1 (β-catenin)	1:500	<i>BD Biosciences</i>	610154
CTIP2	1:500	<i>Abcam</i>	ab18465
DoubleCortin (DCX)	1:2,000	<i>Merck Millipore</i>	ab2253
ECE2	1:300	<i>Novus Biologicals</i>	NBP1-81495
F-ACTIN (Phalloidin-594)	1:40	<i>Thermo Fisher</i>	A12381
GAPDH	1:6,000	<i>Merck Millipore</i>	CB1001
GFP	1:1,000	<i>Aves Lab</i>	GFP-1020
MAP2	1:500	<i>Sigma Aldrich</i>	M4403
NEUN	1:500	<i>Merck Millipore</i>	MAB377
PAX6	1:500	<i>Biologend</i>	PRB-278p
Phospho-Ezrin (Thr567)/Radiixin (Thr564)/Moesin (Thr558) (41A3)	1:1000	<i>Cell Signalling</i>	3149S
Phospho-Histone H3 (PH3)	1:500	<i>Millipore</i>	06-570
P-VIMENTIN (Ser55)		<i>Biozol</i>	D076-3
SATB2	1:500	<i>Abcam</i>	ab51502
SSEA1 (eBioMC-480 (MC-480)), Alexa Fluor 488	1:200	<i>eBioscience™</i>	53-8813-41
TUBB3	1:500	<i>Sigma Aldrich</i>	T8660

Generation of isogenic *ECE2* Exon3/4 KO iPSC line. Two CrRNAs (one each in Exon 3 and Exon 4) of the *ECE2* gene were selected based on Geneious Prime, CCTop [64] and the guide design tool by Zhang lab (CRISPR.MIT.EDU). The selected Exon 3-CrRNA (5' GTTAGGCTCACGCACGCAGC 3') and Exon 4- CrRNA (5' GTTCCAGCGAGAACGCCCAT 3') were individually assembled and *in vitro* transcribed into guideRNA (gRNA) using the EnGen sgRNA Synthesis Kit, *S. pyogenes* (#E3322S, NEB). The *in vitro* transcribed guides were assembled into a gRNA-CAS9-NLS RNP complex by incubating the CAS9-NLS (#M0646M, NEB) and both *in vitro* transcribed gRNAs for 20 min at RT, followed by electroporation into single cells of the control iPSC line (see above) using Amaxa 4D nucleofector (Lonza). Electroporated cells were plated onto a 10 cm Geltrex (#A1413302, Thermo Fisher) coated dish supplemented with mTesR1 (#85850, StemCell Technologies) and Y-27632 (#72308, StemCell Technologies). The electroporated cells were allowed to recover for 10 days with daily media changes of mTeSR1 before single cell live sorting into Geltrex coated 96 well plates using CloneR (#05888, StemCell Technologies). The iPSC colonies were screened for INDELS using the protocol by Yusa K (doi:10.1038/nprot.2013.126) with the following primers:

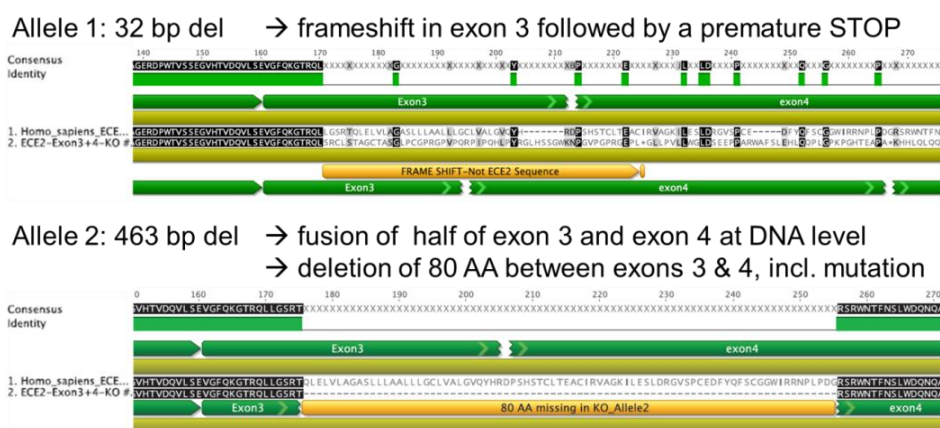
FW: 5' -CAGACTCAAGGCTCAACTCACTGGCTGGCCTCATTG- 3'

RV: 5' -CCATCAAACCCATCTGCACTTCTCAATAGTCC- 3'.

Putative positive clones were grown as individual KO lines. Genomic DNA was isolated from the generated KO iPSC lines using QIAamp DNA Mini Kit (#51306, Qiagen) and used as template with the above-mentioned primer pair. The resulting PCR product (906 bp) was cloned using NEB PCR Cloning Kit (#E1202S, NEB) and Sanger sequenced to screen the individual genomic alleles. All the Sanger sequencing was performed at the Sequencing facility of the Max Planck Institute of Molecular Cell Biology and Genetics, Dresden, Germany.

Manufacturer's recommendations and kit protocols were followed for all the kits and reagents mentioned above.

Two *ECE2* KO clones with the following modifications resulted, shown aligned to the consensus sequence (Yellow boxes summarize the introduced changes):



RNA isolation and RT-qPCR for *ECE2/Ece2* levels in miRNA validation and in NPCs and neurons. Cells were washed and scraped with cold PBS and the pellet was lysed in QIAzol® Lysis Reagent (#79306, Qiagen). RNA was extracted using RNA Clean & Concentrator Kit (#R1015, Zymo Research) and cDNA was synthesised from 2 µg RNA each using SuperScript III reverse transcriptase (#18080-044, Thermo Fisher) with

Oligo(dT)₁₂₋₁₈ primers (#18418012, *Thermo Fisher*) according to the manufacturer's protocol. Subsequently, qPCR was performed in triplicates on a LightCycler® 480 II (*Roche*) using the LightCycler® 480 SYBR Green I Master (#04707516001, *Roche*) with the following reaction mix 1 µL of each primer (5 µM), SYBR Green I Master 5 µL, H₂O 2 µL and 1 µL of cDNA. The primers sequences were the following for *ECE2*:

FW: 5'- AGAAGTCCTGTGTGCCGAGG- 3'

RV: 5'- ATGCGGTCCGGATTTTCGCT- 3'

and for *GAPDH*:

FW: 5'- AATCCCATCACCATCTTCCAGGA- 3'

RV: 5'- TGGACTCCACGACGTA CT CAG- 3'.

qPCR was done with: initial denaturation at 95 °C for 10 min, then 45 cycles of 95 °C 10 s, 60 °C 10 s and 72 °C 10 s) and a melting curve from 95 °C to 65 °C with 15s per step. C_p values were determined from the second derivative maximum of the amplification curve and fold expression was calculated using the $\Delta\Delta C_p$ method.

In situ hybridisation on cerebral organoids sections. *In-situ* hybridization (ISH) was performed based on exons 7-12 of full-length *ECE2* coned into pBluescript SK(+) (ordered from *Genscript*). For the generation of probes, 20 µg plasmid were digested for linearization with EcoRV for the sense and Kpn1 for the antisense probe (*NEB*). DNA was extracted using phenol-chloroform-isoamyl alcohol, pelleted using ammonium acetate and resuspended in RNase free water. *In vitro* transcription was performed from 1 µg each of the linearized plasmids using T7 polymerase for the sense probe and T3 for the antisense probe, together with the Digoxigenin (DIG) RNA labeling mix (*Roche*) according to the manufacturer's protocol.

For detection of mRNA transcripts, 16 µm frozen sections were hybridized with 1 µl probe in 150 µl hybridization buffer (formamide 50%, 1x SSC buffer (20x stock: 3M sodium chloride, 300 mM trisodium citrate, adjusted to pH 7.0 with HCl), 2% SDS, 50 µg/ml yeast tRNA (*Roche*), 2% blocking reagent (*Roche*) 2%, 50 µg /ml heparin (*Sigma*)) per slide at 65 °C overnight.

The next day, hybridization buffer was replaced by washing buffer (50% formamide, 1x SSC, 0.1 % Tween20 in H₂O) and the sections were washed at 65 °C for 10 min. This step was repeated twice for 30 min. Subsequently, the washing buffer was replaced by MABT (5x stock: 100 mM maleic acid, 150 mM sodium chloride, 0.1 % Tween20 in H₂O, pH adjusted to 7.5 with sodium hydroxide). Sections were incubated in MABT twice for 30 minutes at RT. Subsequently, sections were blocked using ISH blocking buffer (1x MABT, 2% blocking reagent (*Roche*), 2% FCS in H₂O) for 1 h at RT. Anti-DIG Fab Fragments (*Roche*) were then diluted 1:2,500 in ISH blocking buffer and incubated on the sections at 4 °C overnight.

The next day, sections were washed with MABT solution 5 times for 20 min. Afterwards, sections were incubated twice for 10 min in AP staining solution (100 mM Tris, pH 9.5, 50 mM magnesium chloride, 200 mM sodium chloride, 0.1 % Tween20 in H₂O). The AP staining solution was then replaced by AP staining solution containing NBT and BCIP (both *Roche*) in a 0.35% concentration, using 150 µl per slide. The color reaction was allowed to proceed overnight at 4°C and stopped by washing the sections with PBS. Sections were then stained with DAPI (0.02 mg/ml in PBS) to visualize nuclei.

Drug treatment and 2D timelapse imaging of young neurons. For timelapse imaging, NPCs were plated on a polyornithin/laminin coated 24-well-plate and left in neural progenitor medium (DMEM/F12 with HEPES and Glutamine, N2 1:100, B27 without

Vitamin A 1:50) without bFGF for 4 days with medium changes every other day to allow the cells to start differentiation. The control condition (CTRL) was additionally treated with DMSO 1:1,000, whereas in the other wells, 1 μ M Phosphoramidon (PHOS) (#R7385, *Sigma*) was added for ECE2 enzymatic inhibition [40]. After this, cells were imaged for 17 h using a Zeiss Axiovision Observer fluorescence microscope (*Zeiss*), maintaining 37°C and 5% carbon dioxide concentration. The cells were imaged every 10 min, several positions being taken per well. From the time lapse movies, movement data of single cells was derived using the Manual Tracking plugin for ImageJ [44]. No centering correction was applied. From the tracking data, cell movement parameters were calculated using Microsoft Excel 2013. Neuronal identity of tracked cells was confirmed after the time lapse imaging by TUBB3 immunostaining.

The average velocity was directly calculated from the measured velocities. The number of resting timepoints (TP) was calculated by counting the number of time points with a velocity of 0, and dividing this number by the length of the whole dataset for each cell. The tortuosity was calculated as division of the length of the path actually migrated by the net displacement of a cell from the beginning to the end of the track. Data is shown as z-scores calculated relative to the mean and standard deviation of the control within each experiment (N= total number of cells from two independent experiments). Stastical significance was tested via 2-tailed Chi-Square test.

Image acquisition. All imaging except for time lapse microscopy was performed using a Leica SP8 with the LASX Software from Leica and 25 x and 40 x water immersion objectives. Images were acquired in sequential xyz mode with at least 1024 x 1024 pixels and 1-1.5 μ m thickness of optical z layers. Images were saved as .lif file format to contain the metadata for the subsequent image analysis.

Image analysis. Image analysis was done in Fiji [44] using the manual cell counter and length and area measurement tools, as well as the Scalebar tool. Images are shown as Z-stacks. For the quantification of ectopic neurons upon *ECE2* KD, all NEUN+ cells in the progenitor zone within the electroporated area were counted. For normalization to the electroporation size, this number was related to the number of GFP+ RG. The size of cerebral organoids was measured based on the perimeter from brightfield images acquired at a Zeiss Axiovision Observer fluorescence microscope (*Zeiss*) with at least 10 organoids per timepoint and batch. Cell quantifications in the developing mouse cortex 1 dpe were done on a single image of the z-stack with the brightest staining in the middle of the stack by binning of the electroporated area, from apical to basal surface, into 5 equally big areas. Afterwards, single cells were counted using the manual cell counter. For quantification of brains 3 dpe, 6 brains per condition were analysed concerning the presence of ectopically positioned progenitors or deep- or upper layer neurons (at least 5 cells per parameter) and concerning the quality of the apical belt, including the appearance of additional ectopic apical surface in a yes-or-no system. Quantification of PH3+ mitotic apical neural progenitor cells in COs was done by counting apically localised PH3+ cells and normalization to the ventricle's apical surface length.

Quantification of intruding MAP2. To assess zonal disorganization in COs upon *ECE2* KO, the amount of ventricles in CTRL and *ECE2* KO organoids with intruding MAP2+ neuronal processes and/or with MAP2+ cell bodies localized in the progenitor zone were counted. In detail, ventricular zones containing more than 3 MAP2+ processes were categorized as "intruding processes" and those with MAP2+ cell bodies fell into the second, even more disorganized category.

Measurement of the thickness of apical F-ACTIN. The thickness of the apical F-ACTIN belt in ventricle-like zones of COs was determined by drawing and measuring the area of the Phalloidin-594-positive belt, measuring the length of the apical belt in its middle in parallel to the apical ventricular surface and dividing the area by the length.

Quantification of Acetylated tubulin. The quality of the microtubule cytoskeleton in COs was assessed by IHC for acetylated tubulin as marker for stabilized microtubules. Independent germinal zones of COs were rated as “1” if the acetylated tubulin staining revealed a radial organization of fibers in the progenitor zone, whereas “0” was given to ventricles with a reduced signal or with disorganized microtubule structure.

Quantification of Arl13B. Similar to quantification of acetylated tubulin, apical ARL13B in CO ventricles was rated as “1” for high signal and density of primary cilia and as “0” in case of reduced signal intensity and/or reduced apical localization of primary cilia.

FACS Analysis. For every FACS sample, 3 cerebral organoids were pooled. Organoids were washed with PBS and then enzymatically dissociated to single cells using Accutase (*StemCell Technologies*) for 3 x 10 min at 37 °C with gentle trituration using a P1000 pipette in between. After dissociation, samples were washed with PBS and centrifuged at 1,200 rpm for 5 min. Subsequently, the suspension was filtered through a 100 µm cell strainer and cells were collected by centrifugation at 1,200 rpm for 5 min. Cells were then fixed with 5 ml ice cold 70 % EtOH for 1h at -20 °C. Afterwards, they were centrifuged for 30 min at 2000 rpm and 4 °C, resuspended in 5 ml staining buffer (1 % FBS in PBS) for washing and centrifuged by further centrifugation for 30 min at 2000 rpm and 4 °C, afterwards removing all except for 50 µl supernatant containing the cells that were kept at 4 °C. A few µl of each sample were collected and pooled to be used as isotype controls (IC). Staining was performed the next day by diluting primary antibodies in staining buffer (Concentrations different from Antibodies Table: gp-α-DCX 1:1,000; mlgG1-α-MAP2 1:500; rb-α-PAX6 1:300; rb-α-PH3 1:300) and adding 20 µl resulting staining solution to each sample and incubating on ice for 30 min, followed by addition of 1 ml staining buffer each and 30 min centrifugation for washing. Supernatant was again removed, leaving the cells in 50 µl leftover staining buffer. They were resuspended with staining solution containing the AlexaFluor-conjugated secondary antibodies (1:800 final dilution), incubated for another 30 min on ice and washed as before. IC were also immunostained with secondary antibodies. The labeled cells were then resuspended in PBS for FACS analysis. FACS analysis was performed using a FACS Aria (BD) in BD FACS Flow TM Medium with a nozzle diameter of 100 µm and a flow rate below 500 events/sec. Debris and cell aggregates were gated out by forward scatter (FSC) – side scatter (SSC); single cells were gated out by FSC-W/FSC-A. Gating strategies for fluorophores were selected using ICs for the different secondary antibodies. Examples of the gating strategy are shown in **Figure EV3**.

Statistics. Statistics for quantifications of immunohistochemical stainings in COs and embryonic mouse brain was performed in SigmaPlot (Version 13.0; Systat Software, San Jose, CA) unless stated otherwise below. Data was tested for normal distribution by Shapiro-Wilk test. Normally distributed data was analysed further by Brown-Forsythe test for equal variance. One-way ANOVA and Tukey test was then applied for normally distributed data of equal variance. Kruskal-Wallis ANOVA on Ranks and Dunn’s Pairwise Multiple Comparison were used for non-normally distributed data. Exact binomial test was done using Graphpad Prism. Mann Whitney U test and hierarchical clustering analysis using chi-square test were done in STATISTICA (StatSoft Inc.). For timelapse imaging

results, statistical significance was tested in SPSS (Statistical Package for Social Science, IBM®) via 2-tailed Chi-Square test. For electroporation of COs, 4 batches of organoids were analysed for each construct with several organoids each. Data is shown with n = total number of electroporated ventricles analysed per construct from organoids from all batches combined. For *in vivo* analyses after *in utero* electroporation, 3 CTRL and 4 *Ece2* KD brains were analysed with at least 2 sections per brain in the binning analysis 1 dpe (E13-14) and 6 brains per condition for 3 dpe (E13-16). For *ECE2* KO COs, FACS analysis, WB and MS was performed on 3 independent batches and IHC was performed on COs from 2 different batches. In detail, 3 organoids were combined to be one FACS or WB sample (1 n), 20 organoids per condition and batch were combined for MS, and IHC was done using 6 organoids per condition and batch. Whenever data is shown as box plot, the mean is marked by a red line, the median with a black line, and the box represents 25th and 75th percentiles with whiskers extending to 10th and 90th percentiles, with all outliers shown.

Westernblot. Cells or whole cerebral organoids were collected and washed with PBS prior to lysis in lysis buffer (62.5 mM Tris-HCl pH 6.8, 2% SDS, and 10% saccharose in H₂O with protease inhibitor mix (*Roche*) added just before use) and protein concentration was determined with the Pierce™ BCA Protein Assay Kit (#23227, *Thermo Fisher*). 20 μ g protein per lane were then loaded and separated by SDS-PAGE with 10-12% gels. Proteins were transferred onto a nitrocellulose membrane (*GE Healthcare*) with blotting buffer (129 mM Glycine, 25 mM Tris-base, methanol 20%) for 90 min at 100 V. After blotting, the membrane was blocked with 5 % milk powder in TBS-T before incubation with the primary antibody in 2.5 % Milk in TBS-T at 4°C overnight (see *Table: Primary antibodies*). After washes with TBS-T, membranes were incubated with HRP-conjugated secondary antibody diluted 1:10,000 in 2.5 % milk in TBS-T for 1h at RT. For protein detection, membranes were incubated with ECL detection reagent (*Millipore*) and visualized using the ChemiDoc system (*Biorad*). Band intensities were quantified using the ImageLab™ Software (*Biorad*).

Whole-mount staining and clearing (iDISCO). For staining and clearing of whole organoids, the iDISCO method was used [43] with the antibodies staining ARL13B, NEUN and DCX and DAPI for nuclear counterstain. Prior to use in whole-mount staining, antibodies were tested for methanol (MeOH) compatibility as suggested. The staining and clearing protocol was then followed with minor changes. In detail, organoids were dehydrated with increasing volumes of MeOH in water (20%, 40%, 60%, 80% and 100% MeOH), 1h incubation at RT each, while shaking. Organoids were washed further with 100% MeOH and incubated 1h at 4°C. Then, organoids were incubated with a 66% DiChloroMethane (DCM)/33% MeOH solution overnight at RT in continuous agitation. The following day, they were washed twice in 100% MeOH for 15 min at RT. Samples were subsequently bleached in 5% H₂O₂ in MeOH overnight at 4°C. The samples were then rehydrated with decreasing volumes of MeOH in water (80%, 60%, 40%, 20% and PBS), continuously shaking for 1h each at RT. After this, the samples were permeabilized using a 0.2% TritonX solution in PBS twice for 1h at RT. In order to further facilitate the permeabilization of primary antibodies in following steps, the samples were incubated in permeabilization solution (0.2% TritonX in PBS + 2% DMSO, 0.3M Glycine) at 37°C for 1 day. Following permeabilization, samples were incubated with 0.2% TritonX in PBS + 10% DMSO and 6% Normal Goat Serum at 37°C for 1d for blocking. Primary antibodies (rb- α -ARL13B 1:200, mlgG1- α -NEUN 1:200, gp- α -DCX 1:800) were diluted in washing solution (0.2% Tween-20 in PBS, 10 mg/ml heparin) supplemented with 5% DMSO and

3% NGS and added to the samples, incubating at 37°C for 2d. Afterwards, samples were washed with washing solution 5 times over the course of 1d. The AlexaFluor-conjugated secondary antibodies were diluted 1:300 (DAPI 1:1000) in washing solution, adding 3% NGS without DMSO, and incubated for 2d at 37°C. Organoids were then washed 4-5 times over 1d before clearing.

For clearing, organoids were first dehydrated with increasing concentrations of MeOH in water (20%, 40%, 60% 80% and 100%) for 1h each at RT with continuous agitation. The 100% MeOH was repeated twice and the organoids kept overnight at this stage. The following day, they were transferred to a solution containing 66% DCM/33% MeOH at RT in continuous agitation. Organoids were washed twice with 100% DCM for 15 minutes in order to completely remove the MeOH. Eventually, the solution was removed and samples were placed in 100% DiBenzyl Ether (DBE) without agitation for clearing. Samples were covered completely with the DBE solution to prevent oxidation.

Organoids were positioned in self-made silicon chambers filled with DBE for imaging at the Leica SP8 laser scanning microscope. Videos were generated using Imaris Software.

Whole proteome analysis from COs. COs were washed twice with PBS and homogenized in ice-cold lysis buffer (1% (v/v) NP40, 1% (w/v) sodium deoxycholate and 1 tablet protease inhibitor (cOmplete™, Mini, EDTA-free protease inhibitor cocktail, Roche) in 10 mL PBS) using ultrasonication at 40 % intensity for 10 s. Lysis was done for 30 min at 4 °C while rotating. The insoluble fraction was pelletized (10 min, 14,000 g, 4 °C) and protein concentration was determined by bicinchoninic acid assay (BCA, Carl Roth GmbH + Co.). For the next analysis, 200 µg of the total protein was used. Proteins were precipitated by addition of 900 µL acetone and incubation overnight at -20 °C. The protein pellet was harvested by centrifugation at 9,000 g for 15 min at 4 °C and washed once with 0.5 mL of ice cold methanol. Proteins were reconstituted in 200 µL digestion buffer (20 mM HEPES, pH 7.5, 7 M urea, 2 M thiourea), reduced (0.2 µL 1 M DTT, 45 min, 25 °C) and alkylated (2 µL, 30 min, 25 °C, in the dark). The alkylation reaction was quenched by addition of 0.8 µL 1M DTT and incubation for 30 min at 25 °C. Proteins were pre-digested with 1 µL LysC (Wako) at 25 °C for 4 h. 600 µL 50 mM TEAB buffer was added and the proteins were digested overnight with 1.5 µL sequencing grade trypsin (0.5 mg/mL, Promega) at 37 °C. The following day the samples were acidified with 10 µL formic acid to a pH of 2 – 3. Peptides were desalted on 50 mg SepPak C18 cartridges (Waters Corp.) on a vacuum manifold. The cartridges were equilibrated with 1 mL acetonitrile, 1 mL 80% acetonitrile and 3 mL 0.5% formic acid. The samples were loaded on the cartridges and subsequently washed with 5 mL 0.5% formic acid. The peptides were eluted with two times 250 µL 80% acetonitrile, 0.5% formic acid. Samples were combined and dried by lyophilization. Peptides were reconstituted in 30 µL 1% (v/v) formic acid, prepared for mass spectrometry by filtering through a membrane filter (Ultrafree-MC and -LC, Durapore PVDF-0.22 µm, Merck Millipore) and transferred into mass vials.

Secretome analysis from COs. For secretome analysis, 5 ml culture medium (NDM+A) was collected from 60d old COs after 4 days of conditioning. The medium was cleared from dead cells and debris by centrifugation at 600 rpm for 5 min. To the cleared medium, 30 ml MeOH was added for protein precipitation at -20 °C overnight. Precipitated protein was then harvested by centrifugation at 9,000 g and 4 °C for 15 min. Secretome samples were then further prepared for proteomic analysis as described above for the whole CO proteome.

Mass Spectrometry. MS analysis was performed on Q Exactive Plus instrument coupled to an Ultimate3000 Nano-HPLC via an electrospray easy source (all Thermo Fisher Scientific). Samples were loaded on a 2 cm PepMap RSLC C18 trap column (particles 3 μm , 100A, inner diameter 75 μm , Thermo Fisher Scientific) with 0.1% TFA and separated on a 50 cm PepMap RSLC C18 column (particles 2 μm , 100A, inner diameter 75 μm , Thermo Fisher Scientific) constantly heated at 50 °C. The gradient was run from 5-32% acetonitrile, 0.1% formic acid during a 152 min method (7 min 5%, 105 min to 22%, 10 min to 32%, 10 min to 90%, 10 min wash at 90%, 10 min equilibration at 5%) at a flow rate of 300 nL/min. For measurements of chemical-proteomic samples on the Q Exactive Plus instrument survey scans (m/z 300-1,500) were acquired in the orbitrap with a resolution of 70,000 at m/z 200 and the maximum injection time set to 80 ms (target value 3e6). Data dependent HCD fragmentation scans of the 12 most intense ions of the survey scans were acquired in the orbitrap at a resolution of 17,500, maximum injection time of 50 ms as well as minimum and maximum AGC targets of 5e3 and 5e4, respectively. The isolation window was set to 1.6 m/z . Unassigned and singly charged ions were excluded for measurement and the dynamic exclusion of peptides enabled for 60 s. The lock-mass ion 445.12002 from ambient air was used for real-time mass calibration on the Q Exactive Plus. Data were acquired using Xcalibur software version 3.1sp3 (Thermo Fisher Scientific).

Raw files were analysed using MaxQuant software (1.6.2.10). Searches were performed against the Uniprot database for Homo sapiens (taxon identifier: 9606, 21st December 2018, including isoforms). At least two unique peptides were required for protein identification. False discovery rate determination was carried out using a decoy database and thresholds were set to 1 % FDR both at peptide-spectrum match and at protein levels.

Phosphosites were identified by MaxQuant default settings for pSTY and quantified by LFQ. Average protein occupancy of the phosphosites were compared between CTRL and KO COs (**Tables EV7-9**). Phosphosites identified only in CTRL or KO COs (**Table EV8**) were required to be found at least twice within the replicates with localization probability higher than 70%.

Statistical analysis of the MaxQuant result table proteinGroups.txt was done with Perseus 1.5.1.6. Putative contaminants and reverse hits were removed. LFQ intensities were log2-transformed, hits with less than 3 valid values in each group were removed and $-\log_{10}(\text{p-values})$ were obtained by a two-sided one sample Student's t-test over replicates with the initial significance level of $p = 0.05$ adjustment by the multiple testing correction method of Benjamini and Hochberg (FDR = 0.05), the $-\log_{10}$ of p-values were plotted by volcano plot function. Final volcano plots were edited in Origin.

GO Term analysis. Protein interaction network analysis was performed using STRING.db [51]. For GO Term analysis of proteins significantly downregulated in *ECE2* KO COs underlying the categories in **Figure 5B**, both STRING.db [51] and PANTHER (pantherdb.org; [50]), choosing *homo sapiens* as species, were used to identify overrepresented functional protein groups and single proteins falling into those. For the category 'neurodevelopmental disorder', the effect of known mutations in each gene was analysed using DECIPHER [49] and focusing on SNVs and small indels (monogenic variants). Dysregulated phosphosites from **Table EV7**, illustrated in **Figure 5D**, were uploaded into PANTHER database and searched for enrichment of cellular component complete using Fisher's exact test and FDR threshold of 0.05.

References

1. Götz M, Huttner WB (2005) The cell biology of neurogenesis. *Nat Rev Mol Cell Biol* **6**: 777–788.
2. Kriegstein AR, Noctor SC (2004) Patterns of neuronal migration in the embryonic cortex. *Trends Neurosci* **27**: 392–399.
3. Lui JH, Hansen D V, Kriegstein AR (2011) Development and evolution of the human neocortex. *Cell* **146**: 18–36.
4. Taverna E, Götz M, Huttner WB (2014) The Cell Biology of Neurogenesis: Toward an Understanding of the Development and Evolution of the Neocortex. *Annu Rev Cell Dev Biol* **30**: 465–502.
5. Nadarajah B, Brunstrom JE, Grutzendler J, Wong RO, Pearlman AL (2001) Two modes of radial migration in early development of the cerebral cortex. *Nat Neurosci* **4**: 143–50.
6. Buchsbaum IY, Cappello S (2019) Neuronal migration in the CNS during development and disease: insights from in vivo and in vitro models. *Development* **146**.
7. Barkovich AJ, Kuzniecky RI (2000) Gray matter heterotopia. *Neurology* **55**: 1603–1608.
8. Dubeau F, Tampieri D, Lee N, Andermann E, Carpenter S, Leblanc R, Olivier A, Radtke R, Villemure JG, Andermann F (1995) Periventricular and subcortical nodular heterotopia. A study of 33 patients. *Brain* **118** (Pt 5): 1273–1287.
9. Cappello S, Böhringer CRJ, Bergami M, Conzelmann K-K, Ghanem A, Tomassy GS, Arlotta P, Mainardi M, Allegra M, Caleo M, et al. (2012) A Radial Glia-Specific Role of RhoA in Double Cortex Formation. *Neuron* **73**: 911–924.
10. Cappello S, Gray MJ, Badouel C, Lange S, Einsiedler M, Srour M, Chitayat D, Hamdan FF, Jenkins ZA, Morgan T (2013) Mutations in genes encoding the cadherin receptor-ligand pair DCHS1 and FAT4 disrupt cerebral cortical development. *Nat Genet* **45**: 1300–1308.
11. Carabalona A, Beguin S, Pallesi-Pocachard E, Buhler E, Pellegrino C, Arnaud K, Hubert P, Oualha M, Siffroi JP, Khantane S, et al. (2012) A glial origin for periventricular nodular heterotopia caused by impaired expression of Filamin-A. *Hum Mol Genet* **21**: 1004–1017.
12. Kielar M, Tuy FPD, Bizzotto S, Lebrand C, de Juan Romero C, Poirier K, Oegema R, Mancini GM, Bahi-Buisson N, Olaso R, et al. (2014) Mutations in Eml1 lead to ectopic progenitors and neuronal heterotopia in mouse and human. *Nat Neurosci* **17**: 923–933.
13. Klaus J, Kanton S, Kyrousi C, Ayo-Martin AC, Di Giaimo R, Riesenberger S, O'Neill AC, Camp JG, Tocco C, Santel M, et al. (2019) Altered neuronal migratory trajectories in human cerebral organoids derived from individuals with neuronal heterotopia. *Nat Med* **1**.
14. Fox JW, Lamperti ED, Eksioğlu YZ, Hong SE, Feng Y, Graham DA, Scheffer IE, Dobyns WB, Hirsch BA, Radtke RA, et al. (1998) Mutations in filamin 1 prevent migration of cerebral cortical neurons in human periventricular heterotopia. *Neuron* **21**: 1315–1325.
15. Lu J, Tiao G, Folkert R, Hecht J, Walsh C, Sheen V (2006) Overlapping expression of ARFGEF2 and filamin A in the neuroependymal lining of the lateral ventricles: Insights into the cause of periventricular heterotopia. *J Comp Neurol* **494**: 476–484.
16. Parrini E, Ramazzotti A, Dobyns WB, Mei D, Moro F, Veggiotti P, Marini C, Brillstra EH, Dalla Bernardina B, Goodwin L, et al. (2006) Periventricular heterotopia: phenotypic heterogeneity and correlation with Filamin A mutations. *Brain* **129**: 1892–1906.

17. Sheen VL, Basel-Vanagaite L, Goodman JR, Scheffer IE, Bodell A, Ganesh VS, Ravenscroft R, Hill RS, Cherry TJ, Shugart YY, et al. (2004) Etiological heterogeneity of familial periventricular heterotopia and hydrocephalus. *Brain Dev* **26**: 326–334.
18. Bardón-Cancho EJ, Muñoz-Jiménez L, Vázquez-López M, Ruíz-Martín Y, García-Morín M, Barredo-Valderrama E (2014) Periventricular nodular heterotopia and dystonia due to an ARFGEF2 mutation. *Pediatr Neurol* **51**: 461–464.
19. Lu J, Sheen V (2005) Periventricular heterotopia. *Epilepsy Behav* **7**: 143–149.
20. Sheen VL (2014) Filamin A mediated Big2 dependent endocytosis. **2**: 1–6.
21. Sheen VL, Ganesh VS, Topcu M, Sebire G, Bodell A, Hill RS, Grant PE, Shugart YY, Imitola J, Khoury SJ, et al. (2004) Mutations in ARFGEF2 implicate vesicle trafficking in neural progenitor proliferation and migration in the human cerebral cortex. *Nat Genet* **36**: 69–76.
22. Shin H-W, Shinotsuka C, Nakayama K (2005) Expression of BIG2 and analysis of its function in mammalian cells. *Methods Enzymol* **404**: 206–215.
23. Trimborn M, Bell SM, Felix C, Rashid Y, Jafri H, Griffiths PD, Neumann LM, Krebs A, Reis A, Sperling K, et al. (2004) Mutations in microcephalin cause aberrant regulation of chromosome condensation. *Am J Hum Genet* **75**: 261–266.
24. Badouel C, Zander MA, Liscio N, Bagherie-Lachidan M, Sopko R, Coyaud E, Raught B, Miller FD, McNeill H (2015) Fat1 interacts with Fat4 to regulate neural tube closure, neural progenitor proliferation and apical constriction during mouse brain development. *Development* **142**: 2781–2791.
25. Oegema R, Baillat D, Schot R, van Unen LM, Brooks A, Kia SK, Hoogeboom AJM, Xia Z, Li W, Cesaroni M, et al. (2017) Human mutations in integrator complex subunits link transcriptome integrity to brain development. *PLoS Genet* **13**: e1006809.
26. Broix L, Jagline H, Ivanova E, Schmucker S, Drouot N, Clayton-Smith J, Pagnamenta AT, Metcalfe KA, Isidor B, Louvier UW, et al. (2016) Mutations in the HECT domain of NEDD4L lead to AKT-mTOR pathway deregulation and cause periventricular nodular heterotopia. *Nat Genet* **48**: 1349–1358.
27. Heinzen EL, O'Neill AC, Zhu X, Allen AS, Bahlo M, Chelly J, Chen MH, Dobyns WB, Freytag S, Guerrini R, et al. (2018) De novo and inherited private variants in MAP1B in periventricular nodular heterotopia. *PLOS Genet* **14**: e1007281.
28. O'Neill AC, Kyrousi C, Einsiedler M, Burtcher I, Drukker M, Markie DM, Kirk EP, Götz M, Robertson SP, Cappello S (2018) Mob2 Insufficiency Disrupts Neuronal Migration in the Developing Cortex. *Front Cell Neurosci* **12**: 57.
29. O'Neill AC, Kyrousi C, Klaus J, Leventer RJ, Kirk EP, Fry A, Pilz DT, Morgan T, Jenkins ZA, Drukker M, et al. (2018) A Primate-Specific Isoform of PLEKHG6 Regulates Neurogenesis and Neuronal Migration. *Cell Rep* **25**: 2729–2741.e6.
30. Cellini E, Vetro A, Conti V, Marini C, Doccini V, Clementella C, Parrini E, Giglio S, Della Monica M, Fichera M, et al. (2019) Multiple genomic copy number variants associated with periventricular nodular heterotopia indicate extreme genetic heterogeneity. *Eur J Hum Genet* **1**.
31. Boyer LF, Campbell B, Larkin S, Mu Y, Gage FH (2012) Dopaminergic differentiation of human pluripotent cells. *Curr Protoc Stem Cell Biol* Chapter **1**: Unit1H.6.
32. Lancaster MA, Knoblich JA (2014) Generation of cerebral organoids from human pluripotent stem cells. *Nat Protoc* **9**: 2329–2340.
33. Tabata H, Nakajima K (2001) Efficient in utero gene transfer system to the developing mouse brain using electroporation: visualization of neuronal migration in the developing cortex. *Neuroscience* **103**: 865–872.
34. Mzhavia N, Pan H, Che F-Y, Fricker LD, Devi LA (2003) Characterization of endothelin-converting enzyme-2. Implication for a role in the nonclassical processing of regulatory peptides. *J Biol Chem* **278**: 14704–14711.

35. Pan H, Mzhavia N, Devi L (2004) Endothelin Converting Enzyme-2: A Processing Enzyme Involved in the Generation of Novel Neuropeptides. *Protein Pept Lett* **11**: 461–469.
36. Palmer JC, Baig S, Kehoe PG, Love S (2009) Endothelin-converting enzyme-2 is increased in Alzheimer's disease and up-regulated by Abeta. *Am J Pathol* **175**: 262–270.
37. Pacheco-Quinto J, Eckman EA (2013) Endothelin-converting enzymes degrade intracellular β -amyloid produced within the endosomal/lysosomal pathway and autophagosomes. *J Biol Chem* **288**: 5606–5615.
38. Rodriguiz RM, Gadnidge K, Ragnauth A, Dorr N, Yanagisawa M, Wetsel WC, Devi LA (2008) Animals lacking endothelin-converting enzyme-2 are deficient in learning and memory. *Genes Brain Behav* **7**: 418–426.
39. Burke EE, Chenoweth JG, Shin JH, Collado-Torres L, Kim SK, Micali N, Wang Y, Straub RE, Hoepfner DJ, Chen H-Y, et al. (2018) Dissecting transcriptomic signatures of neuronal differentiation and maturation using iPSCs. *bioRxiv* 380758.
40. Emoto N, Yanagisawa M (1995) Endothelin-converting enzyme-2 is a membrane-bound, phosphoramidon-sensitive metalloprotease with acidic pH optimum. *J Biol Chem* **270**: 15262–15268.
41. Florio M, Huttner WB (2014) Neural progenitors, neurogenesis and the evolution of the neocortex. *Development* **141**: 2182–2194.
42. Reed NA, Cai D, Blasius TL, Jih GT, Meyhofer E, Gaertig J, Verhey KJ (2006) Microtubule acetylation promotes kinesin-1 binding and transport. *Curr Biol* **16**: 2166–2172.
43. Renier N, Wu Z, Simon DJ, Yang J, Ariel P, Tessier-Lavigne M (2014) IDISCO: A simple, rapid method to immunolabel large tissue samples for volume imaging. *Cell* **159**.
44. Schindelin J, Arganda-Carreras I, Frise E, Kaynig V, Longair M, Pietzsch T, Preibisch S, Rueden C, Saalfeld S, Schmid B, et al. (2012) {Fiji}: an open-source platform for biological-image analysis. *Nat Methods* **9**: 676–682.
45. Camp JG, Badsha F, Florio M, Kanton S, Gerber T, Wilsch-Bräuninger M, Lewitus E, Sykes A, Hevers W, Lancaster M, et al. (2015) Human cerebral organoids recapitulate gene expression programs of fetal neocortex development. *Proc Natl Acad Sci U S A* **112**: 15672–15677.
46. Pollen AA, Bhaduri A, Andrews MG, Nowakowski TJ, Meyerson OS, Mostajo-Radji MA, Di Lullo E, Alvarado B, Bedolli M, Dougherty ML, et al. (2019) Establishing Cerebral Organoids as Models of Human-Specific Brain Evolution. *Cell* **176**: 743–756.e17.
47. Quadrato G, Nguyen T, Macosko EZ, Sherwood JL, Min Yang S, Berger DR, Maria N, Scholvin J, Goldman M, Kinney JP, et al. (2017) Cell diversity and network dynamics in photosensitive human brain organoids. *Nature* **545**: 48–53.
48. McClure-Begley TD, Ebmeier CC, Ball KE, Jacobsen JR, Kogut I, Bilousova G, Klymkowsky MK, Old WM (2018) Cerebral organoid proteomics reveals signatures of dysregulated cortical development associated with human trisomy 21. *bioRxiv* 315317.
49. Firth H V., Richards SM, Bevan AP, Clayton S, Corpas M, Rajan D, Vooren S Van, Moreau Y, Pettett RM, Carter NP (2009) DECIPHER: Database of Chromosomal Imbalance and Phenotype in Humans Using Ensembl Resources. *Am J Hum Genet* **84**: 524–533.
50. Mi H, Huang X, Muruganujan A, Tang H, Mills C, Kang D, Thomas PD (2017) PANTHER version 11: expanded annotation data from Gene Ontology and Reactome pathways, and data analysis tool enhancements. *Nucleic Acids Res* **45**: D183–D189.
51. Szklarczyk D, Morris JH, Cook H, Kuhn M, Wyder S, Simonovic M, Santos A, Doncheva NT, Roth A, Bork P, et al. (2017) The STRING database in 2017: quality-

- controlled protein–protein association networks, made broadly accessible. *Nucleic Acids Res* **45**: D362–D368.
52. Del Toro D, Ruff T, Cederfjäll E, Villalba A, Seyit-Bremer G, Borrell V, Klein R (2017) Regulation of Cerebral Cortex Folding by Controlling Neuronal Migration via FLRT Adhesion Molecules. *Cell* **169**: 621–635.e16.
 53. Davenport AP, Kuc RE (2000) Cellular expression of isoforms of endothelin-converting enzyme-1 (ECE-1c, ECE-1b and ECE-1a) and endothelin-converting enzyme-2. *J Cardiovasc Pharmacol* **36**: S12-4.
 54. Fietz S a., Lachmann R, Brandl H, Kircher M, Samusik N, Schroder R, Lakshmanaperumal N, Henry I, Vogt J, Riehn A, et al. (2012) Transcriptomes of germinal zones of human and mouse fetal neocortex suggest a role of extracellular matrix in progenitor self-renewal. *Proc Natl Acad Sci* **109**: 11836–11841.
 55. Florio M, Albert M, Taverna E, Namba T, Brandl H, Lewitus E, Haffner C, Sykes A, Wong FK, Peters J, et al. (2015) Human-specific gene ARHGAP11B promotes basal progenitor amplification and neocortex expansion. *Science* (80-) **347**: 1465–1470.
 56. Long KR, Newland B, Florio M, Kalebic N, Langen B, Kolterer A, Wimberger P, Huttner WB (2018) Extracellular Matrix Components HAPLN1, Lumican, and Collagen I Cause Hyaluronic Acid-Dependent Folding of the Developing Human Neocortex. *Neuron* **99**: 702–719.e6.
 57. Pollen AA, Nowakowski TJ, Chen J, Retallack H, Sandoval-Espinosa C, Nicholas CR, Shuga J, Liu SJ, Oldham MC, Diaz A, et al. (2015) Molecular Identity of Human Outer Radial Glia during Cortical Development. *Cell* **163**:
 58. Song Y, Brady ST (2015) Post-translational modifications of tubulin: pathways to functional diversity of microtubules. *Trends Cell Biol* **25**: 125–136.
 59. Cooper GM, Stone EA, Asimenos G, NISC Comparative Sequencing Program ED, Green ED, Batzoglu S, Sidow A (2005) Distribution and intensity of constraint in mammalian genomic sequence. *Genome Res* **15**: 901–913.
 60. Ng PC, Henikoff S (2003) SIFT: Predicting amino acid changes that affect protein function. *Nucleic Acids Res* **31**: 3812–3814.
 61. Rentzsch P, Witten D, Cooper GM, Shendure J, Kircher M (2019) CADD: predicting the deleteriousness of variants throughout the human genome. *Nucleic Acids Res* **47**: D886–D894.
 62. Adzhubei IA, Schmidt S, Peshkin L, Ramensky VE, Gerasimova A, Bork P, Kondrashov AS, Sunyaev SR (2010) A method and server for predicting damaging missense mutations. *Nat Methods* **7**: 248–249.
 63. Saito T (2006) In vivo electroporation in the embryonic mouse central nervous system. *Nat Protoc* **1**: 1552–1558.
 64. Stemmer M, Thumberger T, del Sol Keyer M, Wittbrodt J, Mateo JL (2015) CCTop: An Intuitive, Flexible and Reliable CRISPR/Cas9 Target Prediction Tool. *PLoS One* **10**: e0124633.

EXPANDED VIEW FIGURES

ECE2 regulates Neurogenesis and Neuronal Migration during Human Cortical Development

Isabel Y. Buchsbaum, Pavel Kielkowski, Grazia Giorgio, Adam C. O'Neill, Rossella di Giaimo, Christina Kyrousi, Shahryar Khattak, Stephan A. Sieber, Stephen P. Robertson and Silvia Cappello

Figure legends expanded view (EV)

Figure EV1: aRG delamination 4dpe upon *ECE2* KD in *in vitro* human model systems. **A, B,** Schemes depicting the generation of NPCs and neurons in 2D (**A**) [31] and in 3D in cerebral organoids (COs, **B**) [32]. **C,** Analysis of immunostaining of COs 4 dpe upon *ECE2* KD by electroporation shows delamination of transfected aRG, in contrast to bipolar morphology of aRG in the control condition (aRG = apical radial glia, dpe = days post electroporation; transfected cells are shown in green, MAP2+ neuronal processes in magenta; Scalebar = 50µm).

Figure EV2: *Ece2* KD *in vivo* leads to changes in apico-basal polarity and in progenitor and neuron positioning. **A-G,** 1 dpe upon *Ece2* KD, proliferative progenitors acquire ectopic positions (**A-C**). Some deep- (**D, E**) and upper-layer (**F**) neurons show the same tendency. **A,** Quantification of distribution of Pax6+ transfected progenitors upon *Ece2* KD relative to CTRL shows tendential shift to bin 2 (n=3 CTRL and 4 *Ece2* KD brains; $P = 0.082$ in One-way ANOVA; data shown as mean±SEM). **E,** Quantification of ectopic deep-layer neurons 1 dpe shows trend to ectopic, less basal position upon *Ece2* KD (n=3 CTRL and 4 *Ece2* KD brains; $P = 0.156$ in One-way ANOVA; data shown as mean±SEM). **G,** aRG morphology is changed and the apical surface shows patches lacking apically localised Arl13b 1 dpe. **H,** Example images of 3 dpe showing delaminated ectopic progenitors form rosettes and nodules. **A-H,** Electroporated cells shown in green; Scalebar = 100 µm.

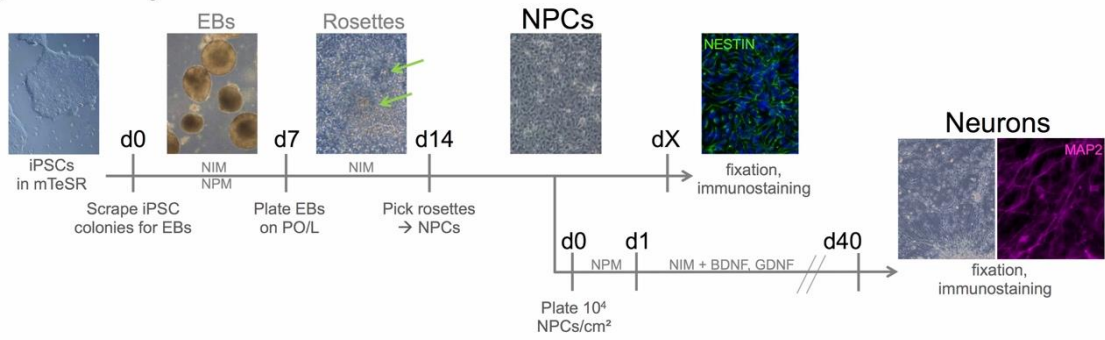
Figure EV 3: *ECE2* inhibition and KO in COs reveal its influence on cell fate. **A,** IHC for cleaved Caspase-3 shows no difference in cell death upon *ECE2* inhibition (Scalebar = 50 µm). **B,** FACS plots illustrating gating strategies for SSEA, BLBP and MAP2 gated cells in CTRL and PHOS treated COs. Gates were established using 2ndary antibody only as isotype control. **C,** Example images of IHC of germinal zones in COs after two weeks of PHOS treatment with mitotic cells stained for PH3 (green) (Scalebar = 50 µm). **D,** Quantification of PH3+ cells per length of apical surface in PHOS-treated vs. CTRL COs reveals no difference (Data shown as box plots with median as black line, mean red line; n=number of analysed ventricles from 2 batches of COs; One

Way ANOVA: $P = 0.633$). **E**, Brightfield images of *ECE2* KO and isogenic control iPSCs and of COs generated from them. **F**, Size measurement *ECE2* KO vs. CTRL COs revealed no consistent difference (Data shown as z-scores; $n=4$ batches of COs with at least 10 COs each per timepoint, area measured from 2D BF images in Fiji [44]). **G**, FACS plots illustrating the gating strategies for PAX6, PH3 and MAP2 gated cells in CTRL and *ECE2* KO COs. Gates were established from the 2ndary only control. **H**, Example images of IHC for PH3+ cells in 60d old CTRL and *ECE2* KO COs (Scalebar = 50 μm). **I**, Quantification of PH3+ cycling cells in 60d old COs, normalised to length of the apical surface of ventricle-like structures, shows an increase upon *ECE2* KO (Data shown as box plots with median as black line, mean red line; n =number of analysed ventricles from 2 batches of COs; One Way ANOVA: $**P = 0.004$). **J**, Example images of progenitor zone (SOX2) and neuronal layer (MAP2) staining by IHC (Scalebar = 50 μm).

Figure EV4: The apical belt is disrupted in the absence of ECE2. **A**, WB on CO lysate for CTNNB1 with GAPDH as loading control. **B**, Quantification from WB shows a slight reduction in CTNNB1 in *ECE2* KO COs (Data shown as box plots with median as black line, mean red line; $n=3$ batches of COs with 3 COs each; One Way ANOVA: n.s., $P = 0.178$). **C**, Protein interaction analysis [51] shows network with ECE2 (red circle) and 3 interacting proteins that were identified as downregulated upon KO (green squares), including the known PH gene *FLNA*. **D**, WB of iPSC lysate confirms a strong reduction of pERM, detected by MS of *ECE2* KO COs. **E**, Network analysis [51] reveals that downregulated proteins in *ECE2* KO COs are part of a tightly interconnected PPI network with ECM proteins as the biggest subnetwork.

Figure EV1

A 2D Monolayer



B 3D Cerebral Organoids

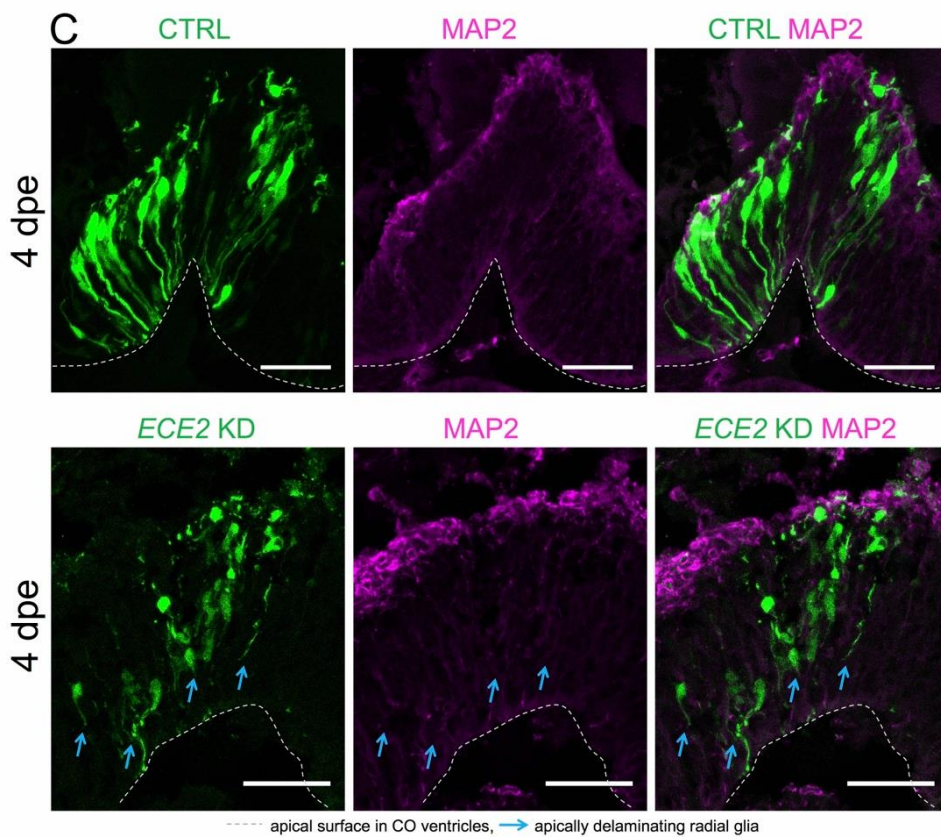
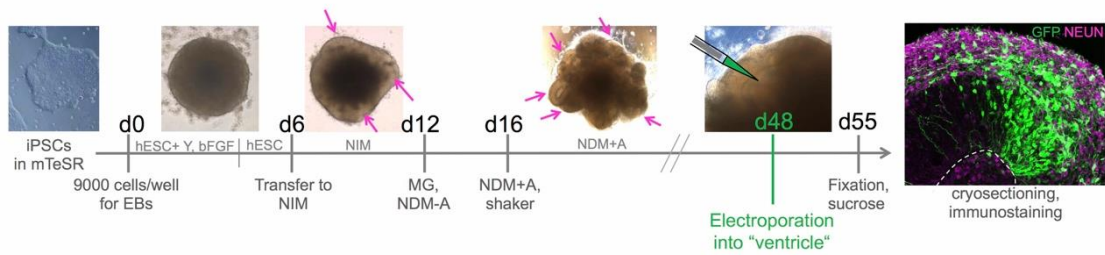


Figure EV2

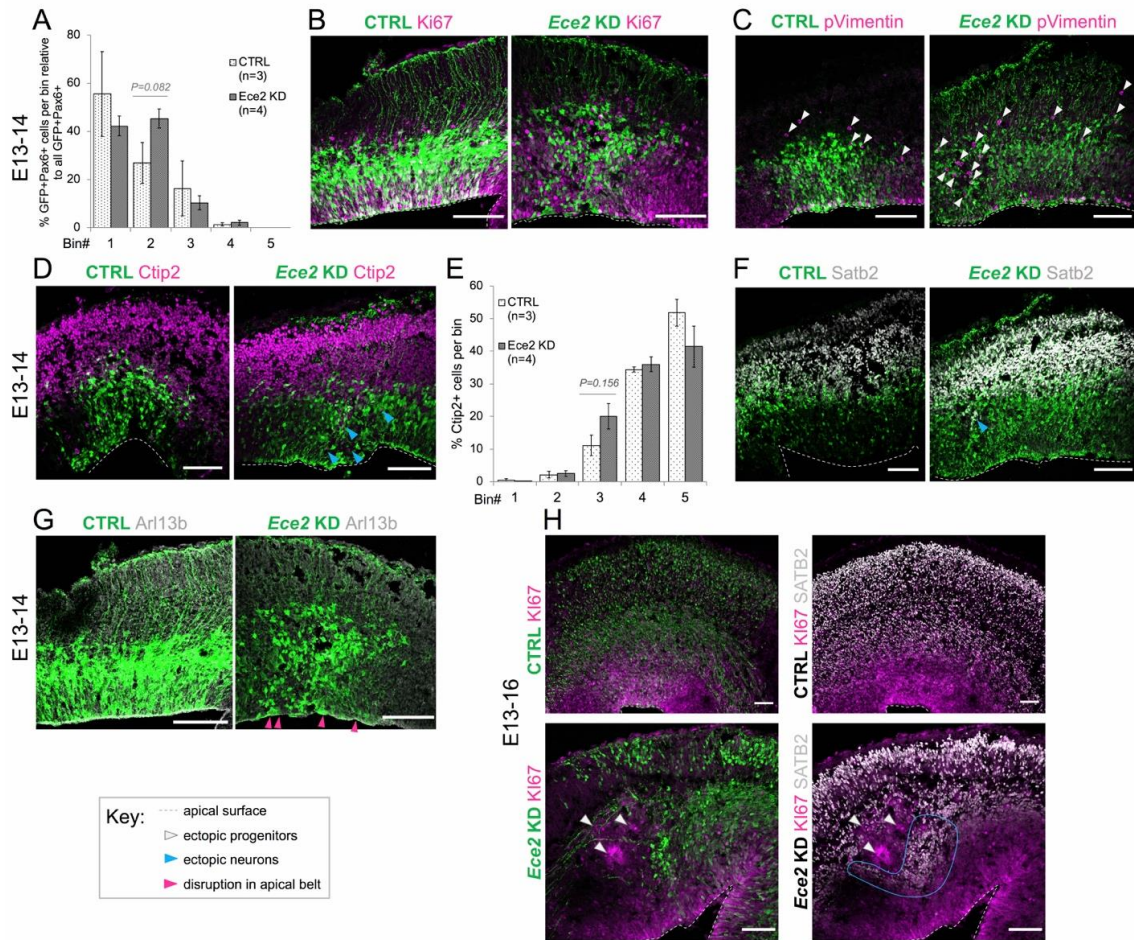


Figure EV3

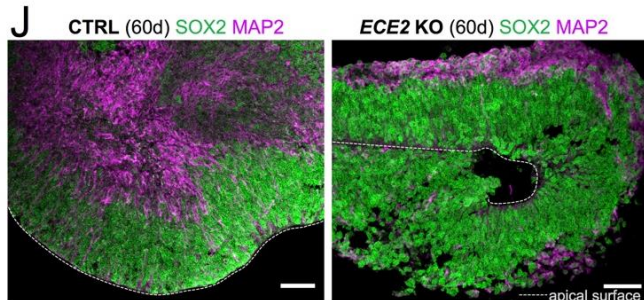
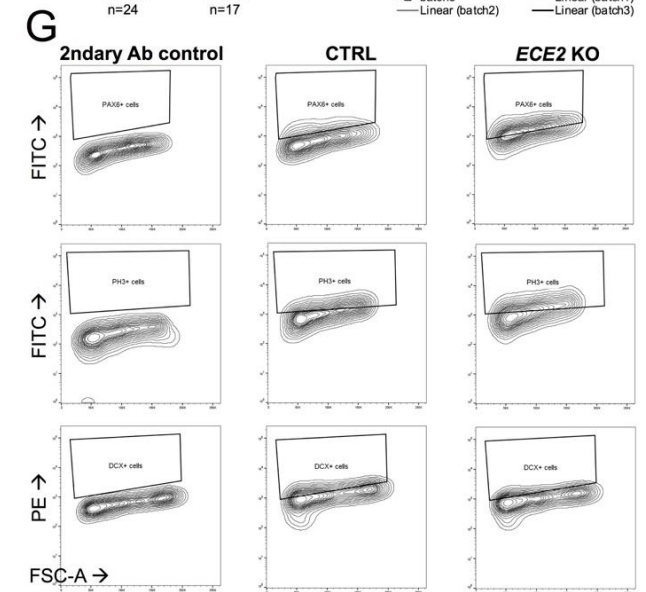
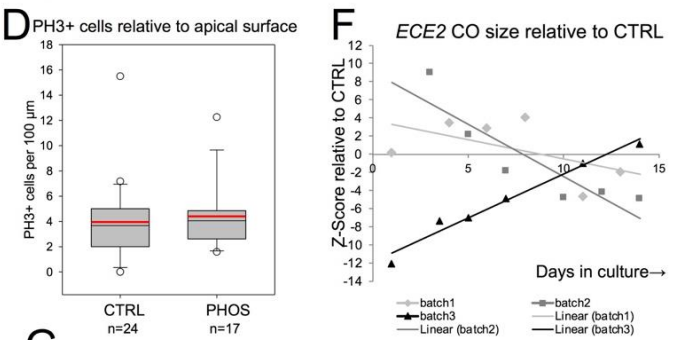
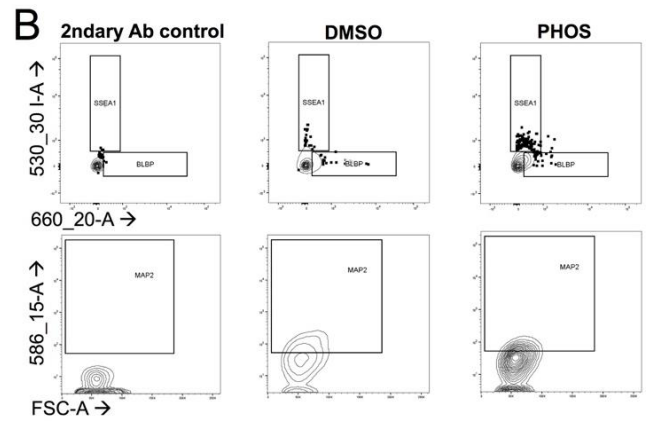
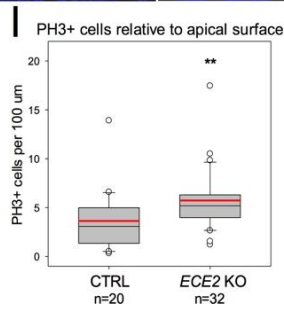
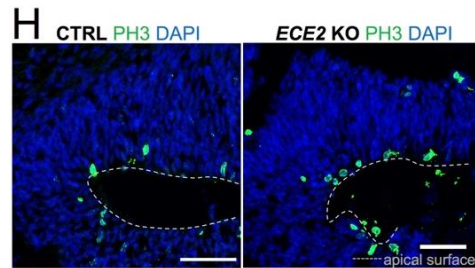
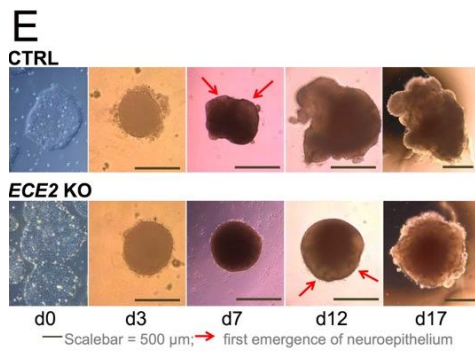
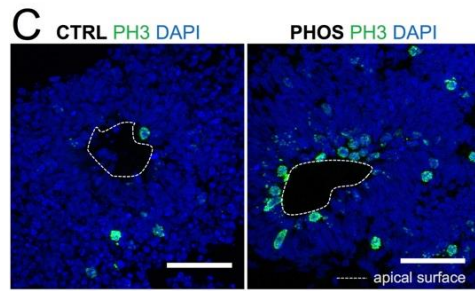
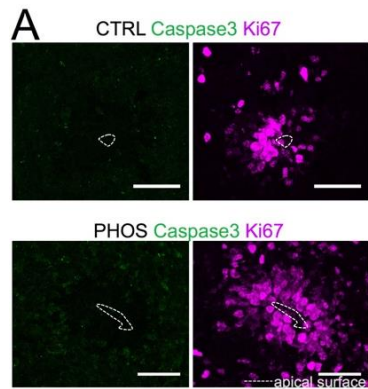
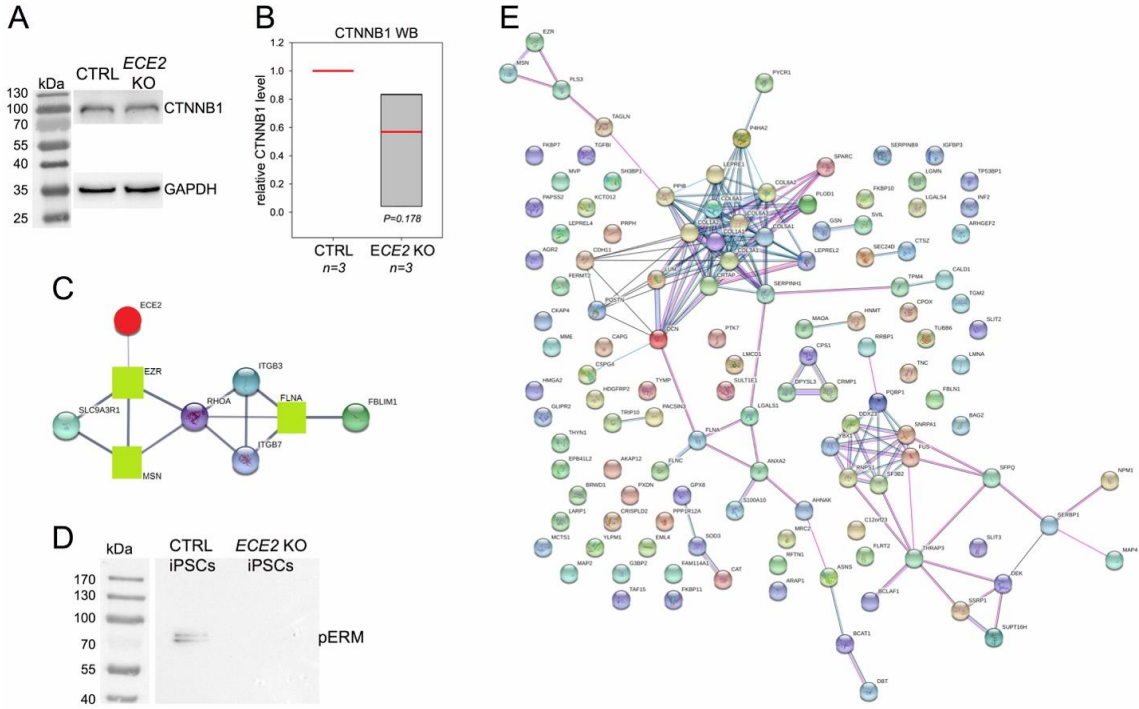


Figure EV4



EXPANDED VIEW TABLES

The Expanded View Tables of this study have been deposited online in the “Nextcloud Bio II” LMU data cloud.

5. DISCUSSION

In the main parts of this discussion, the presented studies will be related to separately. I will summarize the findings of each study, followed by a discussion of the findings that goes beyond the compact discussion that is part of the paper or manuscript and that shall place the findings into a bigger context. Then I will wrap up mechanisms and pathways commonly identified between the different studies. This leads us to a summary of what knowledge this work has added to the field.

In the discussion of the individual projects, the *ECE2* project (**Chapter 4**) will be discussed most extensively because the *ECE2* manuscript was only submitted and sent to reviewers shortly before submission of this thesis, thus instigating the need for most detailed critical analysis of this study.

5.1. SPG11 - A DEVELOPMENTAL ROLE FOR A KNOWN NEUROLOGICAL DISEASE GENE

In the first study (**Chapter 2**; (Pérez-Brangulí et al., 2018)), we analyzed the neurodevelopmental role of the HSP gene *SPG11*. For simplicity, “(derived from patients with) HSP caused by *SPG11* mutations” will be abbreviated here as “SPG11”. The spectrum of disorders associated with *SPG11* mutations has traditionally been classified as neurodegenerative, including young onset Amyotrophic Lateral Sclerosis and Charcot-Marie-Tooth disease in addition to spastic paraplegia (Montecchiani et al., 2016; Orlacchio et al., 2010; Stevanin et al., 2007). The fact that affected patients show cognitive impairment, thin corpus callosum, enlarged ventricles, and reduced grey matter thickness (Faber et al., 2018; Hehr et al., 2007; Pensato et al., 2014; Stromillo et al., 2011), is a hint for a possible involvement of *SPG11* in neurodevelopment. A preceding study revealed a proliferation defect in NPCs generated from SPG11 patient-derived iPSCs that could be rescued by inhibition of the kinase GSK3 β (Mishra et al., 2016). Here, we used NPCs, neurospheres and COs to further analyze this defect. Both 2D and 3D *in vitro* models recapitulated the formerly described impairment of progenitor proliferation, which resulted in premature neurogenesis and smaller CO size. An early reduction in mitotic NPCs in COs lead to a reduced thickness of the progenitor zone over time and an enlargement of ventricle-like structures in patient-derived COs, reminiscent of the enlarged lateral ventricles in patient brains (Pensato et al., 2014). Besides, progenitor zone and neuronal layer were less separated, in line with premature differentiation compared to controls. Making use of the internal organization of COs, we identified a switch towards more horizontal, asymmetric aRG divisions at the basis of the impaired self-renewal and premature neurogenesis. This was further supported by the detection of a prolonged cell cycle by single cell tracking of NPCs and a reduced final number of neurons produced from the smaller NPC pool in neurospheres. As a hint to a possible mechanism, we observed holes in the apical β -catenin belt, although apico-basal polarity was established in SPG11 COs. Indeed, we found that upon *SPG11* KD in Hek293 cells and in patient-derived COs, the amount of phosphorylated β -catenin was increased due to reduction in inactivated GSK3 β . Phosphorylation of β -catenin promotes its ubiquitination and proteasome degradation (Orford et al., 1997). The amount of GSK3 β -interactor pCREB (Ilouz et al., 2006) was also increased, with pCREB acting as

driver of neurogenic gene transcription (Mantamadiotis et al., 2012). Thus, the increased amount of active GSK3 β lead to decreased proliferation through promoted degradation of β -catenin and to increased differentiation through activation of CREB. As reduced grey matter thickness in the patients may also originate from increased cell death, we tested this in a NPC-differentiation approach and in COs. Interestingly, whereas apoptosis was increased already after 2 weeks of neuronal differentiation in 2D, we saw no difference in apoptosis in COs.

In an effort to rescue the observed phenotypes in SPG11-derived model systems, we overexpressed (OX) *SPG11* in NPCs, which reversed the premature neurogenesis. Accordingly, addition of GSK3 inhibitors CHIR99021 (CHIR) and Tideglusib (Tide) to NPCs, neurospheres and COs rescued the NPC proliferation and premature neurogenesis defect and significantly increased the size of patient-derived COs. While CHIR affected also control CO size, the GSK3 β -targeting Tide specifically rescued only patient CO size without affecting controls.

From these summarized findings of our study, we can conclude that the *SPG11*-encoded spatacsin plays a role in negatively regulating GSK3 β activity as a major component of the canonical Wnt pathway (see summary scheme in **Figure 6**). This is in line with a preceding pioneer study on the neurodevelopmental role of *SPG11* (Mishra et al., 2016): An analysis of differentially expressed genes in control and SPG11 patient iPSCs-derived NPCs revealed downregulation of Wnt pathway activators and upregulation of its negative regulators. Additionally, cytoskeletal and motor components were dysregulated and so were genes involved in the autophagosomal and lysosomal pathway (Mishra et al., 2016).

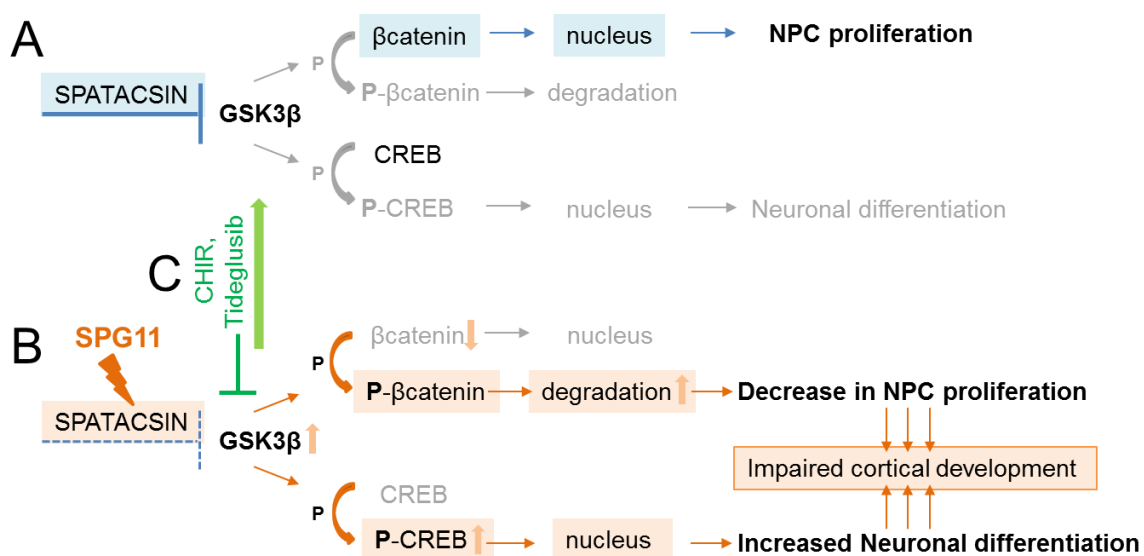


Figure 6: Suggested mechanism underlying neurodevelopmental defects in HSP-SPG11. **A**, **B**, Wnt/ β -catenin pathway components that are implicated in the neurodevelopmental defect in SPG11 and their role in the regulation of NPC proliferation *versus* neuronal differentiation are illustrated for the healthy control (**A**) and SPG11 patient condition (**B**). *SPG11*-encoded spatacsin is suggested to play a role in the inhibition of active GSK3 β . **C**, Application of GSK3(β) inhibitors to SPG11 patient-derived neural *in vitro* cultures partially rescues the defects of premature neurogenesis at the expense of NPC proliferation.

Cerebral organoids reveal novel functions of SPG11. Two different mouse models were generated in the past that differently and only partly recapitulated phenotypes found in SPG11 patients (Branchu et al., 2017; Varga et al., 2015). Namely, the first mouse model, generated by insertion of a genetrap cassette in the first intron of the *Spg11* gene, only showed a loss of cortical neurons and Purkinje cells and an autophagy defect, without an effect on the animals' motor and cognitive performance (Varga et al., 2015). The newer mouse model, generated by insertion of stop codons into exon 32 of *Spg11*, mimicking the most frequent mutations found in patients, differed from the first one in that it showed upper and lower motoneuron degeneration, progressive thinning of the corpus callosum, cognitive and motor behavioral defects, and accumulation of lipids in lysosomes (Branchu et al., 2017). In parallel to the improvement of mouse models, human models were developed that can serve the identification of human-specific aspects of SPG11. Based on growing knowledge on differences in mouse and human cortical development, they may help to circumvent the difficulty of mouse models of human disease mutations to recapitulate the expected phenotype. To this end, the recent focus of SPG11 research has been on the use of human iPSC-derived *in vitro* systems.

While a former study used 2D *in vitro* models only (Mishra et al., 2016), ours gave valuable insights into the role of *SPG11* in neurodevelopment by using 3D models. COs represent a more "complete" system than 2D models, closely recapitulating human fetal development (Camp et al., 2015; Paşca et al., 2015).

While upon 2D neuronal differentiation from NPCs, *SPG11* mutant cells showed increased apoptosis in both our and the previous study, this was not the case in cerebral organoids. The phenotypes identified in COs suggest that cortical atrophy and reduced grey matter thickness found in SPG11 patient brains (Faber et al., 2018) result merely from defective NPC proliferation during development, with a smaller progenitor pool producing fewer neurons. Postnatally, over time, problems in homeostasis of the long axon may then contribute to them dying back, resulting in a loss of grey matter over the years. In line with that, the cortical grey matter thickness is most severely affected in motor regions (Faber et al., 2018).

Consistent with β -catenin's known developmental role in G1 phase progression and proliferation (Chenn and Walsh, 2003; Woodhead et al., 2006), we identified changes in cell cycle length, division angle and proliferation in SPG11 NPCs and COs, which were rescued by re-establishment of β -catenin levels through GSK3 inhibition. The observed changes in cell cycle length and division angles upon *SPG11* mutations resemble findings reported for Miller-Dieker syndrome patient-derived COs (Bershteyn et al., 2017; Iefremova et al., 2017): Changes in the division angle of aRG and a prolongation of the bRG cell cycle were found to underlie increased neurogenic divisions in this severe form of lissencephaly type I. Besides, the β -catenin signaling axis was disturbed in these models (Iefremova et al., 2017), equally to our SPG11 COs. It would thus be interesting to analyse the gyrification index in SPG11 patients to decipher if misregulation of the same molecular pathway leads to a similar phenotype.

The change in division angle may be caused by GSK3 overactivation: GSK3s regulate the activity of several MAPs (Zhou and Snider, 2005), and so might control mitotic spindle reorganization during cell division. The division angle of apical progenitors is decisive for the distribution of polarity proteins, cell fate determinants, the apical membrane compartment, and the centrosomes into the daughter cells (Götz and Huttner, 2005; Taverna et al., 2014; Wang et al., 2009a). The apically concentrated Rho GTPase Cdc42, for example, regulates both AJ integrity and cell fate: cKO of *Cdc42* in the developing

mouse telencephalon leads to loss of AJs, followed by aRG delamination, which then undergo basal mitoses and change their cell fate to basal progenitors (Cappello et al., 2006). We thus made use of the 3D organization of COs to analyze the quality of the apical AJs, among others established by apically concentrated β -catenin, and found indeed a defect (see Figure S1b-c of the SPG11 study in **Chapter 2**). The change in fate towards premature neurogenesis may thus also be caused by the loss of AJs. Changes in GSK3-mediated phosphorylation of MT-stabilizing MAPs (Zhou and Snider, 2005) would cause changes in the integrity and dynamics of the MT cytoskeleton and MT-based trafficking (Pérez-Brangulí et al., 2014) and contribute to changes in MT-based polarity both in apical progenitors and in migrating neurons (Etienne-Manneville, 2010). The fact that we found the progenitor zone and neuronal layer in SPG11 COs less separated than in controls also fits into this line of thought: The delaminating progenitors may lose their polarization and spatial orientation and prematurely start the expression of neuronal markers within the progenitor zone.

The treatment of COs with the two different GSK3 inhibitors revealed that the GSK3 β -specific Tide rescued the patient phenotype of premature differentiation by restoring progenitor proliferation. While CHIR equally affected both control and patient-derived COs, Tide had only a slight effect on control COs. This suggests that Tide acts more specifically on GSK3 β than other GSK3 inhibitor, bringing a chance for it to cause fewer side effects when administered to patients. Moreover, this experiment stresses the great potential of COs in the identification of disease mechanisms and the development of therapy strategies.

Remaining questions around SPG11 in cortical development. We suggest the reduced grey matter thickness in SPG11 patients to developmentally originate from the smaller progenitor pool size used for the generation of neurons – but we did not quantify the amount of neurons produced in CO germinal zones. To further support this hypothesis, it would be of interest to analyze the proportion of progenitors to neurons in COs. The measurement of the thickness of the neuronal layer after IHC staining is difficult: It differs with the location of a germinal zone within an organoid - Germinal zones being located at the rim of organoids differ from those inside the CO, and germinal zones in isolation are different from those surrounded by others, which makes it hard to distinguish CP-like zones of neighboring ventricles. This is why we focused our analysis in COs on the proliferation capacity and progenitor pool size as inferred from mitotic cells and the thickness of the progenitor zone. In the meantime, we established FACS analysis of COs in our lab (see (Klaus et al., 2019) and **Chapter 4**), which enables to gain a quick and unbiased impression of cell type proportions within COs. FACS analysis of control and SPG11 COs at different ages may thus be a good method to fill this gap.

Other processes that spatacsin has been implicated in are lipid turnover by autophagy and via the lysosome (Branchu et al., 2017; Chang et al., 2014; Vantaggiato et al., 2019; Varga et al., 2015), axonal vesicle transport and cytoskeletal integrity (Pérez-Brangulí et al., 2014) with accumulation of lipid material in lysosomal structures in patient brains (Denora et al., 2016). Specifically, the transport of synaptic vesicles and the amount of stabilized microtubules, characterized by ac-tub, were changed in SPG11 patient iPSC-derived neurons. Besides, the morphology of neurites was less complex (Pérez-Brangulí et al., 2014). A recent study showed that the treatment of SPG11 neurons with Tide ameliorated both phenotypes of membraneous inclusions and of changed neurite morphology (Pozner et al., 2018). It would thus be interesting to use the CO model to further investigate these questions: Is the cytoskeleton of NPC and neurons in SPG11

COs changed compared to control? Do neurons in SPG11 COs also show accumulation of lipid materials – and is this rescued by Tide treatment? It has been suggested that the defects in neurite morphology, lipid turnover, and axonal transport may contribute to changes in neuronal activity (Pérez-Brangulí et al., 2014). This may, together with reduced grey matter thickness, contribute to cognitive defects characterized in SPG11 patients. Thus, electrophysiology on patient-derived COs may help to tell if neuronal activity is actually affected.

SPG11 is not the first neurodegenerative disorder for which a developmental aspect was identified. For example, a developmental origin of Timothy syndrome, a monogenic multisystem disorder in which patients present with cardiac and extracardiac defects including ASD and epilepsy, has been characterized using assembloids (Birey et al., 2017). Several other genes whose mutations cause HSP play a role in protein and lipid homeostasis, lysosome physiology, and autophagy, e.g. *SPG15*, *17*, *39*, *46-52*, and *SPG54* (Tesson et al., 2015). These processes are especially crucial in the maintenance of the long axons of motoneurons (Boutry et al., 2019; Elert-Dobkowska et al., 2019). It would thus be interesting to analyze if there is also a developmental aspect to these forms of HSP.

Besides, GSK3s phosphorylate a myriad of targets and thus plays diverse roles in neurodevelopment (see also **Chapter 1.1.3** and **1.1.4**): GSK3s act as key regulators in multiple neurodevelopmental processes, including neurogenesis, neuronal migration, neuronal polarization, and axon growth and guidance (Hur and Zhou, 2010). For example, GSK3 has been associated with microcephaly (Novorol et al., 2013; Spittaels et al., 2002), fragile x syndrome (Portis et al., 2012), and psychiatric disorders such as schizophrenia and depression (Matsuda et al., 2019), as well as with neurodegenerative Alzheimer's disease (Hooper et al., 2008; Parr et al., 2012). Hence, this suggests a potential contribution of the GSK3 inhibitor spatacsin to these diseases. Especially the etiologies of microcephaly and lissencephaly type I, which may be caused by proliferation defects or increased apoptosis, shows some overlap with our study, as we have seen reduced progenitor proliferation and premature neurogenesis. It would thus be highly interesting to identify the exact mechanism through which SPG11 inhibits GSK3 β .

A function of spatacsin in autophagy and lysosome reformation has been implicated by different studies (Branchu et al., 2017; Chang et al., 2014; Vantaggiato et al., 2019; Varga et al., 2015). The importance of autophagy for several aspects of neurodevelopment has been demonstrated in the past (reviewed in (Lee et al., 2013)) and it has also been shown that defective autophagy can contribute to neurodegenerative disorders such as Alzheimer's and Parkinson's disease has also been shown (reviewed in (Nixon, 2013)). In neurodevelopment, autophagy-mediated recycling of (membrane) lipids, mitochondria and proteins is required in differentiation, for morphological changes such as during migration and neuritogenesis, and in synaptogenesis. Disruptions of autophagy-related pathways such as the mTOR and the Rap pathway thus lead to neurodevelopmental disorders such as ASD (Lee et al., 2013). It would thus be highly interesting to analyze the exact molecular function of spatacsin in autophagy, which may contribute to both developmental and degenerative aspects of SPG11.

Heterogeneity of SPG11 and HSPs. The diversity of cellular processes that spatacsin has been implicated in, combined with the many substrates of its downstream factor GSK3 β , leads to a huge heterogeneity in phenotypes in SPG11 patients. No correlation between genotype and phenotype has been shown in SPG11 patients, which means that

the same mutation can lead to different phenotypes, affecting different regions of the nervous system besides the cortico-spinal tract, and mutations in different parts of the gene may lead to the same physiological outcome (Branchu et al., 2017; Pensato et al., 2014; Stevanin et al., 2007). On top of that, the genetic background and epigenetic and environmental factors may add to the variability.

For example, a recent study characterized grey and white matter changes in MRI, neuropathological, and other symptoms in a cohort of 25 SPG11 patients (see **Figure 7**; (Faber et al., 2018)) and found 84% of patients fulfilling the criteria for dementia and 28% with the criteria for parkinsonism, which is coherent with the previously reported 30% (Anheim et al., 2009), and supported by basal ganglia abnormalities that became apparent in patient brain MRIs (Faber et al., 2018). The phenotypes caused by *SPG11* mutations overlap with other spastic paraplegia genes (Pensato et al., 2014). *SPG11* is not the only HSP gene making HSPs a diverse spectrum of disorders – many HSP-causing pathological mutations, including frameshift, nonsense, truncating, missense mutations, large exon deletions, and splice site mutations in more than 60 genes, have been reported to lead to HSP and other co-occurring neuropathies (see **Figure 8**; (Tesson et al., 2015)) (Boutry et al., 2019).

The categorization of HSP caused by mutations in *SPG11* as a complex form of HSP is thus well supported. Our work further suggests its classification as a neurodevelopmental disorder.

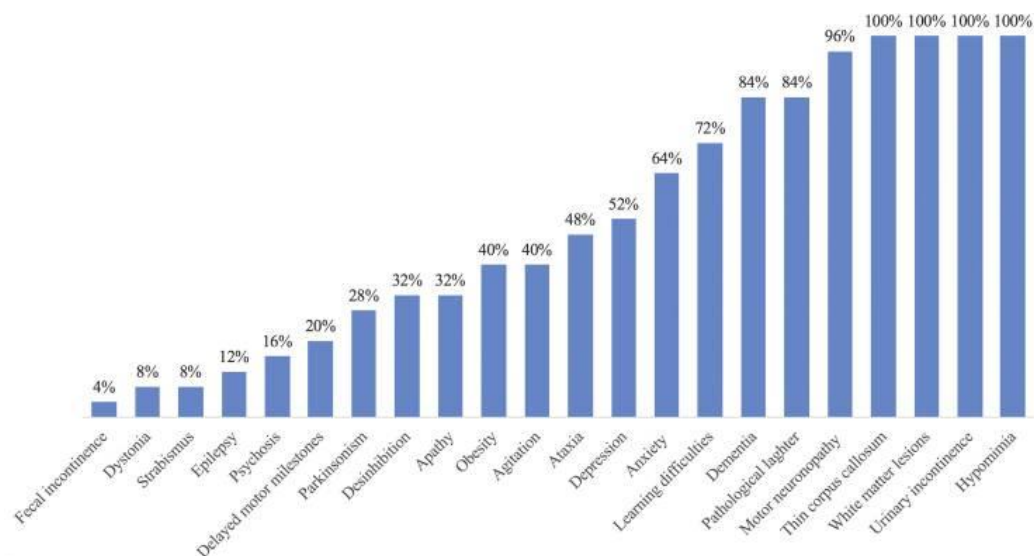


Figure 7: Frequencies of phenotypic traits identified in 25 SPG11 patients underline the heterogeneity of SPG11-HSP. Image reused from (Faber et al., 2018).

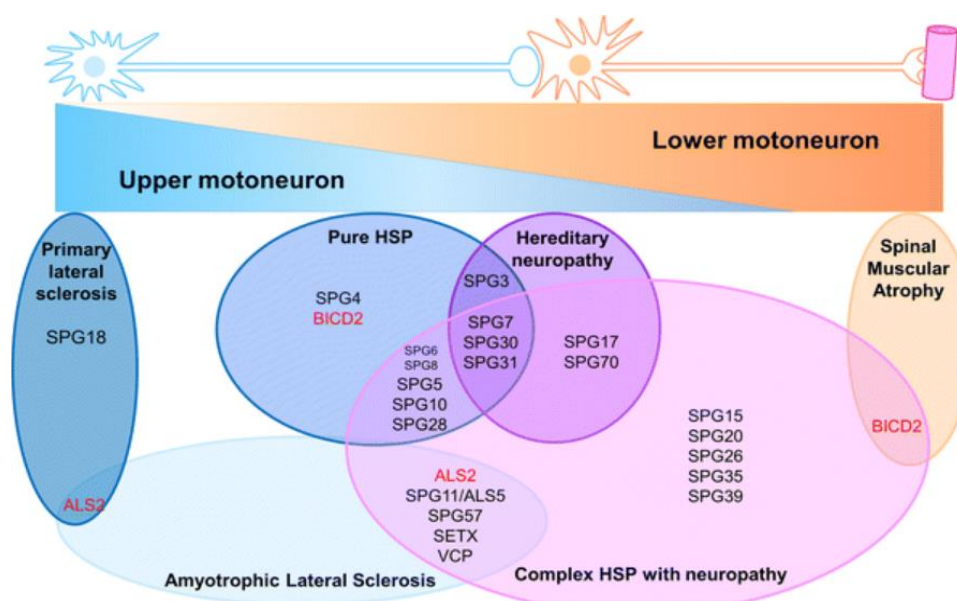


Figure 8: Scheme illustrating phenotypic heterogeneity associated with HSP and the classification of HSP genes according to the upper and lower motor neuron diseases phenotypic presentation. Image reused from (Tesson et al., 2015).

Altogether, we show evidence linking SPG11-HSP to neurodevelopmental disorders and underline the potential of human *in vitro* models in the identification of human-specific cellular and molecular mechanisms and in therapy development for precision medicine.

5.2. AMPYLATION - A NOVEL PARAMETER TO FINE-TUNE NEUROGENESIS

The process of interest in the second study (**Chapter 3**; (Kielkowski et al., Under Revision)) was the PTM AMPylation, which has been understudied due to the lack of methods for its monitoring. We thus designed a cell-permeable probe that is intracellularly metabolized to alkine-tagged ATP and utilized for AMPylation of substrate proteins. This probe thus labels AMPylated proteins and enables their detection under physiological conditions. We then used this probe to identify AMPylated proteins in several human cancer cell lines and fibroblasts, as well as in iPSC, NPCs, and neurons which model different stages of neurodevelopment in a 2D environment, and COs as 3D model of the early fetal human brain. In all analyzed cell types and COs, metabolic enzymes represented the largest functional group of AMPylated proteins. Interestingly, the set of AMPylated proteins was different and only partly overlapping for the analysed cell types. ER stress induction by thapsigargin (tg) lead to a change in AMPylated proteins, indicating cell type and environmental condition-specific AMPylation. In neuroblastoma cells, a large number of proteins were AMPylated at baseline conditions and even more got induced upon ER stress, hinting at a critical role for AMPylation in the nervous system.

Functionally, we showed that AMPylation of cathepsins (as example enzymes) at serine residues in close vicinity to their active site cysteine obstructed their proteolytic activity, probably through steric hindrance of substrate binding.

In neurons, a large and unique set of proteins was AMPylated, with an additional enrichment of cytoskeletal and motor proteins. This suggested a remodeling of the AMPylation pattern in the course of neuronal differentiation, as the small set of AMPylated proteins in NPCs was completely distinct to that in neurons.

We paralleled the identification of AMPylated proteins in the different cell types through proteomics by immunohistochemical characterization of their intracellular localization, as well as of the localization of the eukaryotic AMPylating enzyme FICD. This revealed a localization of FICD and its targets to the ER and cytoplasm. In neurons, we found high levels of FICD and a huge number of AMPylated proteins, both being enriched in the processes. To analyze the role of AMPylation in cortical development, we manipulated the levels of the AMPylating and de-AMPylating enzyme FICD. KD of *FICD* in differentiating NPCs and in germinal zones of COs lead to an increase in cells that remained proliferative. OX of wildtype and a constitutively active mutant *FICD* (*FICD E234G*) in COs increased the amount of neurons produced by electroporated progenitors. Finally, to exclude that a function of FICD other than its AMPylating activity caused the observed change in neurogenesis, we electroporated COs with an enzymatically inactive mutant of *FICD* (*FICD H363A*). This revealed no difference to control, stressing that indeed AMPylation remodeling by FICD fine-tunes neurogenesis. The Scheme in **Figure 9** summarizes these findings from COs.

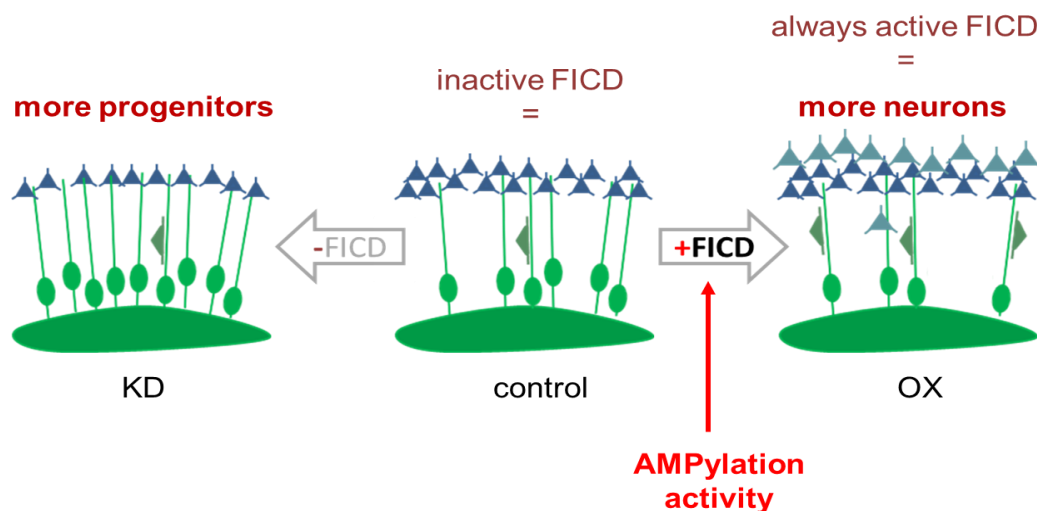


Figure 9: Scheme depicting the effect of *FICD* KD or OX by electroporation of aRG in germinal zones of COs. *FICD* KD (left) leads to an increase in progenitors 7 dpe, while OX of wildtype *FICD* and the constitutively active mutant *FICD E234G* (right) increases the neuronal production compared to control (middle). Electroporation of catalytically inactive *FICD H363A* is indifferent from the control and thus reveals that the AMPylation activity of FICD underlies its influence on neurogenesis.

FICD/AMPylation functions in the nervous system – known and inferred. The Fic domain is highly conserved across species, suggesting a critical role for Fic domain containing proteins and for AMPylation remodeling in cellular functions (Ham et al., 2014). In the discussion of this study, I will focus on cellular functions relevant to cortical development.

A function of FICD-mediated AMPylation in the nervous system has been suggested by previous studies: In *C.elegans*, AMPylation of chaperones was shown to modulate the

aggregation and with that the toxicity of polypeptides implicated in neurodegenerative diseases, for example Amyloid- β and α -synuclein (Truttmann et al., 2018). Another study found that the direct AMPylation of α -synuclein reduced its neurotoxicity by hindering it from permeabilizing and invading the ER and by interfering with its aggregation to fibrils. They suggested – same as what we proposed for AMPylation of CTSB – steric hindrance by the covalently bound AMP to be at the origin of these effects (Mattoo et al., 2019). This molecular mechanism of activity regulation, also suggested for the ER chaperone BiP, the first eukaryotic target ever described (Ham et al., 2014), may be a common one in all AMPylated enzymes.

In addition to this proposed protective role of AMPylation in neurodegeneration, a role for *drosophila* AMPylating enzyme Fic was described. Flies lacking *Fic* are blind due to a neurotransmission defect, caused by a glia-specific defect in histamine recycling. Thus, Fic-mediated AMPylation may play a role in the endocytosis needed for the re-uptake of the neurotransmitter (Rahman et al., 2012).

Bacterial Fic domain containing AMPylating enzymes, more than a thousand of which were identified, act on cytoskeleton-associated proteins: Secreted Fic proteins AMPylate mammalian host cell Rho GTPases RhoA, Rac1, and Cdc42, rendering them inactive, which leads to cytoskeletal collapse of the host cell (Mattoo et al., 2011; Worby et al., 2009). Host cell endocytosis and exocytosis were also found to be altered by bacterial AMPylation of Rab1 (Mukherjee et al., 2011). If conserved, AMPylation remodeling of the cytoskeleton to affect endocytosis represents a good candidate mechanism that may underlie the defect in histamine recycling in the *Fic* deficient flies (Rahman et al., 2012).

What remains unresolved in our study and shall thus be addressed here is the question of the exact mechanism underlying FICD's influence on neural progenitor proliferation versus differentiation. Although we identified numerous AMPylated proteins in the relevant cell types and in COs, we don't know the AMPylation remodeling of which one(s) led to increased neurogenesis upon *FICD* OX. Using the term "remodeling", we are being careful to avoid a clear statement if the phenotype arose from AMPylation or deAMPylation, as FICD can do both reversibly (Casey et al., 2017). Our stainings in probe-treated COs, though, revealed an increase in AMPylated proteins in the transition zone from progenitors to neurons. Also in 2D, we identified far more AMPylated proteins in neurons (71 compared to 6 in NPCs). Panther gene ontology (GO) term analysis of all AMPylated proteins in the screened cell types revealed an enrichment of neuron-specific pathways, namely Rho-GTPase and FGF signaling and neurodegenerative disease pathways related to Alzheimer's and Huntington's disease. The following hypotheses will therefore be based on those proteins in neurons and COs that are AMPylated, and not deAMPylation, as we have no means of analyzing deAMPylation of proteins by *FICD* WT/E234G OX.

It may be that the (de)AMPylation of one or a few proteins changes their structure and thereby alters their function, which may cause the increased neurogenesis. Though, it could also be the combined additive effects of the modification of numerous or all of them. This way, slight changes in their structure and activity may sum up and altogether contribute to the observed phenotype. Of course, it would be interesting to nail down the responsible target(s). Considering the large number of 71 AMPylated proteins in 2D neurons and 34 in COs and that the phenotype is relatively mild (albeit statistically significant), this would be a Sisyphean task, though. Unfortunately, we did not succeed in the identification of AMPylation site in all proteins, which may have given a clue to the functional impact of the modification. In neurons and COs, according to protein interaction

network analysis in String.db (Szklarczyk et al., 2017), the most enriched functional protein groups act in 1) MT-based processes and vesicle-mediated transport, 2) Chaperone-mediated proteostasis, 3) basic metabolism, 4) ECM constitution, and 5) RNA splicing and mRNA stability. In the following, I will forward a few different hypotheses that try to explain the AMPylation of which protein groups may have the power to influence neurogenesis.

The cytoskeleton and transport hypothesis. The most attractive candidate proteins in which we would like to know the exact AMPylation site are tubulins and myosin and kinesin motors. Tubulins are known to be highly modified by PTMs in their C-terminal region, which is exposed at the outer surface of MTs, and these PTMs are implicated in the regulation of MT stability, MT dynamics, and the interaction of MTs with binding partners (Ayala et al., 2007). The interaction of motor protein complexes with MTs and the activity of kinesins, myosins, and dyneins are in turn also fine-tuned by PTMs (Muretta et al., 2018). For example, reorganization of the MT cytoskeleton – regulated by PTMs and MAPs – is at the basis of neuronal polarization required for migration and underlies the establishment of neuronal morphology (Song and Brady, 2015) (see **1.1.3** and **1.1.4**). Other PTMs on cytoskeletal proteins, for example palmitoylation of MAP6 (Tortosa et al., 2017) and phosphorylation of MAP2 (Sánchez et al., 2000) promotes their stabilizing interaction with MTs. Thus, AMPylation may be a novel PTM exerting a function in neurogenesis through the fine-tuning of cytoskeletal and motor protein structure and function. When overexpressing FICD WT or E234G in COs, we found not only more differentiated neurons: Some of them also differentiated prematurely within the progenitor zone of the CO ventricle as indicated by intruding MAP2+ neuronal processes and NEUN+ neuronal nuclei at the apical surface (see blue and pink arrowheads in Figure 7c, d in **Chapter 3**). This suggests that cytoskeletal remodeling through FICD-mediated AMPylation may directly influence neuronal migration.

Knowledge of the exact AMPylation sites in tubulins and motor proteins would enable *in silico* prediction of the effect the modification has on MT dynamics, on the interaction of MTs with motors and other MAPs, and on the activity of molecular motors. In a next step, one could use site-directed mutagenesis and assays such as EB1/3 life imaging for MT dynamics to analyze the functional effect of AMPylation.

Closely connected with cytoskeletal and motor function and their regulation by PTMs is vesicle trafficking, which is pivotal for cellular polarization and migration (Etienne-Manneville, 2010), for example through directional transport of transmembrane proteins required for cell adhesion and for response to extracellular signals by cytoskeletal rearrangement (see also **1.1.3**). AMPylated proteins both in neurons and in COs are highly enriched for biological function in vesicle transport (see **Figure 10A** for the COs).

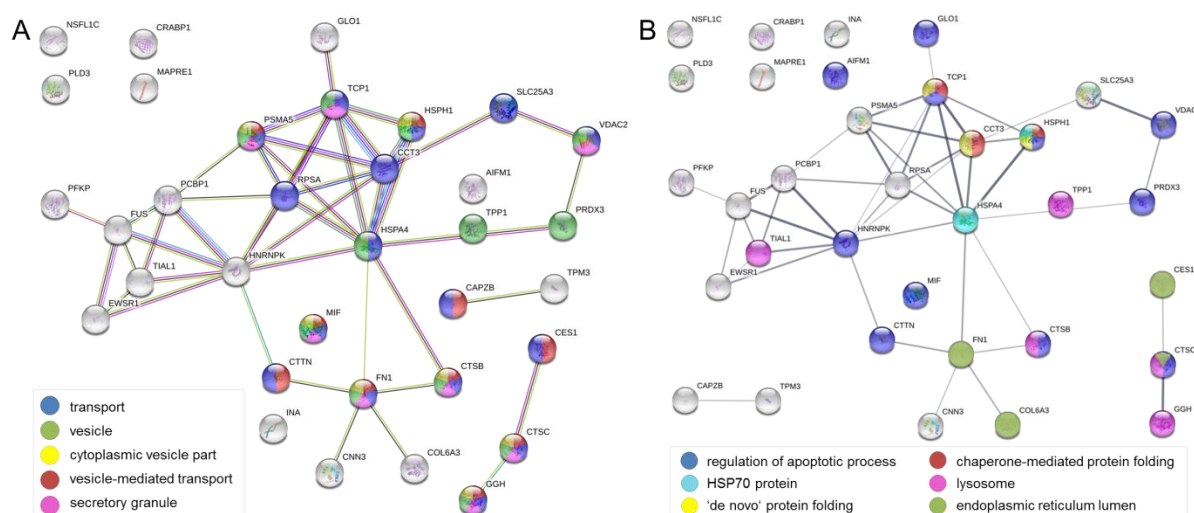


Figure 10: Proteins with function in vesicle trafficking (A) and proteostasis (B) are enriched among CO AMPylation targets. Respective proteins were highlighted after protein interaction network analysis in String.db (Szkarczyk et al., 2017).

The proteostasis hypothesis. Another candidate group of proteins is suggested from the eukaryotic FICD function most consistently found in publications: FICD-mediated AMPylation and deAMPylation of chaperones. The ER-based chaperone BiP/HSPA5 was shown to be both AMPylated and de-AMPylated by FICD (Casey et al., 2017; Ham et al., 2014). This altered BiP's ATPase activity and the downstream activation of the UPR and suggested a crucial role for AMPylation remodeling in the regulation of protein homeostasis in the ER (Preissler et al., 2017b; Sanyal et al., 2015). Yeast Ficd was found to inactivate the cytosolic heat shock protein Hsp70, which showed a function for AMPylation in protein homeostasis outside the ER (Truttmann et al., 2017). In our study, we identified several proteins that function in protein homeostasis including synthesis, folding, and lysosome-based degradation – summarized as “proteostasis” – to be AMPylated in COs (**Figure 10B**). In a series of experiments, we incubated the screened cell types and COs with ER-stress-inducing tg. During ER stress, unfolded proteins accumulate and this activates the UPR and chaperones and, if the stress cannot be reversed, apoptosis is induced. Interestingly, while tg treatment increased the amount of significantly AMPylated proteins in all other cell types, neurons responded very specifically to tg with the upregulation of two proteins – BiP/HSPA5 and SQSTM1. And also FICD expression was higher in neurons compared to NPCs as detected by our study and others (Mattoo et al., 2019). These findings from COs and neurons indicate a critical role for proteostasis in neurodevelopment: The complex process of development, where change of cell fate and localization from progenitor to neuron requires complete change of the morphology, is based on the cytoskeleton and transport processes. And for the morphological and functional remodeling to work properly, protein production, correct folding, and turnover are required. Growing evidence suggests indeed a pivotal role for ER proteostasis through UPR in brain development (Martínez et al., 2018), and its dysfunction at the basis of psychiatric disorders (Olivero et al., 2018) and neurodegenerative diseases (Hetz and Mollereau, 2014; Martínez et al., 2018; Olivero et al., 2018). In line with this, the role of *drosophila* Fic-mediated AMPylation in visual transmission and adaptation to stress has been shown to execute through ER homeostasis (Ham et al., 2014; Moehlman et al., 2018; Rahman et al., 2012).

The metabolism hypothesis. AMPylated proteins in all analyzed cell types were highly enriched for functions in basal metabolism such as citric acid cycle and glycolysis. Interestingly, though, there was only one protein target in common between neurons and other cell types, the PFKP. During (neuronal) differentiation, the cellular energy metabolism changes profoundly (Gascón et al., 2017): While proliferating stem and cancer cells depend on glycolysis and highly express glycolysis regulating enzymes, their metabolism shifts to mitochondria-based oxidative phosphorylation with differentiation (Gascón et al., 2017; Zhang et al., 2012b). In glycolysis as “incomplete” glucose metabolization, side products remain that are subsequently used for the production of metabolites required in dividing cells, such as nucleotides, amino acids and lipids (Zhang et al., 2012b). This finding of metabolic change preceding cell fate change has revolutionized the field of direct reprogramming for example from astrocytes to neurons, where formation of reactive oxygen species that are a toxic byproduct of oxidative phosphorylation are now reduced to improve reprogramming efficiency and survival (Gascón et al., 2016). In the differentiation process from stem cells to neurons (both *in vitro* from iPSCs via NPCs to neurons and *in vivo*), the metabolic switch is regulated by downregulation of key glycolytic enzymes and upregulation of enzyme splice variants and of mitochondrial biogenesis required for oxidative phosphorylation (Gascón et al., 2017). We identified an enrichment for proteins involved in amino acid biogenesis among AMPylation targets in NPCs, namely ASNS and PSAT1 – which were not AMPylated in neurons. In neurons, for example proteins acting in glucose and galactose metabolism and in small molecule biosynthesis were enriched among the AMPylated targets. It would of course be interesting to understand the molecular effect of AMPylation of each of these enzymes – activation or inhibition.

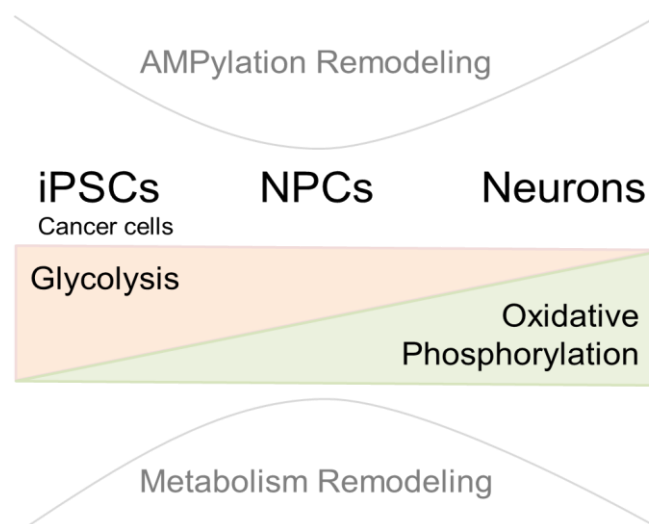


Figure 11: Hourglass model of AMPylation remodeling and metabolism remodeling suggests a role for AMPylation in the metabolic change from glycolysis to oxidative phosphorylation that NPCs undergo in neuronal differentiation. The sketched hourglass shape is adopted from Fig. 4b of the AMPylation study (**Chapter 3**), in which we described the AMPylation remodeling process in the differentiation from iPSCs via NPCs to neurons as an hourglass model-like process.

The fact that in all cell types, AMPylated proteins were significantly enriched for metabolic functions, combined with reported molecular regulation of enzyme function through AMPylation, are strong indicators for a role of AMPylation in this metabolic switch: On top

of differential gene expression, AMPylation may represent a fast and reversible mechanism to adjust to metabolic needs. This way, AMPylation remodeling may support metabolism remodeling during neurogenesis (see **Figure 11**). And thus, increased AMPylation upon *FICD OX* may lead to increased / faster neurogenesis.

The ECM hypothesis. To the reader, it may be surprising that the set of AMPylated proteins in COs does not equal the sum of those identified in NPCs and neurons but is actually distinct. This difference may be explained by COs being a more complete system than just the 3D organization of the same cell types (Camp et al., 2015; Paşca et al., 2015). For example, ECM components are produced that stabilize the internal architecture and are involved in signaling and guidance processes (Long and Huttner, 2019). Accordingly, GO Term analysis of the AMPylated proteins in COs revealed enrichment for “extracellular exosome” components. Considering the role that was ascribed to ECM components in the regulation of human cortical development and gyrification by others (Long and Huttner, 2019; Long et al., 2018) and us ((Kyrrousi et al.; Under Revision); see ECE2 study **Chapter 4** (Buchsbaum et al., Under Revision)), this is highly interesting. ECM remodeling through AMPylation may serve as an additional hypothesis of how *FICD* may influence neurogenesis. On the other hand, COs were repeatedly shown to contain additional cell types, such as astrocytes (Paşca et al., 2015; Sloan et al., 2017) and cells of mesodermal origin (Camp et al., 2015; Quadrato et al., 2017) which may give rise to microglia during CO differentiation (Ormel et al., 2018) and contribute to differences between targets identified in 2D and 3D models. As COs contain several different cell types, the background in the proteomic analysis of AMPylated proteins is higher and consequently, fewer proteins appear to be significantly AMPylated. Interestingly, “myelin sheath” was another GO term enriched solely in CO targets (String.db (Szkłarczyk et al., 2017)), highlighting a closer resemblance of COs to the developing human cortex than 2D *in vitro* models (Camp et al., 2015).

The alternative splicing hypothesis. A further hypothesis I would like to forward is based on another functional group enriched in AMPylated proteins in neurons: factors acting in RNA splicing and mRNA stability. It has been shown that alternative splicing as a crucial step to correct gene expression is tightly regulated during neural development: Switch between alternative splice variants of the same gene defines neuronal maturation stages (Weyn-Vanhentenryck et al., 2018). Alternative splicing is regulated by distinct RNA binding proteins. This functional group of proteins is exclusively AMPylated in neurons, which may thus indicate an additional level of regulation, fine-tuning neurodevelopmental stage-specific alternative splicing.

The phosphorylation competition hypothesis. The amino acids that can get stably AMPylated are those carrying a hydroxyl group in their amino acid side chain: serine, threonine and tyrosine (Casey and Orth, 2018). These are also the amino acids most commonly phosphorylated (Cohen, 2000). Besides, both phosphorylation and AMPylation use ATP as a substrate (Casey and Orth, 2018). Phosphorylation being the most widespread PTM, it has been estimated that about 30% of proteins in a mammalian cell are phosphorylated at any time, thereby mediating numerous pathways (Cohen, 2000). The last hypothesis I want to bring up here is therefore, that AMPylation of amino acids may compete with phosphorylation of the same site. Both PTMs add a negative charge to the side chain, but AMPylation is a more bulky modification than phosphorylation, that may thus have a different effect on the protein structure and characteristics. For example, in the ER chaperone BiP and other Hsp70 homologs, the highly conserved Tyr366 was

identified as site for FICD-mediated AMPylation (Ham et al., 2014). Tyr366 is in close proximity to the ATP binding site of BiP, thus its AMPylation was suggested to sterically hinder ATP hydrolysis (Ham et al., 2014). The same site can also be phosphorylated (<https://www.phosphosite.org/> (Hornbeck et al., 2015)) – thus, AMPylation may compete with phosphorylation. As already alluded to, cytoskeletal, motor and MT associated proteins also get heavily modified by phosphorylation (see 1.1.4 and *The cytoskeleton and transport hypothesis*), while we identified a number of them as AMPylation targets. For example, of the 71 AMPylated proteins in neurons, 58 are also prone to be phosphorylated (classified as “phosphoprotein” in String.db (Szklarczyk et al., 2017)) and of the 34 targets in COs, 25 are also phospho-proteins. A shift in the balance of AMPylation and phosphorylation may thus change the dynamics of the MT cytoskeleton and the interaction with motors and other MAPs, and affect all other protein groups functionally discussed above. This may in turn influence relevant processes of neurodevelopment.

Further unresolved questions of this study. In our study, we further characterized the localization of both FICD and AMPylated proteins in different cell types and COs. In line with previous findings, we detected co-localization of FICD with the ER (Preissler et al., 2017b; Sanyal et al., 2015), but also outside the ER (Rahman et al., 2012; Truttmann et al., 2017). A recent study developed a novel labeling and imaging technique of membrane-bound proteins and detected FICD exclusively in the ER, which can be close to Golgi or mitochondria (Sengupta et al., 2019). Our results, though, are in line with another study that generated an atlas of subcellular localization of thousands of proteins by fractionation of cellular compartments followed by proteomics (Orre et al., 2019). As did we, they found 1) that FICD localizes to several subcellular compartments in addition to the ER and 2) that intracellular FICD localisation is cell-type specific (Orre et al., 2019). A localization of AMPylated proteins outside the ER makes sense considering their individual function. For example, we find MAP2 and TUBB3 in neuronal processes labeled with our probe, which indicates that AMPylation does not affect their natural localization to MTs. The tubulous system of the ER in neurons extends into their neurites (Wu et al., 2017), which fits to this observation as this would enable local AMPylation by ER-based FICD.

Concerning the localization of AMPylated proteins to the nucleus of all screened cell types except for fibroblasts, it remains questionable which AMPylating enzyme acts there. Proteins involved in alternative splicing that we detected as AMPylated in neurons are an example of AMPylated targets with nuclear localization – for others see Table S8.

The finding that fibroblasts show no AMPylated proteins localized to the nucleus, although FICD was found to be spread throughout the cells, further supports the specificity of the nuclear probe staining in other cell types. To further investigate if AMPylation of nuclear structures is specific for differentiation or cell type identity, we will next analyze probe localization in different stages of iPSC-to-astrocyte *in vitro* differentiation as additional neural cell type.

Differences in localization of FICD and AMPylated proteins within the screened cell types, which only partly overlapped, indicate the presence of additional AMPylating enzymes with a possibly different cellular distribution. During this project, the discovery of a new eukaryotic AMPylator was reported: The highly conserved pseudokinase SeIO (Sreelatha et al., 2018). The putative AMP transferase activity of this pseudokinase opens up the possibility that the number of eukaryotic AMPylating enzymes is larger than previously expected. Also, homologs of the bacterial glutamine synthase adelylyltransferase

(Kingdon et al., 1967), another AMPylator without a Fic domain, may be identified. As only a subset of targets in cancer cell lines responded to changes in FICD levels, they may for example be AMPylated by SelO. It will thus be interesting to manipulate the expression of SelO in 2D and 3D *in vitro* models of neurodevelopment and to identify targets of SelO in human cells.

FICD was shown to be glycosylated (Sanyal et al., 2015). The importance of N-glycosylation for different aspects of neural development has been well documented, acting for example through influencing protein stability and activity (Scott and Panin, 2014a). For instance, N-glycans were found to play key roles in neural cell adhesion and axonal targeting during development (Scott and Panin, 2014a) and in neural excitability and synaptic transmission (Scott and Panin, 2014b). It would thus be of interest to analyse the molecular effect of N-glycosylation on FICD function. As the glycosylated residue (Asn275) is close to the conserved autoinhibitory Glu234 (Preissler et al., 2017a), its modification with bulky glycan residues may for example affect FICD's autoregulation (Engel et al., 2012).

Altogether, we suggest an additive effect of small changes in the structure and function of many proteins (with heterogeneous functions in cytoskeleton, motors, metabolism, splicing, and ECM) to underlie the subtle but significant changes in neurogenesis upon *FICD* OX and KD. The heterogeneity of processes the AMPylated proteins are involved in led to diverse hypotheses that try to explain the role of AMPylation in neurogenesis. A combination of all hypotheses may also be true – and all of them remain to be confirmed. Further, our findings suggest that mutations of prospective AMPylation sites could affect neurodevelopment. Due to the lacking knowledge of exact AMPylation sites for instance in tubulin and MT-associated proteins, we are unable to proof our hypotheses. But several single nucleotide variants which lead to depletion or addition of “AMPylatable” amino acids have been identified in patients with neurodevelopmental disorders (see **Table 3**; Decipher (Firth et al., 2009)). And the effect of FICD on neurogenesis was clearly dependent on its AMPylation activity as it was absent when we electroporated COs with the active site mutant H363A. So far, one patient with a point mutation in FICD has been reported by Deciphering Developmental Disorders (DDD) database (see **Table 3** (Firth et al., 2009)). Interestingly, this individual shows abnormality of the eye and the nervous system – which further supports a role for FICD-mediated AMPylation in neurodevelopment.

Table 3: DDD patient with FICD variant and Decipher patients with tubulin, kinesin and myosin variants resulting in gain or loss of possible AMPylation site and nervous system phenotypes.

Gene (Transcript)	Position	Size	Consequence	Inheritance	Genotype	Pathogenicity / Contribution	Phenotype(s)
FICD	Chr12:108912413-108912413 C>T	SNV	missense variant	De novo constitutive	Heterozygous	Uncertain	Abnormality of head or neck Abnormality of the eye Abnormality of the nervous system Growth abnormality
TUBB3 (ENST00000556922)	Chr16:90001548-90001548 c.1730C>T p.Ser577Leu	SNV	missense variant	Paternally inherited, mosaic in father	Heterozygous	Likely pathogenic Full	Abnormality of connective tissue Abnormality of the eye
TUBB3 (ENST00000556922)	Chr16:90001548-90001548 c.1730C>T p.Ser577Leu	SNV	missense variant	De novo constitutive	Heterozygous		Abnormality of the digestive system Abnormality of the eye Abnormality of head or neck: postnatal microcephaly Abnormality of the nervous system
TUBB3 (ENST00000556922)	Chr16:90001151-90001151 c.1333G>A p.Gly445Ser	SNV	missense variant	Maternally inherited, constitutive in mother	Heterozygous	Pathogenic Full	Abnormality of the eye Abnormality of head or neck Abnormality of the musculature Abnormality of the nervous system
TUBB3 (ENST00000556922)	Chr16:90001454-90001454 c.1636A>T p.Thr546Ser	SNV	missense variant	De novo constitutive	Heterozygous		Abnormality of the digestive system Abnormality of head or neck: postnatal microcephaly Abnormality of the integument Abnormality of the nervous system: generalized-onset seizures
TUBB2B (ENST00000259818)	Chr6:3227774-3227774 c.4C>A p.Arg2Ser	SNV	missense variant	Unknown	Heterozygous	Uncertain Uncertain	Abnormality of the eye Abnormality of head or neck Abnormality of the nervous system: seizures
KIF5C (ENST00000435030)	Chr2:149835499-149835499 c.1357G>T p.Asp453Tyr	SNV	missense variant	Paternally inherited, constitutive in father	Heterozygous	Uncertain Uncertain	Abnormality of the digestive system Abnormality of head or neck Abnormality of the nervous system: focal-onset seizure
KIF5C (ENST00000435030)	Chr2:149799272-149799272 c.587C>A p.Thr196Ly	SNV	missense variant	De novo constitutive	Heterozygous		Abnormality of the nervous system
MYH3 (ENST00000583535)	Chr17:10550528-10550528 c.869T>G p.Ile290Ser	SNV	missense variant	De novo constitutive	Heterozygous	Pathogenic Full	Abnormality of the ear Growth abnormality Abnormality of head or neck Abnormality of prenatal development or birth Abnormality of the skeletal system
MYH3 (ENST00000583535)	Chr17:10554954-10554954 c.380A>G p.Asn127Ser	SNV	missense variant	Maternally inherited, constitutive in mother	Heterozygous	Uncertain Uncertain	Abnormality of the ear Abnormality of head or neck Abnormality of the musculature
MYH3 (ENST00000583535)	Chr17:10554954-10554954 c.380A>G p.Asn127Ser	SNV	missense variant	Maternally inherited, constitutive in mother	Heterozygous	Uncertain Uncertain	Abnormality of the ear Abnormality of the eye Abnormality of head or neck Abnormality of the musculature
MYH3 (ENST00000583535)	Chr17:10532970-10532970 c.5740G>A p.Ala1914Thr	SNV	missense variant	Paternally inherited, constitutive in father	Heterozygous	Uncertain None	Growth abnormality Abnormality of head or neck Abnormality of the integument Abnormality of limbs Abnormality of the nervous system Abnormality of the skeletal system

Information extracted from the Decipher database (Firth et al., 2009).

5.3. ECE2 - A NOVEL PH CANDIDATE WITH OLD AND NOVEL DISEASE-CAUSING MECHANISMS

In the third study (**Chapter 4**; (Buchsbaum et al. , Under Revision)), we identified *ECE2* as a promising novel candidate gene for PH. Biallelic point mutations, detected in two unrelated patients with MRIs showing heterotopic nodules of grey matter lining the lateral ventricles, were predicted to have a disease-causing effect. Hence, our studies focused on mimicking LOF both in human iPSC-derived *in vitro* and mouse *in vivo* model systems. The characterization of *ECE2* expression in human *in vitro* models revealed highest expression in neurons and an additional enrichment at the apical surface of CO ventricles. Acute KD in COs lead to ectopic positioning of non-transfected differentiated neurons to the VZ, adjacent to transfected aRG. The patient phenotype of ectopically positioned neurons was thus partly recapitulated *in vitro*, the underlying mechanisms being predominantly non-cell-autonomous. Moreover, inhibition of *ECE2* activity in young, migrating iPSC-derived neurons caused significant changes in their migratory dynamics. In the developing mouse cortex, acute *Ece2* KD resulted in loosening of apical AJs and consequently in delamination of progenitor cells towards ectopic, more basal locations (1 dpe) where they formed ectopic rosettes, giving rise to ectopic neurons that formed nodules containing deep and upper layer neurons (3dpe). Also *in vivo*, the patient phenotype was thus partly recapitulated. Both malpositioned progenitors and neurons were mostly non-transfected, underscoring again non-cell-autonomous contribution to the malformation upon *ECE2* mutation.

Further, chronic inhibition of total *ECE2* by Phos treatment and permanent loss of *ECE2* by genome-edited KO in iPSCs was used to reveal cellular functions of *ECE2* and both produced very similar phenotypes in COs. Namely, the cell composition was changed to an increased number of progenitors at the expense of neurons. Cytoskeletal components including actin and MTs were disorganized with impaired apico-basal polarity and apical neuro-ependymal lining. Considering the highest expression levels of *ECE2* in neurons and at the apical surface, a role for *ECE2* both in apical belt integrity or apico-basal polarity and in neuronal differentiation are likely – and was indeed revealed in our experiments. Additionally, significantly more neuronal cell bodies failed to leave the VZ in *ECE2* KO COs compared to control, reminiscent of PH. Proteomics of *ECE2* KO COs confirmed a reduction in factors needed for normal cortical development, including actin and MT cytoskeletal components, cell polarity, migration, and adhesion regulators, and even downregulation of some proteins known to play a role in neurodevelopmental disorders. In addition to these proteins with known functions in cortical development, whole-CO and secretome proteomics revealed a reduction in ECM proteins and receptors, which may be responsible for non-cell-autonomous changes in neuronal migration and in cell fate. Proteomics further revealed changes in phosphorylation of cytoskeletal and motor proteins, indicating an involvement of *ECE2* in the regulation of PTMs.

In total, our findings add *ECE2* to the list of genes whose mutations may underlie PH and stress that – although genetically heterogeneous – PH is often caused by similar cellular mechanisms. Besides, we suggest deregulation of the ECM as a novel causative mechanism.

How minor genomic changes can disrupt cortical development. Together with other recent examples (Heinzen et al., 2018; Klaus et al., 2019; O'Neill et al., 2018a; O'Neill et al., 2018b), our study shows how genomic changes as small as SNVs can disrupt

processes pivotal to cortical development. Besides, it underlines the power of next generation genetic analyses, such as the WES used here on DNA from healthy parents and affected children, for the identification of responsible genes. Specifically for *ECE2*, one healthy allele seems to be sufficient for its function as the parents of the two patients with biallelic variants are heterozygous carriers of SNVs. Of course, by analyzing only the protein-coding genes in the patient exome, intronic variants may have been missed and the detection of copy number variants, which are enriched in PH (Cellini et al., 2019), is also limited in WES.

The power of combining model systems and unbiased analysis methods. As was elaborated on in sufficient detail in the introduction of this thesis, it has been difficult in the past to recapitulate patient phenotypes of NMDs in mice carrying human patient mutations in the homologous gene. To this end, we combined here *in vitro* and *in vivo* model systems to understand the role of *ECE2* in cortical development and disease. The phenotypes observed upon *ECE2/Ece2* KD were highly similar in both models and were reminiscent of PH, indicating that the role for *ECE2* may be comparable in mouse and human cortical development. As a next step, we generated *ECE2* KO iPSCs via the relatively novel genome editing method CRISPR/Cas9 (Ben Jehuda et al., 2018) in collaboration with Shahryar Khattak. In the analysis of derived *ECE2* KO COs and isogenic controls, we applied several unbiased methods to identify differences. Using FACS, we were able to detect changes in composition of the COs in terms of progenitors and neurons, both upon chronic inhibition of *ECE2* enzymatic activity and upon *ECE2* KO. These changes could not be detected by immunohistochemical analysis of electroporated organoids, neither from *in vivo* analysis. This may be due to the sparse transfection upon electroporation and due to the non-cell-autonomous role of *ECE2*: Upon *ECE2* KD in few cells, the neighboring, non-transfected cells can still generate and secrete products of *ECE2* enzymatic activity. Thus, it is highly valuable to combine acute with chronic or permanent manipulation methods to distinguish cell-intrinsic from non-autonomous mechanisms. A similar discrepancy between underlying genetics in the mouse models of a human NMD was described for *Dcx*: While *Dcx* KO mice showed no cortical lamination defect, acute shRNA-mediated *Dcx* KD in rats lead to a better morphological and functional recapitulation of the human cortical phenotypes, including aberrant electrophysiology reminiscent of epilepsy (Nosten-Bertrand et al., 2008; Ramos, 2005).

The second unbiased method we applied in the analysis of *ECE2* KO and control COs was MS-based proteomics, which we used for the analysis of whole organoids lysate to identify changes in protein expression and to decipher differentially phosphorylated cytoskeletal and motor protein, and for the analysis of culture medium to identify changes in the CO secretome. Our study is among the first to use proteomics in COs. The only other study that reported the use of proteomics in COs applied it to identify differences between trisomy 21 (Down syndrome) and control COs (McClure-Begley et al., 2018). In an analysis of COs of different stages, they revealed that MS-detected proteins reflect well the neurodevelopmental trajectory in COs – similarly to scRNA-seq as was shown several times (Camp et al., 2015; Pollen et al., 2019; Quadrato et al., 2017). Comparing trisomy 21 patient-derived and control COs, they found a number of dysregulated proteins and demonstrated reversal of this dysregulation by drug treatment (McClure-Begley et al., 2018). Interestingly, some proteins identified to be changed in trisomy 21 overlap with proteins we detected as downregulated upon *ECE2* KO. Namely, several collagens and collagen-binding TGFBI were expressed at lower level in patient-like COs

in both studies. This indicates overlapping mechanisms at the basis of different developmental disorders. We further demonstrated the possibility to detect even differences in secretome, although this method requires improvement due to high background from culture medium components.

This example stresses how useful unbiased analysis methods are to detect phenotypes in the rather variable COs. Besides, the fact that we can detect (dysregulated) proteins both in CO lysate and secretome shows the advantage of 3D over 2D *in vitro* human models as COs generate an elaborated ECM.

With this study, we set an example on how combining objective analysis methods and *in vivo* and *in vitro* models can help to reveal phenotypes and mechanisms that may have remained hidden with standard ISH-based quantification methods.

Setting *ECE2* in the context of other PH-genes. The aim with which we started the *ECE2* project was to identify novel genes whose mutations lead to PH, but also to highlight mechanisms that commonly arise from the heterogeneous genetic causes. To this end, several examples shall be given here that put PH caused by biallelic mutations in *ECE2* into a wider context of the disorder.

As detected by proteomics of COs, *FLNA* was downregulated upon *ECE2* KO. Mutations in *FLNA* were identified as genetic cause for familial PH more than 20 years ago (Fox et al., 1998). The F-actin cross-linking protein is essential for cytoskeleton rearrangement and cell migration and both insufficiency and excess of *FLNA* were shown to inhibit migration (Carabalona et al., 2012; Sarkisian et al., 2006), indicating the importance of precise regulation of *FLNA* expression during neuronal migration. Upon acute *FlnA* KD in rats, the polarized RG structure is disrupted in a similar way to what we detected upon *ECE2* KD and both cell cycle progression and neuronal migration towards the CP are altered (Carabalona et al., 2012). Similar phenotypes were identified in mice with mutations in *Mekk4* and upon *Rcan1* KD in rats, both of which act in the *FLNA* pathway. The intrinsic downregulation of *FLNA* in *ECE2* KO COs may thus represent a cell-autonomous contribution to the observed neuronal migration defect (Zhang et al., 2013). The close relative of *FLNA* that was also downregulated in upon *ECE2* KO, *FLNC*, has not been associated with neurological disorders yet, although being expressed in the brain at low levels (Sheen et al., 2002) (proteinatlas.org). It has been associated with myopathies (Fürst et al., 2013).

A process that has been implicated as main disease-causing mechanism in PH is vesicle trafficking (Sheen, 2014). Mutations in *ARFGEF2*, which encodes the vesicle transport protein Big2, cause autosomal recessive PH with microcephaly (Sheen et al., 2004a). Big2 and the related *Napa*, whose cKO leads to PH in the developing mouse brain (Ferland et al., 2009), mediate Golgi transport, trans-Golgi to endosome transport, and vesicle fusion. *FLNA* is also involved in Golgi membrane budding and trafficking of transport vesicles (Sheen, 2014). The more recently identified PH-gene *TMTC3* colocalizes with the vesicular GABA transporter vGat and was thus suggested to mediate synaptic vesicle transport (Farhan et al., 2017). All these genes play into the final common pathway of disrupted vesicle trafficking, leading to impaired cell adhesion and loss of neuroependymal integrity. Among the significantly enriched GO Terms of the proteins downregulated upon *ECE2* KO are several ones that fit into this pathway (String.db (Szklarczyk et al., 2017)): “positive regulation of cytoplasmic transport” (MSN, EZR, MAP2), “membrane to membrane docking” and “positive regulation of early endosome to late endosome trafficking” (MSN and EZR), and “vesicle budding from

membrane" (S100A10, ANXA2, SEC24D, CTSZ). This indicates that vesicle trafficking may also be affected by the lack of ECE2.

Vesicle trafficking depends on both actin and MT cytoskeleton and their transport processes. Upon *ECE2* KO, IHC analyses and proteomics of COs revealed a disruption of both actin and MT cytoskeleton(-associated) integrity. This included differential phosphorylation of some MAPs, motor, and vesicle trafficking proteins, and downregulation of a tubulin and several MAPs such as MAP2, MAP4 and EM41. Interestingly, EML1 has been associated with primary cilia function and positioning and with MT dynamics: In *Eml1* mutant HeCo mice, neural progenitors acquire ectopic positions due to ectopic primary cilia and abnormal spindle orientation and location and give rise to ectopic neurons (Bizzotto et al., 2017; Kielar et al., 2014). Furthermore, a role for primary cilia in the etiology of PH was recently suggested from KD of the novel PH-associated gene *MOB2* *in vivo* and in COs (O'Neill et al., 2018a): MOB2 was found to play a role in cilia number and positioning, nuclear-cilia coupling and with that in neuronal positioning. Additionally, Mob2 was implicated in phosphorylation of FlnA, impairing actin cytoskeletal remodeling and suggesting a link between FlnA and the primary cilium (O'Neill et al., 2018a).

We see a reduction in apically localized primary cilia upon acute *Ece2* KD *in vivo*, upon chronic ECE2 inhibition in COs, and in *ECE2* KO COs (with concomitant spread of ARL13B+ cilia throughout the thickness of the VZ in COs and the VZ and SVZ in the mouse cortex). This indicates that progenitors delaminate and generate neurons at ectopic locations. The cilium-localized GTPase ARL13B regulates both cell migration and cell cycle progression (Pruski et al., 2016) and its reduction and redistribution upon *ECE2* KD, KO or inhibition may be at the core of the observed changes in migration and proliferation. Whenever apical cilia acquire non-apical positions, affected cells lack their contact to the signals within the cerebrospinal fluid. Besides, the delaminating cells are placed into a different microenvironmental niche. These effects may contribute to the observed changes upon lack of ECE2.

Closely related to cytoskeletal integrity and to vesicle transport mediating their positioning are apical AJ proteins or, more generally, cell adhesion proteins. We found a significant reduction in numerous cell adhesion and polarity proteins in *ECE2* KO COs with loosening of the AJ belt and delamination of NPCs. Also the increased expression of ECE2 at the apical ventricular surface in COs suggests a function of ECE2 in the apical aRG compartment. In mice, several studies revealed the importance of the actin cytoskeleton and its anchoring to AJs for NMDs: Conditional deletion of α -E-catenin disrupted the coupling of AJ proteins with intracellular actin fibers, lead to loss of apico-basal polarity and increased G/F actin ratio and resulted in SBH (Schmid et al., 2014). *Rapgef2* and 6 were also implicated in AJs (Maeta et al., 2016): (c)KO of one or both *Rapgef*s resulted in RG scaffold disruption and delamination through the loss of AJs, with the ectopic RG and IPCs giving rise to a huge ectopic cortical mass. Similarly, loss of the polarity regulator Lgl1 in the mouse cortex disrupted AJs, leading to ectopic aRG and IPCs, disorganized aRG fibers with rosette-like deformation, and ectopic neurons (Zhang et al., 2019). Besides, aRG lacking Lgl1 showed hyperproliferation and impaired neuronal differentiation (Zhang et al., 2019), stressing a role for AJs and polarity proteins in cell fate. From co-occurrence of PH with microcephaly it becomes obvious that PH genes can regulate proliferation. For example, PH patients with *ARFGEF2* mutations have microcephaly and males with *FLNA* mutations that die at birth have thinner cortices (Guerrini et al., 2004). Moreover, mutations in the cadherin-ligand pair *FAT4* and *DCHS1*

cause PH (Cappello et al., 2013), which has recently been recapitulated and further investigated in COs (Klaus et al., 2019). Reduced expression of *Fat4* or *Dchs1* in the developing mouse cortex lead to increased progenitor and reduced neuronal numbers and resulted in accumulation of ectopic neurons (Cappello et al., 2013). In COs with *FAT4* or *DCHS1* mutations, IHC of nestin and IHC and WB of ac-tub cytoskeletal markers showed a similar disruption of the neuro-ependymal integrity as we found in the absence of *ECE2*. Besides, apico-basal polarity was affected with premature progenitor delamination and neuronal migration deficit in a subset of patient-derived neurons. For instance, scRNA-seq revealed a reduction in *FLRT2*, involved in cell-cell adhesion, cell migration and axon guidance, which we also found downregulated in *ECE2* KO COs via proteomics (Klaus et al., 2019). Recent findings on the role of *FLRT1* and *FLRT3* in neuronal migration (del Toro et al., 2017) suggest that the reduced *FLRT2* level in *ECE2* KO COs may contribute to the observed neuronal migration defect.

Opposite to the phenotype upon acute KD of *Fat4* and *Dchs1* in the developing mouse cortex, the proportion of proliferating progenitors was decreased and neuronal differentiation was increased in patient-derived COs (Klaus et al., 2019). Also *Cdc42* and *RhoA* disruptions cause changes in progenitor proliferation and brain size (Cappello et al., 2006; Katayama et al., 2011). cKO of *RhoA* destabilized both actin and MT cytoskeleton in RG, with increased G/F actin ratio. Although cKO neurons would migrate normally, these RG defects produced SBH due to non-cell-autonomous mechanisms – similar to what we saw upon *ECE2* KD. The recently discovered PH candidate gene *PLEKHG6* was also found to regulate NPC differentiation and neuronal migration via *RHOA* and its KD in COs phenotypically recapitulated PH (O'Neill et al., 2018b).

An additional functional group of proteins we identified as downregulated in *ECE2* KO COs play a role in splicing and/or mRNA stability. These 13 proteins formed a tight sub-network of interactors in protein-protein interaction analysis. RNA processing and transcription regulation have been implicated in brain development and PH etiology before: The integrator complex gene *INTS8* plays an important role in transcriptome integrity and PH patient mutations and *INTS8* deletion alter gene expression and neuronal differentiation (Oegema et al., 2017) (see also *The alternative splicing hypothesis* in **Chapter 5.2**).

Altogether, these comparisons to known PH genes in human and mouse show that the regulation of cytoskeleton, cell adhesion, polarity, migration, and proliferation *versus* differentiation are common mechanisms in PH. They are regulated by a heterogeneous set of proteins – and we suggest that *ECE2* is a new one of them.

ECE2 and the ECM in PH. In addition to implication of *ECE2* in the above discussed processes known to be important in cortical development and to be disrupted in NMDs, we identified a less studied but important functional group: ECM proteins. ECM components represented the biggest group of downregulated proteins in *ECE2* KO COs and their secretome with 49 implicated proteins. In the context of *ECE2* as a membrane-bound protease that resides in the lumen of acidified trans-Golgi (Emoto and Yanagisawa, 1995), a function of *ECE2* in the production of secreted factors is not surprising. Neither was it surprising to us because the mechanism underlying the observed phenotypes reminiscent of PH clearly had non-cell-autonomous aspects involved. ECM proteins such as collagens, galectins, and lumican have been shown to be highly important during brain development, where they regulate – among others – proliferation, migration, and differentiation of neural cells (Dityatev and Fellin, 2008; Long and Huttner, 2019). Collagen I and lumican have been shown to drive folding of the

human neocortex (Long et al., 2018). The collagen VI (COLVI) family, three members of which were downregulated in *ECE2* KO COs, forms characteristic beaded microfilament nets in the ECM, where it modulates the stiffness and mechanical properties of the ECM, but also impacts several intracellular processes and pathways (Gregorio et al., 2018). COLVI is involved in basal lamina organization and neural homeostasis, with a neuroprotective effect in stress and ageing (Gregorio et al., 2018). Furthermore, collagens and ECM remodeling are relevant to the onset of epilepsies, which patients with PH often present with (Dityatev and Fellin, 2008), thus highlighting a fundamental role of the ECM in brain physiology and pathology. For example, mutations in *COL6A2* were linked to progressive myoclonus epilepsy (Karkheiran et al., 2013). Interestingly, *COL6A1* was reported within a set of genes that are upregulated in the human cerebral cortex with respect to non-human primates, indicating a human-specific role of this gene in brain development and evolution (Caceres et al., 2003).

Another ECM gene that our group identified as PH candidate is *LGALS3BP* (Kyrousi et al.; Under Revision). Interestingly, *LGALS3BP* is a galectin binding protein – and we found galectins-1 and -4 reduced in *ECE2* KO COs, indicating another link between different cases of PH.

Ezrin and moesin, which are downregulated upon *ECE2* KO, are both implicated in vesicle trafficking (see above) and are involved in establishing a connection between ECM receptors and the intracellular actin cytoskeleton (Kawaguchi et al., 2017). Besides, they integrate Rho GTPase signaling and thereby affect the actin cytoskeleton, for example by recruiting and locally activating PLEKHG6 and RhoG to the apical side (D'Angelo et al., 2007).

Protein phosphorylation in PH. The importance of posttranslational modifications in functional fine-tuning of proteins involved in cortical development has been extensively demonstrated (see examples in 1.1.4). Here, we were especially interested in phosphorylation as the most widespread PTM (Cohen, 2000), which is abundant on cytoskeletal and associated proteins in neurons to regulate their morphology and polarity (Song and Brady, 2015) (see also 5.1 and 5.2). For example, phosphorylation of Ser2086 in MAP4 was only detected in the CTRL COs, whereas Ser25 and Ser1653 of MAP1B were exclusively phosphorylated in *ECE2* KO COs. Although the differentially phosphorylated sites did not overlap with the positions of the SNVs in *MAP1B*, a gene in which variants were recently discovered to cause PH (Heinzen et al., 2018), this further supports a general deregulation of the microtubule cytoskeleton in the absence of *ECE2*. A motor protein site only phosphorylated after upon *ECE2* KO was Ser207 in DYNC1LI1 and phosphorylation of Ser942 in the vesicle transport factor USO1 was exclusively detected in the CTRL. These differences between CTRL and KO indicate changes in vesicle transport, which have formerly been found to underlie PH (Cellini et al., 2019; Sheen et al., 2004a). Ser292 of the actin organizer CDC42EP4 and Ser24 in the tight junction protein TJP2 were only phosphorylated in the CTRL, which may further support observed changes in the actin cytoskeleton, in line with loosening of the apical adherens belt. Further, the proteins with up- or downregulated phospho-sites upon *ECE2* KO were enriched for GO functions in actin binding and organization (String.db. (Szkarczyk et al., 2017)).

Based on our findings of differential protein phosphorylation upon *ECE2* KO, we propose that misregulation of PTMs such as phosphorylation can also contribute to the etiology of PH. In this context it would be of interest to analyse CTRL and *ECE2* KO COs for

dysregulation of additional PTMs with known nervous systems functions, such as acetylation and polyglutamylation (see 1.1.4).

Unresolved questions for future investigations. So far, the focus of this discussion was on similarities of *ECE2* KD and KO phenotypes with other cases of PH (and SBH). But several open questions remain that would be highly interesting to resolve.

First of all, we called the ectopic accumulation of neural progenitors around an ectopic apical surface, which we observed 3dpe upon *Ece2* KD *in vivo*, “rosette”. This term, reused from 2D *in vitro* systems, describes the inside-out organization of neural progenitors and neurons around an apical surface. Rosettes have been described in mouse models of PH before, for example upon ectopic expression of reelin (Kubo et al., 2010) and upon *RhoA* cKO (Katayama et al., 2011). In these studies, the circular shape of cell aggregates was more clearly defined and the apical surface seemed bigger, plus several rosettes formed per brain. It may thus be interesting to 1) analyze the effect of *Ece2* KD after more time post electroporation and 2) to further characterize if – as is the case upon ectopic reelin expression (Kubo et al., 2010) – rosettes give rise to neurons that arrange in inside-out manner, also forming a dendrite-rich ectopic MZ. We called the ectopic clusters of neurons in the developing mouse brain that form upon *Ece2* KD “nodules”, as they are reminiscent of heterotopic nodules in patient brains, which line the surface of the lateral ventricles. For these nodules, it would also be of interest to analyze the outcome at later timepoints: Which final localization will the ectopic neurons acquire? Do the neurons within nodules undergo terminal differentiation and become synaptically and electrophysiologically active? Do they establish connectivity to the overlying normotopic cortical neurons? Is their activity epileptogenic (Chevassus-au-Louis et al., 1999; Kothare et al., 1998)?

In addition to nodules in the cortical parenchyma, basal ectopic neurons were observed upon *Ece2* KD *in vivo* (see **Figure 12**). These may either resemble cobblestone-like overmigrating neurons that occur in lissencephaly type II due to disruption of the basal membrane or may actually not overmigrate but represent the start of a cortical fold. The difference between these options can be analysed by IHC staining for basal lamina components such as laminin and, again, a longer timepoint after electroporation would be instrumental.

In the context of cortical folding, I would like to mention the study of de Juan Romero *et al.* who analyzed differential gene expression in the different germinal layers of the developing cortex between future gyri and sulci in the ferret cortex (de Juan Romero *et al.*, 2015). For instance, high levels of *Trnp1* are responsible for tangential expansion of NSCs and localize to sulci in human fetal cortex, whereas in gyri, which are regions of low *Trnp1* expression, radial expansion increases of the number of intermediate progenitors and basal radial glial cells. Accordingly, KD of *Trnp1* in the developing mouse cortex can induce folding (Stahl *et al.*, 2013). Similarly, differential expression of adhesion molecules FLRT1 and FLRT3 in future gyri and sulci underlies gyrification of the human and ferret cortex - but without involvement of progenitor cell amplification: differential intercellular neuronal adhesion acts as a regulator of cortical folding with increased radial migration of excitatory neurons in the absence of FLRT adhesion molecules (del Toro *et al.*, 2017).

The downregulation of FLRT2 protein levels that we detected in *ECE2* KO COs may contribute to the overmigration phenotype discussed above. Interestingly, the fold change of expression in gyrus over sulcus in ferret shows a similar pattern for different genes involved in PH (data extracted from (de Juan Romero *et al.*, 2015)): gene expression of most of them is higher in the oSVZ of gyri and may additionally be higher in iSVZ and VZ:

Fold-change Gyrus/Sulcus, with $p < 0.05$: *FAT4* 1.06 (VZ), 1.65 (ISVZ), 1.5 (OSVZ)
DCHS1 1.58 (VZ), 1.57 (OSVZ)

And this relation is also similar for *ECE2* and a collagen downregulated upon its KO:

ECE2 0.8 (ISVZ), 1.35 (OSVZ)
COL6A1 1.98 (VZ), 1.22 (ISVZ), 1.38 (OSVZ)

This suggests some extent of involvement of PH genes, including *ECE2*, in gyrification. Another hint in that direction is that *ECE2* seems to have a role in the production of lumican and collagens as these were downregulated in the absence of *ECE2*. LUM and COL1 were shown to be required for folding of human fetal cortical explant and to induce folding when added externally (Long et al., 2018). Here, we need to consider also the question how similar is the ECM in the fetal cortex and in COs – which to my knowledge has not been studied to date.

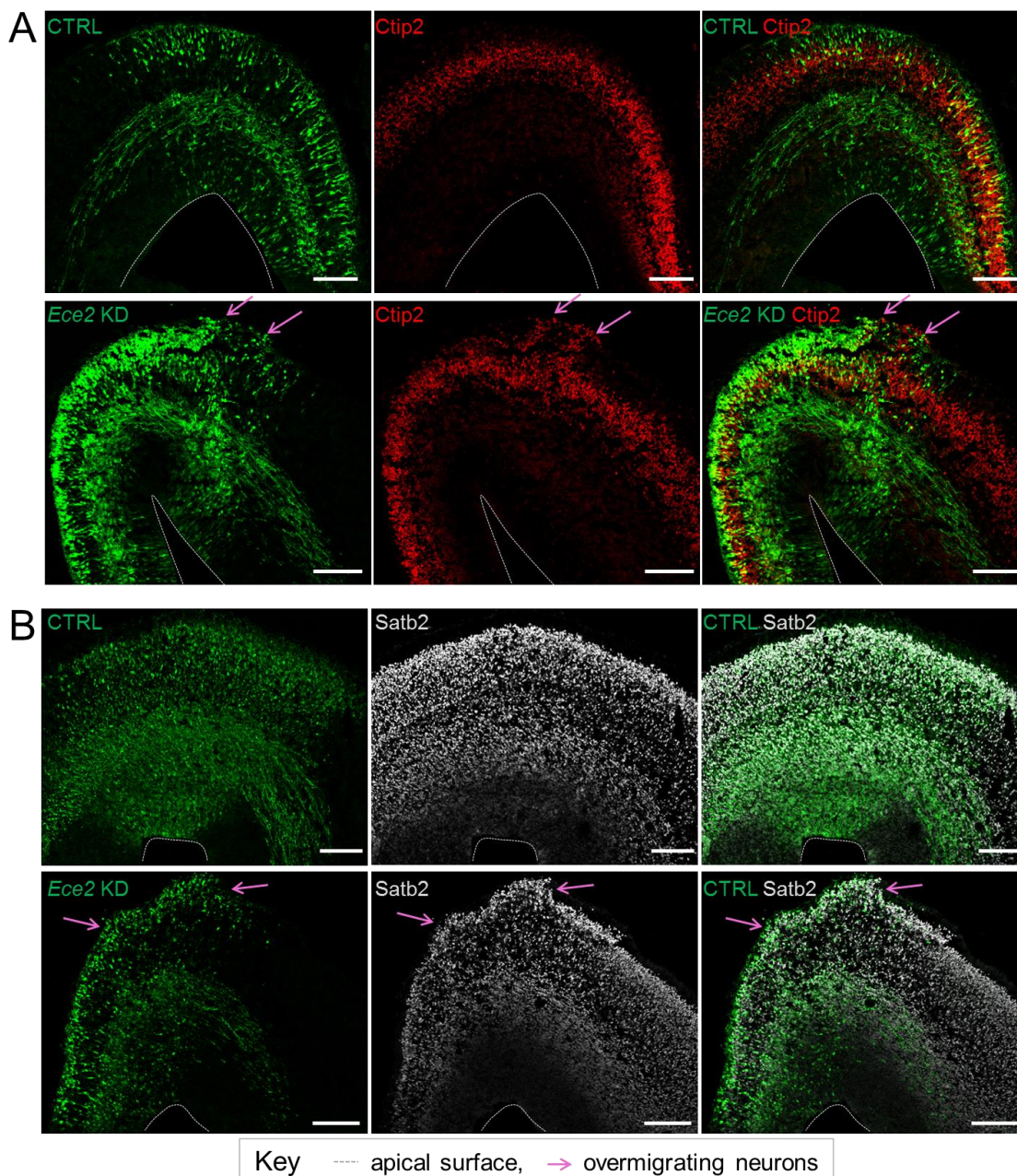


Figure 12: Overmigration of neurons upon acute *Ece2* KD *in vivo*. Examples of images of E13-16 electroporated control (CTRL) and *Ece2* KD brains illustrating overmigrating deep- (A) and upper layer neurons (B) upon *Ece2* KD (Scalebar = 100 μ m).

A later timepoint of analysis would also be interesting in *ECE2* KO and control COs, for example 90d, to see if the relative composition of progenitors and neurons changes. Is there just a delay in neuronal differentiation that normalizes later on or does the larger progenitor pool at the analyzed timepoint of 60d result in a final overproduction of neurons?

For the two patients with biallelic variants in *ECE2* and PH, we don't have information about any other cortical phenotype so far. With the hints that we got from both *in vivo* and *in vitro* analyses about differences in progenitor *versus* neuron numbers and possible overmigration, it would be highly interesting to analyze the patient MRIs in more detail. Measurement of the grey matter thickness and determination of the gyrification index would be useful parameters. In order to have good reason to request the help from clinicians for these analyses, we need to prove, though, that the patient mutations lead to a loss of function of the enzyme, which we model here via its KD/KO. An approach to showing that the patient mutations indeed disrupt the protein function would be to introduce them into an *ECE2* OX plasmid via site-specific mutagenesis. Making use of the fact that *ECE2* is an enzyme, we can then test the effect of the patient mutations in an enzymatic activity assay, for example with a fluorogenic substrate (Ouimet et al., 2010). Having the normal and patient-like *ECE2* constructs, the next step will be to overexpress them both in COs and in the developing mouse cortex.

Another feature typical for PH is epilepsy that may arise from the ectopic neuronal nodules (Kothare et al., 1998). Although *ECE2* patients did not present with seizures, it may be interesting to perform electrophysiology in *ECE2* KO COs and in mice in which *Ece2* is acutely downregulated. A novel advancement in 3D cell culture are assembloids/fused-organoids, in which spheroids of different regional identity are generated by separate patterning and subsequently fused together. The result is a relatively high complexity with defined identities, such as dorsal and ventral telencephalon (Bagley et al., 2017; Birey et al., 2017; Xiang et al., 2017) (see 1.4.2). For example, the fusion of dorsally and ventrally patterned spheroids with different genetic background (i.e. patient and control) can be used to distinguish cell-autonomous from non-cell-autonomous disease mechanisms. As epilepsy often results from an imbalance of excitation and inhibition, assembloids are highly useful for studying not only radial migration of excitatory neurons within the developing cortex, but also the tangential migration of interneurons from ventral to dorsal cortex and their integration (Bagley et al., 2017; Birey et al., 2017; Xiang et al., 2017). A possible involvement of GABAergic interneurons in the etiology of PH was shown e.g. for *TMTC3* (Farhan et al., 2017) and a reduction in inhibitory synaptic activity within both heterotopic and normotopic cortex has been described for irradiation models of neuronal heterotopia (Chen and Roper, 2003). A recent study identified *Ece2* expression in synaptosomes of parvalbumin-expressing interneurons in the cortex and hippocampus of adult mice (Pacheco-Quinto et al., 2016). An analysis of the relative contribution of different interneuron subtypes to heterotopia in post-mortem brains showed that – although interneurons of all subtypes may be present within the heterotopia – the density of parvalbumin-positive neurons was lower than in the cortex (Thom et al., 2004). The same was found for an irradiation model of heterotopia: The densities of both parvalbumin- and somatostatin-positive interneurons were significantly

decreased in cortical dysplasia and heterotopia, which may contribute to hyperexcitability (Akakin et al., 2013). These findings indicate that ECE2 may also function in interneurons and its reduction may contribute to epileptogenic potential of heterotopic nodules. This could be further studied in the developing brain using assembloids and *in utero* electroporation directed at *Ece2* KD in the ventral telencephalon.

Comorbidity of PH with different neuropsychiatric disorders has been reported for many cases (Fry et al., 2013; Lippi, 2017). For example, schizophrenia (Nopoulos et al., 1995) and others like major depressive disorder, bipolar disorder, ASD (Fry et al., 2013) were described. Also *de novo* variants in *ECE2* have been detected in patients with ASD (De Rubeis et al., 2014; Iossifov et al., 2012) that may contribute to the etiology of ASD. ASD is also often caused by imbalance of excitation and inhibition, so again assembloids would be a good model to use for further studies in this direction.

Finally, the big remaining question after our study is: What is the exact molecular pathway of ECE2 action in the developing cortex? We don't know enough on how ECE2 executes all the deciphered functions. Information that can be found in literature is very sparse: ECE2 expression was shown to be restricted to a secretory intracellular compartment in neural tissues, namely to the trans-Golgi, whose acidified pH fits the pH-optimum of ECE2 activity (Davenport and Kuc, 2000; Emoto and Yanagisawa, 1995; Pan et al., 2004). The catalytic peptidase domain facing the Golgi lumen is common to all isoforms (Mzhavia et al., 2003) and the patient mutations localize to this domain. ECE2 produces not only the vasoconstrictor endothelin-1 that influences cerebral blood flow (Ehrenreich and Schilling, 1995; Mzhavia et al., 2003), but also a number of regulatory neuropeptides by cleavage of precursors at non-classical amino acid residues (Mzhavia et al., 2003; Pan et al., 2004). Neuropeptides are produced and released from storage and synaptic vesicles by both neurons and glia for their communication and act via metabotropic and G-protein coupled receptors (Leng and Ludwig, 2008; van den Pol, 2012). This modulates intracellular pathways, for example resulting in changes in gene expression and glial cell morphology (Oliet and Bonfardin, 2010; van den Pol, 2012). One possible hypothesis could thus be that ECE2 – via the production of neuropeptides – influences a diversity of pathways. So far, only two related studies analyzed ECE2-mediated hydrolysis of the biologically active peptides that were previously found to be cleaved by other related metalloproteases (Mzhavia et al., 2003; Pan et al., 2004). They found that ECE2 partially hydrolyzed big-endothelin-1, bradykinin, neurotensin, angiotensin I, substance P, peptide E, BAM 22P, and little PEN-LEN, and completely hydrolyzed BAM 18P and dynorphin B at selective sites (Mzhavia et al., 2003). PEN-LEN peptides are inhibitors of prohormone-convertase 1, which acts in the generation of a large number of neuroendocrine peptides. Hydrolysis of PEN-LEN by ECE2 thus leads to loss of this inhibition and change in the levels of neuroendocrine peptides (Mzhavia et al., 2003). Proenkephalin-derived peptide E, BAM 18 and BAM 22 are opioids that bind μ -opioid receptors, whereas the resulting BAM 16 and BAM 12 peptides exhibit κ -opioid receptors (Davis et al., 1990). This suggests a role of ECE2 in selective activation of different opioid receptors (Pan et al., 2004). In addition to its role in opioid peptide production and hydrolysis, ECE2 was reported to be involved in the recycling of μ -receptors when these are co-localized in the same vesicle (Gupta et al., 2015). Opioids function in the regulation of pain, stress and affect (Valentino and Volkow, 2018). Furthermore, the endogenous opioid system has been implicated in crucial neurodevelopmental functions, which may explain some of the phenotypes we observed upon reduction or KO of *ECE2*. For example, agonist-mediated activation of μ - and κ -opioid receptors acts via ERK and

MAPK pathways to modulate the cell fate decision and differentiation of NPCs to neurons, astrocytes and myelinating oligodendrocytes (Hahn et al., 2010; Kim et al., 2006; Vestal-Laborde et al., 2014): Opioids drive embryonic stem cell differentiation and inhibit NPC proliferation *in vitro* (Kim et al., 2006). Another study found that binding of opioid agonists to the δ -opioid receptor promoted neural differentiation from multipotent forebrain stem cells through activation of Trk-dependent tyrosine kinase (Narita et al., 2006). Thus, reduced production of opioid peptides upon lack of ECE2 may contribute to the increased proportion of progenitors over neurons that we observed in *ECE2* KO COs. This neuropeptide production hypothesis, exemplified with opioids, is of course only one of many possible ones: The mentioned studies only analyzed neuropeptides known to be hydrolyzed by the relatives of ECE2, ECE1 and neprilysin (Mzhavia et al., 2003; Pan et al., 2004). There may thus be many more intracellular and secreted products of ECE2 protease activity that remain to be elucidated and may help to shed light on the molecular mechanisms of ECE2 neurodevelopmental roles.

Summary of the *ECE2* study. Altogether, we have shown in this study that the phenotypes resulting from ECE2 inhibition, KD and KO strongly suggest its role in cortical development and in the etiology of PH. Our aim in this project was to identify common pathways and mechanisms underlying PH. This was fulfilled with the identification of cell polarity, adhesion, and migration and underlying actin and MT cytoskeleton as most important mechanisms. In addition, we identified the secretion and regulation of ECM components (and of PTMs) as so far less studied components contributing to non-cell-autonomous phenotypes.

5.4. SUMMARY OF THE KNOWLEDGE GAINED IN THIS THESIS

In the course of this discussion, it should have become already clear that, although the three studies presented in this thesis differ in focus, they share common pathways and mechanisms whose function is required in cortical development. The following graph aims at summarizing the most important findings of all studies individually and at highlighting common processes they identified as pivotal (**Figure 13**).

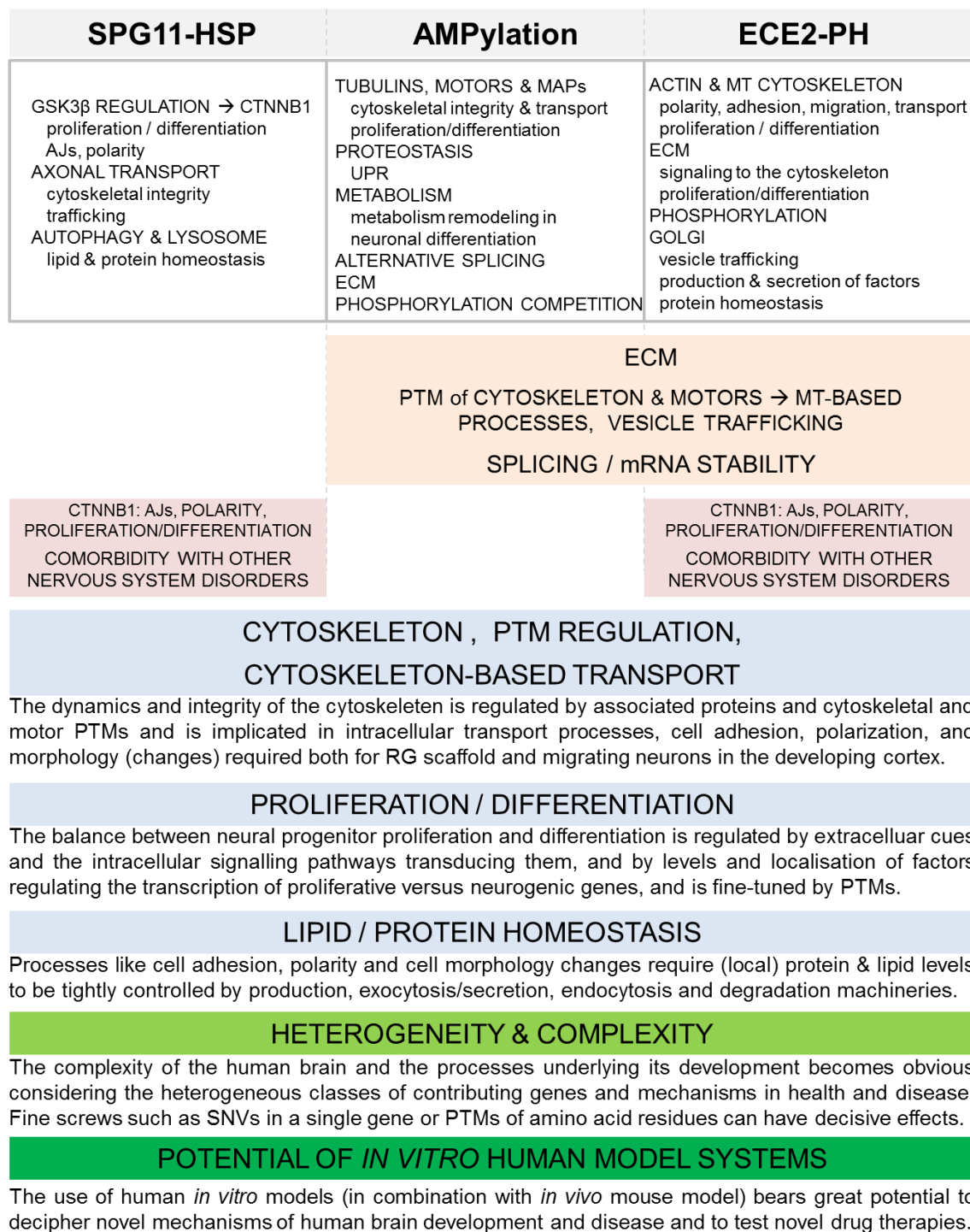


Figure 13: Key findings of each study and highlighted common mechanisms.

Altogether, the studies presented and discussed in this thesis highlight the heterogeneity and complexity of the processes underlying the development of the human cerebral cortex – both in health and disease. The overlapping functions of different genes in different stages of neurodevelopment and between mechanisms underlying different disorders suggests a classification of MCDs as spectrum disorders.

The fact that subtle changes as small as SNVs and resulting amino acid changes and disruption of PTM target sites can lead to cortical malformations therefore stresses the requirement for tight regulation on genome, transcriptome, proteome, and “posttranslatome” levels.

Besides, it is hardly surprising that a partly developmental origin has been ascribed to epilepsies, many psychiatric disorders, and even neurodegenerative diseases.

The combination of *in vivo* mouse and *in vitro* human model systems with genome editing and unbiased analysis methods will help to further illuminate the fascinating yet unresolved questions of how our brain evolved and develops. And how our enlarged cerebral cortex made us – if we believe in it – the pride of creation.

REFERENCES

- Adzhubei, I. A., Schmidt, S., Peshkin, L., Ramensky, V. E., Gerasimova, A., Bork, P., Kondrashov, A. S. and Sunyaev, S. R.** (2010). A method and server for predicting damaging missense mutations. *Nat. Methods* **7**, 248–249.
- Aebersold, R., Agar, J. N., Amster, I. J., Baker, M. S., Bertozzi, C. R., Boja, E. S., Costello, C. E., Cravatt, B. F., Fenselau, C., Garcia, B. A., et al.** (2018). How many human proteoforms are there? *Nat. Chem. Biol.* **14**, 206–214.
- Aiken, J., Buscaglia, G., Bates, E. A. and Moore, J. K.** (2017). The α -Tubulin gene TUBA1A in Brain Development: A Key Ingredient in the Neuronal Isotype Blend. *J. Dev. Biol.* **5**,.
- Akakin, D., Martinez-Diaz, H., Chen, H.-X. and Roper, S. N.** (2013). Reduced densities of parvalbumin- and somatostatin-expressing interneurons in experimental cortical dysplasia and heterotopia in early postnatal development. *Epilepsy Res.* **104**, 226–233.
- Anderson, S. A., Eisenstat, D. D., Shi, L. and Rubenstein, J. L.** (1997). Interneuron migration from basal forebrain to neocortex: dependence on Dlx genes. *Science* **278**, 474–6.
- Anderson, S. A., Marin, O., Horn, C., Jennings, K. and Rubenstein, J. L.** (2001). Distinct cortical migrations from the medial and lateral ganglionic eminences. *Development* **128**, 353–363.
- Anheim, M., Lagier-Tourenne, C., Stevanin, G., Fleury, M., Durr, A., Namer, I. J., Denora, P., Brice, A., Mandel, J. L., Koenig, M., et al.** (2009). SPG11 spastic paraplegia. *J. Neurol.* **256**, 104–108.
- Assémat, E., Bazellières, E., Pallesi-Pocachard, E., Le Bivic, A. and Massey-Harroche, D.** (2008). Polarity complex proteins. *Biochim. Biophys. Acta - Biomembr.* **1778**, 614–630.
- Ayala, R., Shu, T. and Tsai, L.-H.** (2007). Trekking across the Brain: The Journey of Neuronal Migration. *Cell* **128**, 29–43.
- Badouel, C., Zander, M. A., Liscio, N., Bagherie-Lachidan, M., Sopko, R., Coyaud, E., Raught, B., Miller, F. D. and McNeill, H.** (2015). Fat1 interacts with Fat4 to regulate neural tube closure, neural progenitor proliferation and apical constriction during mouse brain development. *Development* **142**, 2781–2791.
- Bae, B.-I., Jayaraman, D. and Walsh, C. A.** (2015). Genetic Changes Shaping the Human Brain. *Dev. Cell* **32**, 423–434.
- Bagley, J. A., Reumann, D., Bian, S., Lévi-Strauss, J. and Knoblich, J. A.** (2017). Fused cerebral organoids model interactions between brain regions. *Nat. Methods* **14**, 743–751.
- Bardón-Cancho, E. J., Muñoz-Jiménez, L., Vázquez-López, M., Ruíz-Martín, Y., García-Morín, M. and Barredo-Valderrama, E.** (2014). Periventricular nodular heterotopia and dystonia due to an ARFGEF2 mutation. *Pediatr. Neurol.* **51**, 461–4.
- Barkovich, A. J. and Kuzniecky, R. I.** (2000). Gray matter heterotopia. *Neurology* **55**, 1603–8.
- Barkovich, A. J., Guerrini, R., Kuzniecky, R. I., Jackson, G. D. and Dobyns, W. B.** (2012). A developmental and genetic classification for malformations of cortical development: update 2012. *Brain* **135**, 1348–69.
- Behar, T. N., Smith, S. V., Kennedy, R. T., McKenzie, J. M., Maric, I. and Barker, J. L.**

- (2001). GABA(B) receptors mediate motility signals for migrating embryonic cortical cells. *Cereb. Cortex* **11**, 744–53.
- Ben Jehuda, R., Shemer, Y. and Binah, O.** (2018). Genome Editing in Induced Pluripotent Stem Cells using CRISPR/Cas9. *Stem Cell Rev. Reports* **14**, 323–336.
- Bershteyn, M., Nowakowski, T. J., Pollen, A. A., Di Lullo, E., Nene, A., Wynshaw-Boris, A. and Kriegstein, A. R.** (2017). Human iPSC-Derived Cerebral Organoids Model Cellular Features of Lissencephaly and Reveal Prolonged Mitosis of Outer Radial Glia. *Cell Stem Cell* **20**, 435–449.e4.
- Betizeau, M., Cortay, V., Patti, D., Pfister, S., Gautier, E., Bellemin-Ménard, A., Afanassieff, M., Huissoud, C., Douglas, R. J., Kennedy, H., et al.** (2013). Precursor Diversity and Complexity of Lineage Relationships in the Outer Subventricular Zone of the Primate. *Neuron* **80**, 442–457.
- Birey, F., Andersen, J., Makinson, C. D., Islam, S., Wei, W., Huber, N., Fan, H. C., Metzler, K. R. C., Panagiotakos, G., Thom, N., et al.** (2017). Assembly of functionally integrated human forebrain spheroids. *Nature* **545**, 54–59.
- Bizzotto, S. and Francis, F.** (2015). Morphological and functional aspects of progenitors perturbed in cortical malformations. *Front. Cell. Neurosci.* **9**, 30.
- Bizzotto, S., Uzquiano, A., Dingli, F., Ershov, D., Houllier, A., Arras, G., Richards, M., Loew, D., Minc, N., Croquelois, A., et al.** (2017). Eml1 loss impairs apical progenitor spindle length and soma shape in the developing cerebral cortex. *Sci. Rep.* **7**, 17308.
- Bonnet, C., Boucher, D., Lazereg, S., Pedrotti, B., Islam, K., Denoulet, P. and Larcher, J. C.** (2001). Differential Binding Regulation of Microtubule-associated Proteins MAP1A, MAP1B, and MAP2 by Tubulin Polyglutamylation. *J. Biol. Chem.* **276**, 12839–12848.
- Borrell, V. and Reillo, I.** (2012). Emerging roles of neural stem cells in cerebral cortex development and evolution. *Dev Neurobiol* **72**, 955–971.
- Boutry, M., Morais, S. and Stevanin, G.** (2019). Update on the Genetics of Spastic Paraplegias. *Curr. Neurol. Neurosci. Rep.* **19**, 18.
- Boyer, L. F., Campbell, B., Larkin, S., Mu, Y. and Gage, F. H.** (2012). Dopaminergic differentiation of human pluripotent cells. *Curr. Protoc. Stem Cell Biol.* **Chapter 1**, Unit1H.6.
- Branchu, J., Boutry, M., Sourd, L., Depp, M., Leone, C., Corriger, A., Vallucci, M., Esteves, T., Matusiak, R., Dumont, M., et al.** (2017). Loss of spatascins function alters lysosomal lipid clearance leading to upper and lower motor neuron degeneration. *Neurobiol. Dis.* **102**, 21–37.
- Brennan, K. J., Simone, A., Jou, J., Gelboin-Burkhart, C., Tran, N., Sangar, S., Li, Y., Mu, Y., Chen, G., Yu, D., et al.** (2011). Modelling schizophrenia using human induced pluripotent stem cells. *Nature* **473**, 221–5.
- Broix, L., Jagline, H., Ivanova, E., Schmucker, S., Drouot, N., Clayton-Smith, J., Pagnamenta, A. T., Metcalfe, K. A., Isidor, B., Louvier, U. W., et al.** (2016). Mutations in the HECT domain of NEDD4L lead to AKT-mTOR pathway deregulation and cause periventricular nodular heterotopia. *Nat. Genet.* **48**, 1349–1358.
- Broncel, M., Serwa, R. A., Bunney, T. D., Katan, M. and Tate, E. W.** (2016). Global Profiling of Huntingtin-associated protein E (HYPE)-Mediated AMPylation through a Chemical Proteomic Approach. *Mol. Cell. Proteomics* **15**, 715–25.
- Buchsbaum, I. Y. and Cappello, S.** (2019). Neuronal migration in the CNS during development and disease: insights from in vivo and in vitro models. *Development*

146.

- Buchsbaum, I. Y., Kielkowski, P., Giorgio, G., O'Neill, A. C., Di Giaimo, R., Kyrousi, C., Khattak, S., Sieber, S. A., Robertson, S. P. and Cappello, S.** ECE2 regulates Neurogenesis and Neuronal Migration during Cortical Development. Under Revision in *EMBO Reports*.
- Burke, E. E., Chenoweth, J. G., Shin, J. H., Collado-Torres, L., Kim, S. K., Micali, N., Wang, Y., Straub, R. E., Hoepfner, D. J., Chen, H.-Y., et al.** (2018). Dissecting transcriptomic signatures of neuronal differentiation and maturation using iPSCs. *bioRxiv* 380758.
- Caceres, M., Lachuer, J., Zapala, M. A., Redmond, J. C., Kudo, L., Geschwind, D. H., Lockhart, D. J., Preuss, T. M. and Barlow, C.** (2003). Elevated gene expression levels distinguish human from non-human primate brains. *Proc. Natl. Acad. Sci.* **100**, 13030–13035.
- Camargo Ortega, G., Falk, S., Johansson, P. A., Peyre, E., Broix, L., Sahu, S. K., Hirst, W., Schlichthaerle, T., De Juan Romero, C., Draganova, K., et al.** (2019). The centrosome protein AKNA regulates neurogenesis via microtubule organization. *Nature* **567**, 113–117.
- Camp, J. G., Badsha, F., Florio, M., Kanton, S., Gerber, T., Wilsch-Bräuninger, M., Lewitus, E., Sykes, A., Hevers, W., Lancaster, M., et al.** (2015). Human cerebral organoids recapitulate gene expression programs of fetal neocortex development. *Proc. Natl. Acad. Sci. U. S. A.* **112**, 15672–15677.
- Cappello, S.** (2013). Small Rho-GTPases and cortical malformations: fine-tuning the cytoskeleton stability. *Small GTPases* **4**, 51–56.
- Cappello, S., Attardo, A., Wu, X., Iwasato, T., Itohara, S., Wilsch-Brauninger, M., Eilken, H. M., Rieger, M. A., Schroeder, T. T., Huttner, W. B., et al.** (2006). The Rho-GTPase *cdc42* regulates neural progenitor fate at the apical surface. *Nat Neurosci* **9**, 1099–1107.
- Cappello, S., Böhringer, C. R. J., Bergami, M., Conzelmann, K.-K., Ghanem, A., Tomassy, G. S., Arlotta, P., Mainardi, M., Allegra, M., Caleo, M., et al.** (2012). A Radial Glia-Specific Role of RhoA in Double Cortex Formation. *Neuron* **73**, 911–924.
- Cappello, S., Gray, M. J., Badouel, C., Lange, S., Einsiedler, M., Srour, M., Chitayat, D., Hamdan, F. F., Jenkins, Z. A. and Morgan, T.** (2013). Mutations in genes encoding the cadherin receptor-ligand pair *DCHS1* and *FAT4* disrupt cerebral cortical development. *Nat. Genet.* **45**, 1300–1308.
- Carabalona, A., Beguin, S., Pallesi-pocachard, E., Buhler, E., Pellegrino, C., Arnaud, K., Hubert, P., Oualha, M., Siffroi, J. P., Khantane, S., et al.** (2012). A glial origin for periventricular nodular heterotopia caused by impaired expression of Filamin-A. *Hum. Mol. Genet.* **21**, 1004–1017.
- Casey, A. K. and Orth, K.** (2018). Enzymes Involved in AMPylation and deAMPylation. *Chem. Rev.* **118**, 1199–1215.
- Casey, A. K., Moehlman, A. T., Zhang, J., Servage, K. A., Krämer, H. and Orth, K.** (2017). Fic-mediated deAMPylation is not dependent on homodimerization and rescues toxic AMPylation in flies. *J. Biol. Chem.* **292**, 21193–21204.
- Caviness, V. S. and Takahashi, T.** (1995). Proliferative events in the cerebral ventricular zone. *Brain Dev.* **17**, 159–63.
- Cellini, E., Vetro, A., Conti, V., Marini, C., Doccini, V., Clementella, C., Parrini, E., Giglio, S., Della Monica, M., Fichera, M., et al.** (2019). Multiple genomic copy number variants associated with periventricular nodular heterotopia indicate extreme genetic heterogeneity. *Eur. J. Hum. Genet.* **1**.

- Chae, T. H., Kim, S., Marz, K. E., Hanson, P. I. and Walsh, C. A.** (2004). The *hyh* mutation uncovers roles for α Snap in apical protein localization and control of neural cell fate. *Nat. Genet.* **36**, 264–270.
- Chambers, S. M., Fasano, C. A., Papapetrou, E. P., Tomishima, M., Sadelain, M. and Studer, L.** (2009). Highly efficient neural conversion of human ES and iPS cells by dual inhibition of SMAD signaling. *Nat Biotechnol* **27**, 275–280.
- Chang, W., Gruber, D., Chari, S., Kitazawa, H., Hamazumi, Y., Hisanaga, S. and Bulinski, J. C.** (2001). Phosphorylation of MAP4 affects microtubule properties and cell cycle progression. *J. Cell Sci.* **114**, 2879–87.
- Chang, B. S., Ly, J., Appignani, B., Bodell, A., Apse, K. A., Ravenscroft, R. S., Sheen, V. L., Doherty, M. J., Hackney, D. B., O'Connor, M., et al.** (2005). Reading impairment in the neuronal migration disorder of periventricular nodular heterotopia. *Neurology* **64**, 799–803.
- Chang, J., Lee, S. and Blackstone, C.** (2014). Spastic paraplegia proteins spastizin and spatascin mediate autophagic lysosome reformation. *J. Clin. Invest.* **124**, 5249–5262.
- Charrier, C., Joshi, K., Coutinho-Budd, J., Kim, J.-E., Lambert, N., De-Marchena, J., Jin, W.-L., Vanderhaeghen, P., Ghosh, A., Sassa, T., et al.** (2012). Inhibition of SRGAP2 Function by Its Human-Specific Paralogs Induces Neoteny during Spine Maturation. *Cell* **149**, 923–935.
- Charvet, C. J., Striedter, G. F. and Finlay, B. L.** (2011). Evo-Devo and Brain Scaling: Candidate Developmental Mechanisms for Variation and Constancy in Vertebrate Brain Evolution. *Brain. Behav. Evol.* **78**, 248–257.
- Chen, H.-X. and Roper, S. N.** (2003). Reduction of Spontaneous Inhibitory Synaptic Activity in Experimental Heterotopic Gray Matter. *J. Neurophysiol.* **89**, 150–158.
- Chenn, A. and Walsh, C. A.** (2003). Increased neuronal production, enlarged forebrains and cytoarchitectural distortions in beta-catenin overexpressing transgenic mice. *Cereb Cortex* **13**, 599–606.
- Chevassus-au-Louis, N., Jorquera, I., Ben-Ari, Y. and Represa, A.** (1999). Abnormal Connections in the Malformed Cortex of Rats with Prenatal Treatment with Methylazoxymethanol May Support Hyperexcitability. *Dev. Neurosci.* **21**, 385–392.
- Cobos, S. N., Bennett, S. A. and Torrente, M. P.** (2018). The impact of histone post-translational modifications in neurodegenerative diseases. *Biochim. Biophys. Acta - Mol. Basis Dis.*
- Cohen, P.** (2000). The regulation of protein function by multisite phosphorylation--a 25 year update. *Trends Biochem. Sci.* **25**, 596–601.
- Cohen, J.** (2018). Neanderthal brain organoids come to life. *Science (80-.).* **360**, 1284–1284.
- Conti, V., Carabalona, A., Pallesi-Pocachard, E., Parrini, E., Leventer, R. J., Buhler, E., McGillivray, G., Michel, F. J., Striano, P., Mei, D., et al.** (2013). Periventricular heterotopia in 6q terminal deletion syndrome: Role of the C6orf70 gene. *Brain* **136**, 3378–3394.
- Cooper, G. M., Stone, E. A., Asimenos, G., NISC Comparative Sequencing Program, E. D., Green, E. D., Batzoglou, S. and Sidow, A.** (2005). Distribution and intensity of constraint in mammalian genomic sequence. *Genome Res.* **15**, 901–13.
- Crosby, A. H. and Proukakis, C.** (2002). Is the Transportation Highway the Right Road for Hereditary Spastic Paraplegia? *Am. J. Hum. Genet.* **71**, 1009–1016.
- Cugola, F. R., Fernandes, I. R., Russo, F. B., Freitas, B. C., Dias, J. L. M.,**

- Guimarães, K. P., Benazzato, C., Almeida, N., Pignatari, G. C., Romero, S., et al.** (2016). The Brazilian Zika virus strain causes birth defects in experimental models. *Nature* **534**, 267–271.
- Cushion, T. D., Dobyens, W. B., Mullins, J. G. L., Stoodley, N., Chung, S.-K., Fry, A. E., Hehr, U., Gunny, R., Aylsworth, A. S., Prabhakar, P., et al.** (2013). Overlapping cortical malformations and mutations in TUBB2B and TUBA1A. *Brain* **136**, 536–548.
- D’Angelo, R., Aresta, S., Blangy, A., Del Maestro, L., Louvard, D. and Arpin, M.** (2007). Interaction of Ezrin with the Novel Guanine Nucleotide Exchange Factor PLEKHG6 Promotes RhoG-dependent Apical Cytoskeleton Rearrangements in Epithelial Cells. *Mol. Biol. Cell* **18**, 4780–4793.
- D’Arcangelo, G., G. Miao, G., Chen, S.-C., Scares, H. D., Morgan, J. I. and Curran, T.** (1995). A protein related to extracellular matrix proteins deleted in the mouse mutant reeler. *Nature* **374**, 719–723.
- Davenport, A. P. and Kuc, R. E.** (2000). Cellular expression of isoforms of endothelin-converting enzyme-1 (ECE-1c, ECE-1b and ECE-1a) and endothelin-converting enzyme-2. *J. Cardiovasc. Pharmacol.* **36**, S12-4.
- Davis, T. P., Hoyer, G. L., Davis, P. and Burks, T. F.** (1990). Proenkephalin A-derived peptide E and its fragments alter opioid contractility in the small intestine. *Eur. J. Pharmacol.* **191**, 253–61.
- de Juan Romero, C., Bruder, C., Tomasello, U., Sanz-Anquela, J. M., Borrell, V., Romero, C. D. J., Bruder, C., Tomasello, U. and Sanz-Anquela, J. M.** (2015). Discrete domains of gene expression in germinal layers distinguish the development of gyrencephaly. *EMBO J.* 1–16.
- De Rubeis, S., He, X., Goldberg, A. P., Poultney, C. S., Samocha, K., Ercument Cicek, A., Kou, Y., Liu, L., Fromer, M., Walker, S., et al.** (2014). Synaptic, transcriptional and chromatin genes disrupted in autism. *Nature* **515**, 209–215.
- Dehay, C. and Kennedy, H.** (2007). Cell-cycle control and cortical development. *Nat Rev Neurosci* **8**, 438–450.
- Dehay, C., Kennedy, H. and Kosik, K. S.** (2015). The Outer Subventricular Zone and Primate-Specific Cortical Complexification. *Neuron* **85**, 683–694.
- Dehmelt, L. and Halpain, S.** (2004). Actin and microtubules in neurite initiation: Are MAPs the missing link? *J. Neurobiol.* **58**, 18–33.
- Del Bene, F., Wehman, A. M., Link, B. A. and Baier, H.** (2008). Regulation of neurogenesis by interkinetic nuclear migration through an apical-basal notch gradient. *Cell* **134**, 1055–1065.
- del Toro, D., Ruff, T., Cederfjäll, E., Villalba, A., Seyit-Bremer, G., Borrell, V. and Klein, R.** (2017). Regulation of Cerebral Cortex Folding by Controlling Neuronal Migration via FLRT Adhesion Molecules. *Cell* **169**, 621–635.e16.
- Dennis, M. Y. and Eichler, E. E.** (2016). Human adaptation and evolution by segmental duplication. *Curr. Opin. Genet. Dev.* **41**, 44–52.
- Denora, P. S., Smets, K., Zolfanelli, F., Ceuterick-de Groote, C., Casali, C., Deconinck, T., Sieben, A., Gonzales, M., Zuchner, S., Darios, F., et al.** (2016). Motor neuron degeneration in spastic paraplegia 11 mimics amyotrophic lateral sclerosis lesions. *Brain* **139**, 1723–34.
- Di Lullo, E. and Kriegstein, A. R.** (2017). The use of brain organoids to investigate neural development and disease. *Nat. Rev. Neurosci.* **18**,.
- Dityatev, A. and Fellin, T.** (2008). Extracellular matrix in plasticity and epileptogenesis.

- Neuron Glia Biol.* **4**, 235.
- Doan, N. T., Kaufmann, T., Bettella, F., Jørgensen, K. N., Brandt, C. L., Moberget, T., Alnæs, D., Douaud, G., Duff, E., Djurovic, S., et al.** (2017). Distinct multivariate brain morphological patterns and their added predictive value with cognitive and polygenic risk scores in mental disorders. *NeuroImage Clin.* **15**, 719–731.
- Dubeau, F., Tampieri, D., Lee, N., Andermann, E., Carpenter, S., Leblanc, R., Olivier, A., Radtke, R., Villemure, J. G. and Andermann, F.** (1995). Periventricular and subcortical nodular heterotopia. A study of 33 patients. *Brain* **118** (Pt 5), 1273–87.
- Dunn, S., Morrison, E. E., Liverpool, T. B., Molina-Paris, C., Cross, R. A., Alonso, M. C. and Peckham, M.** (2008). Differential trafficking of Kif5c on tyrosinated and detyrosinated microtubules in live cells. *J. Cell Sci.* **121**, 1085–1095.
- Ehrenreich, H. and Schilling, L.** (1995). New developments in the understanding of cerebral vasoregulation and vasospasm: the endothelin-nitric oxide network. *Cleve. Clin. J. Med.* **62**, 105–16.
- Eiraku, M., Watanabe, K., Matsuo-Takasaki, M., Kawada, M., Yonemura, S., Matsumura, M., Wataya, T., Nishiyama, A., Muguruma, K. and Sasai, Y.** (2008). Self-organized formation of polarized cortical tissues from ESCs and its active manipulation by extrinsic signals. *Cell Stem Cell* **3**, 519–532.
- Eiraku, M., Takata, N., Ishibashi, H., Kawada, M., Sakakura, E., Okuda, S., Sekiguchi, K., Adachi, T. and Sasai, Y.** (2011). Self-organizing optic-cup morphogenesis in three-dimensional culture. *Nature* **472**, 51–56.
- Elert-Dobkowska, E., Stepniak, I., Krysa, W., Ziora-Jakutowicz, K., Rakowicz, M., Sobanska, A., Pilch, J., Antczak-Marach, D., Zaremba, J. and Sulek, A.** (2019). Next-generation sequencing study reveals the broader variant spectrum of hereditary spastic paraplegia and related phenotypes. *Neurogenetics*.
- Elkabetz, Y., Panagiotakos, G., Shamy, G. Al, Socci, N. D. and Tabar, V.** (2008). Human ES cell-derived neural rosettes reveal a functionally distinct early neural stem cell stage. 152–165.
- Emoto, N. and Yanagisawa, M.** (1995). Endothelin-converting enzyme-2 is a membrane-bound, phosphoramidon-sensitive metalloprotease with acidic pH optimum. *J. Biol. Chem.* **270**, 15262–8.
- Engel, P., Goepfert, A., Stanger, F. V., Harms, A., Schmidt, A., Schirmer, T. and Dehio, C.** (2012). Adenylation control by intra- or intermolecular active-site obstruction in Fic proteins. *Nature* **482**, 107–110.
- Epi4K Consortium, Epilepsy Phenome/Genome Project, Allen, A. S., Berkovic, S. F., Cossette, P., Delanty, N., Dlugos, D., Eichler, E. E., Epstein, M. P., Glauser, T., et al.** (2013). De novo mutations in epileptic encephalopathies. *Nature* **501**, 217–21.
- Espuny-Camacho, I., Michelsen, K. A., Gall, D., Linaro, D., Hasche, A., Bonnefont, J., Bali, C., Orduz, D., Bilheu, A., Herpoel, A., et al.** (2013). Pyramidal neurons derived from human pluripotent stem cells integrate efficiently into mouse brain circuits in vivo. *Neuron* **77**, 440–456.
- Espuny-Camacho, I., Arranz, A. M., Fiers, M., Snellinx, A., Ando, K., Munck, S., Bonnefont, J., Lambot, L., Corthout, N., Omodho, L., et al.** (2017). Hallmarks of Alzheimer’s Disease in Stem-Cell-Derived Human Neurons Transplanted into Mouse Brain. *Neuron* **93**, 1066–1081.e8.
- Etienne-Manneville, S.** (2004). Cdc42 - the centre of polarity. *J. Cell Sci.* **117**, 1291–1300.
- Etienne-Manneville, S.** (2010). From signaling pathways to microtubule dynamics: the key players. *Curr. Opin. Cell Biol.* **22**, 104–111.

- Evans, M. J. and Kaufman, M. H.** (1981). Establishment in culture of pluripotential cells from mouse embryos. *Nature* **292**, 154–156.
- Faber, I., Martinez, A. R. M., de Rezende, T. J. R., Martins, C. R., Martins, M. P., Lourenço, C. M., Marques, W., Montecchiani, C., Orlacchio, A., Pedroso, J. L., et al.** (2018). SPG11 mutations cause widespread white matter and basal ganglia abnormalities, but restricted cortical damage. *NeuroImage. Clin.* **19**, 848–857.
- Farhan, S. M. K., Nixon, K. C. J., Everest, M., Edwards, T. N., Long, S., Segal, D., Knip, M. J., Arts, H. H., Chakrabarti, R., Wang, J., et al.** (2017). Identification of a novel synaptic protein, TMTCC3, involved in periventricular nodular heterotopia with intellectual disability and epilepsy. *Hum. Mol. Genet.* **26**, 4278–4289.
- Ferland, R. J., Batiz, L. F., Neal, J., Lian, G., Bundock, E., Lu, J., Hsiao, Y.-C., Diamond, R., Mei, D., Banham, A. H., et al.** (2009). Disruption of neural progenitors along the ventricular and subventricular zones in periventricular heterotopia. *Hum. Mol. Genet.* **18**, 497–516.
- Fiddes, I. T., Lodewijk, G. A., Mooring, M., Bosworth, C. M., Ewing, A. D., Mantalas, G. L., Novak, A. M., van den Bout, A., Bishara, A., Rosenkrantz, J. L., et al.** (2018). Human-Specific NOTCH2NL Genes Affect Notch Signaling and Cortical Neurogenesis. *Cell* **173**, 1356–1369.e22.
- Fietz, S. A. and Huttner, W. B.** (2010). Cortical progenitor expansion, self-renewal and neurogenesis—a polarized perspective. *Curr Opin Neurobiol.*
- Fietz, S. A., Kelava, I., Vogt, J., Wilsch-Brauninger, M., Stenzel, D., Fish, J. L., Corbeil, D., Riehn, A., Distler, W., Nitsch, R., et al.** (2010). OSVZ progenitors of human and ferret neocortex are epithelial-like and expand by integrin signaling. *Nat Neurosci* **13**, 690–699.
- Fietz, S. a., Lachmann, R., Brandl, H., Kircher, M., Samusik, N., Schroder, R., Lakshmanaperumal, N., Henry, I., Vogt, J., Riehn, A., et al.** (2012). Transcriptomes of germinal zones of human and mouse fetal neocortex suggest a role of extracellular matrix in progenitor self-renewal. *Proc. Natl. Acad. Sci.* **109**, 11836–11841.
- Firth, H. V., Richards, S. M., Bevan, A. P., Clayton, S., Corpas, M., Rajan, D., Vooren, S. Van, Moreau, Y., Pettett, R. M. and Carter, N. P.** (2009). DECIPHER: Database of Chromosomal Imbalance and Phenotype in Humans Using Ensembl Resources. *Am. J. Hum. Genet.* **84**, 524–533.
- Fish, J. L., Dehay, C., Kennedy, H. and Huttner, W. B.** (2008). Making bigger brains—the evolution of neural-progenitor-cell division. *J Cell Sci* **121**, 2783–2793.
- Flaherty, E. K. and Brennand, K. J.** (2017). Using hiPSCs to model neuropsychiatric copy number variations (CNVs) has potential to reveal underlying disease mechanisms. *Brain Res.* **1655**, 283–293.
- Fleck, M. W., Hirotsune, S., Gambello, M. J., Phillips-Tansey, E., Soares, G., Mervis, R. F., Wynshaw-Boris, A. and McBain, C. J.** (2000). Hippocampal abnormalities and enhanced excitability in a murine model of human lissencephaly. *J. Neurosci.* **20**, 2439–50.
- Florio, M. and Huttner, W. B.** (2014). Neural progenitors, neurogenesis and the evolution of the neocortex. *Development* **141**, 2182–2194.
- Florio, M., Albert, M., Taverna, E., Namba, T., Brandl, H., Lewitus, E., Haffner, C., Sykes, A., Wong, F. K., Peters, J., et al.** (2015). Human-specific gene ARHGAP11B promotes basal progenitor amplification and neocortex expansion. *Science (80-.).* **347**, 1465–1470.
- Florio, M., Borrell, V. and Huttner, W. B.** (2017). Human-specific genomic signatures of

- neocortical expansion. *Curr. Opin. Neurobiol.* **42**, 33–44.
- Fox, J. W., Lamperti, E. D., Eksioglu, Y. Z., Hong, S. E., Feng, Y., Graham, D. A., Scheffer, I. E., Dobyns, W. B., Hirsch, B. A., Radtke, R. A., et al.** (1998). Mutations in filamin 1 prevent migration of cerebral cortical neurons in human periventricular heterotopia. *Neuron* **21**, 1315–1325.
- Francis, F., Meyer, G., Fallet-Bianco, C., Moreno, S., Kappeler, C., Socorro, A. C., Tuy, F. P. D., Beldjord, C. and Chelly, J.** (2006). Human disorders of cortical development: from past to present. *Eur. J. Neurosci.* **23**, 877–893.
- Fromer, M., Pocklington, A. J., Kavanagh, D. H., Williams, H. J., Dwyer, S., Gormley, P., Georgieva, L., Rees, E., Palta, P., Ruderfer, D. M., et al.** (2014). De novo mutations in schizophrenia implicate synaptic networks. *Nature* **506**, 179–184.
- Frotscher, M.** (2010). Role for Reelin in stabilizing cortical architecture. *Trends Neurosci* **33**, 407–414.
- Fry, A. E., Kerr, M. P., Gibbon, F., Turnpenny, P. D., Hamandi, K., Stoodley, N., Robertson, S. P. and Pilz, D. T.** (2013). Neuropsychiatric Disease in Patients With Periventricular Heterotopia. *J. Neuropsychiatry Clin. Neurosci.* **25**, 26–31.
- Fürst, D. O., Goldfarb, L. G., Kley, R. A., Vorgerd, M., Olivé, M. and van der Ven, P. F. M.** (2013). Filamin C-related myopathies: pathology and mechanisms. *Acta Neuropathol.* **125**, 33–46.
- Gabriel, E., Wason, A., Ramani, A., Gooi, L. M., Keller, P., Pozniakovskiy, A., Poser, I., Noack, F., Telugu, N. S., Calegari, F., et al.** (2016). CPAP promotes timely cilium disassembly to maintain neural progenitor pool. *EMBO J.* **35**, 803–819.
- Gabriel, E., Ramani, A., Karow, U., Gottardo, M., Natarajan, K., Gooi, L. M., Goranci-Buzhala, G., Krut, O., Peters, F., Nikolic, M., et al.** (2017). Recent Zika Virus Isolates Induce Premature Differentiation of Neural Progenitors in Human Brain Organoids. *Cell Stem Cell* **20**, 397–406.e5.
- Gallo, G. and Letourneau, P. C.** (2000). Neurotrophins and the dynamic regulation of the neuronal cytoskeleton. *J. Neurobiol.* **44**, 159–73.
- Gao, F. J., Hebbar, S., Gao, X. A., Alexander, M., Pandey, J. P., Walla, M. D., Cotham, W. E., King, S. J. and Smith, D. S.** (2015). GSK-3 β Phosphorylation of Cytoplasmic Dynein Reduces Ndel1 Binding to Intermediate Chains and Alters Dynein Motility. *Traffic* **16**, 941–61.
- Gascón, S., Murenu, E., Masserdotti, G., Ortega, F., Russo, G. L., Petrik, D., Deshpande, A., Heinrich, C., Karow, M., Robertson, S. P., et al.** (2016). Identification and Successful Negotiation of a Metabolic Checkpoint in Direct Neuronal Reprogramming. *Cell Stem Cell* **18**, 396–409.
- Gascón, S., Masserdotti, G., Russo, G. L. and Götz, M.** (2017). Direct Neuronal Reprogramming: Achievements, Hurdles, and New Roads to Success. *Cell Stem Cell* **21**, 18–34.
- Gaspard, N., Bouchet, T., Hourez, R., Dimidschstein, J., Naeije, G., van den Aemele, J., Espuny-Camacho, I., Herpoel, A., Passante, L., Schiffmann, S. N., et al.** (2008). An intrinsic mechanism of corticogenesis from embryonic stem cells. *Nature* **455**, 351–357.
- Georges-Labouesse, E., Mark, M., Messaddeq, N. and Gansmuller, A.** (1998). Essential role of alpha 6 integrins in cortical and retinal lamination. *Curr Biol* **8**, 983–986.
- Gertz, C. C. and Kriegstein, A. R.** (2015). Neuronal Migration Dynamics in the Developing Ferret Cortex. *J. Neurosci.* **35**, 14307–14315.

- Gil-Sanz, C., Landeira, B., Ramos, C., Costa, M. R. and Müller, U.** (2014). Proliferative defects and formation of a double cortex in mice lacking *Mlt4* and *Cdh2* in the dorsal telencephalon. *J. Neurosci.* **34**, 10475–87.
- Goetz, S. C. and Anderson, K. V.** (2010). The primary cilium: a signalling centre during vertebrate development. *Nat. Rev. Genet.* **11**, 331–344.
- Gonzalez-Billault, C., Muñoz-Llancao, P., Henriquez, D. R., Wojnacki, J., Conde, C. and Caceres, A.** (2012). The role of small GTPases in neuronal morphogenesis and polarity. *Cytoskeleton* **69**, 464–485.
- Gorlin, J. B., Yamin, R., Egan, S., Stewart, M., Stossel, T. P., Kwiatkowski, D. J. and Hartwig, J. H.** (1990). Human endothelial actin-binding protein (ABP-280, nonmuscle filamin): a molecular leaf spring. *J. Cell Biol.* **111**, 1089–105.
- Götz, M. and Huttner, W. B.** (2005). The cell biology of neurogenesis. *Nat Rev Mol Cell Biol* **6**, 777–788.
- Greenwood, J. S. F., Wang, Y., Estrada, R. C., Ackerman, L., Ohara, P. T. and Baraban, S. C.** (2009). Seizures, enhanced excitation, and increased vesicle number in *Lis1* mutant mice. *Ann. Neurol.* **66**, 644–653.
- Gregorio, I., Braghetta, P., Bonaldo, P. and Cescon, M.** (2018). Collagen VI in healthy and diseased nervous system.
- Guemez-Gamboa, A., Coufal, N. G. and Gleeson, J. G.** (2014). Primary Cilia in the Developing and Mature Brain. *Neuron* **82**, 511–521.
- Guerrini, R. and Dobyns, W. B.** (2014). Malformations of cortical development: clinical features and genetic causes. *Lancet Neurol* **13**, 710–726.
- Guerrini, R. and Parrini, E.** (2010). Neuronal migration disorders. *Neurobiol. Dis.* **38**, 154–166.
- Guerrini, R., Mei, D., Sisodiya, S., Sicca, F., Harding, B., Takahashi, Y., Dorn, T., Yoshida, A., Campistol, J., Krämer, G., et al.** (2004). Germline and mosaic mutations of *FLN1* in men with periventricular heterotopia. *Neurology* **63**, 51–6.
- Guo, J., Yang, Z., Song, W., Chen, Q., Wang, F., Zhang, Q. and Zhu, X.** (2006). Nudel contributes to microtubule anchoring at the mother centriole and is involved in both dynein-dependent and -independent centrosomal protein assembly. *Mol Biol Cell* **17**, 680–689.
- Gupta, A., Fujita, W., Gomes, I., Bobeck, E. and Devi, L. A.** (2015). Endothelin-converting enzyme 2 differentially regulates opioid receptor activity. *Br. J. Pharmacol.* **172**, 704–19.
- Hahn, J. W., Jagwani, S., Kim, E., Rendell, V. R., He, J., Ezerskiy, L. A., Wesselschmidt, R., Coscia, C. J. and Belcheva, M. M.** (2010). Mu and kappa opioids modulate mouse embryonic stem cell-derived neural progenitor differentiation via MAP kinases. *J. Neurochem.* **112**, 1431–1441.
- Hajdinjak, M., Fu, Q., Hübner, A., Petr, M., Mafessoni, F., Grote, S., Skoglund, P., Narasimham, V., Rougier, H., Crevecoeur, I., et al.** (2018). Reconstructing the genetic history of late Neanderthals. *Nature* **555**, 652–656.
- Ham, H., Woolery, A. R., Tracy, C., Stenesen, D., Krämer, H. and Orth, K.** (2014). Unfolded protein response-regulated *Drosophila* Fic (dFic) protein reversibly AMPylates BiP chaperone during endoplasmic reticulum homeostasis. *J. Biol. Chem.* **289**, 36059–69.
- Han, Y. G., Spassky, N., Romaguera-Ros, M., Garcia-Verdugo, J. M., Aguilar, A., Schneider-Maunoury, S. and Alvarez-Buylla, A.** (2008). Hedgehog signaling and primary cilia are required for the formation of adult neural stem cells. *Nat Neurosci*

- 11, 277–284.
- Hansen, D. V., Lui, J. H., Parker, P. R. and Kriegstein, A. R.** (2010). Neurogenic radial glia in the outer subventricular zone of human neocortex. *Nature* **464**, 554–561.
- Hartmann, D., De Strooper, B. and Saftig, P.** (1999). Presenilin-1 deficiency leads to loss of Cajal-Retzius neurons and cortical dysplasia similar to human type 2 lissencephaly. *Curr. Biol.* **9**, 719–27.
- He, M., Zhang, Z. -h., Guan, C. -b., Xia, D. and Yuan, X. -b.** (2010). Leading Tip Drives Soma Translocation via Forward F-Actin Flow during Neuronal Migration. *J. Neurosci.* **30**, 10885–10898.
- Hedberg, C. and Itzen, A.** (2015). Molecular Perspectives on Protein Adenylylation. *ACS Chem. Biol.* **10**, 12–21.
- Hehr, U., Bauer, P., Winner, B., Schule, R., Olmez, A., Koehler, W., Uyanik, G., Engel, A., Lenz, D., Seibel, A., et al.** (2007). Long-term course and mutational spectrum of *spatacsin* -linked spastic paraplegia. *Ann. Neurol.* **62**, 656–665.
- Heinzen, E. L., O'Neill, A. C., Zhu, X., Allen, A. S., Bahlo, M., Chelly, J., Chen, M. H., Dobyns, W. B., Freytag, S., Guerrini, R., et al.** (2018). De novo and inherited private variants in MAP1B in periventricular nodular heterotopia. *PLOS Genet.* **14**, e1007281.
- Hetz, C. and Mollereau, B.** (2014). Disturbance of endoplasmic reticulum proteostasis in neurodegenerative diseases. *Nat. Rev. Neurosci.* **15**, 233–249.
- Higginbotham, H., Guo, J., Yokota, Y., Umberger, N. L., Su, C.-Y., Li, J., Verma, N., Hirt, J., Ghukasyan, V., Caspary, T., et al.** (2013). Arl13b-regulated cilia activities are essential for polarized radial glial scaffold formation. *Nat. Neurosci.* **16**, 1000–7.
- Hippenmeyer, S., Youn, Y. H., Moon, H. M., Miyamichi, K., Zong, H., Wynshaw-Boris, A. and Luo, L.** (2010). Genetic mosaic dissection of Lis1 and Ndel1 in neuronal migration. *Neuron* **68**, 695–709.
- Hirabayashi, Y., Itoh, Y., Tabata, H., Nakajima, K., Akiyama, T., Masuyama, N. and Gotoh, Y.** (2004). The Wnt/ -catenin pathway directs neuronal differentiation of cortical neural precursor cells. *Development* **131**, 2791–2801.
- Holtfreter, J.** (1944). Neural differentiation of ectoderm through exposure to saline solution. *J. Exp. Zool.* **95**, 307–343.
- Hooper, C., Killick, R. and Lovestone, S.** (2008). The GSK3 hypothesis of Alzheimer's disease. *J. Neurochem.* **104**, 1433–1439.
- Hornbeck, P. V., Zhang, B., Murray, B., Kornhauser, J. M., Latham, V. and Skrzypek, E.** (2015). PhosphoSitePlus, 2014: mutations, PTMs and recalibrations. *Nucleic Acids Res.* **43**, D512-20.
- Hur, E.-M. and Zhou, F.-Q.** (2010). GSK3 signalling in neural development. *Nat. Rev. Neurosci.* **11**, 539–551.
- Iefremova, V., Manikakis, G., Krefft, O., Jabali, A., Weynans, K., Wilkens, R., Marsoner, F., Brändl, B., Müller, F.-J., Koch, P., et al.** (2017). An Organoid-Based Model of Cortical Development Identifies Non-Cell-Autonomous Defects in Wnt Signaling Contributing to Miller-Dieker Syndrome. *Cell Rep.* **19**, 50–59.
- Ikegami, K., Heier, R. L., Taruishi, M., Takagi, H., Mukai, M., Shimma, S., Taira, S., Hatanaka, K., Morone, N., Yao, I., et al.** (2007). Loss of γ -tubulin polyglutamylated in ROSA22 mice is associated with abnormal targeting of KIF1A and modulated synaptic function. *Proc. Natl. Acad. Sci.* **104**, 3213–3218.
- Ilieva, M., Fex Svenningsen, Å., Thorsen, M. and Michel, T. M.** (2018). Psychiatry in a Dish: Stem Cells and Brain Organoids Modeling Autism Spectrum Disorders. *Biol.*

- Psychiatry* **83**, 558–568.
- Ilouz, R., Kowalsman, N., Eisenstein, M. and Eldar-Finkelman, H.** (2006). Identification of Novel Glycogen Synthase Kinase-3 β Substrate-interacting Residues Suggests a Common Mechanism for Substrate Recognition. *J. Biol. Chem.* **281**, 30621–30630.
- Iossifov, I., Ronemus, M., Levy, D., Wang, Z., Hakker, I., Rosenbaum, J., Yamrom, B., Lee, Y., Narzisi, G., Leotta, A., et al.** (2012). De Novo Gene Disruptions in Children on the Autistic Spectrum. *Neuron* **74**, 285–299.
- Jabaudon, D. and Lancaster, M.** (2018). Exploring landscapes of brain morphogenesis with organoids. *Development* **145**, dev172049.
- Jamuar, S. S. and Walsh, C. A.** (2015). Genomic variants and variations in malformations of cortical development. *Pediatr. Clin. North Am.* **62**, 571–85.
- Jimenez-Sanchez, G., Childs, B. and Valle, D.** (2001). Human disease genes. *Nature* **409**, 853–855.
- Johansson, P. A., Irmeler, M., Acampora, D., Beckers, J., Simeone, A. and Gotz, M.** (2013). The transcription factor Otx2 regulates choroid plexus development and function. *Development* **140**, 1055–1066.
- Jossin, Y. and Cooper, J. A.** (2011). Reelin, Rap1 and N-cadherin orient the migration of multipolar neurons in the developing neocortex. *Nat. Neurosci.* **14**, 697–703.
- Ju, X.-C., Hou, Q.-Q., Sheng, A.-L., Wu, K.-Y., Zhou, Y., Jin, Y., Wen, T., Yang, Z., Wang, X. and Luo, Z.-G.** (2016). The hominoid-specific gene TBC1D3 promotes generation of basal neural progenitors and induces cortical folding in mice. *Elife* **5**,.
- Kadoshima, T., Sakaguchi, H., Nakano, T., Soen, M., Ando, S., Eiraku, M. and Sasai, Y.** (2013). Self-organization of axial polarity, inside-out layer pattern, and species-specific progenitor dynamics in human ES cell-derived neocortex. *Proc. Natl. Acad. Sci. U. S. A.* **110**, 20284–20289.
- Kadowaki, M., Nakamura, S., Machon, O., Krauss, S., Radice, G. L. and Takeichi, M.** (2007). N-cadherin mediates cortical organization in the mouse brain. *Dev Biol* **304**, 22–33.
- Kandel, E. R.** (2000). Neuroscience: Breaking Down Scientific Barriers to the Study of Brain and Mind. *Science* (80-).
- Karaca, E., Harel, T., Pehlivan, D., Jhangiani, S. N., Gambin, T., Coban Akdemir, Z., Gonzaga-Jauregui, C., Erdin, S., Bayram, Y., Campbell, I. M., et al.** (2015). Genes that Affect Brain Structure and Function Identified by Rare Variant Analyses of Mendelian Neurologic Disease. *Neuron* **88**, 499–513.
- Karkheiran, S., Krebs, C. E., Makarov, V., Nilipour, Y., Hubert, B., Darvish, H., Frucht, S., Shahidi, G. A., Buxbaum, J. D. and Paisán-Ruiz, C.** (2013). Identification of COL6A2 mutations in progressive myoclonus epilepsy syndrome. *Hum. Genet.* **132**, 275–283.
- Karzbrun, E., Kshirsagar, A., Cohen, S. R., Hanna, J. H. and Reiner, O.** (2018). Human brain organoids on a chip reveal the physics of folding. *Nat. Phys.* **14**, 515–522.
- Kasioulis, I., Das, R. M. and Storey, K. G.** (2017). Inter-dependent apical microtubule and actin dynamics orchestrate centrosome retention and neuronal delamination. *Elife* **6**,.
- Katayama, K., Melendez, J., Baumann, J. M., Leslie, J. R., Chauhan, B. K., Nemkul, N., Lang, R. A., Kuan, C. Y., Zheng, Y. and Yoshida, Y.** (2011). Loss of RhoA in neural progenitor cells causes the disruption of adherens junctions and

- hyperproliferation. *Proc Natl Acad Sci U S A* **108**, 7607–7612.
- Kawaguchi, K., Yoshida, S., Hatano, R. and Asano, S.** (2017). *Pathophysiological Roles of Ezrin/Radixin/Moesin Proteins*.
- Kawasaki, H., Toda, T. and Tanno, K.** (2013). In vivo genetic manipulation of cortical progenitors in gyrencephalic carnivores using in utero electroporation. *Biol. Open* **2**, 95–100.
- Kielar, M., Tuy, F. P. D., Bizzotto, S., Lebrand, C., De Juan Romero, C., Poirier, K., Oegema, R., Mancini, G. M., Bahi-Buisson, N., Olasso, R., et al.** (2014). Mutations in *Eml1* lead to ectopic progenitors and neuronal heterotopia in mouse and human. *Nat. Neurosci.* **17**,.
- Kielkowski, P., Buchsbaum, I. Y., Kirsch, V. C., Bach, N. C., Drukker, M., Cappello, S. and Sieber, S. A.** FICD activity and AMPylation remodelling modulate human neurogenesis. Under Revision in *Nature Comm.*
- Kim, E., Clark, A. L., Kiss, A., Hahn, J. W., Wesselschmidt, R., Coscia, C. J. and Belcheva, M. M.** (2006). μ - and κ -Opioids Induce the Differentiation of Embryonic Stem Cells to Neural Progenitors. *J. Biol. Chem.* **281**, 33749–33760.
- King, S. M.** (2000). The dynein microtubule motor. *Biochim. Biophys. Acta - Mol. Cell Res.* **1496**, 60–75.
- Kingdon, H. S., Shapiro, B. M. and Stadtman, E. R.** (1967). Regulation of glutamine synthetase. 8. ATP: glutamine synthetase adenylyltransferase, an enzyme that catalyzes alterations in the regulatory properties of glutamine synthetase. *Proc. Natl. Acad. Sci. U. S. A.* **58**, 1703–10.
- Kitamura, K., Itou, Y., Yanazawa, M., Ohsawa, M., Suzuki-Migishima, R., Umeki, Y., Hohjoh, H., Yanagawa, Y., Shinba, T., Itoh, M., et al.** (2009). Three human ARX mutations cause the lissencephaly-like and mental retardation with epilepsy-like pleiotropic phenotypes in mice. *Hum. Mol. Genet.* **18**, 3708–24.
- Klaus, J., Kanton, S., Kyrousi, C., Ayo-Martin, A. C., Di Giaino, R., Riesenberger, S., O'Neill, A. C., Camp, J. G., Tocco, C., Santel, M., et al.** (2019). Altered neuronal migratory trajectories in human cerebral organoids derived from individuals with neuronal heterotopia. *Nat. Med.* **1**.
- Kothare, S. V, VanLandingham, K., Armon, C., Luther, J. S., Friedman, A. and Radtke, R. A.** (1998). Seizure onset from periventricular nodular heterotopias: depth-electrode study. *Neurology* **51**, 1723–7.
- Kreff, O., Jabali, A., Iefremova, V., Koch, P. and Ladewig, J.** (2018). Generation of Standardized and Reproducible Forebrain-type Cerebral Organoids from Human Induced Pluripotent Stem Cells. *J. Vis. Exp.*
- Kriegstein, A. and Alvarez-Buylla, A.** (2009). The glial nature of embryonic and adult neural stem cells. *Annu Rev Neurosci* **32**, 149–184.
- Kriegstein, A. R. and Noctor, S. C.** (2004). Patterns of neuronal migration in the embryonic cortex. *Trends Neurosci.* **27**, 392–399.
- Kriks, S., Shim, J.-W., Piao, J., Ganat, Y. M., Wakeman, D. R., Xie, Z., Carrillo-Reid, L., Auyeung, G., Antonacci, C., Buch, A., et al.** (2011). Dopamine neurons derived from human ES cells efficiently engraft in animal models of Parkinson's disease. *Nature* **480**, 547–551.
- Kubo, K.-I., Honda, T., Tomita, K., Sekine, K., Ishii, K., Uto, A., Kobayashi, K., Tabata, H. and Nakajima, K.** (2010). Development/Plasticity/Repair Ectopic Reelin Induces Neuronal Aggregation with a Normal Birthdate-Dependent "Inside-Out" Alignment in the Developing Neocortex. *J. Neurosci.* **30**, 10953–10966.

- Kumar, S., Lee, I. H. and Plamann, M.** (2000). Cytoplasmic dynein ATPase activity is regulated by dynactin-dependent phosphorylation. *J. Biol. Chem.* **275**, 31798–804.
- Kyrousi, C., O'Neill, A. C., Brazovskaja, A., He, Z., Coquand, L., Di Giaimo, R., Mei, D., Lenge, M., Cruceanu, C., Buchsbaum, I. Y., et al.** LGALS3BP modulates local gyrification in the human brain. Under Revision in *Cell*.
- Lancaster, M. A. and Knoblich, J. A.** (2014). Generation of cerebral organoids from human pluripotent stem cells. *Nat Protoc* **9**, 2329–2340.
- Lancaster, M. A., Renner, M., Martin, C. A., Wenzel, D., Bicknell, L. S., Hurles, M. E., Homfray, T., Penninger, J. M., Jackson, A. P. and Knoblich, J. A.** (2013). Cerebral organoids model human brain development and microcephaly. *Nature* **501**, 373–379.
- Lancaster, M. A., Corsini, N. S., Wolfinger, S., Gustafson, E. H., Phillips, A. W., Burkard, T. R., Otani, T., Livesey, F. J. and Knoblich, J. A.** (2017). Guided self-organization and cortical plate formation in human brain organoids. *Nat. Biotechnol.* **35**, 659–666.
- Lee, K.-M., Hwang, S.-K. and Lee, J.-A.** (2013). Neuronal Autophagy and Neurodevelopmental Disorders. *Exp. Neurobiol.* **22**, 133–142.
- Leng, G. and Ludwig, M.** (2008). Neurotransmitters and peptides: whispered secrets and public announcements. *J. Physiol.* **586**, 5625–5632.
- Levine, A. J. and Brivanlou, A. H.** (2007). Proposal of a model of mammalian neural induction. *Dev Biol* **308**, 247–256.
- Lewitus, E., Kelava, I. and Huttner, W. B.** (2013). Conical expansion of the outer subventricular zone and the role of neocortical folding in evolution and development. *Front. Hum. Neurosci.* **7**, 424.
- Lewitus, E., Kelava, I., Kalinka, A. T., Tomancak, P. and Huttner, W. B.** (2014). An Adaptive Threshold in Mammalian Neocortical Evolution. *PLoS Biol.* **12**, e1002000.
- Li, Y., Wang, J., Zhou, Y., Li, D. and Xiong, Z.-Q.** (2015). Rcan1 deficiency impairs neuronal migration and causes periventricular heterotopia. *J. Neurosci.* **35**, 610–20.
- Li, R., Sun, L., Fang, A., Li, P., Wu, Q. and Wang, X.** (2017). Recapitulating cortical development with organoid culture in vitro and modeling abnormal spindle-like (ASPM related primary) microcephaly disease. *Protein Cell* **8**, 823–833.
- Lian, G. and Sheen, V. L.** (2015). Cytoskeletal proteins in cortical development and disease: actin associated proteins in periventricular heterotopia. *Front. Cell. Neurosci.* **9**, 1–13.
- Lindborg, B. A., Brekke, J. H., Vegoe, A. L., Ulrich, C. B., Haider, K. T., Subramaniam, S., Venhuizen, S. L., Eide, C. R., Orchard, P. J., Chen, W., et al.** (2016). Rapid Induction of Cerebral Organoids From Human Induced Pluripotent Stem Cells Using a Chemically Defined Hydrogel and Defined Cell Culture Medium. *Stem Cells Transl. Med.* **5**, 970–9.
- Lippi, G.** (2017). Neuropsychiatric symptoms and diagnosis of grey matter heterotopia: A case-based reflection. *S. Afr. J. Psychiatr.* **23**, 923.
- Liu, Z., Li, X., Zhang, J.-T., Cai, Y.-J., Cheng, T.-L., Cheng, C., Wang, Y., Zhang, C.-C., Nie, Y.-H., Chen, Z.-F., et al.** (2016). Autism-like behaviours and germline transmission in transgenic monkeys overexpressing MeCP2. *Nature* **530**, 98–102.
- Long, K. R. and Huttner, W. B.** (2019). How the extracellular matrix shapes neural development. *Open Biol.* **9**, 180216.
- Long, K. R., Newland, B., Florio, M., Kalebic, N., Langen, B., Kolterer, A., Wimberger, P. and Huttner, W. B.** (2018). Extracellular Matrix Components

- HAPLN1, Lumican, and Collagen I Cause Hyaluronic Acid-Dependent Folding of the Developing Human Neocortex. *Neuron* **99**, 702–719.e6.
- Lovestone, S., Hartley, C. L., Pearce, J. and Anderton, B. H.** (1996). Phosphorylation of tau by glycogen synthase kinase-3 beta in intact mammalian cells: the effects on the organization and stability of microtubules. *Neuroscience* **73**, 1145–57.
- Lu, J. and Sheen, V.** (2005). Periventricular heterotopia. *Epilepsy Behav.* **7**, 143–9.
- Lu, J., Tiao, G., Folkerth, R., Hecht, J., Walsh, C. and Sheen, V.** (2006). Overlapping expression of ARFGEF2 and filamin A in the neuroependymal lining of the lateral ventricles: Insights into the cause of periventricular heterotopia. *J. Comp. Neurol.* **494**, 476–484.
- Lu, I.-L., Chen, C., Tung, C.-Y., Chen, H.-H., Pan, J.-P., Chang, C.-H., Cheng, J.-S., Chen, Y.-A., Wang, C.-H., Huang, C.-W., et al.** (2018). Identification of genes associated with cortical malformation using a transposon-mediated somatic mutagenesis screen in mice. *Nat. Commun.* **9**, 2498.
- Lui, J. H., Hansen, D. V and Kriegstein, A. R.** (2011). Development and evolution of the human neocortex. *Cell* **146**, 18–36.
- Lukaszewicz, A., Savatier, P., Cortay, V., Giroud, P., Huissoud, C., Berland, M., Kennedy, H. and Dehay, C.** (2005). G1 Phase Regulation, Area-Specific Cell Cycle Control, and Cytoarchitectonics in the Primate Cortex. *Neuron* **47**, 353–364.
- Ma, X. and Adelstein, R. S.** (2014). The role of vertebrate nonmuscle Myosin II in development and human disease. *Bioarchitecture* **4**, 88–102.
- Maas, C., Belgardt, D., Lee, H. K., Heisler, F. F., Lappe-Siefke, C., Magiera, M. M., van Dijk, J., Hausrat, T. J., Janke, C. and Kneussel, M.** (2009). Synaptic activation modifies microtubules underlying transport of postsynaptic cargo. *Proc. Natl. Acad. Sci.* **106**, 8731–8736.
- Madison, J. M., Zhou, F., Nigam, A., Hussain, A., Barker, D. D., Nehme, R., van der Ven, K., Hsu, J., Wolf, P., Fleishman, M., et al.** (2015). Characterization of bipolar disorder patient-specific induced pluripotent stem cells from a family reveals neurodevelopmental and mRNA expression abnormalities. *Mol. Psychiatry* **20**, 703–717.
- Maeta, K., Edamatsu, H., Nishihara, K., Ikutomo, J., Bilasy, S. E. and Kataoka, T.** (2016). Crucial Role of Rapgef2 and Rapgef6, a Family of Guanine Nucleotide Exchange Factors for Rap1 Small GTPase, in Formation of Apical Surface Adherens Junctions and Neural Progenitor Development in the Mouse Cerebral Cortex. *eNeuro* **3**,.
- Mansour, A. A., Gonçalves, J. T., Bloyd, C. W., Li, H., Fernandes, S., Quang, D., Johnston, S., Parylak, S. L., Jin, X. and Gage, F. H.** (2018). An in vivo model of functional and vascularized human brain organoids. *Nat. Biotechnol.* **36**, 432–441.
- Mantamadiotis, T., Papalexis, N. and Dworkin, S.** (2012). CREB signalling in neural stem/progenitor cells: Recent developments and the implications for brain tumour biology. *BioEssays* **34**, 293–300.
- Marchetto, M. C. N., Carromeu, C., Acab, A., Yu, D., Yeo, G. W., Mu, Y., Chen, G., Gage, F. H. and Muotri, A. R.** (2010). A Model for Neural Development and Treatment of Rett Syndrome Using Human Induced Pluripotent Stem Cells. *Cell* **143**, 527–539.
- Mariani, J., Simonini, M. V, Palejev, D., Tomasini, L., Coppola, G., Szekely, A. M., Horvath, T. L. and Vaccarino, F. M.** (2012). Modeling human cortical development in vitro using induced pluripotent stem cells. *Proc Natl Acad Sci U S A* **109**, 12770–12775.

- Mariani, J., Coppola, G., Zhang, P., Abyzov, A., Provini, L., Tomasini, L., Amenduni, M., Szekely, A., Palejev, D., Wilson, M., et al.** (2015). FOXP1-Dependent Dysregulation of GABA/Glutamate Neuron Differentiation in Autism Spectrum Disorders. *Cell* **162**, 375–390.
- Marín, O.** (2013). Cellular and molecular mechanisms controlling the migration of neocortical interneurons. *Eur. J. Neurosci.* **38**, 2019–2029.
- Marín, O. and Rubenstein, J. L. R.** (2003). CELL MIGRATION IN THE FOREBRAIN. *Annu. Rev. Neurosci.* **26**, 441–483.
- Marsh, E., Fulp, C., Gomez, E., Nasrallah, I., Minarcik, J., Sudi, J., Christian, S. L., Mancini, G., Labosky, P., Dobyns, W., et al.** (2009). Targeted loss of Arx results in a developmental epilepsy mouse model and recapitulates the human phenotype in heterozygous females. *Brain* **132**, 1563–76.
- Martínez, G., Khatiwada, S., Costa-Mattioli, M. and Hetz, C.** (2018). ER Proteostasis Control of Neuronal Physiology and Synaptic Function. *Trends Neurosci.* **41**, 610–624.
- Mary, S., Charrasse, S., Meriane, M., Comunale, F., Travo, P., Blangy, A. and Gauthier-Rouvière, C.** (2002). Biogenesis of N-cadherin-dependent cell-cell contacts in living fibroblasts is a microtubule-dependent kinesin-driven mechanism. *Mol. Biol. Cell* **13**, 285–301.
- Matsuda, S., Ikeda, Y., Murakami, M., Nakagawa, Y., Tsuji, A., Kitagishi, Y., Matsuda, S., Ikeda, Y., Murakami, M., Nakagawa, Y., et al.** (2019). Roles of PI3K/AKT/GSK3 Pathway Involved in Psychiatric Illnesses. *Diseases* **7**, 22.
- Mattoo, S., Durrant, E., Chen, M. J., Xiao, J., Lazar, C. S., Manning, G., Dixon, J. E. and Worby, C. A.** (2011). Comparative Analysis of *Histophilus somni* Immunoglobulin-binding Protein A (IbpA) with Other Fic Domain-containing Enzymes Reveals Differences in Substrate and Nucleotide Specificities. *J. Biol. Chem.* **286**, 32834–32842.
- Mattoo, S., Sanyal, A., Dutta, S., Chandran, A., Koller, A., Camara, A., Watson, B. G., Sengupta, R., Ysselstein, D., Montenegro, P., et al.** (2019). Alpha-Synuclein is a Target of Fic-mediated Adenylation/AMPylation: Implications for Parkinson's Disease. *bioRxiv* 525659.
- McClure-Begley, T. D., Ebmeier, C. C., Ball, K. E., Jacobsen, J. R., Kogut, I., Bilousova, G., Klymkowsky, M. K. and Old, W. M.** (2018). Cerebral organoid proteomics reveals signatures of dysregulated cortical development associated with human trisomy 21. *bioRxiv* 315317.
- Mège, R.-M., Gavard, J. and Lambert, M.** (2006). Regulation of cell–cell junctions by the cytoskeleton. *Curr. Opin. Cell Biol.* **18**, 541–548.
- Mertens, J., Wang, Q.-W., Kim, Y., Yu, D. X., Pham, S., Yang, B., Zheng, Y., Diffenderfer, K. E., Zhang, J., Soltani, S., et al.** (2015). Differential responses to lithium in hyperexcitable neurons from patients with bipolar disorder. *Nature* **527**, 95–99.
- Mi, H., Huang, X., Muruganujan, A., Tang, H., Mills, C., Kang, D. and Thomas, P. D.** (2017). PANTHER version 11: expanded annotation data from Gene Ontology and Reactome pathways, and data analysis tool enhancements. *Nucleic Acids Res.* **45**, D183–D189.
- Ming, G., Tang, H. and Song, H.** (2016). Advances in Zika Virus Research: Stem Cell Models, Challenges, and Opportunities. *Cell Stem Cell* **19**, 690–702.
- Mishra, H. K., Prots, I., Havlicek, S., Kohl, Z., Perez-Branguli, F., Boerstler, T., Anneser, L., Minakaki, G., Wend, H., Hampl, M., et al.** (2016). GSK3 β -dependent

- dysregulation of neurodevelopment in SPG11-patient induced pluripotent stem cell model. *Ann. Neurol.* **79**, 826–840.
- Moehlman, A. T., Casey, A. K., Servage, K., Orth, K. and Krämer, H.** (2018). Adaptation to constant light requires Fic-mediated AMPylation of BiP to protect against reversible photoreceptor degeneration. *Elife* **7**,.
- Montecchiani, C., Pedace, L., Lo Giudice, T., Casella, A., Mearini, M., Gaudiello, F., Pedroso, J. L., Terracciano, C., Caltagirone, C., Massa, R., et al.** (2016). ALS5/SPG11/KIAA1840 mutations cause autosomal recessive axonal Charcot-Marie-Tooth disease. *Brain* **139**, 73–85.
- Moon, H. M., Youn, Y. H., Pemble, H., Yingling, J., Wittmann, T. and Wynshaw-Boris, A.** (2014). LIS1 controls mitosis and mitotic spindle organization via the LIS1-NDEL1-dynein complex. *Hum. Mol. Genet.* **23**, 449–66.
- Moore, C. A., Perderiset, M., Francis, F., Chelly, J., Houdusse, A. and Milligan, R. A.** (2004). Mechanism of microtubule stabilization by doublecortin. *Mol. Cell* **14**, 833–9.
- Mora-Bermúdez, F., Badsha, F., Kanton, S., Camp, J. G., Vernot, B., Köhler, K., Voigt, B., Okita, K., Maricic, T., He, Z., et al.** (2016). Differences and similarities between human and chimpanzee neural progenitors during cerebral cortex development. *Elife* **5**,.
- Morris, S. M., Albrecht, U., Reiner, O., Eichele, G. and Yu-Lee, L. Y.** (1998). The lissencephaly gene product Lis1, a protein involved in neuronal migration, interacts with a nuclear movement protein, NudC. *Curr Biol* **8**, 603–606.
- Mukherjee, S., Liu, X., Arasaki, K., McDonough, J., Galán, J. E. and Roy, C. R.** (2011). Modulation of Rab GTPase function by a protein phosphocholine transferase. *Nature* **477**, 103–6.
- Muretta, J. M., Reddy, B. J. N., Scarabelli, G., Thompson, A. F., Jariwala, S., Major, J., Venere, M., Rich, J. N., Willard, B., Thomas, D. D., et al.** (2018). A posttranslational modification of the mitotic kinesin Eg5 that enhances its mechanochemical coupling and alters its mitotic function. *Proc. Natl. Acad. Sci. U. S. A.* **115**, E1779–E1788.
- Mzhavia, N., Pan, H., Che, F.-Y., Fricker, L. D. and Devi, L. A.** (2003). Characterization of endothelin-converting enzyme-2. Implication for a role in the nonclassical processing of regulatory peptides. *J. Biol. Chem.* **278**, 14704–11.
- Nadarajah, B., Brunstrom, J., Grutzendler, J., Wong, R. and Pearlman, A.** (2001). Two modes of radial migration in early development of the cerebral cortex. *Nat. Neurosci.* **4**, 143–150.
- Nadarajah, B., Alifragis, P., Wong, R. O. L. and Parnavelas, J. G.** (2003). Neuronal migration in the developing cerebral cortex: observations based on real-time imaging. *Cereb. Cortex* **13**, 607–611.
- Nagano, T., Morikubo, S. and Sato, M.** (2004). Filamin A and FILIP (Filamin A-Interacting Protein) regulate cell polarity and motility in neocortical subventricular and intermediate zones during radial migration. *J Neurosci* **24**, 9648–9657.
- Nakano, T., Ando, S., Takata, N., Kawada, M., Muguruma, K., Sekiguchi, K., Saito, K., Yonemura, S., Eiraku, M. and Sasai, Y.** (2012). Self-Formation of Optic Cups and Storable Stratified Neural Retina from Human ESCs. *Cell Stem Cell* **10**, 771–785.
- Narita, M., Kuzumaki, N., Miyatake, M., Sato, F., Wachi, H., Seyama, Y. and Suzuki, T.** (2006). Role of delta-opioid receptor function in neurogenesis and neuroprotection. *J. Neurochem.* **97**, 1494–1505.

- Ng, P. C. and Henikoff, S.** (2003). SIFT: Predicting amino acid changes that affect protein function. *Nucleic Acids Res.* **31**, 3812–4.
- Niewmierzycka, A., Mills, J., St-Arnaud, R., Dedhar, S. and Reichardt, L. F.** (2005). Integrin-linked kinase deletion from mouse cortex results in cortical lamination defects resembling cobblestone lissencephaly. *J. Neurosci.* **25**, 7022–31.
- Nixon, R. A.** (2013). The role of autophagy in neurodegenerative disease. *Nat. Med.* **19**, 983–997.
- Noctor, S. C., Martinez-Cerdeno, V., Ivic, L. and Kriegstein, A. R.** (2004). Cortical neurons arise in symmetric and asymmetric division zones and migrate through specific phases. *Nat Neurosci* **7**, 136–144.
- Nonaka-Kinoshita, M., Reillo, I., Artegiani, B., Martínez-Martínez, M. Á., Nelson, M., Borrell, V. and Calegari, F.** (2013). Regulation of cerebral cortex size and folding by expansion of basal progenitors. *EMBO J.* **32**, 1817–28.
- Nopoulos, P. C., Flaum, M., Andreasen, N. C. and Swayze, V. W.** (1995). Gray matter heterotopias in schizophrenia. *Psychiatry Res.* **61**, 11–4.
- Nosten-Bertrand, M., Kappeler, C., Dinocourt, C., Denis, C., Germain, J., Phan Dinh Tuy, F., Verstraeten, S., Alvarez, C., Métin, C., Chelly, J., et al.** (2008). Epilepsy in Dcx knockout mice associated with discrete lamination defects and enhanced excitability in the hippocampus. *PLoS One* **3**, e2473.
- Novorol, C., Burkhardt, J., Wood, K. J., Iqbal, A., Roque, C., Coutts, N., Almeida, A. D., He, J., Wilkinson, C. J. and Harris, W. A.** (2013). Microcephaly models in the developing zebrafish retinal neuroepithelium point to an underlying defect in metaphase progression. *Open Biol.* **3**, 130065–130065.
- Nowakowski, T. J., Pollen, A. A., Sandoval-Espinosa, C. and Kriegstein, A. R.** (2016). Transformation of the Radial Glia Scaffold Demarcates Two Stages of Human Cerebral Cortex Development. *Neuron* **91**, 1219–1227.
- O’Neill, A. C., Kyrousi, C., Einsiedler, M., Burtscher, I., Drukker, M., Markie, D. M., Kirk, E. P., Götz, M., Robertson, S. P. and Cappello, S.** (2018a). Mob2 Insufficiency Disrupts Neuronal Migration in the Developing Cortex. *Front. Cell. Neurosci.* **12**, 57.
- O’Neill, A. C., Kyrousi, C., Klaus, J., Leventer, R. J., Kirk, E. P., Fry, A., Pilz, D. T., Morgan, T., Jenkins, Z. A., Drukker, M., et al.** (2018b). A Primate-Specific Isoform of PLEKHG6 Regulates Neurogenesis and Neuronal Migration. *Cell Rep.* **25**, 2729–2741.e6.
- Oegema, R., Baillat, D., Schot, R., van Unen, L. M., Brooks, A., Kia, S. K., Hoogeboom, A. J. M., Xia, Z., Li, W., Cesaroni, M., et al.** (2017). Human mutations in integrator complex subunits link transcriptome integrity to brain development. *PLoS Genet.* **13**, e1006809.
- Ohnuma, S. and Harris, W. A.** (2003). Neurogenesis and the cell cycle. *Neuron* **40**, 199–208.
- Okada, Y., Suzuki, A., Takagi, S., Hirai, H., Saitoh, R., Adachi, A., Yanagihara, T., Ueki, M., Fujii, T. and Arai, T.** (2004). Polyglutamylation of Tubulin during Differentiation of Neural Precursor Cells. *bioimages* **12**, 71–83.
- Oliet, S. H. R. and Bonfardin, V. D. J.** (2010). Morphological plasticity of the rat supraoptic nucleus - cellular consequences. *Eur. J. Neurosci.* **32**, 1989–1994.
- Olivero, P., Lozano, C., Sotomayor-Zárata, R., Meza-Concha, N., Arancibia, M., Córdova, C., González-Arriagada, W., Ramírez-Barrantes, R. and Marchant, I.** (2018). Proteostasis and Mitochondrial Role on Psychiatric and Neurodegenerative Disorders: Current Perspectives. *Neural Plast.* **2018**, 6798712.

- Orford, K., Crockett, C., Jensen, J. P., Weissman, A. M. and Byers, S. W. (1997). Serine phosphorylation-regulated ubiquitination and degradation of beta-catenin. *J. Biol. Chem.* **272**, 24735–8.
- Orlacchio, A., Babalini, C., Borreca, A., Patrono, C., Massa, R., Basaran, S., Munhoz, R. P., Rogaeva, E. A., St George-Hyslop, P. H., Bernardi, G., et al. (2010). SPATACSIN mutations cause autosomal recessive juvenile amyotrophic lateral sclerosis. *Brain* **133**, 591–598.
- Ormel, P. R., Vieira de Sá, R., van Bodegraven, E. J., Karst, H., Harschnitz, O., Sneeboer, M. A. M., Johansen, L. E., van Dijk, R. E., Scheefhals, N., Berdenis van Berlekom, A., et al. (2018). Microglia innately develop within cerebral organoids. *Nat. Commun.* **9**, 4167.
- Orre, L. M., Vesterlund, M., Pan, Y., Arslan, T., Zhu, Y., Fernandez Woodbridge, A., Frings, O., Fredlund, E. and Lehtiö, J. (2019). SubCellBarCode: Proteome-wide Mapping of Protein Localization and Relocalization. *Mol. Cell* **73**, 166–182.e7.
- Otani, T., Marchetto, M. C., Gage, F. H., Simons, B. D. and Livesey, F. J. (2016). 2D and 3D Stem Cell Models of Primate Cortical Development Identify Species-Specific Differences in Progenitor Behavior Contributing to Brain Size. *Cell Stem Cell* **18**, 467–480.
- Ouimet, T., Orng, S.-V., Poras, H., Gagnidze, K., Devi, L. A., Fournié-Zaluski, M.-C. and Roques, B. P. (2010). Identification of an Endothelin-converting Enzyme-2-specific Fluorogenic Substrate and Development of an in Vitro and ex Vivo Enzymatic Assay. *J. Biol. Chem.* **285**, 34390–34400.
- Pacheco-Quinto, J. and Eckman, E. A. (2013). Endothelin-converting enzymes degrade intracellular β -amyloid produced within the endosomal/lysosomal pathway and autophagosomes. *J. Biol. Chem.* **288**, 5606–15.
- Pacheco-Quinto, J., Eckman, C. B. and Eckman, E. A. (2016). Major amyloid- β -degrading enzymes, endothelin-converting enzyme-2 and neprilysin, are expressed by distinct populations of GABAergic interneurons in hippocampus and neocortex. *Neurobiol. Aging* **48**, 83–92.
- Palmer, J. C., Baig, S., Kehoe, P. G. and Love, S. (2009). Endothelin-converting enzyme-2 is increased in Alzheimer's disease and up-regulated by Abeta. *Am. J. Pathol.* **175**, 262–70.
- Pan, H., Mzhavia, N. and Devi, L. (2004). Endothelin Converting Enzyme-2: A Processing Enzyme Involved in the Generation of Novel Neuropeptides. *Protein Pept. Lett.* **11**, 461–469.
- Pang, T., Atefy, R. and Sheen, V. (2008). Malformations of Cortical Development. *Neurologist* **14**, 181–191.
- Pankratz, M. T., Li, X.-J., LaVaute, T. M., Lyons, E. A., Chen, X. and Zhang, S.-C. (2007). Directed Neural Differentiation of Human Embryonic Stem Cells via an Obligated Primitive Anterior Stage. *Stem Cells* **25**, 1511–1520.
- Parr, C., Carzaniga, R., Gentleman, S. M., Leuven, F. Van, Walter, J. and Sastre, M. (2012). Glycogen Synthase Kinase 3 Inhibition Promotes Lysosomal Biogenesis and Autophagic Degradation of the Amyloid- β Precursor Protein. *Mol. Cell. Biol.* **32**, 4410–4418.
- Parrini, E., Ramazzotti, A., Dobyns, W. B., Mei, D., Moro, F., Veggiotti, P., Marini, C., Brilstra, E. H., Dalla Bernardina, B., Goodwin, L., et al. (2006). Periventricular heterotopia: phenotypic heterogeneity and correlation with Filamin A mutations. *Brain* **129**, 1892–1906.
- Paşca, S. P., Portmann, T., Voineagu, I., Yazawa, M., Shcheglovitov, A., Paşca, A.

- M., Cord, B., Palmer, T. D., Chikahisa, S., Nishino, S., et al.** (2011). Using iPSC-derived neurons to uncover cellular phenotypes associated with Timothy syndrome. *Nat. Med.* **17**, 1657–1662.
- Paşca, S. P., Panagiotakos, G. and Dolmetsch, R. E.** (2014). Generating Human Neurons In Vitro and Using Them to Understand Neuropsychiatric Disease. *Annu. Rev. Neurosci.* **37**, 479–501.
- Paşca, A. M., Sloan, S. A., Clarke, L. E., Tian, Y., Makinson, C. D., Huber, N., Kim, C. H., Park, J.-Y., O'Rourke, N. A., Nguyen, K. D., et al.** (2015). Functional cortical neurons and astrocytes from human pluripotent stem cells in 3D culture. *Nat. Methods* **12**, 671–678.
- Paşca, S. P.** (2018). The rise of three-dimensional human brain cultures. *Nat.* **2018** 5537689 **553**, 437.
- Paturle-Lafanechère, L., Manier, M., Trigault, N., Pirollet, F., Mazarguil, H. and Job, D.** (1994). Accumulation of delta 2-tubulin, a major tubulin variant that cannot be tyrosinated, in neuronal tissues and in stable microtubule assemblies. *J. Cell Sci.* **107 (Pt 6)**, 1529–43.
- Pensato, V., Castellotti, B., Gellera, C., Pareyson, D., Ciano, C., Nanetti, L., Salsano, E., Piscoquito, G., Sarto, E., Eoli, M., et al.** (2014). Overlapping phenotypes in complex spastic paraplegias SPG11, SPG15, SPG35 and SPG48. *Brain* **137**, 1907–1920.
- Pérez-Brangulí, F., Mishra, H. K., Prots, I., Havlicek, S., Kohl, Z., Saul, D., Rummel, C., Dorca-Arevalo, J., Regensburger, M., Graef, D., et al.** (2014). Dysfunction of spatacsin leads to axonal pathology in SPG11-linked hereditary spastic paraplegia. *Hum. Mol. Genet.* **23**, 4859–74.
- Pérez-Brangulí, F., Buchsbaum, I. Y., Pozner, T., Regensburger, M., Fan, W., Schray, A., Börstler, T., Mishra, H., Gräf, D., Kohl, Z., et al.** (2018). Human SPG11 cerebral organoids reveal cortical neurogenesis impairment. *Hum. Mol. Genet.* **28**, 961–971.
- Peyre, E., Silva, C. G. and Nguyen, L.** (2015). Crosstalk between intracellular and extracellular signals regulating interneuron production, migration and integration into the cortex. *Front. Cell. Neurosci.* **9**, 129.
- Pilz, G.-A., Shitamukai, A., Reillo, I., Pacary, E., Schwausch, J., Stahl, R., Ninkovic, J., Snippert, H. J., Clevers, H., Godinho, L., et al.** (2013). Amplification of progenitors in the mammalian telencephalon includes a new radial glial cell type. *Nat. Commun.* **4**, 2125.
- Pollen, A. A., Nowakowski, T. J., Chen, J., Retallack, H., Sandoval-Espinosa, C., Nicholas, C. R., Shuga, J., Liu, S. J., Oldham, M. C., Diaz, A., et al.** (2015). Molecular Identity of Human Outer Radial Glia during Cortical Development. *Cell* **163**.
- Pollen, A. A., Bhaduri, A., Andrews, M. G., Nowakowski, T. J., Meyerson, O. S., Mostajo-Radji, M. A., Di Lullo, E., Alvarado, B., Bedolli, M., Dougherty, M. L., et al.** (2019). Establishing Cerebral Organoids as Models of Human-Specific Brain Evolution. *Cell* **176**, 743–756.e17.
- Portis, S., Giunta, B., Obregon, D. and Tan, J.** (2012). The role of glycogen synthase kinase-3 signaling in neurodevelopment and fragile X syndrome. *Int. J. Physiol. Pathophysiol. Pharmacol.* **4**, 140–8.
- Pozner, T., Schray, A., Regensburger, M., Lie, D. C., Schlötzer-Schrehardt, U., Winkler, J., Turan, S. and Winner, B.** (2018). Tideglusib Rescues Neurite Pathology of SPG11 iPSC Derived Cortical Neurons. *Front. Neurosci.* **12**, 914.

- Preissler, S., Rato, C., Perera, L. A., Saudek, V. and Ron, D.** (2017a). FICD acts bifunctionally to AMPylate and de-AMPylate the endoplasmic reticulum chaperone BiP. *Nat. Struct. Mol. Biol.* **24**, 23–29.
- Preissler, S., Rohland, L., Yan, Y., Chen, R., Read, R. J. and Ron, D.** (2017b). AMPylation targets the rate-limiting step of BiP's ATPase cycle for its functional inactivation. *Elife* **6**,.
- Price, M. G., Yoo, J. W., Burgess, D. L., Deng, F., Hrachovy, R. A., Frost, J. D. and Noebels, J. L.** (2009). A triplet repeat expansion genetic mouse model of infantile spasms syndrome, Arx(GCG)₁₀₊₇, with interneuronopathy, spasms in infancy, persistent seizures, and adult cognitive and behavioral impairment. *J. Neurosci.* **29**, 8752–63.
- Pruski, M., Rajnicek, A., Yang, Z., Clancy, H., Ding, Y.-Q., McCaig, C. D. and Lang, B.** (2016). The ciliary GTPase Arl13b regulates cell migration and cell cycle progression. *Cell Adh. Migr.* **10**, 393–405.
- Qian, X., Nguyen, H. N., Song, M. M., Hadiono, C., Ogden, S. C., Hammack, C., Yao, B., Hamersky, G. R., Jacob, F., Zhong, C., et al.** (2016). Brain-Region-Specific Organoids Using Mini-bioreactors for Modeling ZIKV Exposure. *Cell*.
- Quadrato, G., Nguyen, T., Macosko, E. Z., Sherwood, J. L., Min Yang, S., Berger, D. R., Maria, N., Scholvin, J., Goldman, M., Kinney, J. P., et al.** (2017). Cell diversity and network dynamics in photosensitive human brain organoids. *Nature* **545**, 48–53.
- Rahman, M., Ham, H., Liu, X., Sugiura, Y., Orth, K. and Krämer, H.** (2012). Visual neurotransmission in *Drosophila* requires expression of Fic in glial capitate projections. *Nat. Neurosci.* **15**, 871–5.
- Rakic, P.** (1972). Mode of cell migration to the superficial layers of fetal monkey neocortex. *J Comp Neurol* **145**, 61–83.
- Rakic, P.** (2009). Evolution of the neocortex: a perspective from developmental biology. *Nat Rev Neurosci* **10**, 724–735.
- Ramos, R. L.** (2005). Heterotopia Formation in Rat but Not Mouse Neocortex after RNA Interference Knockdown of DCX. *Cereb. Cortex* **16**, 1323–1331.
- Ran, F. A., Hsu, P. P. D., Wright, J., Agarwala, V., Scott, D. a and Zhang, F.** (2013). Genome engineering using the CRISPR-Cas9 system. *Nat. Protoc.* **8**, 2281–2308.
- Reddington, A. E., Rosser, A. E. and Dunnett, S. B.** (2014). Differentiation of pluripotent stem cells into striatal projection neurons: a pure MSN fate may not be sufficient. *Front. Cell. Neurosci.* **8**, 398.
- Reed, N. A., Cai, D., Blasius, T. L., Jih, G. T., Meyhofer, E., Gaertig, J. and Verhey, K. J.** (2006). Microtubule acetylation promotes kinesin-1 binding and transport. *Curr Biol* **16**, 2166–2172.
- Reillo, I., de Juan Romero, C., García-Cabezas, M. Á. and Borrell, V.** (2011). A Role for Intermediate Radial Glia in the Tangential Expansion of the Mammalian Cerebral Cortex. *Cereb. Cortex* **21**, 1674–1694.
- Ren, Y., Zhao, J. and Feng, J.** (2003). Parkin binds to alpha/beta tubulin and increases their ubiquitination and degradation. *J. Neurosci.* **23**, 3316–24.
- Renier, N., Wu, Z., Simon, D. J., Yang, J., Ariel, P. and Tessier-Lavigne, M.** (2014). IDISCO: A simple, rapid method to immunolabel large tissue samples for volume imaging. *Cell* **159**,.
- Renner, M., Lancaster, M. A., Bian, S., Choi, H., Ku, T., Peer, A., Chung, K. and Knoblich, J. A.** (2017). Self-organized developmental patterning and differentiation in cerebral organoids. *EMBO J.* **36**, 1316–1329.

- Rentzsch, P., Witten, D., Cooper, G. M., Shendure, J. and Kircher, M.** (2019). CADD: predicting the deleteriousness of variants throughout the human genome. *Nucleic Acids Res.* **47**, D886–D894.
- Reynolds, B. A. and Weiss, S.** (1992). Generation of neurons and astrocytes from isolated cells of the adult mammalian central nervous system. *Science (80-)*. **255**, 1707–1710.
- Ridley, A. J., Schwartz, M. A., Burridge, K., Firtel, R. A., Ginsberg, M. H., Borisy, G., Parsons, J. T. and Horwitz, A. R.** (2003). Cell Migration: Integrating Signals from Front to Back. *Science (80-)*. **302**, 1704–1709.
- Riederer, B. M.** (2007). Microtubule-associated protein 1B, a growth-associated and phosphorylated scaffold protein. *Brain Res. Bull.* **71**, 541–558.
- Rodriguez-Boulan, E., Kreitzer, G. and Musch, A.** (2005). Organization of vesicular trafficking in epithelia. *Nat. Rev. Mol. Cell Biol.* **6**, 233–247.
- Rodriguez, R. M., Gadnidge, K., Ragnauth, A., Dorr, N., Yanagisawa, M., Wetsel, W. C. and Devi, L. A.** (2008). Animals lacking endothelin-converting enzyme-2 are deficient in learning and memory. *Genes. Brain. Behav.* **7**, 418–26.
- Romero, D. M., Bahi-Buisson, N. and Francis, F.** (2018). Genetics and mechanisms leading to human cortical malformations. *Semin. Cell Dev. Biol.* **76**, 33–75.
- Rottner, K. and Stradal, T. E.** (2011). Actin dynamics and turnover in cell motility. *Curr. Opin. Cell Biol.* **23**, 569–578.
- Ryan, K., Backos, D. S., Reigan, P. and Patel, M.** (2012). Post-translational oxidative modification and inactivation of mitochondrial complex I in epileptogenesis. *J. Neurosci.* **32**, 11250–8.
- Saito, T.** (2006). In vivo electroporation in the embryonic mouse central nervous system. *Nat Protoc* **1**, 1552–1558.
- Sakakibara, A., Ando, R., Sapir, T. and Tanaka, T.** (2013). Microtubule dynamics in neuronal morphogenesis. *Open Biol.* **3**, 130061.
- Sanchez, C., Diaz-Nido, J. and Avila, J.** (2000). Phosphorylation of microtubule-associated protein 2 (MAP2) and its relevance for the regulation of the neuronal cytoskeleton function. *Prog. Neurobiol.* **61**, 133–68.
- Sanyal, A., Chen, A. J., Nakayasu, E. S., Lazar, C. S., Zbornik, E. A., Worby, C. A., Koller, A. and Mattoo, S.** (2015). A Novel Link between Fic (Filamentation Induced by cAMP)-mediated Adenylylation/AMPylation and the Unfolded Protein Response. *J. Biol. Chem.* **290**, 8482–8499.
- Sapir, T., Elbaum, M. and Reiner, O.** (1997). Reduction of microtubule catastrophe events by LIS1, platelet-activating factor acetylhydrolase subunit. *EMBO J* **16**, 6977–6984.
- Sarkisian, M. R., Bartley, C. M., Chi, H., Nakamura, F., Hashimoto-Torii, K., Torii, M., Flavell, R. A. and Rakic, P.** (2006). MEKK4 signaling regulates filamin expression and neuronal migration. *Neuron* **52**, 789–801.
- Sasaki, E., Suemizu, H., Shimada, A., Hanazawa, K., Oiwa, R., Kamioka, M., Tomioka, I., Sotomaru, Y., Hirakawa, R., Eto, T., et al.** (2009). Generation of transgenic non-human primates with germline transmission. *Nature* **459**, 523–527.
- Schaar, B. T. and McConnell, S. K.** (2005). Cytoskeletal coordination during neuronal migration. *Proc Natl Acad Sci U S A* **102**, 13652–13657.
- Schaefer, A. W., Kabir, N. and Forscher, P.** (2002). Filopodia and actin arcs guide the assembly and transport of two populations of microtubules with unique dynamic parameters in neuronal growth cones. *J Cell Biol* **158**, 139–152.

- Schindelin, J., Arganda-Carreras, I., Frise, E., Kaynig, V., Longair, M., Pietzsch, T., Preibisch, S., Rueden, C., Saalfeld, S., Schmid, B., et al.** (2012). {Fiji}: an open-source platform for biological-image analysis. *Nat. Methods* **9**, 676–682.
- Schmid, M.-T. T., Weinandy, F., Wilsch-Bräuninger, M., Huttner, W. B., Cappello, S., Götz, M., Wilsch-Brauninger, M., Huttner, W. B., Cappello, S. and Gotz, M.** (2014). The role of alpha-E-catenin in cerebral cortex development: radial glia specific effect on neuronal migration. *Front Cell Neurosci* **8**, 215.
- Scott, H. and Panin, V. M.** (2014a). N-Glycosylation in Regulation of the Nervous System. In *Advances in neurobiology*, pp. 367–394.
- Scott, H. and Panin, V. M.** (2014b). The role of protein N-glycosylation in neural transmission. *Glycobiology* **24**, 407–17.
- Sekine, K., Honda, T., Kawauchi, T., Kubo, K. -i. and Nakajima, K.** (2011). The Outermost Region of the Developing Cortical Plate Is Crucial for Both the Switch of the Radial Migration Mode and the Dab1-Dependent ‘‘Inside-Out’’ Lamination in the Neocortex. *J. Neurosci.* **31**, 9426–9439.
- Semenova, I., Burakov, A., Berardone, N., Zaliapin, I., Slepchenko, B., Svitkina, T., Kashina, A. and Rodionov, V.** (2008). Actin Dynamics Is Essential for Myosin-Based Transport of Membrane Organelles. *Curr. Biol.* **18**, 1581–1586.
- Sengupta, R., Poderycki, M. J. and Mattoo, S.** (2019). CryoAPEX - an electron tomography tool for subcellular localization of membrane proteins. *J. Cell Sci.* **132**, jcs222315.
- Sheen, V. L.** (2014). Filamin A mediated Big2 dependent endocytosis. **2**, 1–6.
- Sheen, V. L., Feng, Y., Graham, D., Takafuta, T., Shapiro, S. S. and Walsh, C. A.** (2002). Filamin A and Filamin B are co-expressed within neurons during periods of neuronal migration and can physically interact. *Hum Mol Genet* **11**, 2845–2854.
- Sheen, V. L., Ganesh, V. S., Topcu, M., Sebire, G., Bodell, A., Hill, R. S., Grant, P. E., Shugart, Y. Y., Imitola, J., Khoury, S. J., et al.** (2004a). Mutations in ARFGEF2 implicate vesicle trafficking in neural progenitor proliferation and migration in the human cerebral cortex. *Nat Genet* **36**, 69–76.
- Sheen, V. L., Basel-Vanagaite, L., Goodman, J. R., Scheffer, I. E., Bodell, A., Ganesh, V. S., Ravenscroft, R., Hill, R. S., Cherry, T. J., Shugart, Y. Y., et al.** (2004b). Etiological heterogeneity of familial periventricular heterotopia and hydrocephalus. *Brain Dev.* **26**, 326–334.
- Sheen, V. L., Ferland, R. J., Harney, M., Hill, R. S., Neal, J., Banham, A. H., Brown, P., Chenn, A., Corbo, J., Hecht, J., et al.** (2006). Impaired proliferation and migration in human Miller-Dieker neural precursors. *Ann. Neurol.* **60**, 137–144.
- Shi, Y., Kirwan, P. and Livesey, F. J.** (2012). Directed differentiation of human pluripotent stem cells to cerebral cortex neurons and neural networks. *Nat. Protoc.* **7**, 1836–1846.
- Shin, H.-W., Shinotsuka, C. and Nakayama, K.** (2005). Expression of BIG2 and analysis of its function in mammalian cells. *Methods Enzymol.* **404**, 206–15.
- Silbereis, J. C., Pochareddy, S., Zhu, Y., Li, M. and Sestan, N.** (2016). The Cellular and Molecular Landscapes of the Developing Human Central Nervous System. *Neuron* **89**, 248–268.
- Singh, G., Singh, V. and Schneider, J. S.** (2018). Post-translational histone modifications and their interaction with sex influence normal brain development and elaboration of neuropsychiatric disorders. *Biochim. Biophys. Acta - Mol. Basis Dis.*
- Sirajuddin, M., Rice, L. M. and Vale, R. D.** (2014). Regulation of microtubule motors by

- tubulin isotypes and post-translational modifications. *Nat. Cell Biol.* **16**, 335–344.
- Sloan, S. A., Darmanis, S., Huber, N., Khan, T. A., Birey, F., Caneda, C., Reimer, R., Quake, S. R., Barres, B. A. and Pasca, S. P.** (2017). Human Astrocyte Maturation Captured in 3D Cerebral Cortical Spheroids Derived from Pluripotent Stem Cells. *Neuron* **95**, 779–790.e6.
- Smart, I. H. M., Dehay, C., Giroud, P., Berland, M. and Kennedy, H.** (2002). Unique morphological features of the proliferative zones and postmitotic compartments of the neural epithelium giving rise to striate and extrastriate cortex in the monkey. *Cereb. Cortex* **12**, 37–53.
- Smith, R. S., Kenny, C. J., Ganesh, V., Jang, A., Borges-Monroy, R., Partlow, J. N., Hill, R. S., Shin, T., Chen, A. Y., Doan, R. N., et al.** (2018). Sodium Channel SCN3A (NaV1.3) Regulation of Human Cerebral Cortical Folding and Oral Motor Development. *Neuron* **99**, 905–913.e7.
- Song, Y. and Brady, S. T.** (2015). Post-translational modifications of tubulin: pathways to functional diversity of microtubules. *Trends Cell Biol.* **25**, 125–36.
- Sousa, A. M. M., Meyer, K. A., Santpere, G., Gulden, F. O. and Sestan, N.** (2017). Evolution of the Human Nervous System Function, Structure, and Development. *Cell* **170**, 226–247.
- Spittaels, K., Van den Haute, C., Van Dorpe, J., Terwel, D., Vandezande, K., Lasrado, R., Bruynseels, K., Irizarry, M., Verhoye, M., Van Lint, J., et al.** (2002). Neonatal neuronal overexpression of glycogen synthase kinase-3 β reduces brain size in transgenic mice. *Neuroscience* **113**, 797–808.
- Sreelatha, A., Yee, S. S., Lopez, V. A., Park, B. C., Kinch, L. N., Pilch, S., Servage, K. A., Zhang, J., Jiou, J., Karasiewicz-Urbańska, M., et al.** (2018). Protein AMPylation by an Evolutionarily Conserved Pseudokinase. *Cell* **175**, 809–821.e19.
- Srivastava, A., McGrath, B. and Bielas, S. L.** (2017). Histone H2A Monoubiquitination in Neurodevelopmental Disorders. *Trends Genet.* **33**, 566–578.
- Stahl, R., Walcher, T., De Juan Romero, C., Pilz, G. A., Cappello, S., Irmeler, M., Sanz-Aguela, J. M., Beckers, J., Blum, R., Borrell, V., et al.** (2013). *Trnp1* regulates expansion and folding of the mammalian cerebral cortex by control of radial glial fate. *Cell* **153**, 535–549.
- Stemmer, M., Thumberger, T., del Sol Keyer, M., Wittbrodt, J. and Mateo, J. L.** (2015). CCTop: An Intuitive, Flexible and Reliable CRISPR/Cas9 Target Prediction Tool. *PLoS One* **10**, e0124633.
- Stevanin, G., Santorelli, F. M., Azzedine, H., Coutinho, P., Chomilier, J., Denora, P. S., Martin, E., Ouvrard-Hernandez, A.-M., Tessa, A., Bouslam, N., et al.** (2007). Mutations in SPG11, encoding spatacsin, are a major cause of spastic paraplegia with thin corpus callosum. *Nat. Genet.* **39**, 366–372.
- Stiles, J. and Jernigan, T. L.** (2010). The basics of brain development. *Neuropsychol. Rev.* **20**, 327–48.
- Stouffer, M. A., Golden, J. A. and Francis, F.** (2015). Neuronal migration disorders: Focus on the cytoskeleton and epilepsy. *Neurobiol Dis.*
- Stromillo, M. L., Malandrini, A., Dotti, M. T., Battaglini, M., Borgogni, F., Tessa, A., Storti, E., Denora, P. S., Santorelli, F. M., Gaudiano, C., et al.** (2011). Structural and metabolic damage in brains of patients with SPG11-related spastic paraplegia as detected by quantitative MRI. *J. Neurol.* **258**, 2240–2247.
- Sullivan, P. F., Daly, M. J. and O'Donovan, M.** (2012). Genetic architectures of psychiatric disorders: the emerging picture and its implications. *Nat. Rev. Genet.* **13**, 537–551.

- Sun, T. and Hevner, R. F.** (2014). Growth and folding of the mammalian cerebral cortex: from molecules to malformations. *Nat. Rev. Neurosci.* **15**, 217–232.
- Suzuki, I. K. and Vanderhaeghen, P.** (2015). Is this a brain which I see before me? Modeling human neural development with pluripotent stem cells. 3138–3150.
- Suzuki, I. K., Gacquer, D., Van Heurck, R., Kumar, D., Wojno, M., Bilheu, A., Herpoel, A., Lambert, N., Cheron, J., Polleux, F., et al.** (2018). Human-Specific NOTCH2NL Genes Expand Cortical Neurogenesis through Delta/Notch Regulation. *Cell* **173**, 1370–1384.e16.
- Szklarczyk, D., Morris, J. H., Cook, H., Kuhn, M., Wyder, S., Simonovic, M., Santos, A., Doncheva, N. T., Roth, A., Bork, P., et al.** (2017). The STRING database in 2017: quality-controlled protein–protein association networks, made broadly accessible. *Nucleic Acids Res.* **45**, D362–D368.
- Tabata, H. and Nakajima, K.** (2001). Efficient in utero gene transfer system to the developing mouse brain using electroporation: visualization of neuronal migration in the developing cortex. *Neuroscience* **103**, 865–72.
- Tabata, H. and Nakajima, K.** (2003). Multipolar migration: the third mode of radial neuronal migration in the developing cerebral cortex. *J Neurosci* **23**, 9996–10001.
- Takahashi, K. and Yamanaka, S.** (2006). Induction of pluripotent stem cells from mouse embryonic and adult fibroblast cultures by defined factors. *Cell* **126**, 663–676.
- Tanaka, T., Serneo, F. F., Higgins, C., Gambello, M. J., Wynshaw-Boris, A. and Gleeson, J. G.** (2004). Lis1 and doublecortin function with dynein to mediate coupling of the nucleus to the centrosome in neuronal migration. *J Cell Biol* **165**, 709–721.
- Taverna, E. and Huttner, W. B.** (2010). Neural Progenitor Nuclei IN Motion. *Neuron* **67**, 906–914.
- Taverna, E., Götz, M. and Huttner, W. B.** (2014). The Cell Biology of Neurogenesis: Toward an Understanding of the Development and Evolution of the Neocortex. *Annu. Rev. Cell Dev. Biol.* **30**, 465–502.
- Terman, J. R. and Kashina, A.** (2013). Post-translational modification and regulation of actin. *Curr. Opin. Cell Biol.* **25**, 30–8.
- Tesson, C., Koht, J. and Stevanin, G.** (2015). Delving into the complexity of hereditary spastic paraplegias: how unexpected phenotypes and inheritance modes are revolutionizing their nosology. *Hum. Genet.* **134**, 511–538.
- Thom, M., Martinian, L., Parnavelas, J. G. and Sisodiya, S. M.** (2004). Distribution of Cortical Interneurons in Grey Matter Heterotopia in Patients with Epilepsy. *Epilepsia* **45**, 916–923.
- Thomson, J. A., Itskovitz-Eldor, J., Shapiro, S. S., Waknitz, M. A., Swiergiel, J. J., Marshall, V. S. and Jones, J. M.** (1998). Embryonic stem cell lines derived from human blastocysts. *Science* **282**, 1145–7.
- Tortosa, E., Galjart, N., Avila, J. and Sayas, C. L.** (2013). MAP1B regulates microtubule dynamics by sequestering EB1/3 in the cytosol of developing neuronal cells. *EMBO J.* **32**, 1293–306.
- Tortosa, E., Adolfs, Y., Fukata, M., Pasterkamp, R. J., Kapitein, L. C. and Hoogenraad, C. C.** (2017). Dynamic Palmitoylation Targets MAP6 to the Axon to Promote Microtubule Stabilization during Neuronal Polarization. *Neuron* **94**, 809–825.e7.
- Trimborn, M., Bell, S. M., Felix, C., Rashid, Y., Jafri, H., Griffiths, P. D., Neumann, L. M., Krebs, A., Reis, A., Sperling, K., et al.** (2004). Mutations in microcephalin

- cause aberrant regulation of chromosome condensation. *Am. J. Hum. Genet.* **75**, 261–6.
- Truttmann, M. C., Zheng, X., Hanke, L., Damon, J. R., Grootveld, M., Krakowiak, J., Pincus, D. and Ploegh, H. L.** (2017). Unrestrained AMPylation targets cytosolic chaperones and activates the heat shock response. *Proc. Natl. Acad. Sci.* **114**, E152–E160.
- Truttmann, M. C., Pincus, D. and Ploegh, H. L.** (2018). Chaperone AMPylation modulates aggregation and toxicity of neurodegenerative disease-associated polypeptides. *Proc. Natl. Acad. Sci.* **115**, E5008–E5017.
- Tsai, L. H. and Gleeson, J. G.** (2005). Nucleokinesis in neuronal migration. *Neuron* **46**, 383–388.
- Turner, D. A., Baillie-Johnson, P. and Martinez Arias, A.** (2016). Organoids and the genetically encoded self-assembly of embryonic stem cells. *BioEssays* **38**, 181–191.
- Valentino, R. J. and Volkow, N. D.** (2018). Untangling the complexity of opioid receptor function. *Neuropsychopharmacology* **43**, 2514–2520.
- van den Pol, A. N.** (2012). Neuropeptide transmission in brain circuits. *Neuron* **76**, 98–115.
- Vantaggiato, C., Panzeri, E., Castelli, M., Citterio, A., Arnoldi, A., Santorelli, F. M., Liguori, R., Scarlato, M., Musumeci, O., Toscano, A., et al.** (2019). ZFYVE26/SPASTIZIN and SPG11/SPATACSIN mutations in hereditary spastic paraplegia types AR-SPG15 and AR-SPG11 have different effects on autophagy and endocytosis. *Autophagy* **15**, 34–57.
- Varga, R.-E., Khundadze, M., Damme, M., Nietzsche, S., Hoffmann, B., Stauber, T., Koch, N., Hennings, J. C., Franzka, P., Huebner, A. K., et al.** (2015). In Vivo Evidence for Lysosome Depletion and Impaired Autophagic Clearance in Hereditary Spastic Paraplegia Type SPG11. *PLoS Genet.* **11**, e1005454.
- Vestal-Laborde, A. A., Eschenroeder, A. C., Bigbee, J. W., Robinson, S. E. and Sato-Bigbee, C.** (2014). The Opioid System and Brain Development: Effects of Methadone on the Oligodendrocyte Lineage and the Early Stages of Myelination. *Dev. Neurosci.* **36**, 409–421.
- Vogl, A. M., Brockmann, M. M., Giusti, S. A., Maccarrone, G., Vercelli, C. A., Bauder, C. A., Richter, J. S., Roselli, F., Hafner, A.-S., Dedic, N., et al.** (2015). Neddylation inhibition impairs spine development, destabilizes synapses and deteriorates cognition. *Nat. Neurosci.* **18**, 239–251.
- Wang, X., Tsai, J. W., Imai, J. H., Lian, W. N., Vallee, R. B. and Shi, S. H.** (2009a). Asymmetric centrosome inheritance maintains neural progenitors in the neocortex. *Nature* **461**, 947–955.
- Wang, Z., Sandiford, S., Wu, C. and Li, S. S.-C.** (2009b). Numb regulates cell–cell adhesion and polarity in response to tyrosine kinase signalling. *EMBO J.* **28**, 2360–2373.
- Wang, X., Tsai, J. W., Lamonica, B. and Kriegstein, A. R.** (2011). A new subtype of progenitor cell in the mouse embryonic neocortex. *Nat Neurosci* **14**, 555–561.
- Wen, Z., Christian, K. M., Song, H. and Ming, G.** (2016). Modeling psychiatric disorders with patient-derived iPSCs. *Curr. Opin. Neurobiol.* **36**, 118–127.
- Werner, A., Manford, A. G. and Rape, M.** (2017). Ubiquitin-Dependent Regulation of Stem Cell Biology. *Trends Cell Biol.* **27**, 568–579.
- Weyn-Vanhentenryck, S. M., Feng, H., Ustianenko, D., Duffié, R., Yan, Q., Jacko, M., Martinez, J. C., Goodwin, M., Zhang, X., Hengst, U., et al.** (2018). Precise

- temporal regulation of alternative splicing during neural development. *Nat. Commun.* **9**, 2189.
- Windrem, M. S., Osipovitch, M., Liu, Z., Bates, J., Chandler-Militello, D., Zou, L., Munir, J., Schanz, S., McCoy, K., Miller, R. H., et al.** (2017). Human iPSC Glial Mouse Chimeras Reveal Glial Contributions to Schizophrenia. *Cell Stem Cell* **21**, 195–208.e6.
- Witte, H. and Bradke, F.** (2008). The role of the cytoskeleton during neuronal polarization. *Curr Opin Neurobiol* **18**, 479–487.
- Wloga, D., Joachimiak, E. and Fabczak, H.** (2017). Tubulin Post-Translational Modifications and Microtubule Dynamics. *Int. J. Mol. Sci.* **18**,.
- Wonders, C. P. and Anderson, S. A.** (2006). The origin and specification of cortical interneurons. *Nat. Rev. Neurosci.* **7**, 687–696.
- Woodhead, G. J., Mutch, C. A., Olson, E. C. and Chenn, A.** (2006). Cell-autonomous beta-catenin signaling regulates cortical precursor proliferation. *J Neurosci* **26**, 12620–12630.
- Worby, C. A., Mattoo, S., Kruger, R. P., Corbeil, L. B., Koller, A., Mendez, J. C., Zekarias, B., Lazar, C. and Dixon, J. E.** (2009). The Fic Domain: Regulation of Cell Signaling by Adenylation. *Mol. Cell* **34**, 93–103.
- Wu, Y., Whiteus, C., Xu, C. S., Hayworth, K. J., Weinberg, R. J., Hess, H. F. and De Camilli, P.** (2017). Contacts between the endoplasmic reticulum and other membranes in neurons. *Proc. Natl. Acad. Sci. U. S. A.* **114**, E4859–E4867.
- Xiang, Y., Tanaka, Y., Patterson, B., Kang, Y.-J., Govindaiah, G., Roselaar, N., Cakir, B., Kim, K.-Y., Lombroso, A. P., Hwang, S.-M., et al.** (2017). Fusion of Regionally Specified hPSC-Derived Organoids Models Human Brain Development and Interneuron Migration. *Cell Stem Cell* **21**, 383–398.e7.
- Xie, Z., Sanada, K., Samuels, B. A., Shih, H. and Tsai, L. H.** (2003). Serine 732 phosphorylation of FAK by Cdk5 is important for microtubule organization, nuclear movement, and neuronal migration. *Cell* **114**, 469–82.
- Yamamoto, H., Mandai, K., Konno, D., Maruo, T., Matsuzaki, F. and Takai, Y.** (2015). Impairment of radial glial scaffold-dependent neuronal migration and formation of double cortex by genetic ablation of afadin. *Brain Res* **1620**, 139–152.
- Ye, T., Ip, J. P. K., Fu, A. K. Y. and Ip, N. Y.** (2014). Cdk5-mediated phosphorylation of RapGEF2 controls neuronal migration in the developing cerebral cortex. *Nat. Commun.* **5**, 4826.
- Ye, T., Fu, A. K. Y. and Ip, N. Y.** (2015). Emerging roles of Axin in cerebral cortical development. *Front. Cell. Neurosci.* **9**, 1–8.
- Ying, Q.-L., Stavridis, M., Griffiths, D., Li, M. and Smith, A.** (2003). Conversion of embryonic stem cells into neuroectodermal precursors in adherent monoculture. *Nat. Biotechnol.* **21**, 183–186.
- Yu, T. W., Chahrour, M. H., Coulter, M. E., Jiralerspong, S., Okamura-Ikeda, K., Ataman, B., Schmitz-Abe, K., Harmin, D. A., Adli, M., Malik, A. N., et al.** (2013). Using Whole-Exome Sequencing to Identify Inherited Causes of Autism. *Neuron* **77**, 259–273.
- Yu, I., Garnham, C. P. and Roll-Mecak, A.** (2015). Writing and Reading the Tubulin Code. *J. Biol. Chem.* **290**, 17163–72.
- Zhang, J., Neal, J., Lian, G., Shi, B., Ferland, R. J. and Sheen, V.** (2012a). Brefeldin A-inhibited Guanine Exchange Factor 2 Regulates Filamin A Phosphorylation and Neuronal Migration. *J. Neurosci.* **32**, 12619–12629.

- Zhang, J., Nuebel, E., Daley, G. Q., Koehler, C. M. and Teitell, M. A.** (2012b). Metabolic regulation in pluripotent stem cells during reprogramming and self-renewal. *Cell Stem Cell* **11**, 589–95.
- Zhang, J., Neal, J., Lian, G., Hu, J., Lu, J. and Sheen, V.** (2013). Filamin A Regulates Neuronal Migration through Brefeldin A-Inhibited Guanine Exchange Factor 2-Dependent Arf1 Activation. *J. Neurosci.* **33**, 15735–15746.
- Zhang, T., Zhang, S., Song, X., Zhao, X., Hou, C., Li, Z. and Gao, J.** (2019). Loss of Lgl1 Disrupts the Radial Glial Fiber-guided Cortical Neuronal Migration and Causes Subcortical Band Heterotopia in Mice. *Neuroscience* **400**, 132–145.
- Zhou, F.-Q. and Snider, W. D.** (2005). Cell biology. GSK-3beta and microtubule assembly in axons. *Science* **308**, 211–4.
- Zhu, X., Need, A. C., Petrovski, S. and Goldstein, D. B.** (2014). One gene, many neuropsychiatric disorders: lessons from Mendelian diseases. *Nat. Neurosci.* **17**, 773–781.
- Zhu, X., Ai, Z., Hu, X. and Li, T.** (2016). Efficient Generation of Corticofugal Projection Neurons from Human Embryonic Stem Cells. *Sci. Rep.* **6**, 28572.
- Zhu, Y., Wang, L., Yin, F., Yu, Y., Wang, Y., Shepard, M. J., Zhuang, Z. and Qin, J.** (2017). Probing impaired neurogenesis in human brain organoids exposed to alcohol. *Integr. Biol. (Camb)*. **9**, 968–978.

APPENDIX

I. LIST OF FIGURES

Figure 1: Mammalian cortical development exemplified in the mouse.	4
Figure 2: Differences between Mouse and human dorsal cortical development.	17
Figure 3: Cellular and morphological defects associated with neuronal migration disorders.	19
Figure 4: Heterogeneity and complexity of neuronal migration disorders at the genetic, cellular and clinical levels.	23
Figure 5: <i>In vivo</i> and <i>in vitro</i> model systems of neurodevelopment and its disorders.	29
Figure 6: Suggested mechanism underlying neurodevelopmental defects in HSP-SPG11.	166
Figure 7: Frequencies of phenotypic traits identified in 25 SPG11 patients.	170
Figure 8: Scheme illustrating phenotypic heterogeneity associated with HSP.	171
Figure 9: Scheme depicting the effect of <i>FICD</i> KD or OX by electroporation of aRG in germinal zones of COs.	172
Figure 10: Proteins with function in vesicle trafficking and proteostasis are enriched among CO AMPylation targets.	175
Figure 11: Hourglass model of AMPylation remodeling and metabolism remodeling.	176
Figure 12: Overmigration of neurons upon acute <i>Ece2</i> KD <i>in vivo</i>	188
Figure 13: Key findings of each study and highlighted common mechanisms.	192

II. LIST OF TABLES

Table 1: Traditional classification scheme for malformations of cortical development (MCDs).	18
Table 2: Genes known to cause NMDs in humans upon disruption.	21
Table 3: DDD patient with FICD variant and Decipher patients with tubulin, kinesin and myosin variants resulting in gain or loss of possible AMPylation site and nervous system phenotypes.	180

III. LIST OF ABBREVIATIONS

2D	two-dimensional	MAP	microtubule-associated protein
3D	three-dimensional	MCDs	malformations of cortical development
α	anti	MDS	Miller-Dieker syndrome
ac-tub	acetylated tubulin	MeOH	methanol
AJ	adherens junction	MGE	medial ganglionic eminence
AMP	adenosine monophosphate	min	minute(s)
aRG	apical radial glia	MS	mass spectrometry
ANOVA	analysis of variance	MTs	microtubules
ASD	autism spectrum disorder	MZ	marginal zone
BPs	basal progenitors	NECs	neuroepithelial cells
bIPs	basal intermediate progenitors	NGS	next generation sequencing
bRG	basal radial glia	NMDs	neuronal migration disorders
Cas	CRISPR-associated protein	NPCs	neural progenitor cells
CHIR	CHIR99021	OSVZ	outer subventricular zone
COL	collagen	OX	overexpression
COs	cerebral organoids	PH	periventricular heterotopia
CNVs	copy number variants	Phos	phosphoramidon
CP	cortical plate	(i)PSCs	(induced) pluripotent stem cells
CRISPR	Clustered Regularly Interspaced Short Palindromic Repeats	PTM	posttranslational modification
Ctx	cortex	RNM	radial neuronal migration
d	day(s)	RT	room temperature
detyr-tub	detyrosinated tubulin	SAPs	short apical precursors
E	embryonic day	SBH	subcortical band heterotopia
ECM	extracellular matrix	scRNA-seq	single-cell RNA sequencing
ER	endoplasmic reticulum	SEM	standard error of the mean
F-actin	fibrillar actin	SNV	single nucleotide variant
FACS	fluorescence activated cell sorting	SPG	spastic paraplegia gene
FDA	Food and Drug Administration	Str	striatum
GEs	ganglionic eminences	SP	subplate
GO	gene ontology	SPG	spastic paraplegia gene
h	hour(s)	SPG11	HSP caused by <i>SPG11</i> mutation(s)
HSP	hereditary spastic paraplegia	SVZ	subventricular zone
Hsp	heat shock protein	tg	thapsigargin
IFL	inner fiber layer	Tide	Tideglusib
IKNM	interkinetic nuclear migration	TNM	tangential neuronal migration
ISVZ	inner subventricular zone		

IZ	intermediate zone	tyr-tub	tyrosinated tubulin
KD	knockdown	UPR	unfolded protein response
(c)KO	(conditional) knockout	VZ	ventricular zone
LGE	lateral ganglionic eminence	WES	whole exome sequencing

IV. LIST OF PUBLICATIONS

Under Revision

Pavel Kielkowski⁺, **Isabel Y. Buchsbaum⁺**, Volker C. Kirsch, Nina C. Bach, Micha Drukker, Silvia Cappello, Stephan A. Sieber, *FICD activity and AMPylation remodelling modulate human neurogenesis.*

Under revision in *Nature Communications*.

Christina Kyrousi, Adam C. O'Neill, Agnieszka Brazovskaja, Zhisong He, Laure Coquand, Rossella Di Giaimo, Davide Mei, Matteo Lenge, Cristiana Cruceanu, **Isabel Y. Buchsbaum**, Shahryar Khattak, Guimiot Fabien, Elisabeth Binder, Frances Elmslie, Renzo Guerrini, Alexandre D. Baffet, Barbara Treutlein, Stephen P. Robertson, Silvia Cappello, *LGALS3BP modulates local gyrification in the human brain.*

Under revision in *Cell*.

Isabel Y. Buchsbaum, Pavel Kielkowski, Grazia Giorgio, Adam C. O'Neill, Rossella di Giaimo, Christina Kyrousi, Shahryar Khattak, Stephan A. Sieber, Stephen P. Robertson and Silvia Cappello, *ECE2 regulates Neurogenesis and Neuronal Migration during Cortical Development.*

Under revision in *EMBO Reports*.

Published

Francesc Perez-Branguli⁺, **Isabel Y Buchsbaum⁺**, Tatyana Pozner⁺, Martin Regensburger, Wenqiang Fan, Annika Schray, Tom Borstler, Himanshu Mishra, Daniela Gräf, Zacharias Kohl, Jürgen Winkler, Benedikt Berninger, Silvia Cappello and Beate Winner, *Human SPG11 cerebral organoids reveal cortical neurogenesis impairment. Human Molecular Genetics* 2019 Mar 15; 28(6): 961–971. doi: 10.1093/hmg/ddy397

Isabel Yasmin Buchsbaum and Silvia Cappello, *Neuronal migration in the CNS during development and disease: insights from in vivo and in vitro models. Development* (2019) 146, dev163766. doi:10.1242/dev.163766